学位論文

Search for heavy new particles decaying into $t\bar{t}$ in proton-proton collisions at $\sqrt{s} = 13$ TeV

（重心系エネルギー 13 TeV の陽子陽子衝突における
トップクォーク対に崩壊する重い新粒子の探索）

平成28年7月博士（理学）申請

東京大学大学院理学系研究科
物理学専攻

小林 愛音

Search for heavy new particles decaying into $t\bar{t}$ in proton-proton collisions at $\sqrt{s} = 13$ TeV

Doctor's thesis

Aine Kobayashi

35-137024
Department of Physics
Graduate School of Science, University of Tokyo
8th July 2016

Abstract

The LHC accelerator is expanding the energy frontier of searching new particles and revealing unsolved mystery to understand the universe. The ATLAS experiment is one of the projects operated at the LHC. In Run2, the center-of-mass energy of LHC has increased, the detectors have been upgraded and object reconstruction methods in this study improved for searching heavier mass particles and for precision measurements.

This study searches for beyond the Standard Model (BSM) physics using the $t\bar{t}$ final states, where the signature is a resonant structure in the $t\bar{t}$ mass spectrum. The analysis is based on the production of lepton plus jets channel in the boosted topology recorded by the ATLAS detector with LHC proton-proton collisions at $\sqrt{s} = 13$ TeV. The integrated luminosity was 3.2 fb^{-1} in 2015. For higher efficiency at the boosted regime, small radius jets reconstructed by a track based algorithm was used for b-jet identification, and the Standard Model $t\bar{t}$ background that has the same final state as the signal was reduced using a cut on variables related to the production angle. No significant excess of events above the background expectation was found, and limits were set on the cross-section times branching fraction for the production of top-color assisted technicolor model Z' and RS bulk KK graviton. A new lower limit on the mass of Z' was obtained. Mass of Z' was excluded in the range $m_{Z'} < 2.4$ TeV for $\Gamma_{Z'}/M_{Z'} = 1.2$ % and $m_{Z'} < 3.0$ TeV for $\Gamma_{Z'}/M_{Z'} = 3.0$ %. For the KK graviton, the relative cross-section with respect to the model value was excluded above 2 for $m_{KK} = 1$ TeV and 3 for $m_{KK} = 0.75$ TeV.

Contents

Chapter 1

Introduction

The Standard Model [1] is the most successful particle physics scenario which explains the behavior of matter and interactions. This model has been examined by many experiments.

The basic building blocks of the Standard Model are fermions, gauge bosons and Higgs particle (Figure 1.1). The fermions compose matter, and the bosons mediate fundamental forces in nature, strong interaction, weak interaction and electromagnetic interaction but not for gravitational interaction. The discovery of the Higgs boson [2,3] at the Large Hadron Collider (LHC) [4] in 2012 completed the Standard Model predictions. The Higgs mechanism gives mass for all elementary particles via the spontaneous breakdown of gauge symmetry and the vacuum expectation value of the Higgs field.

However, some theoretical considerations point out that the Standard Model is not the ultimate theory and new physics called Beyond the Standard Model (BSM) is needed. For example, the hierarchy problem, the mass of neutrino, matter-antimatter asymmetry, dark energy and dark matter can not be explained by the Standard Model.

In the four fundamental forces of nature, the electromagnetic interaction and the weak interaction are unified by the electroweak interaction, described as $\mathrm{SU}(2)_\mathrm{L} \times \mathrm{U}(1)_\mathrm{Y}$ gauge theory. Here, the $\mathrm{SU}(2)_\mathrm{L}$ and $\mathrm{U}(1)_\mathrm{Y}$ are independent of each other with coupling constant g2, g1, respectively. Using the strong interaction described as $\mathrm{SU}(3)_\mathrm{C}$ gauge theory with coupling constant g3, the Standard Model can be expressed as $\mathrm{SU}(3)_\mathrm{C} \times \mathrm{SU}(2)_\mathrm{L} \times \mathrm{U}(1)_\mathrm{Y}$ gauge and its interaction was inspected for a long time by many experiments such as in LEP [6] and Tevatron [7] experiments.

Under the spontaneous gauge symmetry breaking, the Grand Unified Theories (GUT) [8–10] try to unify the three of the four fundamental forces, electroweak interaction, and strong interaction. Understanding on the mechanism of the electrodes symmetry breaking is being worked out by the CERN LHC [4] experiment. The large discrepancy between GUT or Plank scale ($M_\mathrm{Pl} = 10^{16} \sim 10^{19}$ GeV) and the electroweak scale ($M_\mathrm{electroweak} \sim 10^2$ GeV) is called the hierarchy problem. Accompanying with this problem, there is fine tuning problem caused by the scale of cutoff Λ which is the upper limit of the Standard Model valid scale, therefore the quantum correlation for the Higgs mass will diverge [11]. For instance, the Higgs mass, $m_h \sim 126$ GeV,

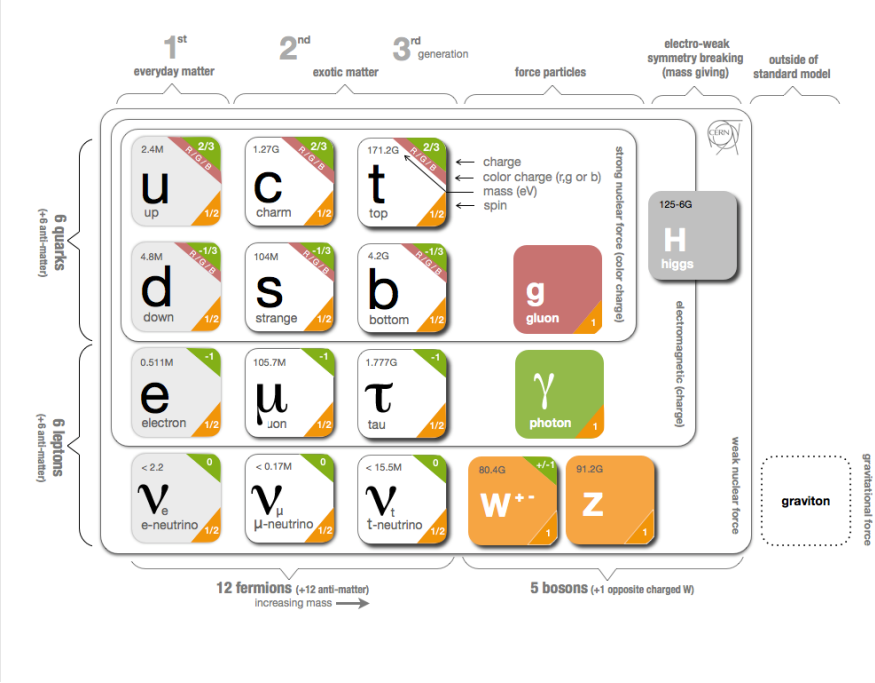

Figure 1.1: The Standard Model, Higgs boson was discovered in July 2012 [5].

can be written with the quantum correlation as;

$$m_h^2 \approx m_{h0}^2 + \frac{\lambda_f^2}{8\pi^2} N_c^f \Lambda^2 \equiv m_{h0}^2 + m_{h\ \text{1-loop}}^2, \tag{1.1}$$

where m_{h0} is the bare Higgs mass and the remainder is the 1-loop correction term. f is a Dirac fermion that receives its mass from the Higgs boson, λ_f is Yukawa coupling and N_c^f is number of colors of fermion f. Here, naturalness is defined as $N^0 \equiv m_{h\ \text{1-loop}}^2/m_h^2$. In order not to the cancellation of the bare mass and the 1-loop correction to the Higgs mass at large Λ, fine tuning $N^0 \sim 10^{30}$ is needed. To explain these problem, there are several models extended from the Standard Model such as supersymmetry (SUSY), extradimension and technicolor.

SUSY

On the assumption of SUSY, a new SUSY particle is predicted for each Standard Model particle which also couples to gauge boson. Then, the Higgs mass can be written as equation 1.2

$$m_h^2 \approx m_{h0}^2 + \frac{\lambda_f^2}{8\pi^2} N_c^f \left(m_{\tilde{f}^2} - m_f^2\right) \ln\left(\Lambda^2/m_{\tilde{f}^2}\right), \tag{1.2}$$

where $\tilde{f}$ is the superpartner of fermion f. Then, the quadratic dependence on Λ is reduced to a logarithmic, hence avoiding the fine tuning provided masses of the SUSY particles are not far from TeV region.

Extradimension

Another class of models is based on higher dimensional space. If gravity propagate in the extra dimension, the gravity force appears weak in the ordinary space-time. In this way, hierarchy problem can be avoided. One of the leading models is Randall-Sundram (RS) model [12–15] which incorporates warped extra dimension, and predicts a number of Kaluza-Klein states in TeV scale.

Technicolor

Top color-assisted technicolor model [16, 17] also naturally explains the gauge hierarchy with new interaction. The Higgs Lagrangian can be modified with a new fermion sector suitable for new strong gauge interaction (technicolor), then both hierarchy problem and fine-tuning can be explained. The details are described in section 2.1.1.

These models predict new particles that couple with top quark, and they may appear as heavy resonances decaying into $t\bar{t}$. There are also other scenarios which predict new particles decaying into $t\bar{t}$ such as SUSY model [18, 19] and scenarios including heavier Higgs bosons [20]. This thesis describes the study performs model independent analysis, and searches new resonances in the $m_{t\bar{t}}$ spectrum.

There is a long history of $t\bar{t}$ resonances searches. Several benchmark models such as technicolor Z' (see section 2.1.1), extra dimension RS model such as KK gluon [21] and KK graviton (see section 2.1.2) have been tested. The CDF [22, 23] and DØ [24] experiments have used ~ 5 fb^{-1} luminosity and excluded a Z' mass < 945 GeV. The CMS experiments in Run1 with the center-of-mass energy $\sqrt{s} = 8$ TeV has set limit on Z' whose width ($\Gamma_{Z'}/M_{Z'}$) was 1.1 % in a mass region of < 2.4 TeV and a KK gluon with mass< 2.8 TeV using the integrated luminosity of 19.7 fb^{-1} combined with the all-hadronic, dileptonic and one lepton decay channels [25]. In the ATLAS Run1 analysis using integrated luminosity about 20 fb^{-1} with center-of-mass energy $\sqrt{s} = 7$ and 8 TeV, the lower limit on the masses of Z' whose width ($\Gamma_{Z'}/M_{Z'}$) was 1.2 % (Figure 1.2) and KK gluon were set at 1.8 TeV and 2.1 TeV, respectively [26, 27].

In Run2, with the higher collision energy of $\sqrt{s} = 13$ TeV, it is expected that the sensitivity to higher mass resonances will increase substantially. For example, the cross section for production of Z' of 2 TeV will increase by factor of 5 compared to $\sqrt{s} = 8$ TeV [28]. In addition, this study introduces improvements of analysis; new b-tagging of higher efficiency, improvement of top tagging and new cuts for reduction of the Standard Model backgrounds.

1.1 Objective and organization

This thesis describes the study of searching heavy new particles decaying into $t\bar{t}$ using $\sqrt{s} =$ 13 TeV with ATLAS experiment. Chapter 2 describes physics motivation for searching such particles. Though keeping model independent search, benchmark models are needed for limit setting. Chapter 3 describes the brief overview of analysis strategy preparing for introduce the LHC ATLAS experiments in Chapter 4 and datasets used in this analysis as described in Chapter 5. Energy frontier experiment LHC allows to access heavier new particle. Chapter 6 shows

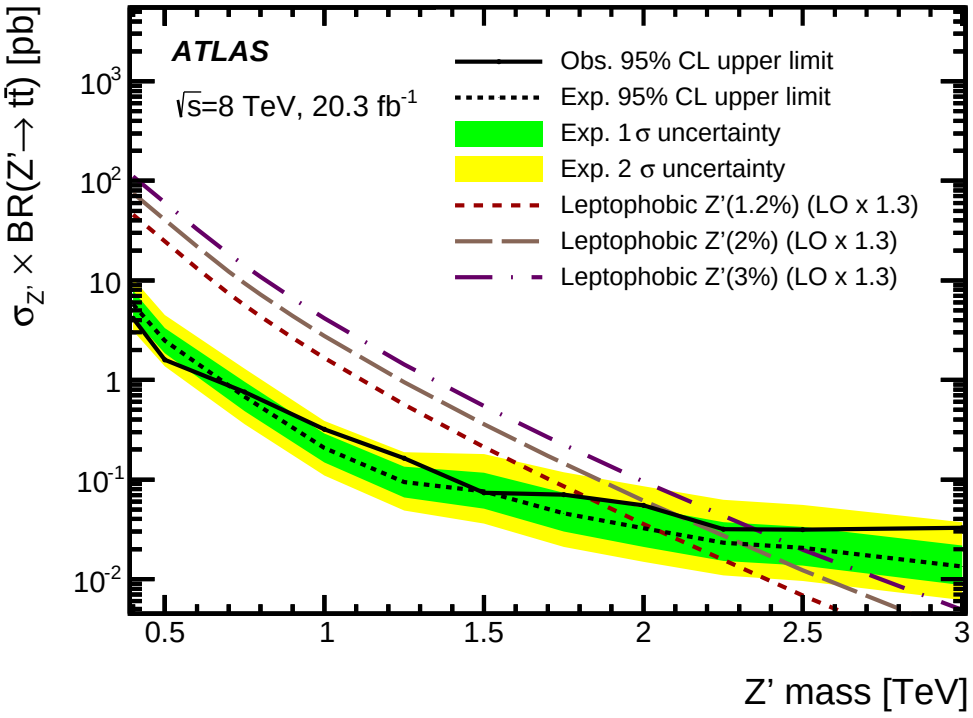

Figure 1.2: The limits on the Topcolor-assisted-technicolour Z' in Run1 analysis [26].

how objects are reconstructed for analysis. Some techniques to search boosted objects are used. As described in Chapter 3, three jets from hadronically decaying top are merged as one large-R jet. In the higher center-of-mass energy, there are pile-up effects (Chapter 5). The technique of large-R jet reconstruction is applied for trimming algorithm to reduce the pile-up problem and to recluster the subjets. How to identify top from multi-jet background are also described. Chapter 7-8 explain event selection using the reconstructed objects. The dominant background is the Standard Model $t\bar{t}$, which is difficult to reduce by a previous strategy. Then, by using the center-of-mass angle related variables, a new cut was developed to reduce the Standard Model background and not to lose signals. In the 'dense' environment where jets are merged, there is a low b-tagging efficiency problem with previous technique. Then, using the new technique, b-tagging with smaller radius track-jet solves this problem and higher efficiency is obtained. A few background components are estimated by data driven method to evaluate correction factors as described in Chapter 9. Chapter 10 discusses the systematic uncertainties mainly related to the reconstructed objects and invariant $t\bar{t}$ spectrum. Chapter 11 presents a procedure for limit setting and results obtained with a profile-likelihood ratio test. Finally, summary and conclusion are given in Chapter 12.

The author checked everything written for necessary procedure for analysis. Especially the author contributed to develop new analysis method; the b-tagging with a smaller radius track-jet and new cut to reduce the Standard Model backgrounds. In addition, the author works for high-p_T b-tagging calibration with di-jet event [29], which expands b-tagging calibration area up to 1 TeV with smaller systematic uncertainties than that of Run1 analysis.

Chapter 2

Physics motivation

Top quark is the heaviest elementary particle in the Standard Model and its mass, ~ 173.2 GeV [30], is close to the electroweak symmetry breaking (ESB) scale and could be related to the hierarchy problem. The existence of a third generation including top quark was predicted by M.Kobayashi and T.Maskawa for explanation of the CP violation via a Kaon decay in 1973 [31]. Top quark was discovered in Tevatron in 1995 [32] by the CDF experiment [33, 34] and DØ experiment [35]. It has a large Yukawa coupling to the Higgs boson and is expected to have couplings to new particles of the beyond the Standard Model. This is why the $t\bar{t}$ resonance has unique role in terms of the searches for beyond the Standard Model physics.

This study aims to find a new resonance in the top-antitop mass spectrum. The decay products have boosted mass spectrum when the invariant $t\bar{t}$ mass is large. From constraint of the CKM matrix, top quark decays predominantly into a b quark and a W boson ($t \to b + W$). This search is designed to be model independent since there are many models predicting new particles decaying into $t\bar{t}$. As benchmark models, Z' and KK graviton are chosen (see section 2.1); their parameters such as production mechanism, spins, acceptance and width are different from each other.

2.1 Benchmark models

The benchmark models used in this analysis described in this section.

2.1.1 Top-color (TC) model

Leptophobic TC Z' boson (Z'_{TC2})

Simple top technicolor models have been excluded by precision measurement of EW scale [36]. Therefore, the extended technicolor (ETC), which has additional gauge interactions is considered as more influential model; top color-assisted technicolor model [16] predicts Z' decay into $t\bar{t}$, and this model requests the existence of new SU(3) symmetries. The Λ_{ETC} is TeV scale, and this gives quark mass to $0.1 \sim 1$ GeV. Furthermore, new slow running of technicolor model called walking

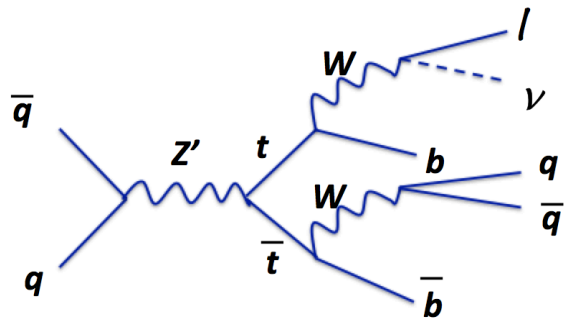

Figure 2.1: The Feynman diagram of the $Z' \to t\bar{t}$.

technicolor can explain the 126 GeV Higgs mass [37]. Also, this model naturally explains the gauge hierarchy. The Feynman diagram of the $Z' \to t\bar{t}$ is shown in Figure 2.1. The cross-section and branching fraction are calculated in references [28, 38, 39] and shown in Figure 2.2. A Z' is produced from $q\bar{q} \to Z'$ process and has spin 1, $\Gamma/m = 0.01 \sim 0.02$.

2.1.2 Randall-Sundrum warped extra-dimension model

Since energy scale of the gravity is too smaller than that of the other forces in the nature, this model predicts an extra dimension in which gravity would propagate [40].

Bulk Kaluza-Klein (KK) Graviton (G_{KK})

A KK graviton is produced from $gg \to G^*$ and $q\bar{q} \to G^*$, has spin 2, $\Gamma/m = 0.03 \sim 0.06$. Figure 2.3 shows the branching ratio for G_{KK}. $G_{KK} \to t\bar{t}$ is the dominant decay mode at high mass region.

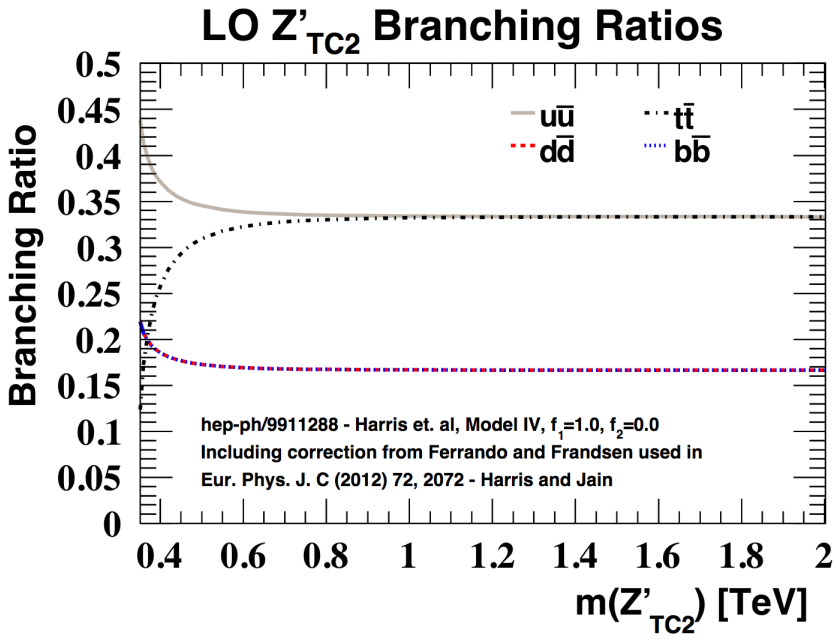

Figure 2.2: The branching ratios for the Z', and does not depend on the Z' width [26, 39].

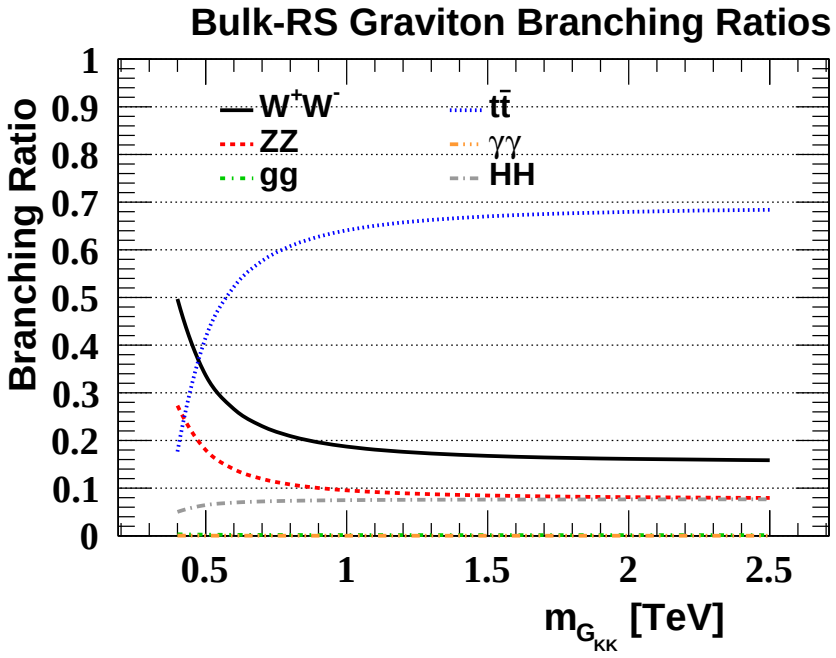

Figure 2.3: The branching ratios for the bulk-RS graviton G_{KK} [41].

Chapter 3

Analysis Strategy

In this thesis, the analysis focuses on searching for high mass $t\bar{t}$ resonances. While it basically follows the Run1 analysis, new techniques have been introduced; an improved b-tagging for achieve high efficiency in crowded jet environment, a top tagging algorithm for background rejection and new cuts to reduce the Standard Model $t\bar{t}$ background as described in Chapter 6-8.

The $t\bar{t}$ final states have three decay modes, categorized by the number of leptons from W bosons in the $t \to bW$ decay (nearly 100 % [1]). The W boson decays into lepton + neutrino or two quark pairs as shown in Figure 2.1. According to the combination of the two final states, there are di-lepton ($t\bar{t} \to b\ell\nu b\ell\nu$ final states), one lepton + jets ($t\bar{t} \to b\ell\nu bqq'$ final states) and all hadronic channel ($t\bar{t} \to bqq'bqq'$ final states). The one lepton + jets channel (semileptonic channel) has a large branching ratio of about 30 % (lepton = e and μ). This channel has smaller multi-jet background compared to the all hadronic channel. While the momentum of the neutrino is not directly measured, the kinematics of the final state objects can be fully reconstructed using the constrains from W decays into $\ell\nu$, and it is not the case for di-lepton + jets channel which involves two missing neutrinos. In this analysis, one-lepton + jets channel is used for the search.

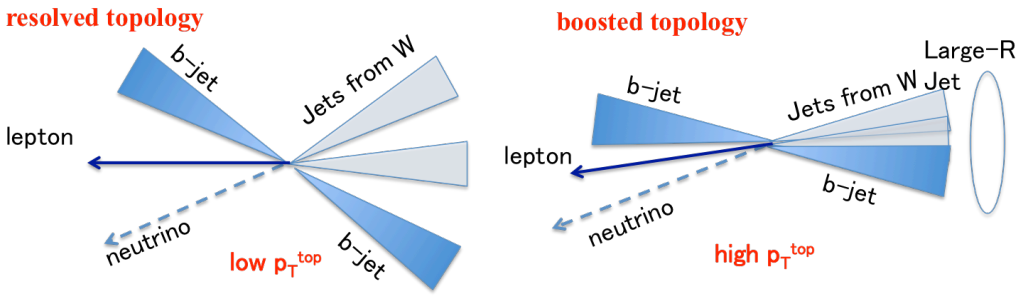

Figure 3.1: Schematic view of the signal topology, resolved regime (left) and boosted regime (right).

Figure 3.1 shows two topologies of the one lepton channel. When the top transverse momen-

tum p_T is low (decay of low mass $t\bar{t}$ system), the three jets from the hadronically decaying top are well separated ('resolved topology'). Kinematics of the top can be reconstructed using these three objects. As $t\bar{t}$ mass increases, the top momentum, p_T become higher. The decay products are highly boosted and enter the regime where jets are not well separated any more. Typical angular separation between 2-body decay products of a boosted heavy particle can be given by:

$$\Delta R \sim \frac{2m}{p_T}, \tag{3.1}$$

where p_T and m are the transverse momentum and the mass of the boosted decaying particle. Here a 2-body decay is considered for simplicity. At p_T above $700 \sim 800$ GeV, the three jets from $Wb \to q\bar{q}'b$ start to merge. Reconstruction of jet kinematics will become difficult in such a 'boosted topology'. Figure 3.2 shows the distance ΔR between W boson and b quark as a function of hadronically decaying top quark p_T. In this thesis, top quark p_T over 300 GeV is defined as boosted topology. A different approach is used here where the hadronically decaying top is reconstructed as a single wide jet which captures all the decay products from the top. As the focus of this analysis is on high mass $t\bar{t}$ resonance, analysis of the boosted topology is the main topic of this thesis. For completeness, a complementary analysis of the resolved topology is described in Appendix 12. Figure 3.3 shows a candidate event of boosted top quark pair production in the 2015 ATLAS data.

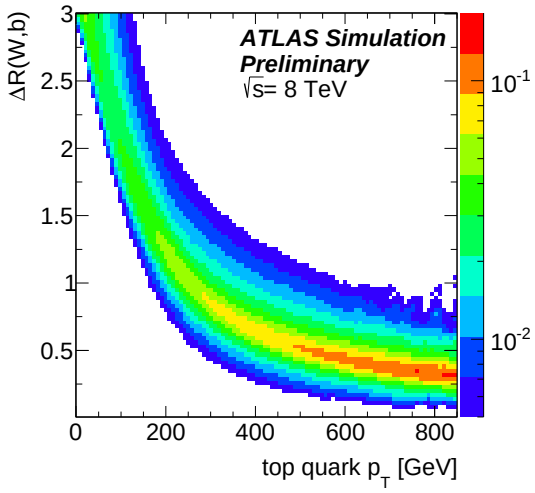

Figure 3.2: The distance ΔR between W boson and b quark from as a function of hadronically decaying top quark p_T [42].

The analysis of boosted $t\bar{t}$ search proceeds as follows.

- The hadronically decaying top is reconstructed as a large-R jet ($t \to Wb \to q\bar{q}'b$). Here, jet reconstruction radius parameter "R" is mentioned in section 6.2.2 and section 6.3.

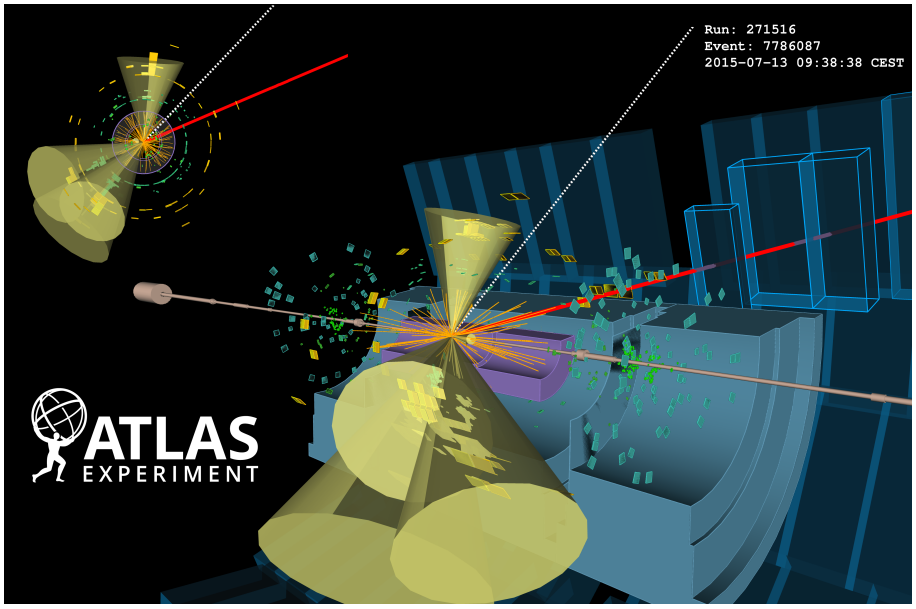

Figure 3.3: An event display of a boosted $t\bar{t}$ candidates ($b\mu\nu bqq$ final states) recorded by the ATLAS detector [43]. The red line shows the muon track (with $p_T \sim 50$ GeV), and the dashed line shows the direction of the neutrino (its magnitude is about 470 GeV). The green and yellow bars represent energy deposits in the calorimeters (the liquid argon and scintillating-tile calorimeters), and the four yellow cones are the small-radius ($R = 0.4$) jets (p_T is about $70 \sim 300$ GeV). The three overlapping small-R jets are reclustered as a large-R jet (radius parameter $R = 1.0$, see section 6.3) of $p_T \sim 600$ and its mass is ~ 180 GeV (the large-R jet is not shown explicitly).

- The leptonically decaying top is reconstructed as two visible objects; a lepton (electron or muon), one small-R jet from the b-quark, and a missing momentum due to the neutrino ($t \to Wb$ with $W \to \ell\nu$).
- At least one b-tagged jet is required to reduce background.
- Kinematics of the two top quarks are reconstructed, and mass of the $t\bar{t}$ system calculated to see if there is an excess in the mass distribution over the Standard Model background due to a new $t\bar{t}$ resonance.

Figure 3.4 shows a few examples of expected $t\bar{t}$ resonance signature as the $m_{t\bar{t}}$ distribution. High mass resonances show a tail of mass distribution to low value. This is mainly caused by two reasons; a part of the top decay products not fully captured by the large-R jet, and the long tail of Breit-Wigner resonance enhanced by the steeply rising parton distribution function (PDF) toward low x. Figure 3.5 shows a comparison of the Standard Model background and $t\bar{t}$ resonance signal. The background is mainly dominated by the Standard Model $t\bar{t}$ production where the final state topology is the same as the $t\bar{t}$ resonance signal. The other components in MC are single top, W+jets, Z+jets and diboson. An attempt of reducing such background is discussed in section 7.3.

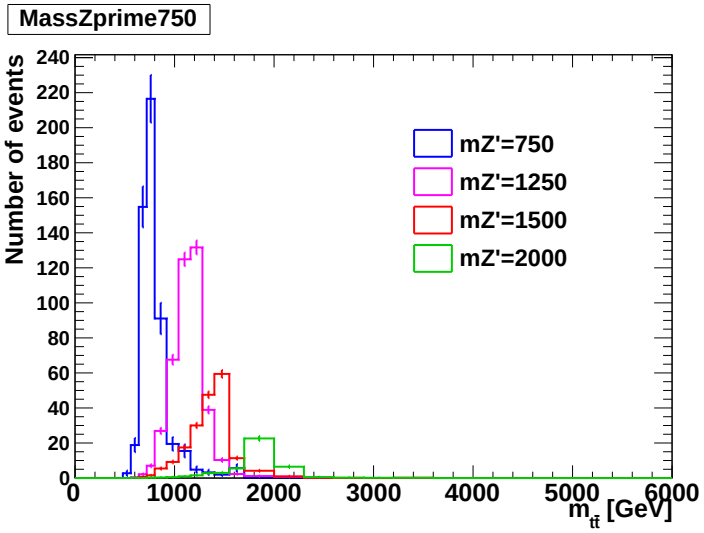

Figure 3.4: Example of the signal reconstructed invariant mass $m_{t\bar{t}}$ distribution.

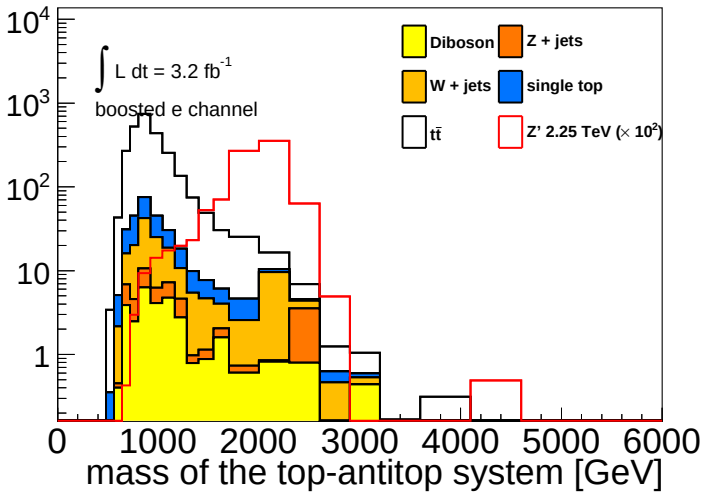

Figure 3.5: Example of the reconstructed invariant mass $m_{t\bar{t}}$ distribution comparing backgrounds (MC only) and signal (Z' histogram is scaled $\times 100$).

Chapter 4

LHC-ATLAS Experiment

This study was performed using the data collected by the ATLAS experiment at the LHC. Searching for new heavy resonances with boosted top signatures requires an energy frontier experiment. The LHC has upgraded the center-of-mass energy of proton-proton collisions. The general purpose detector ATLAS surrounds the collision point and detects event candidates which possibly include new physics. This chapter describes ATLAS detector focusing on the relevant points for this study. Full information can be fond in [44].

4.1 CERN

The European Organization for Nuclear Research, CERN (Conceille Européenne Recherche Nucéaire) [45] is located in the border area between Switzerland and France. CERN is the largest international collaboration to research into particle physics using the most largest instruments in the energy frontier, founded in 1954. As the days pass, CERN's accelerator has been evolved and the accelerators such as Proton Synchrotron and Large Electron-Positron collider (LEP) are utilized. To collide the protons, following accelerators are used; first, Linac2 accelerates protons to the energy of 50 MeV, Proton Synchrotron Booster accelerates the injected beam to the energy of 1.4 GeV, then Proton Synchrotron pushes the beam to 25 GeV and Super Proton Synchrotron accelerates the protons to 450 GeV. The protons are finally sent to the two beam pipes of the LHC ring and accelerated to 6.5 TeV. The four large experiments that uses LHC; ALICE, ATLAS, CMS and LHCb.

4.2 The Large Hadron Collider

The Large Hadron Collider (LHC) [4, 46] is the world largest proton-proton collider with the highest collision energy. It is installed in a circular tunnel of 27 km circumference, located about 100 m underground (see Figure 4.1). The number of events generated for one second in the LHC

collisions can be written in equation 4.1.

$$N_{\text{event}} = L\sigma_{\text{event}} \tag{4.1}$$

where σ_{event} is the cross section, and L is the machine luminosity. The two high luminosity experiments, both ATLAS [47] and CMS [48] designed to have peak luminosity of $L = 10^{34}\text{cm}^{-2}\text{s}^{-1}$.

At the Spring 2015, LHC has re-started head-on collisions with center-of-mass energy of 13 TeV with upgraded accelerator and detectors, and this run is called Run2. The peak instant luminosity recorded in 2015 was $L = 5 \times 10^{33}\text{cm}^{-2}\text{s}^{-1}$. The LHC parameters are summarized in Table 4.1

Table 4.1: LHC parameters [46, 49, 50].

	Design	Run1	Run2 (2015)
Center-of-mass energy (TeV)	14	8	13
Peak luminosity ($\text{cm}^{-2}\text{s}^{-1}$)	1.0×10^{34}	7.7×10^{33}	5.0×10^{33}
Number of bunches	2834	1374	2244
Bunch crossing (ns)	25	50, 75, 150	25, 50

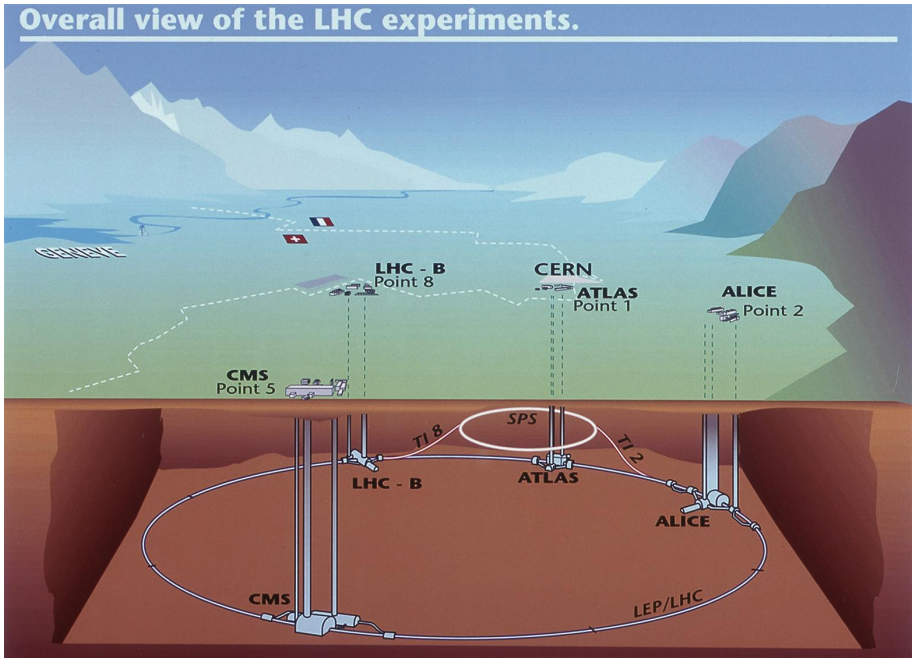

Figure 4.1: LHC and experiments **ATLAS Experiment ©1999-2016 CERN**

4.3 The ATLAS experiment

There are four large particle physics experiments of the interaction points of the LHC ring. ATLAS (A Toroidal LHC ApparatuS) is one of them and is a general purpose detector for new discoveries at the energy frontier. In the past, ATLAS discovered many physics [51], such as Higgs boson [2]. Currently, precision measurement of the Higgs boson and searching for the Beyond the Standard model are hot topics.

4.4 The ATLAS detector

The ATLAS detector (Figure 4.2) has a forward-backward symmetric cylindrical geometry covering nearly 4π solid angle around the collision point. Its size is 44 m long and 22 m diameter, and the weight is 7000 t. From inside, the detector consists of inner tracker, electromagnetic calorimeter, hadron calorimeter, and muon spectrometer. A solenoid magnet is installed between the inner tracker and the electromagnetic calorimeter, providing a uniform magnetic field of 2 T in the tracker volume. Troidal magnets surround the whole calorimeter and provide magnetic field for muon spectrometer. Figure 4.3 shows how the ATLAS detector works. From inside, photons are detected in the electromagnetic calorimeter with electromagnetic shower without tracks in the tracking chamber. Electrons are detected in both tracking chamber and electromagnetic calorimeter. Charged hadrons penetrate both tracking chamber and electromagnetic calorimeter with tracks, and detected in hadronic calorimter with hadrnic shower caused by strong interaction. Neutrons penetrate both tracking chamber and electromagnetic calorimeter without tracks and cause hadronic shower in hadronic calorimeter. Since muon does not have strong interaction, it does not cause the hadronic shower. Also, it has heavy mass (105.6 MeV), it does not cause electromagnetic shower either. Therefore, it penetrates all the ATLAS detector from inside to outside and is detected by the muon spectrometer located in the outer part of the ATLAS detector. After all the detectable objects reconstructed, neutrinos that do not cause any interaction are reconstructed as missing energy of the system.

The details are described below and for more information, see Reference [44]. After the end of the Run1, the ALTAS detector was upgraded for Run2 [52,53]. Damaged detectors and systems have been repaired. High radiation tolerance has been realized by employing robust electronics components since the center-of-mass energy increased from 8 TeV to 13 TeV. Additional muon chambers have been installed to increase the acceptance and additional new pixel detector named insertable *B*-layer (IBL) [54] has been installed as described in section 4.4.3.

4.4.1 Coordinate system

ATLAS used right-handed Cartesian coordinate system with its origin at the nominal interaction point. The beam axis is defined as z-axis. Transverse to the beam direction is the x-y plane. The x-axis points from the interaction point to the center of the LHC ring, and y-axis points upwards. In spherical coordinate, the polar angle from the z-axis is θ and azimuthal angle around the z axis

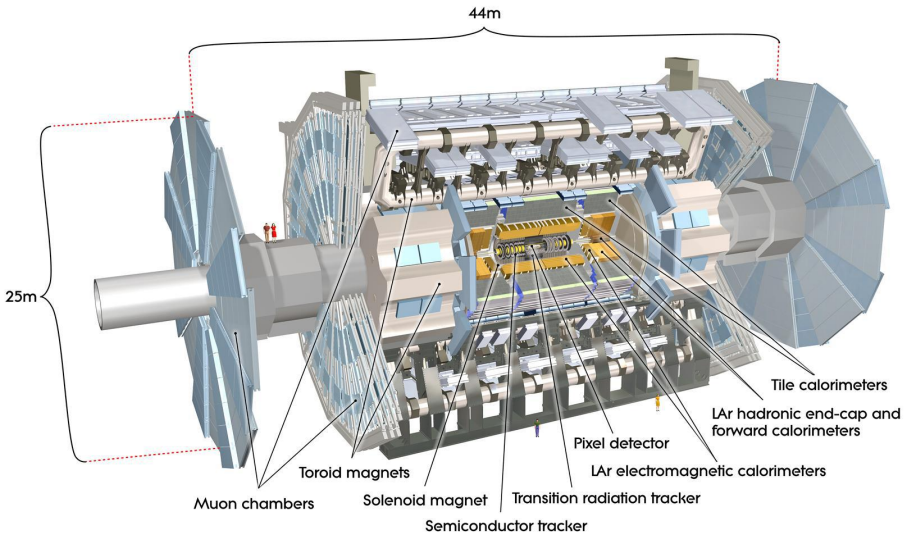

Figure 4.2: A schematic view of the ATLAS detector **ATLAS Experiment ©2008 CERN**

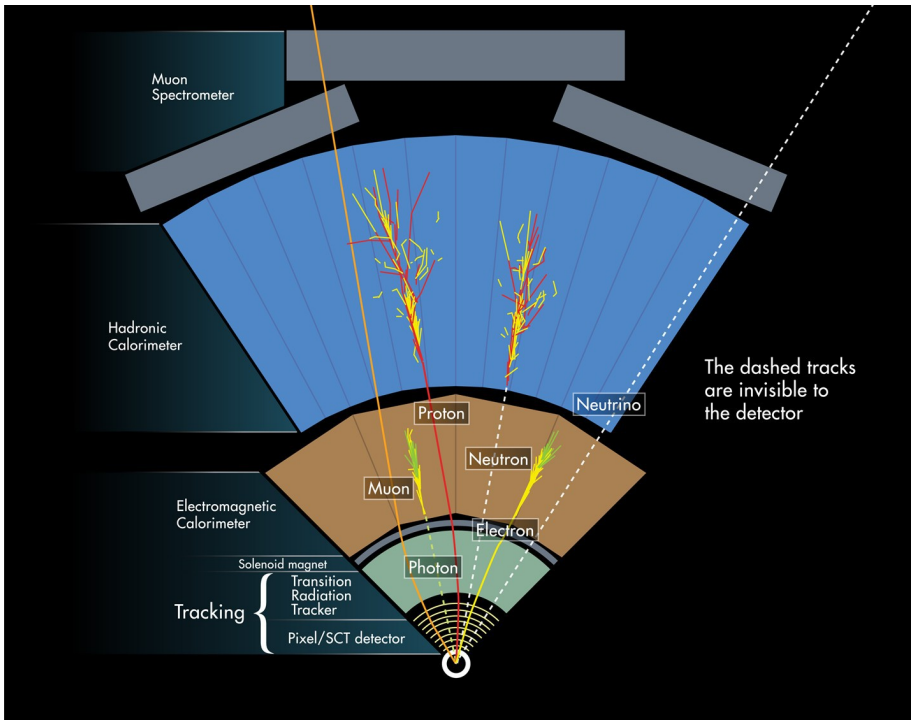

Figure 4.3: A schematic view of how the ATLAS detector functions works **ATLAS Experiment ©2008 CERN**

is ϕ. The nominal interaction point is at the center of the detector. The pseudorapidity is defined as:

$$\eta = -\ln\tan\frac{\theta}{2}. \tag{4.2}$$

And the distance of the two objects ΔR is defined as:

$$\Delta R = \sqrt{(\Delta\eta)^2 + (\Delta\phi)^2}. \tag{4.3}$$

4.4.2 Magnet System

The ATLAS magnet system consists of a thin superconducting solenoid and three large superconducting toroids.

Solenoid Magnet

The solenoid is aligned on the beam axis and has a 2 T axial magnetic field for the inner detector. This bends charged particles to ϕ direction for the measurement of p_T. To keep the resolution of the calorimeter, the thickness is minimized to 0.66 radiation length (X_0). The details are described in [55].

Toroidal Magnet

The geometry of magnet windings and the calorimeter steel is shown in Figure 4.4. It has the an eight fold symmetry coils. A barrel toroid (Figure 4.5) and two end-cap toroids are air-core super conducting coils producing toroidal magnetic field of 0.5 T for the muon detectors in the central region and 1 T in the end-cap region, respectively. This makes magnetic field of ϕ direction to measure muon p_T with good resolution up to large η.

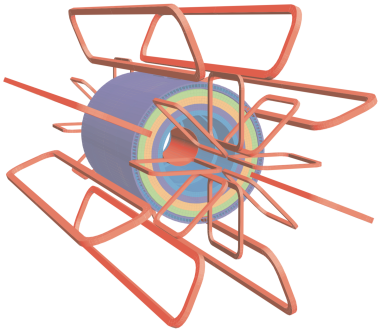

Figure 4.4: The spacial arrangement of the coil windings. The eight barrel toroid coils and the end-cap coils are uniquely arranged [44].

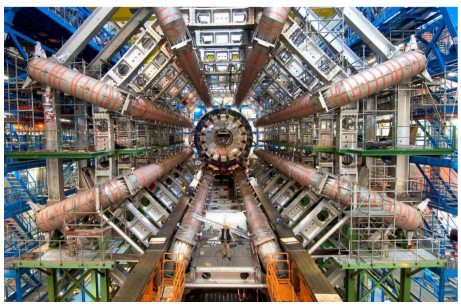

Figure 4.5: Barrel Toroid with symmetry structure from the underground cave in installing [44].

4.4.3 Inner Detector

The role of ATLAS Inner Detector (ID) is to reconstruct charged particle tracks, to measure p_T and charge of the tracks. The ID is immersed in a 2 T solenoid field. As shown in Figure 4.6, it covers the pseudorapidity range $|\eta| < 2.5$. It consists of three independent layers; Pixel detector (with Insertable *B*-layer), Silicon micostrip Tracker (SCT) and Transition Radiation Tracker (TRT). Figure 4.7 shows the schematic view of the inner detector and outer tracking detector.

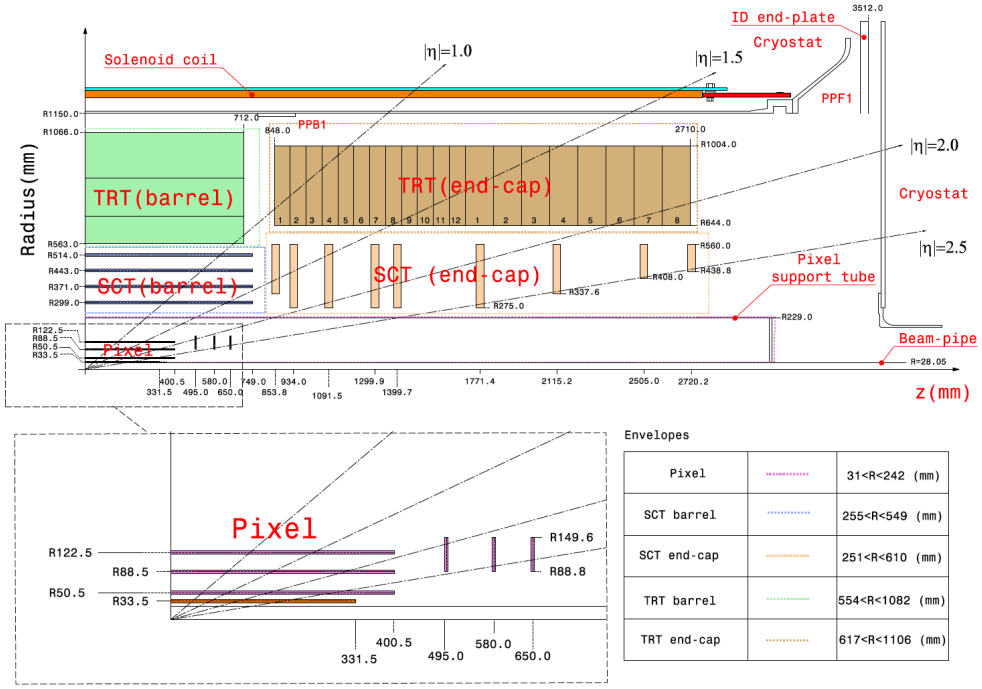

Figure 4.6: Schematic view of the *rz* cross section of the inner detector [56].

Pixel detector

In the inner radius, pixel detectors (Figure 4.8) that determine collision points and vertices have high position resolution of 10 μm for *r*-ϕ direction and 115 μm for *z* direction. The pixel size is 50×400 μm^2 and 50×600 μm^2 and there are a total of 80 M readout channels. In addition to the three barrel layers and two end-caps, the insertable *B*-layer (IBL) [54] has been newly-installed after Run1 as the fourth layer between a new beam pipe and the inner Pixel layer (*B*-layer). The IBL is located close to the interaction point (33.25 mm from the beam) in order to improve the tracking performance. Figure 4.10 shows the definition of transverse and longitudinal track parameters. The d_0 is the transverse impact parameter (the closest approach of the track to the beam axis), and σ_{d0} is its resolution. z_0 is the longitudinal impact parameter with respect to the

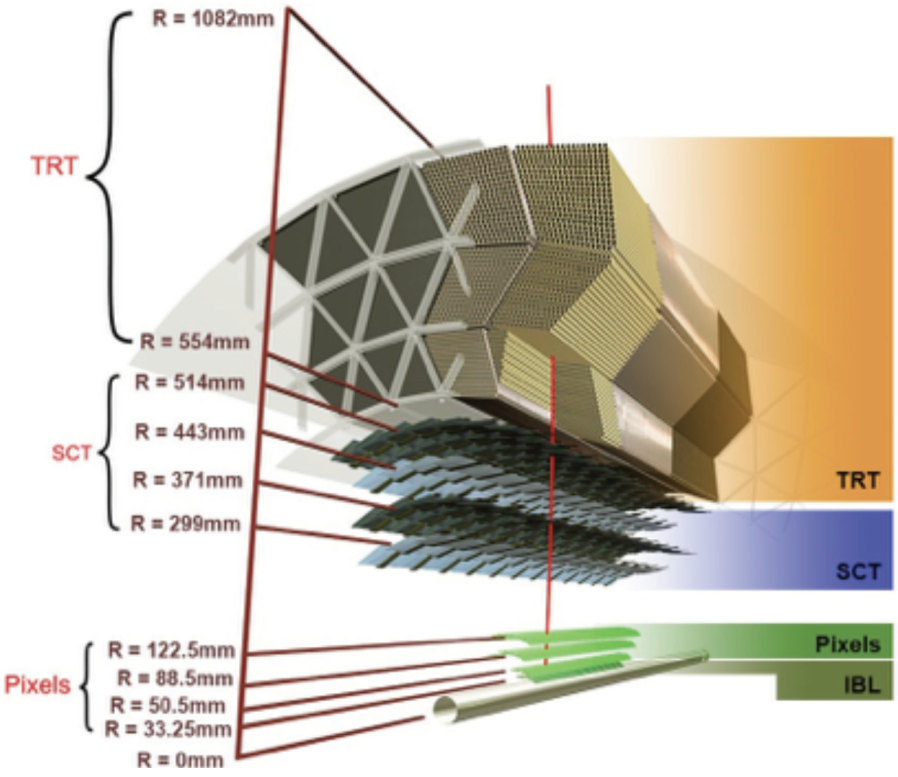

Figure 4.7: Schematic view of the inner derector **ATLAS Experiment ©2016 CERN**

primary vertex, and θ is the polar angle of the track. The transverse impact parameter resolution improved in particular in the low p_T region. Figure 4.9 shows the improvement of a transverse impact parameter resolution σ_{d0}. This is the comparison data without (2012) and with (2015) the IBL.

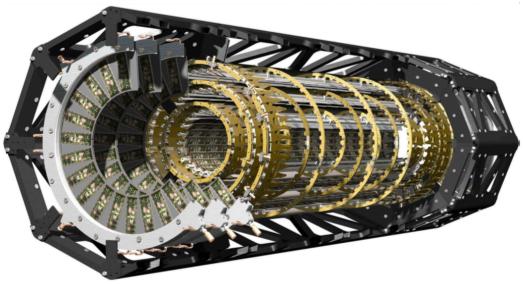

Figure 4.8: The pixel detector, showing individual barrel and end-cap modules [44].

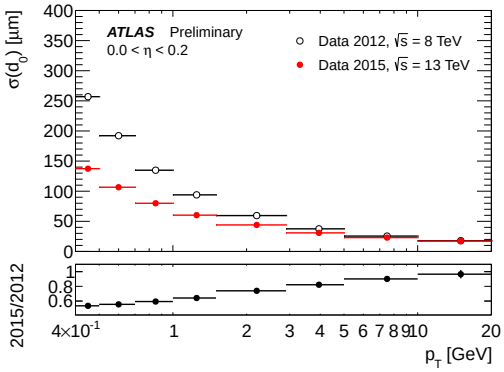

Figure 4.9: The transverse impact parameter resolution d_0, comparing with (2012) and without (2015) the IBL [57].

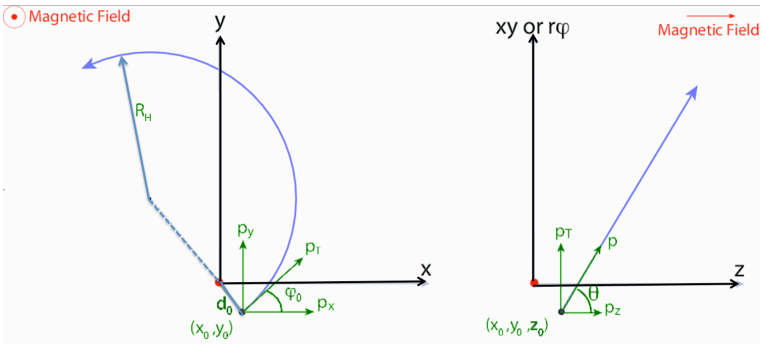

Figure 4.10: The definition of transverse and longitudinal track parameters [58].

Silicon micostrip Tracker (SCT)

The second part of ID is a silicon strip tracker (SCT). It provides high-resolution pattern recognition (17 μm for r-ϕ direction and 580 μm for z direction). As shown in Figure 4.11, each module consists of two back to back sensors of small angle stereo layout ($\pm$20 mrad), and the array of modules are mounted in four coaxial cylinders in the barrel [59, 60] and nine disk layers in each end-cap [61, 62]. The modules cover total of 63 m^2 of the surface and provide hermetic coverage with precision space-point measurements.

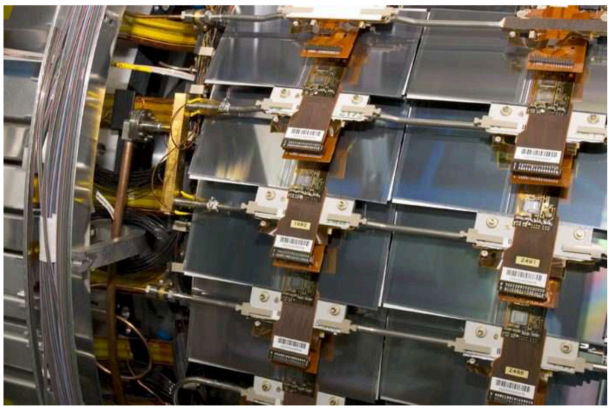

Figure 4.11: The module attached to the SCT scylinders in the barrel region [44].

Transition Radiation Tracker (TRT)

Outside of the SCT is the transition radiation tracker consisting of multi-layers of gaseous straw tube (polymide) elements [63]. It consists of 73 layers of straws in the barrel and 160 layers in the end-caps. The tube diameter is 4 mm and the wall thickness is minimal (35 μm). It is filled with xenon based gas (Xe:CO_2:O_2 = 70 : 27 : 3) to detect x-ray photons of transition radiation from electrons as well as ionization by charged particles.

4.4.4 Calorimetry

The Calorimeter system (Figure 4.12) is located outside of the inner detector covering the range of pseudorapidity $|\eta| < 4.9$. Calorimetry is composed of two parts. One is electromagnetic part that stops electronic magnetic showering and the other is hadronic part that stops hadrons by strong interaction.

Electromagnetic calorimeter (ECAL)

The liquid argon (LAr) sampling calorimeter with Pb plate absorber of accordion shape (Figure 4.13) is located in the barrel region (the pseudorapidity of $|\eta| < 1.475$) and the endcap region (the pseudorapidity of $1.375 < |\eta| < 3.2$). The system measure energy and position of the particles that have electromagnetic interaction. Total thickness of the module is at least 22 radiation length (X_0) at $\eta = 0$. The main part of the calorimeter is segmented in 0.025×0.025 in η-ϕ. The energy resolution of the barrel region measured by the test beam is $\sigma_E/E = 10\ \%/\sqrt{E} \oplus 0.7\ \%$ [64].

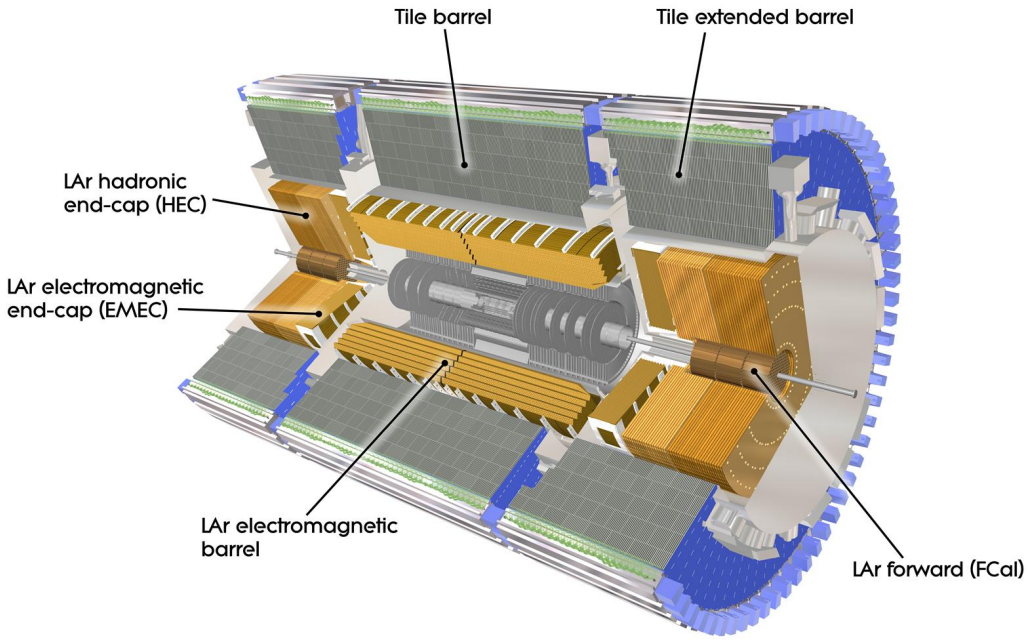

Figure 4.12: A schematic view of the calorimetry system. **ATLAS Experiment ©2008 CERN**

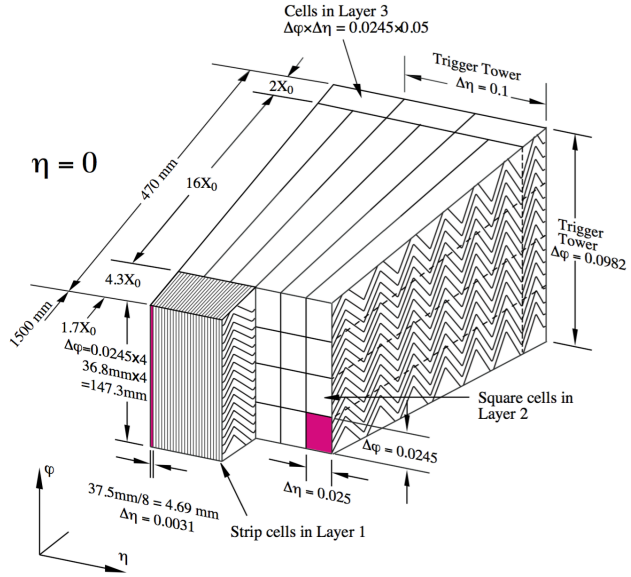

Figure 4.13: Schematic view of a ECAL accordion structure [44].

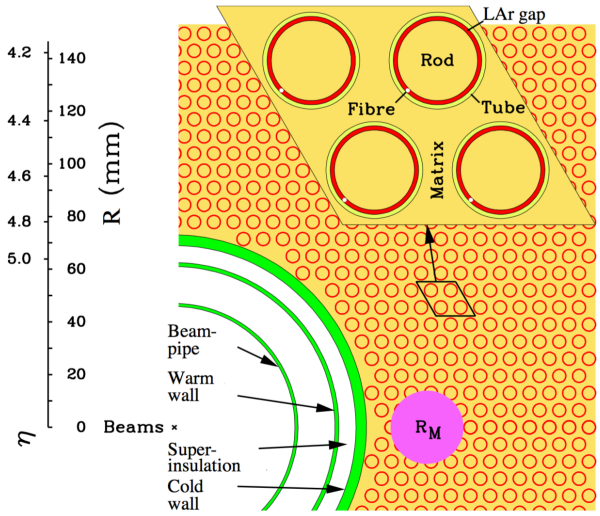

Figure 4.14: FCal electrode structure [44]. R_M is the Molière radius.

EM Forward Calorimeter (FCal)

A special LAr calorimeter is used in the forward region of $3.1 < |\eta| < 4.9$ in the end-cap since the radiation level in the forward region is higher than in the end-cap. Figure 4.14 shows the structure of the FCal electrode with the matrix of copper (Cu) plates, tubes oriented parallel to the beam direction and rods with LAr gap. The small LAr gap leads to a fast signal readout.

Hadron Forward Calorimeter

Hadron forward calorimeter located in the pseudorapidity of $3.1 < |\eta| < 4.9$ is similar to FCal, but uses tungsten (W) as absorber instead of copper. The space between rod and matrix is wide ($\sim 500\ \mu$m) enough to measure the hadronic interaction energy. It also reduces background levels in the muon detector, has 10 interaction lengths thick.

Hadron Tile Calorimeter

The tile calorimeter is placed outside of the EM calorimter covering the pseudorapidity of $|\eta| < 1.7$. It is a sampling calorimeter using steel as the absorber and plastic scintillator for sampling. The total thickness is 9.7 interaction length (λ) at $\eta = 0$.

Hadron Endcap Calorimeter (HEC)

HEC is placed in the pseudorapidity of $1.5 < |\eta| < 3.2$ behind the end-cap LAr EM calorimeter, with copper as the absorber and filled with LAr. The wheels made of copper absorber plates have

cylindrical structure with outer radius of 2030 mm, and consists of two segments in depth. The front segment is made of 24 copper plates of 25 mm thick, and the rear segment consists of 16 copper plates of 50 mm thick.

4.4.5 Muon Spectrometer

The muon spectrometer shown in Figure 4.15 is based on the magnetic deflection of muon tracks in the large superconducting air-core toroid magnets. Its role is to measure a muon momentum in the pseudorapidity range $|\eta| < 2.7$ and generate trigger on muons in the $|\eta| < 2.4$ region. This is designed to have a stand-alone transverse momentum resolution of 10 % for 1 TeV muon. Muon tracks are reconstructed from the hit of the drift tubes described in this section. Figure 4.16 shows the cross-sections in the plane containing the beam axis. In the barrel region, three cylindrical layers around the beam axis to measure tracks are installed. In the transition and end-cap regions, three layers of the chambers are placed perpendicular to the beam axis. The outer view of the muon spectrometer is shown in Figure 4.17.

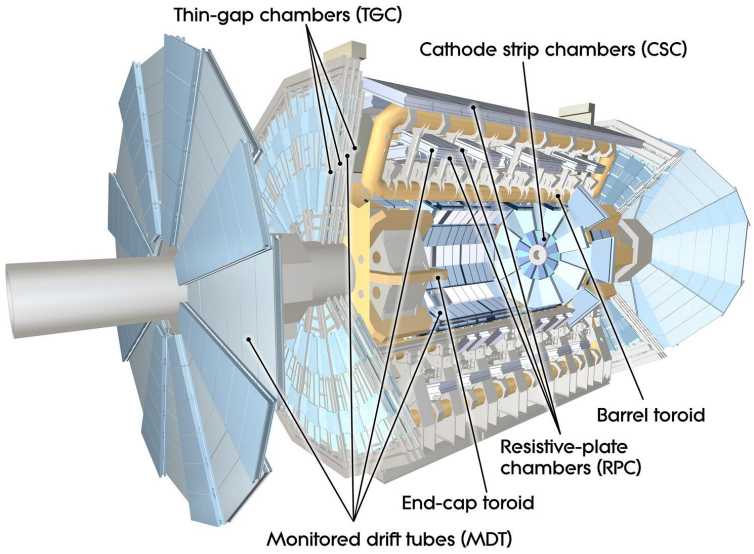

Figure 4.15: A schematic view of the muon spectrometer. **ATLAS Experiment ©2008 CERN**

Muon precision tracking chambers

Monitored Drift Tube (MDT) and Cathode Strip Chamber (CSC) are used as muon tracking chambers.

- Monitored Drift Tube (MDT)
  It is the precision momentum measurement chamber covering the pseudorapidity of $|\eta| <$

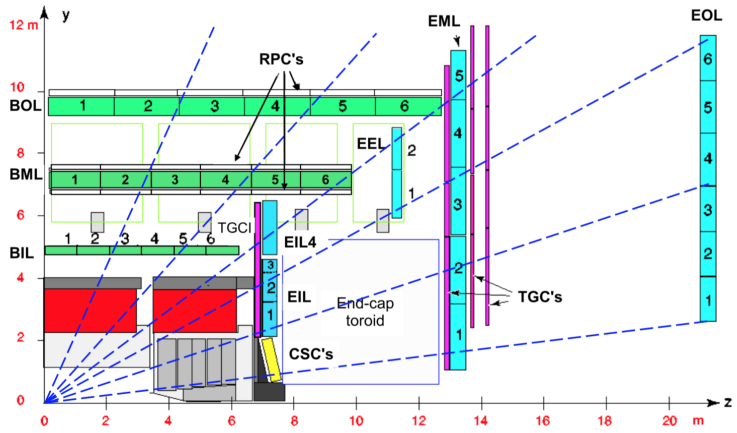

Figure 4.16: Schematic view of the cross-section of the muon system in the bending plane [44].

2.7. This consists of six or eight layers of drift tubes filled with Ar+CO_2 (Argon 93 %) operated under the pressure 3 bar. Three or four drift tube layers are mounted on each side of an MDT chamber, and they are held by spacer bars (Figure 4.18). The average position resolution is 80μm per tube, 35μm per chamber. The details are described in reference [44, 65].

- Cathode Strip Chamber (CSC)
  For high particle fluxes and track density in the forward region of the pseudorapidity of $2.0 < |\eta| < 2.7$, a multiwire proportional chamber CSC is used for the innermost tracking layer since it has higher rate capability and time resolution (7 ns). The CSC can stand high rate operation up to 1000 Hz/cm^2 while the limit of the safe operation of the MDT is about 150 Hz/cm^2.

Muon Triggers

Resistive Plate Chamber (RPC) and Thin Gap Chamber (TGC) are used as the muon trigger chambers. It provide bunch-crossing identification, discriminate muon transverse momentum, and measure the muon non-bending coordinate complementary to the muon precision tracking chambers.

- Resistive Plate Chamber (RPC)
  RPC is gas filled chamber consisting of resistive-plates with 2 mm gaps, and signal is read out by strips. RPC is placed in the barrel region of the pseudorapidity $|\eta| < 1.05$, as shown in Figure 4.19. The system consisting of three chamber layers each containing 2 gas gaps: two layers of the RPC sandwich the middle layer of the MDT, and the third layers is placed outer of the MDT. The outside layer of the RPC is used to provide high-p_T trigger

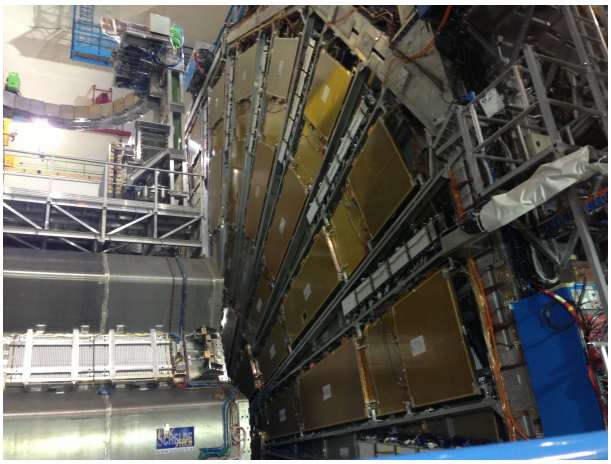

Figure 4.17: Muon chamber from ATLAS visit area (picture taken by the author in August 2013).

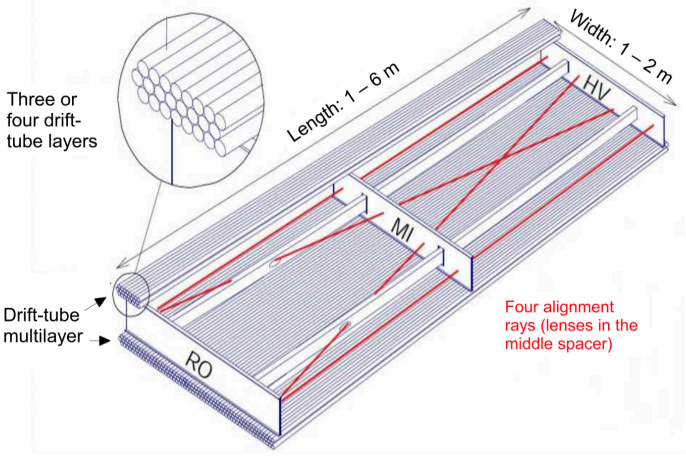

Figure 4.18: An MDT mechanical structure [44].

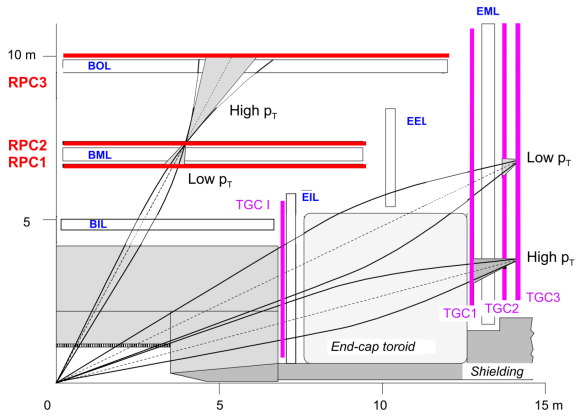

Figure 4.19: The schematic view of the muon trigger system [44].

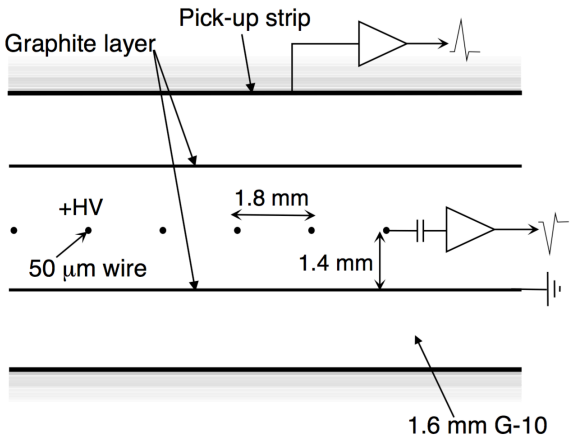

Figure 4.20: Structure of a TGC in the plane orthogonal to the wires. There are anode wires, graphite cathodes, G-10 layers and a pickup strip [44].

(the range $9 \sim 35$ GeV), while the two inner chambers produce low-p_T triggers (the range $6 \sim 9$ GeV). It provide good time resolution (1.5 ns).

- Thin Gap Chamber (TGC)
  TGC is put in front and behind of the two end-cap toroid magnets, corresponding to the pseudorapidity of $1.05 < |\eta| < 2.7$ (end-cap region) as shown in Figure 4.19. It is multi-wire proportional chamber, shown in Figure 4.20. In order to get good time resolution, wire-to-cathode distance of 1.4 mm is smaller than the wire-to-wire distance of 1.8 mm. A highly quenching gas mixture of CO_2 and n-C_5H_{12} (n-pentane) is used. TGC has good granularity for muon p_T discrimination for trigger.

4.4.6 Luminosity measurement

Luminosity detector

Precision luminosity measurement is performed on bunch-by-bunch basis algorithm with luminosity detectors [44,66]. The Beam Conditions Monitor (BCM) consists of four diamond sensors (about 1 cm^2), put around the beampipe at $z = \pm 184$ cm from interaction point. It works as a luminosity counter at $|\eta| = 4.2$ with a time resolution of ~ 0.7 ns. Luminosity measurement using Cérenkov Integrating Detector (LUCID) is an online luminosity monitoring detector located at distance of ± 17 m from the interaction point, close to the TAS (Target Absorber Secondaries) at $5.6 < |\eta| < 6.0$. The luminosity calibration is based on beam separation scan (Van der Meer scan [67,68]), that determines the beam size at the interaction point.

4.4.7 Trigger and Data Acquisition (TDAQ)

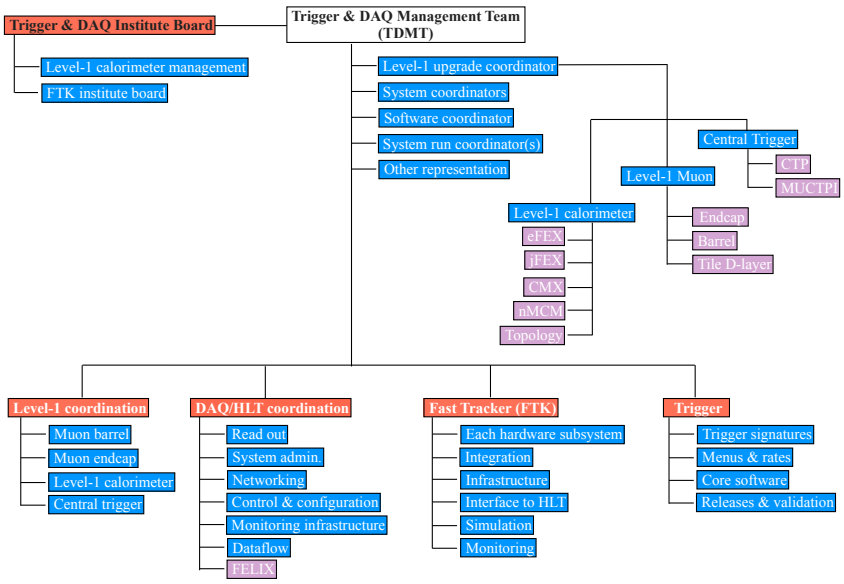

Figure 4.21: Schematic view of the TDAQ organisational structure [69].

Figure 4.21 shows the ATLAS trigger and data acquisition system. The trigger system [70,71] is used to select interesting events for recording. It was upgraded for Run2 and described in Figure 4.22. Since the center-of-mass energy was increased from $\sqrt{s} = 8$ to 13 TeV in Run2, and the luminosity is also expected to increase, the new system is designed to sustain the peak luminosity up to 1.7×10^{34} cm^{-2}s^{-1}; about a factor of 2 higher than Run1 [72].

First, the hardware based Level-1 trigger selects events from 40 MHz to 100 kHz by information of the calorimeters and muon detectors. Since it is important to increase the bandwidth, new Central trigger Processor was installed. The preprocessing of calorimeter signals for Level-1 trigger use FPGA (instead of ASIC in Run1) to suppress pile-up effects by auto-correlation filters and pedestal correction. The muon endcap trigger requires the coincidence with hits from the innermost muon chamber to suppress most of the fake muon triggers. A new topological trigger processor (L1Topo) system enables the Level-1 trigger to add object's kinematics from hardware base information.

The software based high-level trigger (HLT) selects and records events from output of the Level-1 trigger to 1 kHz. In order to bear the high output rate, HLT was upgraded by merging Level-2 and Event Filter (EF) firms in Run1. In this analysis, the event is required to pass the lepton trigger. More details are described in the reference [71].

The huge amount of the data is processed by the effort of the worldwide LHC computing Grid system [73].

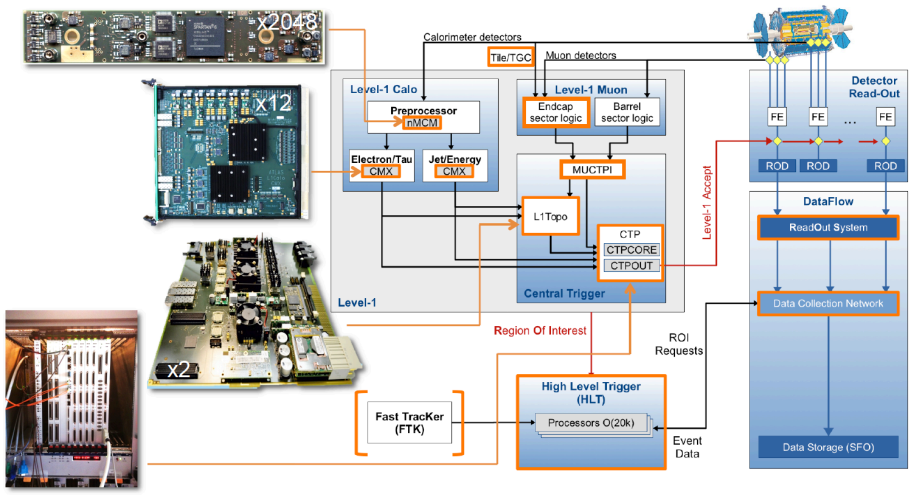

Figure 4.22: The schematic view of the trigger and DAQ system in Run2. New features from Run2 is indicated with orange boxes [71].

Chapter 5

Data and Monte Carlo Samples

This section describes the data and Monte Carlo samples. The data were collected by the ATLAS detector as described in Chapter 4. Appropriate Monte Carlo simulations were prepared.

5.1 Data sample

The data used in this study were recorded by the ATLAS detector in the 2015 proton-proton collisions at $\sqrt{s} = 13$ TeV. Figure 5.1 shows the history of data collection period. ATLAS recorded a total integrated luminosity of 3.9 fb^{-1}. The dataset used in the analysis corresponds to 3.2 fb^{-1} after requirement on good reconstructed physics objects under reliable detector condition.

Due to large inelastic cross-section of pp interaction and high luminosity of LHC, a large number of pp interactions, mostly 'soft' interactions, occur in each bunch crossing called pile-up [75, 76]. Number of pp interactions per crossing depends on the total instantaneous machine luminosity L and the number of colliding bunches per beam N_{bunch}. Mean number of interactions $< \mu >$ is given by:

$$< \mu >= \frac{L \times \sigma_{\text{inel}}}{N_{\text{bunch}} \times f_{\text{LHC}}} \tag{5.1}$$

where σ_{inel} is the total inelastic pp cross-sections (80 mb) and f_{LHC} is the bunch revolution frequency in LHC (about 11 kHz). Figure 5.2(a) shows the distribution of $< \mu >$ during the 2015 run, separately for the early period of 50 ns bunch interval and the later period of 25 ns interval. The average number of interactions was 20 and 17, for the 50 ns and 25 ns period, respectively. Figure 5.2(b) shows the maximum number of inelastic collisions per beam crossing per LHC fill.

Effects of pile-up on event reconstruction arise for example from overlapping calorimeter clusters (called "in-time pile-up"). In addition, influence of detector signals from previous bunch crossings can affect the signal of a triggered event (called "out-of-time pile-up"). Algorithms have been developed to mitigate the pile-up effects (Section 6.2.4). Pile-up events are implemented in the Monte Carlo simulation (Section 5.2).

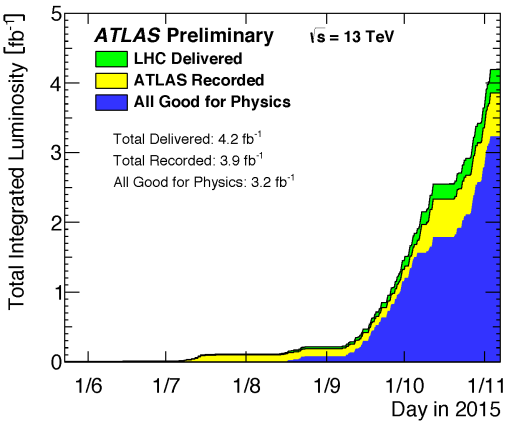

Figure 5.1: The total integrated luminosity taken with the ATLAS detector in 2015. The "LHC Delivered" (green histogram) shows stable beam luminosity with the proton-proton collisions at $\sqrt{s} = 13$ TeV, the "ATLAS Recorded" (yellow histogram) the actual recorded luminosity by the ATLAS detector, and certified to be good quality data, "All Good for physics" (blue histogram) [49, 74].

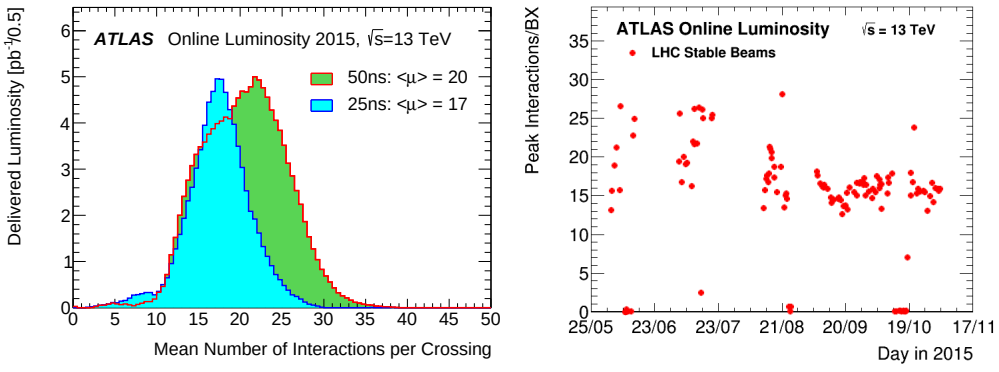

(a) (b)

Figure 5.2: Distribution of number of interactions per crossing shows separately for the periods of 50 ns and 25 ns bunch interval (a) and the maximum number of inelastic collisions per beam crossing per LHC fill (b) during the proton-proton collision stable beam 2015 [74].

5.2 Monte Carlo samples

Monte Carlo data are used to simulate the Standard Model background as well as the BSM signal events. They are generated using physics generators discussed below, and processed through the full detector simulation [77, 78] of ATLAS based on Geant4 [79]. The simulated data are then reconstructed in the same way as the real data.

Pile-up is implemented by overlaying a certain number of simulated 'soft' (minimum bias) events on the 'hard' event. The number of pile-up events are distributed according to the expected luminosity profile of the data sample. The difference of $< \mu >$ distribution in the Monte Carlo sample and the real data is taken into account by re-weighting the Monte Carlo events.

5.2.1 Modelling of scattering processes

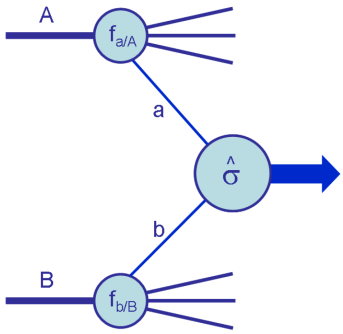

Figure 5.3: Schematic view of a cross section of a hard scattering process [80].

The process of high energy proton-proton collisions at LHC is rather complex, involving both soft QCD processes and hard processes [80]. The latter is the main focus of interest for many of the LHC physics programs, e.g. production of Higgs boson and SUSY particles. The hard interaction is modelled as a collision of a high energy parton (quark or gluon) from one colliding proton with another from the other proton. Figure 5.3 shows a diagrammatic structure of a generic hard scattering process in proton-proton collision. Partons a and b (quarks or gluons) participate the hard interaction $a + b \to X$. The QCD factorization theorem allows the cross-section for $pp \to X$ be expressed as a product of parton distribution function and the cross-section for the hard process.

$$\sigma_{AB} = \int dx_a dx_b f_{a/A}\left(x_a, \mu_F^2\right) f_{b/B}\left(x_b, \mu_F^2\right) \times \hat{\sigma}(ab \to X, \mu_R), \tag{5.2}$$

The distribution of the parton energy fraction x is given by the parton distribution function (PDF) $f(x, \mu_F)$. The factorization scale μ_F defines the boundary of energy scale treated as the hard process and the process inclusively contained in the PDF. μ_R is the renormalization scale for the

QCD running coupling. The effective center-of-mass energy squared of the hard interaction is $s' \approx x_a x_b s$, where s is the center-of-mass energy squared of the colliding protons. Normally the hard process is calculated using perturbation calculation, whereas PDF that involves soft QCD is obtained from measurements of ep deep inelastic scattering [81] at various x and momentum transfer Q^2. In the process where X contains quarks or gluons, the leading logarithm QCD higher order effects are accounted in the form of QCD parton shower. Similar treatment is done also for the QCD initial state radiation. At the end of the parton shower is the process of hadronization for which perturbation calculation is not applicable, and there are some phenomenological models such as the string fragmentation and cluster fragmentation. There are a number of Monte Carlo generators. Each has its strong points and limitations. In many cases the hard processes are calculated in the leading order (LO) of perturbation. There are also programs including higher order (NLO) calculations depending on the processes.

5.2.2 Generators

The generators used in this analysis are described below [82].

PYTHIA

An event generator tool for the high-energy collisions such as e^+e^- and pp, whose process starts from hard process in the initial states, then generate multiple interactions of partons, beam remnants, string fragmentation and particle decays. The showering model is expected to match the theoretical description of QCD showers at the Leading Order (LO). The details are described in Reference PYTHIA6 [83]. The PYTHIA8 [84, 84, 85] the latest version of PYTHIA and rewritten in C++ is also used.

HERWIG

This also reproduce hard processes, parton showering and QCD effects at the Leading Order (LO). It simulates angular ordered parton shower and the hadronization process is modeled by cluster fragmentation. The details are described in Reference [86].

POWHEG

Generate the hardest emission with positive weight event of the Next to Leading Order (NLO) corrections. This is the extensions of the shower algorithms. The details are described in References [87, 88].

SHERPA

Event generator for simulation of High-Energy Reactions of Particles such as e^+e^- and $p\bar{p}$. It simulate better for final states with large number of isolated jets than PYTHIA and HERWIG.

The details are described in Reference such as [89, 90].

MADGRAPH

It is the matrix element generator for parton level simulation and is used for both Standard Model and Beyond the Standard Model [91]. QCD shower and hadronization are simulated by PYTHIA.

MC@NLO

It provides matching calculation for QCD process with a parton showering in the hadronization. To avoid double counting events which come from NLO calculation, the events are provided negative weight as well as positive weight. The details are described in Reference [92].

EVTGEN

It provides better modelling of heavy-flavour hadron decays than PYTHIA and HERWIG [93].

5.2.3 Geant4 simulation

Geant4 [79] is a toolkit to simulate how particles interact in a matter. In the ATLAS experiment, this is used to describe the ATLAS detector components and material distributions and simulate energy deposits in the detectors.

5.3 Signal and background samples

The generators used to produce the Standard Model background samples are summarized in Table 5.1.

Table 5.1: Background samples used in this analysis.

	Generator
$t\bar{t}$	POWHEG+PYTHIA+EVTGEN (NNLO+NNLL)
single top	POWHEG+PYTHIA+EVTGEN (NNLO+NNLL)
W/Z+jets	Sherpa (NNLO)
diboson	Sherpa (NLO)

The Standard Model $t\bar{t}$

The Standard Model $t\bar{t}$ is the main source of background in this analysis since the final state is the same as the signals. The samples are generated by POWHEG + PYTHIA6 with `Perugia2012`

tune [94] for the shower and the underlying-event. The PDF is set to CT10 PDF [95,96] and the p_T-dependent radiation effect parameter is set to top mass.

A reweighting factor taking into account for the interferences with diagrams of an electroweak process is applied to the events. These weights are derived with the NLO electroweak calculations that is implemented in [97–100]. The initial state partons in CT10 PDF is set at the partonic energy$\sqrt{\hat{s}} = m_{t\bar{t}}$ and the scattering angle $z = \cos\theta^*$ are used in the weight calculation.

Single top

Single top process with the leptonic top quark decay results in the one lepton final states. Though the contribution of this process is small in this analysis, semi-leptonic decay muons from the b-quarks or mis-identified jets as leptons could behave similarly to the signals. The samples are also generated by POWHEG + PYTHIA6 with `Perugia2012 tune` and CT10 PDF settings.

W/Z boson production associated with hadron jets (W/Z+jets)

A W boson decays with lepton and neutrino. The $Z/\gamma* \to \ell\ell +$jets process also produces a lepton associated with hadron jets.

They are generated by SHERPA with CT10 PDF setting. MC statistics is high enough that p_T sliced samples are used and that the samples are generated by each of final state flavours.

diboson (VV)

Leptonic decay of W or Z bosons with following processes is simulated; four leptons, three leptons + neutrino, two leptons + two neutrinos, or one lepton + one neutriono + jets. They are generated by SHERPA with optimization of parton shower.

$Z' \to t\bar{t}$ signal samples

The samples are generated with PYTHIA8 with the default generic SSM Z' generation and NNPDF23LO [101] PDF setting for several mass points. Cross-section for Z' signals at each mass point is considered in this analysis as summarized in Table 5.2, where Z' is assumed to have spin 1 and $\Gamma/m = 0.01 \sim 0.02$.

Bulk RS $G_{KK} \to t\bar{t}$ signal samples (G^*)

The samples are generated with MadGraph PYTHIA8 with NNPDF23LO PDF setting for several mass points. Cross-section for G^* signals at each mass point is considered in this analysis, as summarized in Table 5.3, where G^* is assumed to have spin 2 and $\Gamma/m = 0.03 \sim 0.06$.

Table 5.2: Next-to-Leading-order (NLO) theoretical cross-sections for the Z' signal applied with a k-factor 1.3 (ratio of NLO and LO).

Z' mass	LO cross-section [pb]
400 GeV	70.3
500 GeV	40.1
750 GeV	10.7
1 TeV	3.70
1.25 TeV	1.51
1.5 TeV	0.684
1.75 TeV	0.334
2. TeV	0.172
2.25 TeV	0.0924
2.5 TeV	0.0511
2.75 TeV	0.0289
3 TeV	0.0167
4 TeV	0.00213
5 TeV	0.000331

Table 5.3: Cross-section times branching ratio $\sigma_{G_{KK}} \times BR(G_{KK} \to t\bar{t})$ for RS KK graviton.

G_{KK} mass	$\sigma_{G_{KK}} \times BR(G_{KK} \to t\bar{t})$ [pb]
500 GeV	5.84
750 GeV	1.18
1 TeV	0.289
1.5 TeV	0.0305
2 TeV	0.00498
3 TeV	0.000248

Chapter 6

Object Reconstruction

This Chapter describes the methods of the object reconstruction from the detector signal of the ATLAS detector as described in Chapter 4 with dataset described in Chapter 5 for this analysis.

6.1 Primary vertex

The primary vertex of the 'hard' collision is defined to be the vertex with the highest $\Sigma p_{T,track}^2$. At least one vertex which had at least two tracks is required. As shown in Figure 6.1, many vertices due to the pile-up events are seen in one event.

6.2 Jet reconstruction

High energy quarks and gluons are reconstructed as jets in the detector. The jets are reconstructed from the calorimeter clusters ('calo-jets'). Cluster energy is calibrated as the electromagnetic (EM) calorimeter scale.

6.2.1 Topological clustering algorithm

The calo-jets are reconstructed from the three-dimensional topological energy clusters [103]. The clustering starts from the seed cell with significant energy, group neighboring cells into clusters if they has significant energies compared to the expected noise. In case of overlapping showers, the cluster is split into smaller clusters by splitting algorithm [103]. The clustering threshold is optimized such that particle energy deposits are efficiently collected while the electronic and pile-up noise is maximally suppressed.

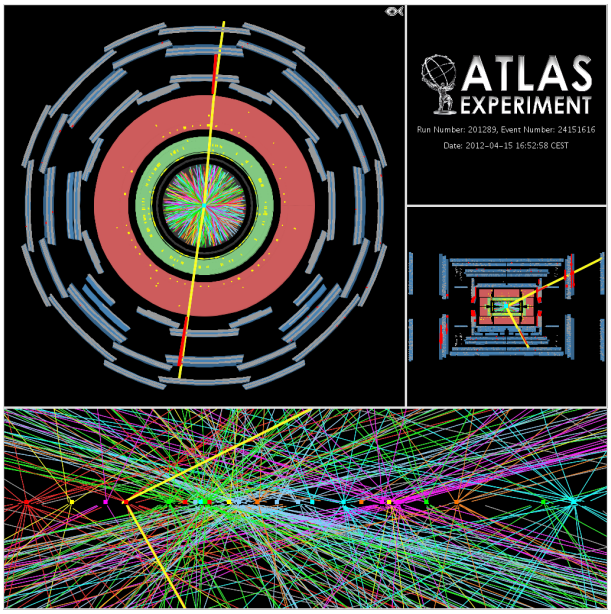

Figure 6.1: High pile-up environment of candidate $Z \to \mu\mu$ event with 25 reconstructed vertices [102].

6.2.2 Anti-k_T algorithm

Jets are reconstructed from calorimeter clusters by anti-k_T algorithm [104], which uses distances d_{ij} (equation 6.1) between entities (clusters, jets) i, j and d_{iB} (equation 6.2) between a cluster i and beam (B).

$$d_{ij} = min\left(k_{Ti}^{2p}, k_{Tj}^{2p}\right)\frac{\Delta_{ij}^2}{R^2}, \tag{6.1}$$

$$d_{iB} = k_{Ti}^{2p}, \tag{6.2}$$

where $\Delta_{ij}^2 = (\eta_i - \eta_j)^2 + (\phi_i - \phi_j)^2$ and k_{Ti}, η_i and ϕ_i are the transverse momentum, pseudo-rapidity and azimuth angle of cluster i. The parameter p is set to -1 in the anti-k_T algorithm. This means that jet is reconstructed around the high-p_T clusters. Originally, this algorithm is developed as k_T algorithm of $p = 1$ with respect to soft radiation, but this analysis mainly uses anti-k_T for its robustness. An appropriate value of R was searched for to give useful performance in jet search and was found to be 0.4 [105]. After calculating d for all entities and if the smallest one is d_{ij}, the four-momenta of the entity i and j are combined to produce a new entity k. If the smallest distance is d_{iB}, the entity i is regarded as a jet, and removed from the list of entity. This procedure is repeated until all the entity is removed. Miss-identified jets due to cosmic rays or detector noise are removed using a jet cleaning algorithm [106].

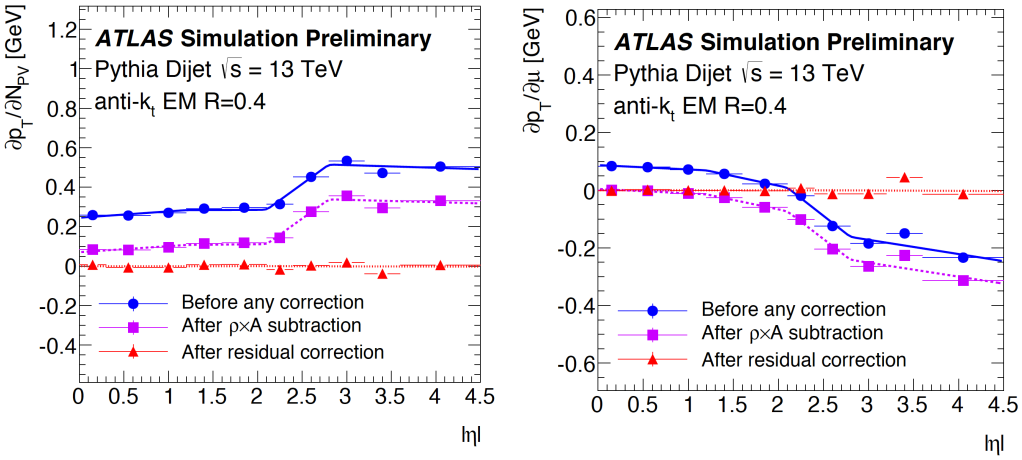

(a) (b)

Figure 6.2: The effect of the correction of the in-time-pile-up, α (a) and out-of-time pile-up, β (b) [107].

6.2.3 Jet energy

Jet energy is affected by the pile-up effects, which is corrected by the following procedure [107]. The corrections are done by an area-based subtraction method [76], which removes the pile-up effect, using the information of the average energy density ρ in the $\eta \times \phi$ plane and information of the area A of the jet in this plane. Using the area-based correction and residual correction, the p_T^{corr} is given by:

$$p_T^{\text{corr}} = p_T^{\text{EM}} - \rho \times A - \alpha \times (N_{\text{PV}} - 1) - \beta \times < \mu >, \tag{6.3}$$

where N_{PV} is the number of primary vertices, $< \mu >$ is the average number of interactions per bunch crossing, α and β are derived from the residual dependence in the simulation, parameterized by η shown in Figure 6.2.

At this point, p_T^{corr} is still in EM scale, i.e. with the definition that the calorimeter response is due to EM showers of γ/e. An additional correction is necessary to account for the difference between γ/e and hadron in the calorimeter response. The correction is obtained using Monte Carlo simulation by comparing the detector level jet energy in EM scale and the truth jet energy [107–109]. The calibration (EM+JES scheme [110]) uses isolated jets, and the procedure is as follows. The jets are required to match to truth jets within

$$\Delta R = \sqrt{(\eta_{\text{calo}} - \eta_{\text{truth}})^2 + (\phi_{\text{calo}} - \phi_{\text{truth}})^2} < 0.3,$$

and have $p_T > 5$ GeV within $\Delta R = 1.0$. The truth jet is required to have $p_T^{\text{truth}} > 7$ GeV within $\Delta R = 0.6$. The ratio of the detector level jet energy to the energy of matched truth jet is used as the calibration factor, parametrized as a function of jet p_T and η.

Finally, the Monte Carlo based corrections are validated using data with 'in-situ' measurement [107]. This exploits the p_T balance in processes such as γ/Z+jet. The calibrated jet p_T is compared to the p_T of reference object (γ, Z) for which the calibration is independently established. Figure 6.3 shows the ratio of jet p_T relative to the p_T of reference object, shown for data and compared with two simulations using different Monte Carlo generators [111]. The data - Monte Carlo difference is taken into account in the jet energy correction. In this calculation, γ/Z+jet and multi-jet event was used. The uncertainty of jet energy scale is estimated from several elements such as uncertainties of parameters in the Monte Carlo simulation, difference between Monte Carlo generators, and comparisons between data and simulations. Jet energy scale uncertainty in the 2015 data used for this analysis is summarized in Figure 6.4.

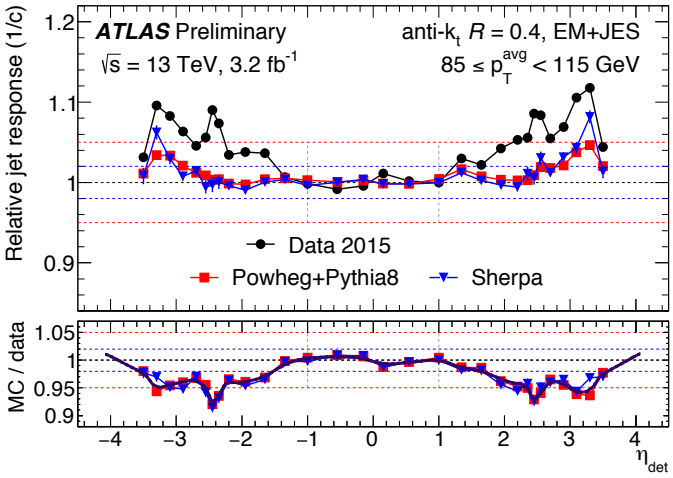

Figure 6.3: Relative jet response for anti-k_T ($R = 0.4$) jets with the EM+JES calibration scheme [112].

6.2.4 JVT algorithm

The jet-vertex-tagger (JVT) algorithm is developed to distinguish pile-up jets from hard-scatter jets, and optimized for $R = 0.4$ jets [113]. JVT is a discriminating variable calculated from likelihood of two quantities, corrJVF (equation 6.4) and R_{p_T} (equation 6.5). The variable corrJVF is based on tracking information only, whereas R_{p_T} uses both tracking and calorimeter information.

The variable corrJVF is based on a similar variable JVF (jet vertex fraction) which was also developed for identifying pile-up jets. It is defined as the scalar p_T sum of tracks associated to the jet and originating from the hard-scatter vertex, divided by the scalar p_T sum of associated tracks from all the vertices (hard-scatter and pile-up). The definition is illustrated in figure 6.5. In

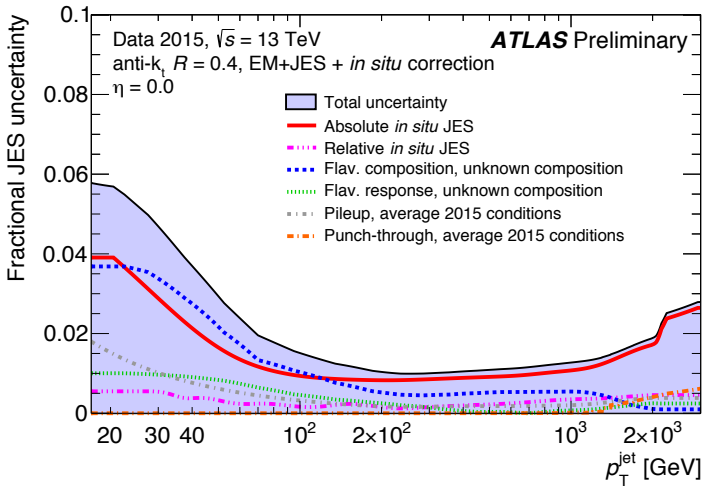

Figure 6.4: Fractional jet energy scale systematic uncertainty components for anti-k_T ($R = 0.4$) jets calibrated with the EM+JES scheme [112].

this simple configuration where there are two vertices and two jets, and if PV1 is the hard-scatter vertex, JVF for jet1 is $(1-f)$ whereas JVF for jet2 (pile-up jet) is 0 when f is the fraction from jet from PV2. The definition of corrJVF (equation 6.4) is modified from JVF in order to eliminate the dependence on the number of pile-up vertices.

$$\text{corrJVF} = \frac{\sum_k p_T^{trk_k}(PV_0)}{\sum_l p_T^{trk_l}(PV_0) + \frac{\sum_{n\geq 1}\sum_l p_T^{trk_l}(PV_n)}{k \cdot n_{trk}^{PU}}}, \tag{6.4}$$

where $\sum_k p_T^{trk_k}(PV_0)$ is the scalar p_T sum of the tracks associated with the jet and originated from the hard scatter vertex (PV_0). $\sum_{n\geq 1}\sum_l p_T^{trk_l}(PV_n)$ is the p_T sum of the associated tracks from the pile-up vertices (PV_n). The latter receives more contribution as the number of pile-up vertices increases. The second term in the denominator is scaled by $k \cdot n_{trk}^{PU}$, where n_{trk}^{PU} is the number of pile-up tracks in the event and k is scaling factor with its value chosen to make the second term approximately independent of the number of vertices. Figure 6.6(a) shows the distribution of corrJVF for pile-up jets and hard-scatter jets.

The parameter R_{p_T} is the sum of associated tracks p_T from the hard-scatter vertex normalized by the jet p_T measured with the calorimeter (equation 6.5). This is also a sensitive variable for discrimination between pile-up and hard-scatter jets.

$$R_{p_T} = \frac{\sum_k p_T^{trk_k}(PV_0)}{p_T^{jet}}. \tag{6.5}$$

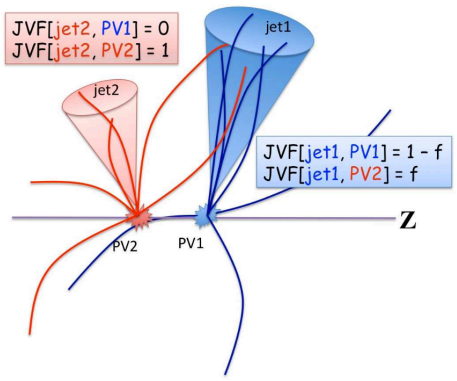

Figure 6.5: Schematic view of the JVF principle [76].

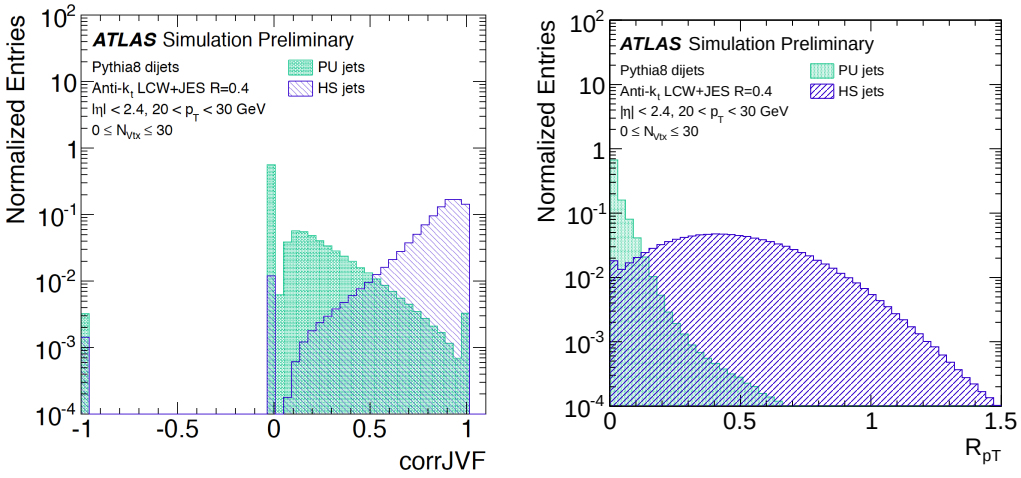

(a) (b)

Figure 6.6: The corrJVF (a) and R_{p_T} (b) distribution for pile-up jets (PU) and hard scattering jets (HS) with $20 < p_T < 30$(GeV) [113].

Figure 6.6(b) shows the distribution of R_{p_T} for pile-up jets and hard-scatter jets.

The JVT variable is constructed from corrJVF and R_{p_T} using a 2-dimensional likelihood, calculated by the k-nearest neighbor (kNN) algorithm [114]. For given values of corrJVF and R_{p_T}, JVT is defined as the ratio of likelihood for hard-scatter jet divided by the sum of likelihoods for hard-scatter and pile-up. The distribution of JVT is shown in figure 6.7. JVT $= -0.1$ is assigned when there is no track associated to the jet. With the JVT discriminant, the pile-up fake rate is suppressed to 0.4 %, 1.0 % and 3 % while keeping the efficiency to the jets from hard

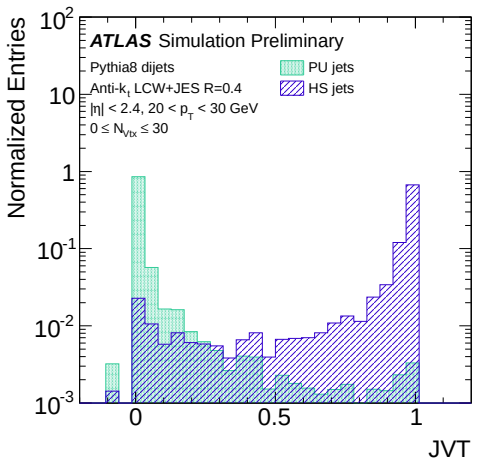

Figure 6.7: The JVT distribution for pile-up jets (PU) and hard scattering jets (HS) with 20 GeV $<$ p_T $<$ 30 GeV [113].

scattering at 80 %, 90 % and 95 %.

6.3 Large-*R* jet

Large-*R* jets are reconstructed by the anti-k_T algorithm (see section 6.2.2) with the radius parameter $R = 1.0$. To remove the pile-up effect [115], a trimming procedure as described in Figure 6.8 is applied [116, 117]. Calo clusters are reclustered to subjets by k_T algorithm [118, 119] ($p = +1$ in equation 6.1) with radius parameter, R_{sub}. Only subjets which have larger transverse momentum than a fraction f_{cut} of the parent jet momentum is used to make final trimmed jet. $R_{\text{sub}} = 0.2$ and $f_{\text{cut}} = 0.05$ is used in this analysis. The value is chosen taking into account the pile-up study. The above procedure is called grooming. Large-*R* jets are calibrated by local cluster weighting (LCW) procedure [120] which corrects for the energy in the dead-material by simulation. The large-*R* jet uncertainties such as jet energy scale (JES) and jet mass scale (JMS) are estimated similarly to small-*R* jets.

6.4 Top tagging

A top tagging algorithm which is described in references [121, 122] is used to identify large-*R* jets from boosted top quarks. The top tagging algorithm uses two variables; the calibrated jet mass $m_{\text{jet}^{\text{calib}}}$ and subjettiness ratio τ_{32}.

The calibrated jet mass $m_{\text{jet}^{\text{calib}}}$

The jet mass before calibration is defined by equation 6.6 with the energy E_i and the three

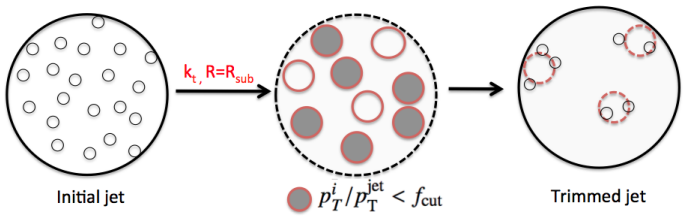

Figure 6.8: Illustration of the jet trimming procedure [117].

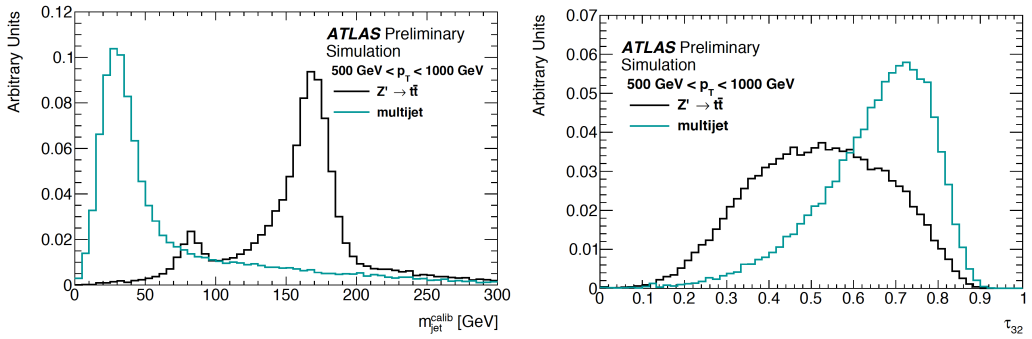

(a) (b)

Figure 6.9: The distribution of $m_{\text{jet}^{\text{calib}}}$ (a) and τ_{32} (b) for $Z' \to t\bar{t}$ and QCD multi-jet events in $500 < p_T < 1000$ GeV bin. The $m_{\text{jet}^{\text{calib}}}$ distributions are obtained $\tau_{32} < 0.7$ and the τ_{32} distribution for $m_{\text{jet}^{\text{calib}}} > 80$ GeV [121].

momentum $\vec{p}_i$ of the i^{th} jet constituent after grooming.

$$(m_{\text{jet}^{\text{uncalib}}})^2 = \left(\sum_i E_i\right)^2 - \left(\sum_i \vec{p}_i\right)^2 . \tag{6.6}$$

Then, $m_{\text{jet}^{\text{calib}}}$ is calculated by jet calibration procedure described in subsection 6.2.3. Distribution of $m_{\text{jet}^{\text{calib}}}$ is shown in figure 6.9(a) for top jets and QCD multi-jets. The top jet distribution is characterized by a peak at the top mass, whereas QCD multi-jets tend to have lower values.

N-subjettiness

The large-R jet hadronically decaying boosted top quark contains three sub-jets originating from b and $W \to q\bar{q}'$. N-subjettiness τ_N is quantity showing how likely the jet has N sub-jets. N-subjettiness for a jet with radius parameter R is defined by [123, 124]:

$$\tau_N = \frac{1}{d_0} \sum_k p_{T_k} \times min(\delta R_{1_k}, \delta R_{2_k}, \delta R_{3_k}, ..., \delta R_{N_k}), \tag{6.7}$$

with

- the transverse momentum p_{T_k} of the jet constituent k
- the distance δR_{i_k} between the subjets i and the constituent k
- $d_0 = \sum_k p_{T_k} \times R$

N-subjettiness takes a small value when the number of sub-jets N is correctly assigned and the directions of sub-jets are also precise. The k_T algorithm is used to re-cluster the large-R jet into a given number of N sub-jets. In order to reduce the effect of recoil from the soft radiation, the 'winner-take-all (WTA)' recombination scheme is used [125]. The N-subjettiness ratio $\tau_{32} = \tau_3/\tau_2$ for $N = 3$ and 2 is found to be a good discriminating variable for separating top jets from QCD multi-jets (more 2-jet like). Figure 6.9(b) shows the distribution of τ_{32} for top jets and QCD multi-jets.

The top tagging is performed by applying cuts on $m_{\text{jet}^{\text{calib}}}$ and τ_{32}. In this analysis, cuts are varied as a function of p_T to obtain a flat 80 % efficiency and maximum multi-jet rejection over the relevant p_T range. Figure 6.10 shows the top tagging efficiency and background rejection as a function of jet p_T .

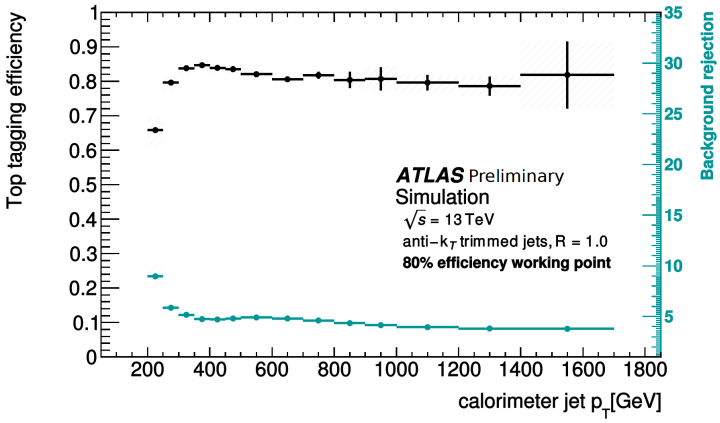

Figure 6.10: Top tagging performance of efficiency and background rejection as a function of jet p_T for simulated $Z' \to t\bar{t}$ events and QCD dijet production. The working point is used 80 % efficiency [121].

6.5 Track-jet

Track-jets are used in this analysis for b-tagging. A track-jet is reconstructed from charged particle tracks associated to the primary vertex. The reconstruction proceeds in two steps. In the first step, tracks are required to satisfy tight requirements; $p_T > 0.5$ GeV, $|d_0| < 1.5$ mm, $|z_0 \sin\theta| < 1.5$ mm and have hits in the inner detector (≥ 1 hit in the pixel detector, ≥ 6 hits in the

silicon strip detector) in order to reduce contributions from pile-up tracks. After jets are reconstructed using the tight tracks and jet axis is also defined, a cone of p_T dependent size is defined around each jet axis and remaining tracks that are within the cone are included in the track-jet. The second step is necessary to include tracks from secondary vertices which carry information for b-tagging but may fail to satisfy the tight track requirements.

Track-jet has better angle resolution than calo-jet, and is not dependent on uncertainties originated from calorimeter cluster, hence is less affected from pile-ups. This allows track-jet to use smaller-R than calo-jet even in dense environment. However, track-jet does not contain neutral particles that have no tracks in the detector, track-jet energy is sum of the charged particles. Therefore it has not good energy resolution as calo-jet (the p_T is about $2/3$ of calo-jet's). Figure 6.11 and Figure 6.12 show the comparison between these two jet p_T . In some analyses track-jets are used to obtain a better measurement of jet direction by ghost-matching a track-jet to the calo-jet [126, 127]. In this analysis, track-jet is used for identifying b-jets in the event selection.

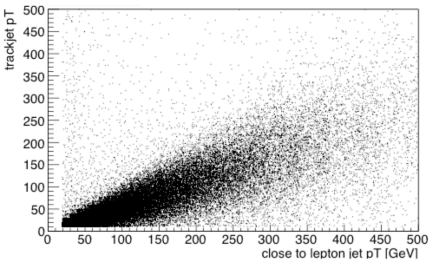

Figure 6.11: Calo-jet p_T V.S. track-jet p_T

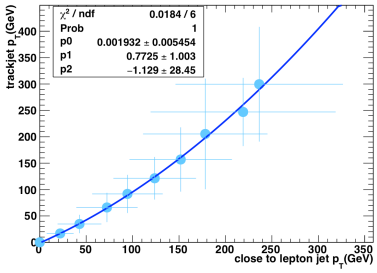

Figure 6.12: Calo-jet p_T V.S. track-jet p_T , fitted by quadratic function $p_0x^2 + p_1x + p_2$.

6.6 Electron reconstruction

Electrons are reconstructed from the EM calorimeter cluster based on the energy deposit inside the pseudo rapidity $|\eta| < 2.47$, then, tracks are matched to the cluster [128]. The fiducial region for electrons are defined to avoid the calorimeter crack region ($1.37 < |\eta| < 1.52$) for a good energy measurement. The energy deposit are summed as a tower in each granularity of the calorimeter, $\Delta\eta \times \Delta\phi = 0.025 \times 0.025$. A 'seed' of cluster is searched by a *sliding-window* algorithm [129] from tower. The sliding window size is 3×5 in units of 0.025×0.025 in $\eta \times \phi$ space. This algorithm is applied for the cluster with total transverse energy > 2.5 GeV. Using the clustering algorithm [103], the clusters are formed around the seeds. This method provides discrimination against multiple photon showers and precise estimation of the impact point.

Tracks are reconstructed either pattern recognition based on the pion hypothesis or track fit based on the electron hypothesis. The pion hypothesis allows the energy loss in the detector material up to 30 %, while electron hypothesis which uses the ATLAS Global χ^2 Track Fitter [130]

allows for larger energy loss. Taking into account for energy-loss, non-linear bremsstrahlung effects and the number of hits in the detector, the obtained tracks are matched to the EM clusters based on η and ϕ information. Electron candidates are then reconstructed. The four-momentum of the electron is determined, the energy is defined by the final calibrated energy cluster and its direction is taken from the track best matched to the original seed cluster.

In order to ensure the electron coming from the primary vertex, the tracks are required to have $d_0/\sigma_{d0} < 5$ and $|z_0 \sin\theta| < 0.5$ mm, where the definition is shown in Figure 4.10. In addition, the events that have hits in the calorimeter crack region $1.37 < |\eta| < 1.52$ is removed for analysis since E_T^{miss} (section 6.8) can not be reliably computed.

The electron identification is a likelihood-based method using the multivariate analysis (MVA) technique [128]. This method uses the probability density functions of signal and background. The discriminant $d_{\mathscr{L}}$ for a given electron is:

$$d_{\mathscr{L}} = \frac{\mathscr{L}_S}{\mathscr{L}_S + \mathscr{L}_B}, \tag{6.8}$$

where

$$\mathscr{L}_{S(B)}(\vec{x}) = \prod_{i=1}^{n} P_{s(b),i}(x_i). \tag{6.9}$$

$\vec{x}$ is the discriminating variable value vector and $P_{s(b),i}(x_i)$ is the signal (background) probability density function of the i^{th} variable for x_i. The definition of discriminating variables are: the energy leakage on the HCAL, EM shower shape, track quality requiring the specified hits on the tracker, the pixel, SCT and TRT. The hits requirement on the *b*-layer drops fake electron from photon conversion. The requirement in the ratio of the number of high threshold hits to the total number of hits in the TRT is used to identify electron tracks based on transition radiation.

There are three reference sets named *loose*, *medium* and *tight* corresponding to their background rejection power [129, 131]. In this analysis, the tight likelihood identification criterion [132] was chosen, whose background jet rejection is about 50000.

Signal electrons are required to be isolated from other activities in order to reject backgrounds such as electrons from photon conversion in hadron decays, electrons from heavy flavour hadron decays, and light hadrons. There are two discriminating variables based on a calorimeter cluster and tracks [128]. In this analysis, the latter is used, which defines a cone ΔR around the candidate electron track from the primary vertex of the hard collision, and then requires the sum of the transverse momenta of all tracks to satisfy quality requirements. Figures 6.13 show the combined electron reconstruction and identification efficiencies in $Z \to ee$ candidates using tag-and-probe method. Good efficiency is obtained except in the calorimeter transition region. The correction factor to be applied for MC is calculated from the difference between MC and data.

6.7 Muon reconstruction

Muons are reconstructed by combining information from the inner detector and the muon spectrometer [133]. In the muon spectrometer, muon reconstruction starts from searching hit patterns.

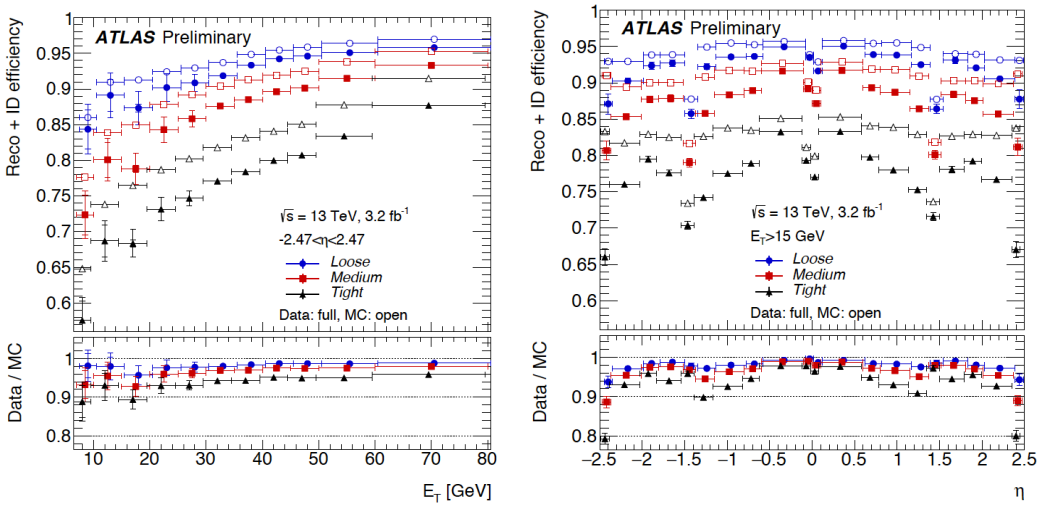

(a) (b)

Figure 6.13: The combined electron reconstruction and identification efficiencies as a function of the transverse energy E_T (a) and pseudorapidity η (b) in $Z \to ee$ candidates [128].

A Hough transform [134] is used to search trajectory in the bending plane of each MDT chamber and nearby trigger chamber. After finding the hits in each station (MDT, RPC, TGC and CSC), muon track candidates are built by fitting together with algorithm that performs a segment-seeded combinations search. The search starts from the seed of the segments in the middle stations of the detector where trigger hits are available, then extends the segments in outer and inner station. The segments are selected by a criterion based on hit multiplicity and fitting quality (χ^2), and then matched using their positions. To build a track, at least two matching segments except barrel-endcap transition region are required. The track candidates are defined if the χ^2 fit satisfies the selection criterion. In order to combine the muon tracks, various algorithms that are based on the information from the inner detector, muon spectrometer, and calorimeters are used [133].

To select prompt muons against backgrounds mainly coming from pion and kaon in-flight decays, several variables provide good discriminant. For example, following variables are used for identifying muons.

- q/p significance, the ratio of the charge and momentum of the muons.
- ρ', the difference between the transverse momentum measurements in the inner detector and muon spectrometer.
- χ^2 of the combined track fit.

Furthermore, specified number of hits in the inner detector and the muon spectrometer are required; number of hits in the pixel ≥ 1, number of hits on the SCT ≥ 5, number of holes in the

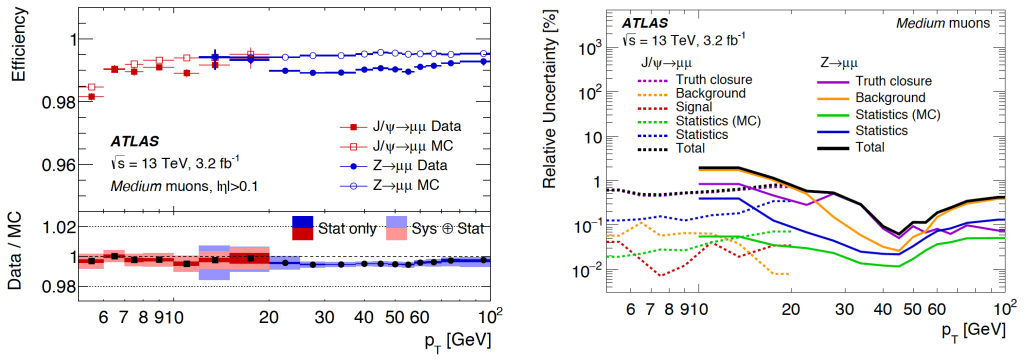

(a) (b)

Figure 6.14: Total reconstruction efficiency (a) and its uncertainty (b) for *medium* as a function of muon p_T in the $Z \to \mu\mu$ and $J/\psi \to \mu\mu$ decay events in the region of $0.1 < |\eta| < 2.5$ [133].

pixel or the SCT < 3, at least 10 % of the TRT hits originally assigned to the track are included in the final fit.

The selection criteria is defined as four categories for specific needs of each physics analysis. In this analysis, *medium* identification criteria is used. This selection, the combined muon is required to have ≥ 3 hits in at least two MDT stations, and extrapolated muon whose trajectory is reconstructed in the muon spectrometer and originating from impact parameter is required to have at least three MDT/CSC stations. In addition, q/p significance < 7 is required. Signal muons are required to be isolated from other activities in order to reject backgrounds such as muons from hadron decay, there are two discriminating variables (the same as electron,a calorimeter-based and a track-based), a track-based isolation is used in this analysis. The reconstruction efficiency and total uncertainty are shown in Figures 6.14.

The muon reconstruction efficiency is close to 99 % in the range of $|\eta| < 2.5$ for $p_T > 5$ GeV. The transverse muon momentum p_T is corrected using the information from inner detector and simulated muon, taking account for muon's second-order effects [135,136]. The scale factor (MC and data ratio) for reconstruction efficiency is measured by data and simulation ratio using a tag-and-probe method based on $Z \to \mu\mu$ and $J/\psi \to \mu\mu$ events [136]. Figure 6.15 shows the muon momentum scale and resolution that are obtained from reconstructed $Z \to \mu\mu$ events [136].

6.8 Missing transverse energy (E_T^{miss}) reconstruction

After all the objects are reconstructed, missing transverse energy (E_T^{miss}) [137, 138] is computed on the assumption of the momentum conservation in the transverse direction. In the ATLAS detector, the E_T^{miss} is reconstructed from calibrated objects; electrons/photons, jets and muons.

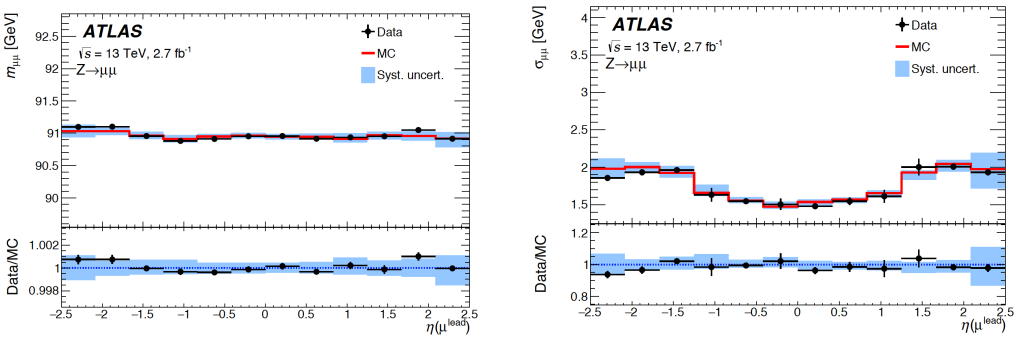

(a) (b)

Figure 6.15: $\mu\mu$ mass (a) and resolution (b) as a function of pseudo rapidity η of leading muon obtained from $Z \to \mu\mu$ [136].

The missing transverse energy E_T^{miss} is a negative vector sum of all objects given by:

$$\vec{E}_T^{\text{miss}} = -\sum \vec{p}_T^{\,e/\gamma} - \sum \vec{p}_T^{\,\mu} - \sum \vec{p}_T^{\,\text{jet}} - \sum \vec{p}_T^{\,\text{soft}}, \tag{6.10}$$

here, soft term is constructed from inner detector tracks and tracks that are not associated to any hard objects (reconstructed either by calorimeter-based methods or track-based methods). The E_T^{miss} resolution as a function of $\sum E_T$ (scalar sum of objects E_T) is shown in Figure 6.16.

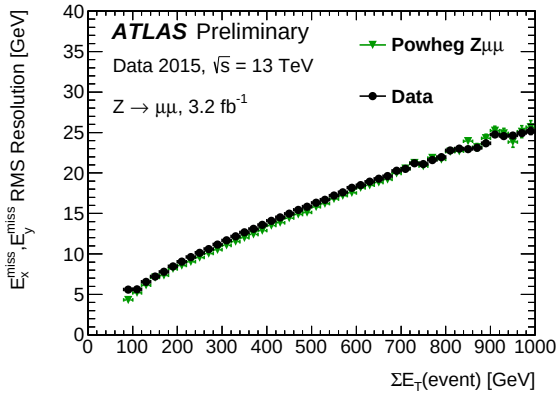

Figure 6.16: The E_T^{miss} resolution as a function of $\sum E_T$ for $Z \to \mu\mu$ event by simulation [139].

Chapter 7

Event Selection

According to the strategy described in Chapter 3, candidate events are selected with the following procedure. As shown in Figure 7.1, $t\bar{t}$ events with high-p_T isolated lepton, small-R jet close to the lepton, large-R jet with top-tagged far from leptonic decay top side, large missing transverse energy, and at least one b-tagged track-jet are required.

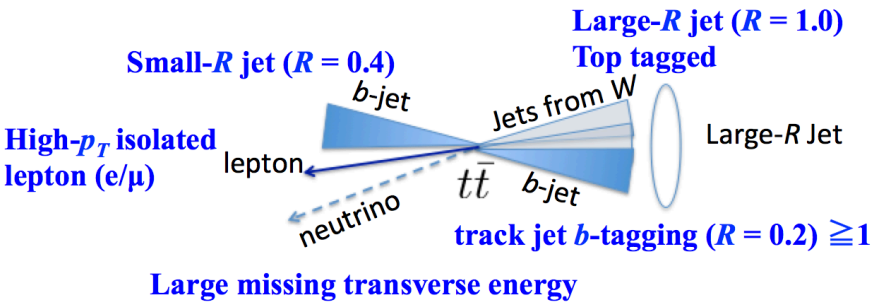

Figure 7.1: The outline of the event selection from reconstructed objects.

7.1 Event selection from reconstructed objects

Events are required to passed good event criteria with stable colliding beams and good operating conditions of relevant sub-detectors. After the requirement, the total luminosity is 3.2 fb^{-1}.

Single lepton triggers

In order to collect events that have lepton plus jets, the events must pass either the single electron or muon triggers. For the electron channel, the trigger requires $E_T > 18$ GeV at the Level 1

and $E_T > 24$ GeV or 120 GeV at the High Level Trigger (HLT). For muon channel, the trigger requires $p_T > 15$ GeV at the Level 1 and $p_T > 20$ GeV or 50 GeV at the HLT. In order to cover the low efficiency in the high-p_T region of Level 1 (mainly comes from the detector geometrical acceptance), HLT trigger with loose isolation criteria is required [71]. The trigger performances used in this analysis are shown in Figure 7.2 and Figure 7.3.

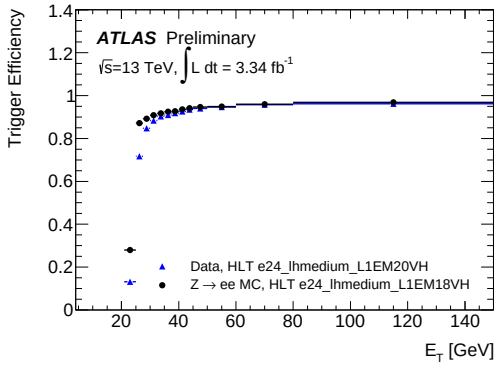

Figure 7.2: Efficiency for single electron triggers used in this analysis as a function of the offline electron candidate's transverse momentum E_T. The efficiency is measured using a tag-and-probe method with $Z \to ee$ decays [140].

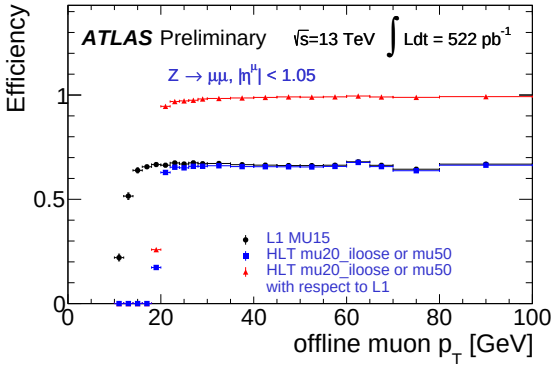

Figure 7.3: Efficiency for single muon triggers used in this analysis as a function of the offline muon candidate's p_T . The efficiency is measured using a tag-and-probe method with $Z \to \mu\mu$ decays [141].

Overlap Removal

Lepton identification and jets reconstruction are performed independently. A single particle can be reconstructed as more than one objects. For example, high energy electron can also be reconstructed as a high energy jet. Another example is a part of hadron jets misidentified as electrons. In order to remove such objects overlap, one of the two objects of $p_T > 25$ GeV is removed if it satisfies the following conditions [26].

- If electron and jet are close within $\Delta R(\text{jet}, \text{e}) < 0.2$, jets are removed, otherwise if $\Delta R(\text{jet}, \text{e}) < 0.4$, electrons are removed.
- The muons with $\Delta R(\mu, \text{jet}) < 0.04 + 10\ \text{GeV}/p_T^{\mu}$ are rejected when the jet has at least three tracks from the primary vertex, if not the case, the jet is rejected.

One lepton

Exactly one lepton (electron or muon) matched to the trigger is required. The lepton is required to have $p_T > 30$ GeV for electron or $p_T > 25$ GeV for muon, and satisfy the Loose

isolation criteria [142] at 99 % efficiency. The scalar sum of transverse momenta of all tracks (with $p_T > 1$ GeV, enough hits in the inner detectors and $|z_0 \sin\theta| < 3$ mm) in a cone of $\Delta R = \min\left(10\,\text{GeV}/p_T^{\ell}, R_{\text{max}}\right)$ around the lepton track originating from the primary vertex are used (R_{max} is 0.2 for the electron and 0.3 for the muon) [128, 143]. The size of ΔR is tuned at different p_T ranges to get constant performance. Figure 7.4 shows the caption for the figures in the following histograms. Figures 7.5-7.7 show the lepton p_T, η and ϕ distribution. The light blue bands indicate systematic uncertainties mentioned in Chapter 10.

Figure 7.4: The caption for the histograms.

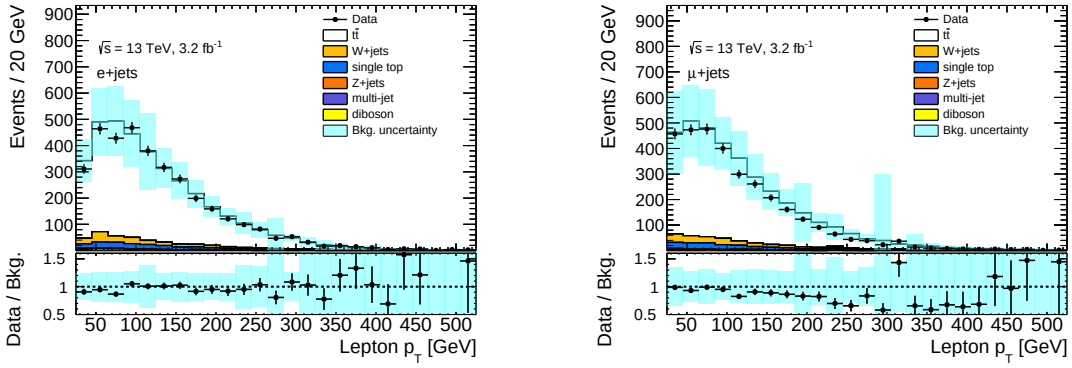

Figure 7.5: Lepton p_T distributions, electron (left) and muon (right).

Small-R jet

At least one small-R jet ($R = 0.4$ calo-jet) with $p_T > 25$ GeV and $|\eta| < 2.5$ is required. For those jets with $p_T < 50$ GeV and $|\eta| < 2.4$, it is required to pass the pile-up rejection criteria $|JVT| > 0.64$ (section 6.2.4). The highest p_T jet close to the lepton with ΔR(jet, lepton) < 1.5 (the same decay hemisphere to the lepton) is used for the reconstruction for semi-leptonially decaying top quark. Figures 7.8–7.9 show the p_T of the selected small-R jets and distance ΔR from leptons, respectively.

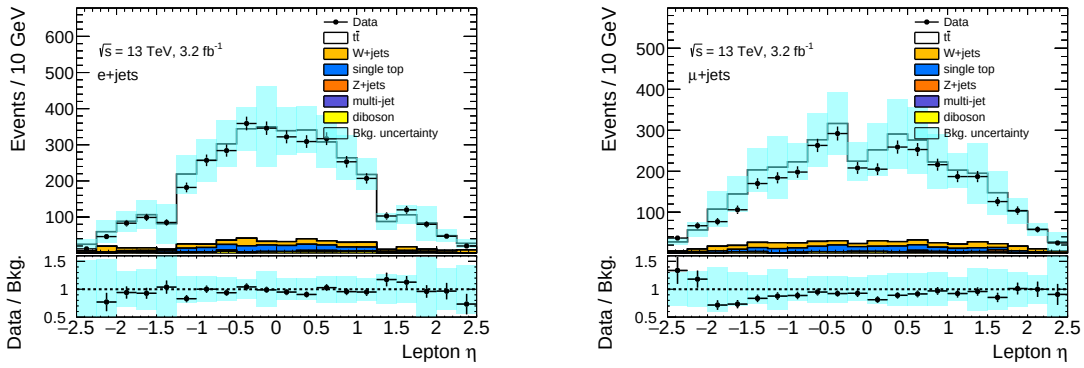

Figure 7.6: Lepton η distributions, electron (left) and muon (right).

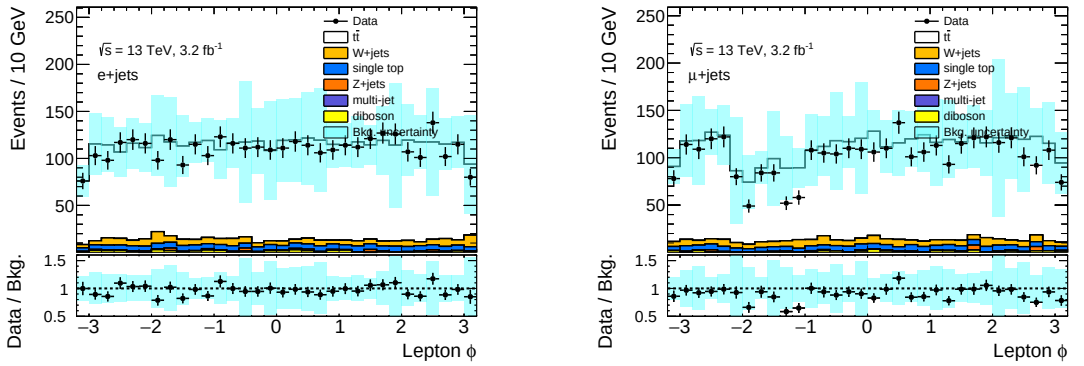

Figure 7.7: Lepton ϕ distributions, electron (left) and muon (right).

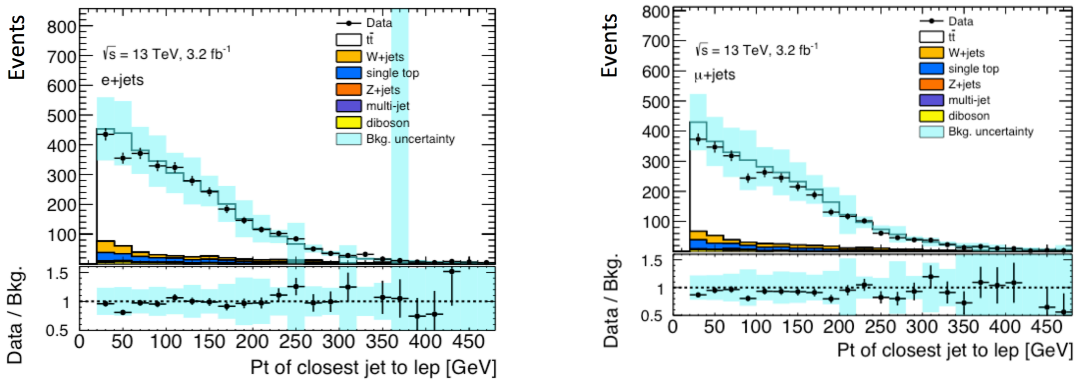

Figure 7.8: The small-R jet closest the lepton p_T distributions, electron channel (left) and muon channel (right).

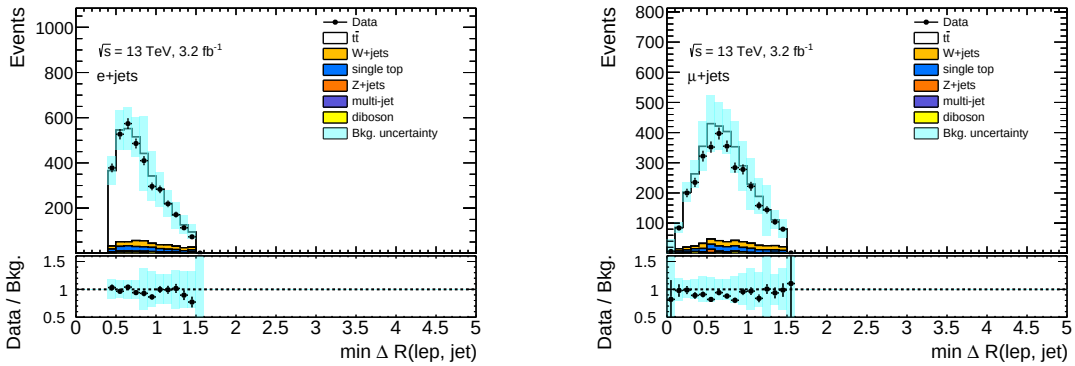

Figure 7.9: The distribution of distance ΔR between the lepton and the small-R jet closest to the lepton, electron (left) and muon (right).

Large-R jet

A highly boosted hadronically decaying top is reconstructed as a large-R jet. It is reconstructed by anti-k_T algorithm with radius parameter $R = 1.0$ as described in section 6.2. At least one large-R jet is required. It is required to have $p_T > 300$ GeV (Chapter 3) and $|\eta| < 2.0$ and to pass the top tagging described in section 6.4. It is also required to be separated from the lepton by $\Delta\phi$(large-R jet, ℓ) > 2.3 (close to backside), and from the small-R jet of leptonically decaying top by ΔR(large-R jet, small-R jet) > 1.5 (not overlapped from each other). Figure 7.10 shows the p_T distributions of large-R jets.

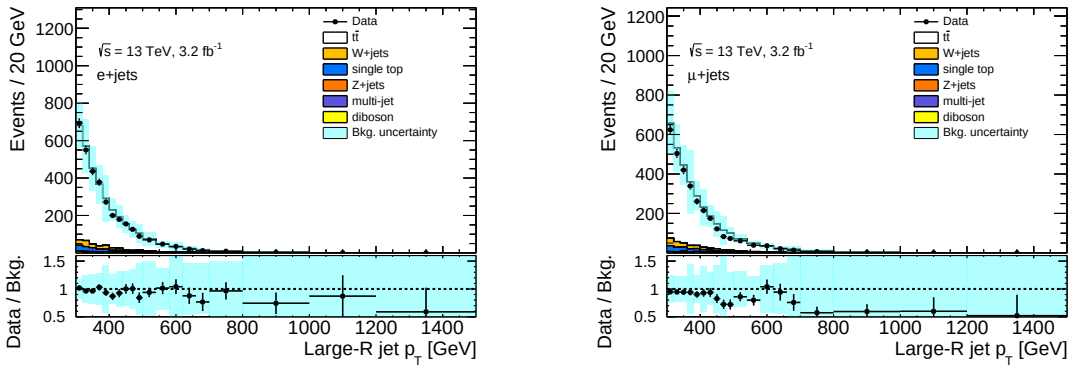

Figure 7.10: Large-R jet p_T distributions, electron channel (left) and muon channel (right).

Large missing transverse energy (E_T^{miss})

Large missing transverse energy (section 6.8) corresponding to the neutrino from semi-leptonic decaying top is required in this analysis.

$$E_T^{\text{miss}} > 20\,\text{GeV} \;\text{ and }\; E_T^{\text{miss}} + m_T(W) > 60\,\text{GeV}. \tag{7.1}$$

Here, the W transverse mass m_T is defined by:

$$m_T = \sqrt{2 p_T^{\ell} E_T^{\text{miss}} \,(1-\cos\phi)}, \tag{7.2}$$

where ϕ is the azimuthal angle between the lepton momentum and E_T^{miss} directions. This cut is effective to remove W boson background which decays into neutrino and lepton, and these criteria are required to suppress the multi-jet background [27]. Figure 7.11 show the distribution for E_T^{miss} and Figure 7.12 shows the W transverse mass distributions, for electron channel (left) and muon channel (right), respectively.

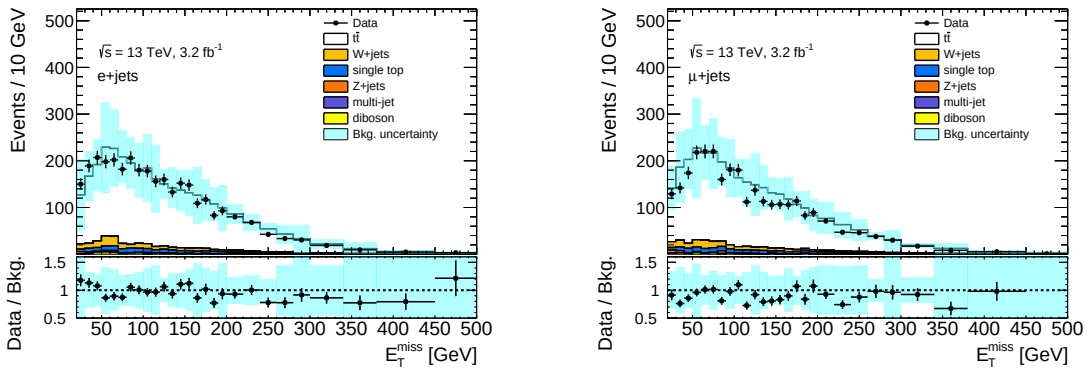

Figure 7.11: E_T^{miss} distributions, electron channel (left) and muon channel (right).

b-**tagging**

The event is required to have at least one b-tagged small-R track-jet (anti-k_T, $R = 0.2$) with $p_T > 10$ GeV and $|\eta| < 2.5$. The detail is described in Chapter 8, the multi-variate discriminant named MV2c20 tagger is applied at the working point of 70 % efficiency of b-tagging for the Standard Model $t\bar{t}$ events [144]. The distribution of number of b-tagged track-jets before dropping no b-tagged events is shown in Figure 7.13.

7.2 Event kinematics reconstruction

Using the reconstructed objects in the selected events, event kinematics are defined.

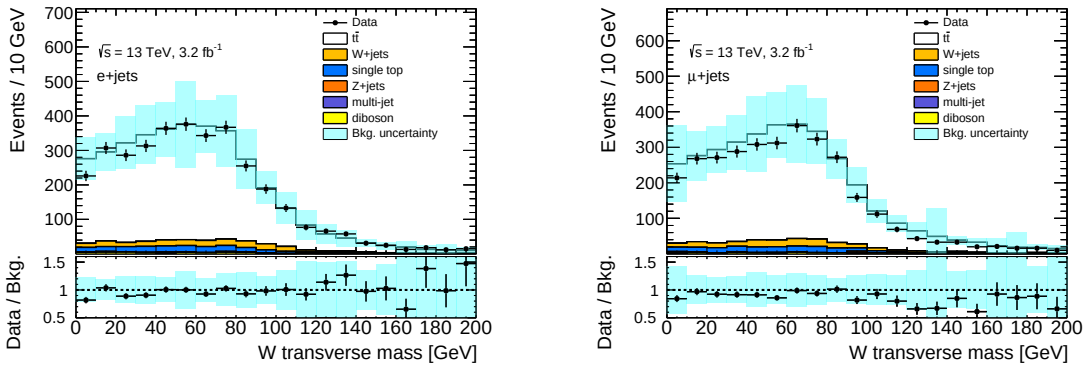

Figure 7.12: W transverse mass distributions, electron channel (left) and muon channel (right).

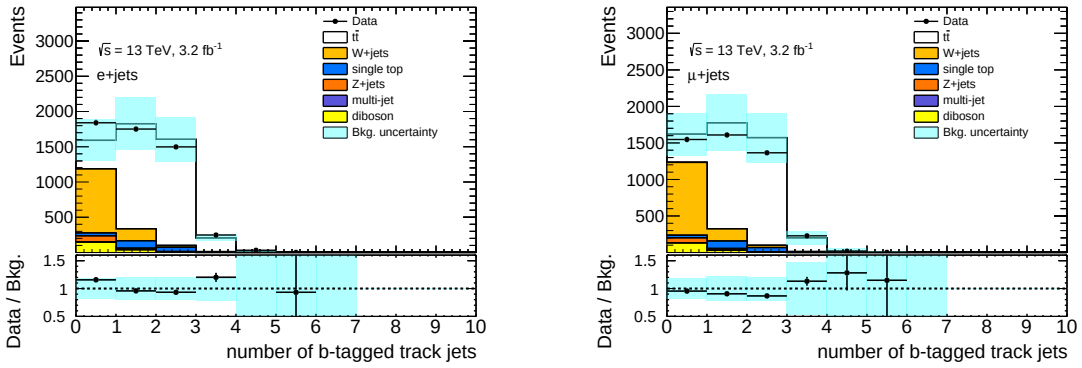

Figure 7.13: Number of *b*-tagged track-jets before dropping no *b*-tagged events, electron channel (left) and muon channel (right).

7.2.1 Neutrino reconstruction

The four-momentum of the neutrino in the semi-leptonic decay of the top is estimated from the missing transverse energy and lepton momentum. The neutrino p_T^ν is regarded as equal to $E_T^{\rm miss}$ of the event. Since it is impossible to measure longitudinal component of the neutrino momentum p_z directly, the constraint from the on-shell production of W boson with mass 80.4 GeV [1] is considered to obtain the neutrino p_z^ν. Under the assumption that the missing energy due to the neutrino and the lepton originate from the W boson decay, neutrino p_z^ν can be calculated by solving the following quadratic equations.

$$(E^\nu)^2 = (p_T^\nu)^2 + (p_z^\nu)^2, \tag{7.3}$$

$$(M_W)^2 = (E^\ell + E^\nu)^2 - (p_T^\ell + p_T^\nu)^2 - (p_z^\ell + p_z^\nu)^2 \tag{7.4}$$

The solution is given by

$$p_z = \frac{(M_W^2 - M_\ell^2 + 2p_T^\ell \cdot p_T^{\rm miss})p_z^\ell \pm \sqrt{D}}{2(E^{\ell 2} - p_z^{\ell 2})}, \tag{7.5}$$

where,

$$D = E^{\ell 2}((M_W^2 - M_\ell^2 + 2p_z{}^\ell \cdot p_T^{\rm miss})^2 - 4(E_T^{\rm miss})^2(E^{\ell 2} - p_z^{\ell 2})). \tag{7.6}$$

If there is only one real solution, it is used as the p_z^ν solution. If there are two real solutions, the one that is the smallest $|p_z^\nu|$ is chosen since it has better invariant mass of the $t\bar{t}$ resolution [26,27]. If there is no real solution, the magnitude of $E_T^{\rm miss}$ vector is varied to have one solution.

7.2.2 Top mass and $t\bar{t}$ mass reconstructions

Top mass

The leptonically decaying top mass is reconstructed by the four momentum of the small-R jet, the lepton and the neutrino. Figures 7.14 and 7.15 show the top mass for the leptonic side and hadronic side, respectively. The light blue bands indicate systematic uncertainties mentioned in Chapter 10.

Invariant mass of top-antitop system $m_{t\bar{t}}$

After all event selections and object reconstructions finished, mass of the top-antitop system ($m_{t\bar{t}}$) is reconstructed. This is calculated from four-vector of the reconstructed objects;

$$m_{t\bar{t}}^2 = |\text{Large-}R\text{ jet} + \text{small-}R\text{ jet} + \text{lepton} + \text{neutrino}|^2, \tag{7.7}$$

where the neutrino is reconstructed as described in subsection 7.2.1. Figures 7.16 show the reconstructed invariant mass $m_{t\bar{t}}$ distribution, electron channel and muon channel.

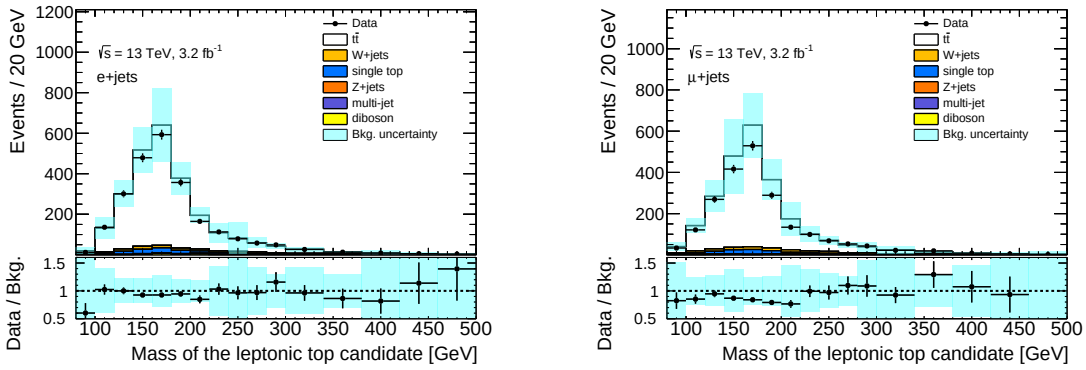

Figure 7.14: The reconstructed top mass distribution for the leptonic side, electron channel (left) and muon channel (right).

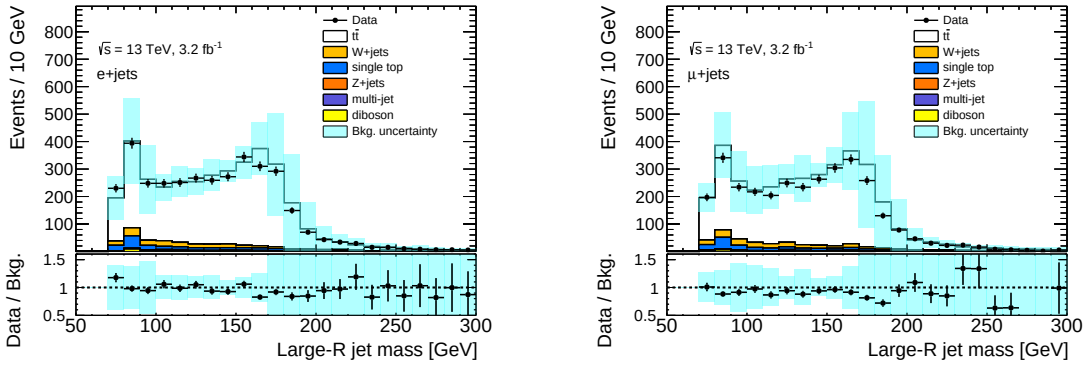

Figure 7.15: The top mass distribution for the hadronic side, Large-R jet mass distributions, for electron channel (left) and muon channel (right). When not so boosted topology, the large-R jet did not contain b-jets in $\Delta R < 1.0$ region, therefore it makes peak at the W mass (80.4 GeV).

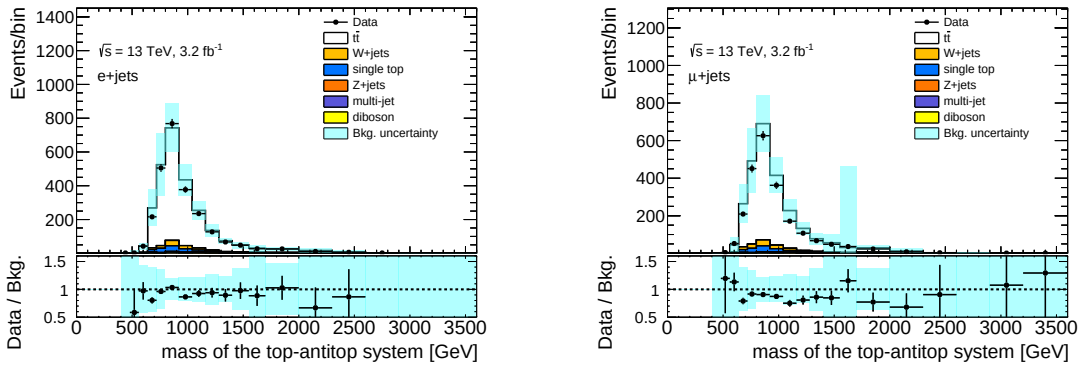

Figure 7.16: The invariant mass of the $t\bar{t}$ system, electron channel (left) and muon channel (right).

Table 7.1: Angular distribution

Process	Distribution
$q\bar{q} \to V$	$1+\cos^2\theta^*$
$gg \to G$	$1-\cos^4\theta^*$
$q\bar{q} \to G$	$1-3\cos^2\theta^*+4\cos^4\theta^*$

7.3 Reduction of Standard Model $t\bar{t}$ events

The main background in the boosted channel especially in the high mass region is the Standard Model $t\bar{t}$ events whose topology is the same as that of signal. There is a difference however in the angular distribution in the $t\bar{t}$ center-of-mass frame reflecting the production mechanism and the properties of the $t\bar{t}$ resonance (e.g. spin). Figure 7.17 shows the $\cos\theta$ distribution for $qq \to Z'$ (spin 1), $gg \to G$ (spin 2) and the Standard Model $t\bar{t}$ from the gluon fusion. Table 7.1 summarizes the angular dependence for the signal processes [145, 146]. The Standard Model $t\bar{t}$ process of the gluon fusion can be expressed as:

$$\frac{d\hat{\sigma}_{gg\to t\bar{t}}}{d\cos\theta} = \frac{\pi\alpha_s^2}{9s}\beta\left(1+2\beta^2-2\cos^2\theta\beta^2-2\beta^4+2\cos^2\theta\beta^4-\cos^4\theta\beta^4\right), \tag{7.8}$$

where s is the center-of-mass energy squared, m_t is the top quark mass, and $\beta = \sqrt{1-4m_t^2/s}$ is the velocity of the top quark. While the Standard Model $t\bar{t}$ distribution is strongly peaked to forward and backward directions, the signal distributions are more central. The center-of-mass angle θ^* is obtained from the laboratory system quantities. Figure 7.18 shows the kinematic variables in the center-of-mass frame and the laboratory frame. Since the difference of rapidity of two particles ($2Y$ in the center-of-mass frame, and $\Delta y = y_1 - y_2$ in the laboratory frame) is invariant under longitudinal Lorenz boost, $\cos\theta^*$ is given by:

$$\cos\theta^* = \frac{1-e^{-(y_1-y_2)}}{1+e^{-(y_1-y_2)}}, \tag{7.9}$$

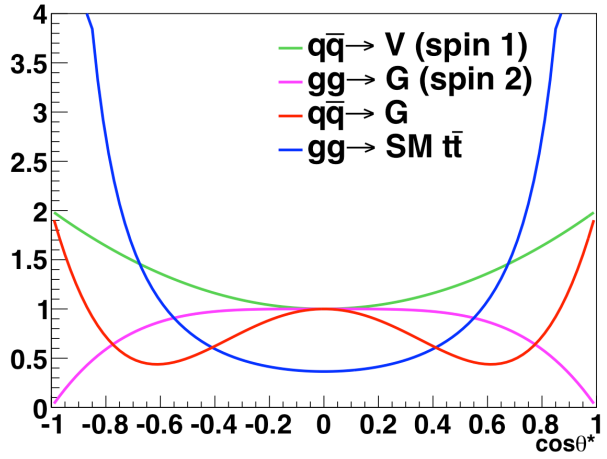

Figure 7.17: The $\cos\theta^*$ distribution for various signals of initial states compared to the Standard Model $t\bar{t}$.

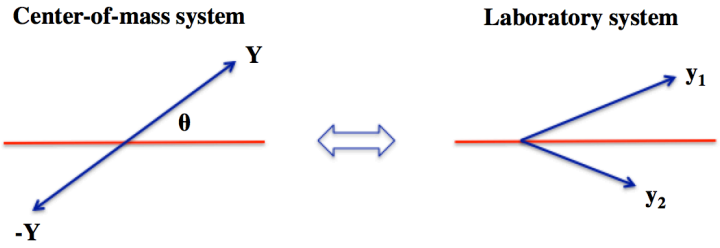

Figure 7.18: The definition of the scattering angle θ^* and rapidity Y in the center-of-mass system, and rapidity y in the laboratory system.

here the relations $Y = -\ln(\tan\frac{\theta}{2})$ and $2Y = y_1 - y_2$ are used. Figure 7.19 shows the Monte Carlo distribution of $\cos\theta^*$ for the Z' signal and background processes with the invariant $t\bar{t}$ mass window $1.6 < m_{t\bar{t}} < 2.2$ GeV. As expected, the Standard Model $t\bar{t}$ is peaked to the small angle while the Z' signal is populated in the large angle region. Equivalent information of Δy and

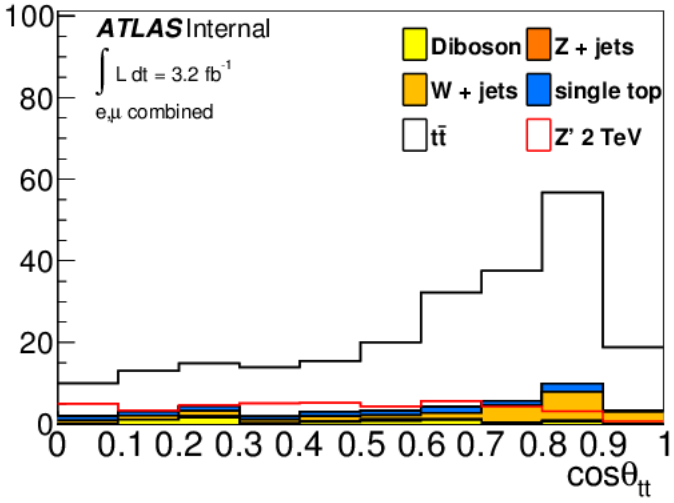

Figure 7.19: The center-of-mass angle $\cos\theta$ distribution of top (with the invariant $t\bar{t}$ mass window is $1.6 < m_{t\bar{t}} < 2.2$ GeV).

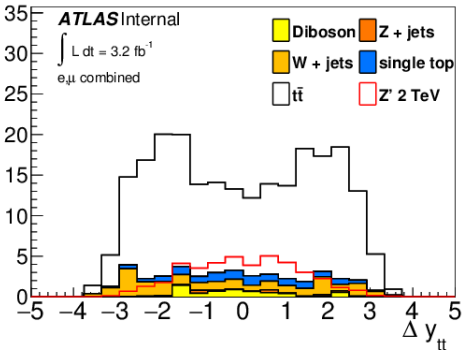

Figure 7.20: The center-of-mass angle Δy distribution of top (with the invariant $t\bar{t}$ mass window is $1.6 < m_{t\bar{t}} < 2.2$ GeV).

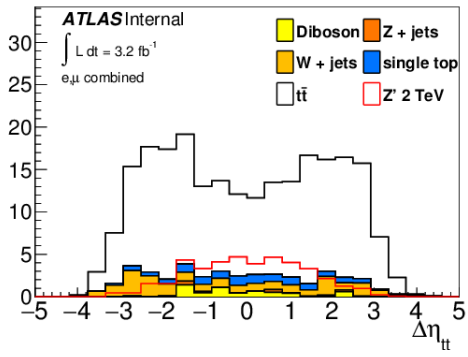

Figure 7.21: The center-of-mass angle $\Delta\eta$ distribution of top (with the invariant $t\bar{t}$ mass window is $1.6 < m_{t\bar{t}} < 2.2$ GeV).

similar quantity using pseudo-rapidity $\Delta\eta$ are shown in Figure 7.20 and Figure 7.21. In this

analysis a cut on $\Delta\eta$ is used. The cut value

$$|\Delta\eta| < 2.0$$

is optimized by maximizing the sensitivity:

$$\text{Sensitivity} = \sqrt{\sum_{i=0}^{\text{nbins}} \left(\frac{s_i}{s_i + b_i}\right)^2}. \tag{7.10}$$

Figure 7.22 and Figure 7.23 show a comparison of $m_{t\bar{t}}$ distribution with and without the $|\Delta\eta|$ cut. The background is reduced by a factor of ~ 2, while the signal is very little affected (the sensitivity is higher about 10 % than nominal). This cut is also effective to reduce another background contributions.

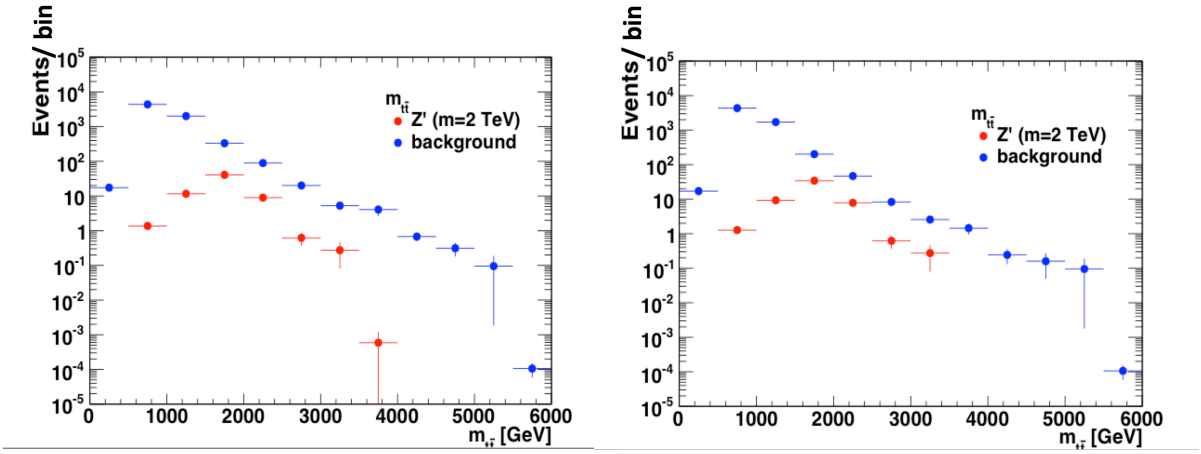

Figure 7.22: The $m_{t\bar{t}}$ shape before (left) and after (right) applied $\Delta\eta > 2.0$.

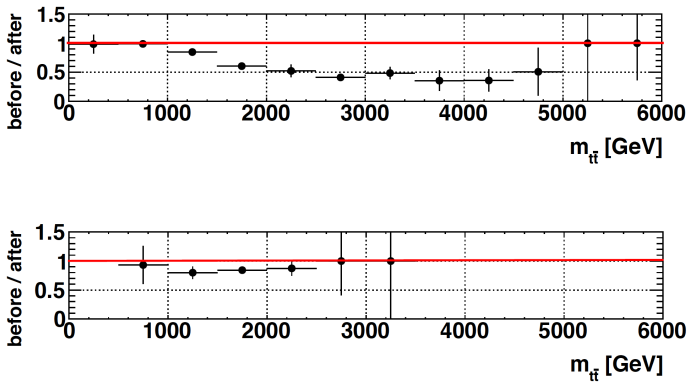

Figure 7.23: The ratio before(new)/after(nominal) $\Delta\eta > 2.0$ applied, background (left) and signal (right). The background can be reduced to the half in this cut though the signals remain.

Chapter 8

b-tagging study

Top quark decays into a b quark and a W boson. In order to reject background events not containing b-quark-induced-jets (b-jets), identification of b-jets, b-tagging is applied in this analysis as mentioned in Chapter 7. Since a B-hadron has relatively long lifetime of $\tau \sim 1.5$ ps, its average decay length is $< L_{xy} >= \beta\gamma c\tau \sim 6.4$ mm. Therefore, a secondary vertex can be reconstructed at a certain distance from the primary vertex and a large impact parameter, which is the distance of closest approach between the extrapolated track and the primary vertex, is expected. The b-tagging algorithm is based on the information of the impact parameters of the inner detector tracks associated with the jets, the secondary vertices and the reconstruction of the decay chain.

8.1 Flavour tagging algorithm – MV2c20

In this study, an ATLAS b-tagging algorithm named MV2c20 is employed, which is based on the multi-variate technique. The MV2c20 uses the combination of 24 input variables from three basic algorithms; impact parameter based algorithms, inclusive secondary vertex reconstruction algorithms and decay chain multi-vertex reconstruction algorithms [147]. The algorithms are developed using $t\bar{t}$ events that contain at least one lepton from a subsequent W decay.

Impact parameter based algorithm

The impact parameter based algorithm uses the transverse and longitudinal impact parameter significances $d_0/\sigma(d_0)$ and $z_0/\sigma(z_0)$ of all the tracks associated with the jet where $\sigma(d_0)$ and $\sigma(z_0)$ are the resolution of the transverse and longitudinal impact parameters, respectively [148].

Secondary Vertex Finding algorithm

Secondary vertex finding algorithm uses the information of the reconstructed secondary vertices displaced from the primary vertex. The secondary vertex is reconstructed from the steps that start from reconstructing two-track vertices except those originating from a long-lived particle, such as K_s^0 or Λ, photon conversions or hadronic interactions with the detector material.

Decay chain multi-vertex algorithm

Decay chain multi-vertex algorithm uses the topological structure of weak b- and c-hadron decays inside the jet [149, 150]. This algorithm reconstructs the hadron decay chain using Kalman Filter; chasing tracks from primary vertex$\rightarrow b \rightarrow c$-hadron.

For constructing the MV2c20 discriminant, a boosted decision tree (BDT) is trained to perform discrimination of b-jets from a mixture of 80 % light-flavour and 20 % c-jets. Figure 8.1(a) shows the output distribution of the MV2c20 for b (green), c (blue) and light (red) flavour jets. From this distribution, the cut corresponding to 70 % efficiency for b-jets (in this analysis, MV2c20 > -0.3098) is chosen as the default b-tagging criterion, the cut is determined from a separate Monte Carlo data of $t\bar{t}$ events. The tagging efficiency with this MV2c20 cut to each jet flavour is shown in Figure 8.1(b). Figure 8.2 shows the performance of the light-jet and c-jet rejection

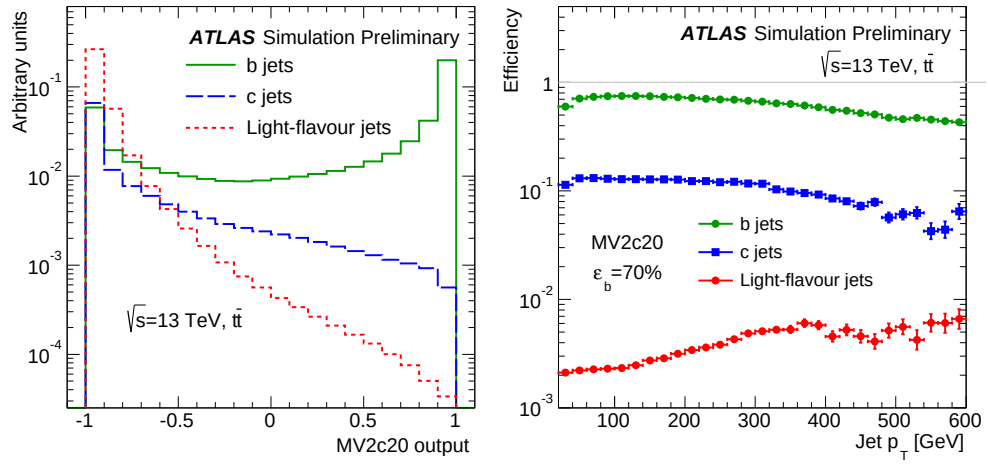

(a) (b)

Figure 8.1: The MV2c20 output for each flavour jets (a) and the tagging efficiency to each flavour jets for MV2c20 as a function of p_T (b) in $t\bar{t}$ event [147].

as a function of the efficiency to b-jets. In this figure, output of another algorithm MV2c00 **??** are shown, too. MV2c00 is trained only for light jets rejection, thus c-jet rejection by MV2c00 is low.

8.2 b-tagging for boosted $t\bar{t}$ resonance search

In the $t\bar{t}$ event topology as described in Chapter 7, a signal event have two b-jets, one is a decay product of the semi-leptonically-decaying top ($t \rightarrow Wb \rightarrow \ell\nu b$) and the other comes from the hadronically-decaying top ($t \rightarrow Wb \rightarrow q\bar{q}'b$). Since the former is isolated from the other jets, the performance of b-tagging study is well established. On the other hand, b-jet from the

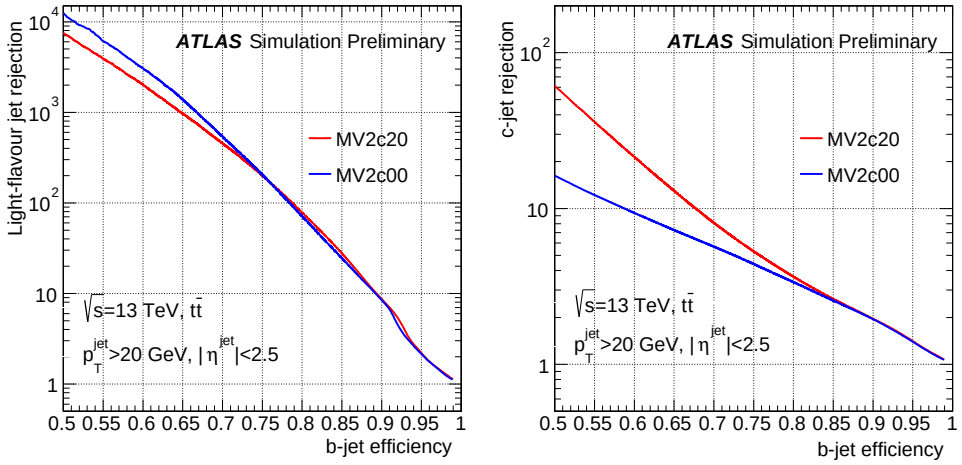

(a) (b)

Figure 8.2: The light-jet (a) and c-jet (b) rejection as a function of b-tagging efficiency for the MV2c20 b-tagging algorithm in $t\bar{t}$ events [147].

hadronically-decaying top is overlapped with other hadron jets from the subsequent W decay. In such 'dense' environment [151], several problems arise as described in the following.

The b-tagging efficiency for anti-k_T calo-jet with radius parameter $R = 0.4$ (which is Standard in Run1 analysis) in the Standard Model $t\bar{t}$ is shown in Figure 8.3. In the figure, the color shows difference mass point ($m_{Z'} = 1.75$ TeV and 4 TeV). Compared to the leptonic top side the performance is worse in the hadronic side. Furthermore, it becomes worse in the high mass Z', that is, in the high p_T hadron jets (Figure 8.4). This can be explained as follows. First, b-tagging algorithm uses only information from tracks. Calo-jet is reconstructed from clusters. For b-tagging, the tracks associated to the calo-jet are used (Figure 8.5, left). Charged-particle's tracks from b-hadron and light-flavour jets from $W \to q\bar{q}$ are overlapped inside the large-R jet cone, which leads to mis-identification of the tracks from the b-hadron in the b-tagging algorithm. For efficient b-tagging, both capturing the tracks from B-hadron and good approximation of B-hadron direction by the jet axis are needed. But those two are compromised in the dense environment. These problems are mitigated by the use of small-R track-jet. Track-jet which explicitly originated from the primary vertex in reconstruction has an advantage on applying b-tagging in such environment (Figures 8.5 and 8.6).

8.2.1 b-tagging performance comparison

The performances of b-tagging algorithm using jets with several radius parameters $R = 0.2$, 0.3 and 0.4 are studied with the signal MC samples (Figure 8.7). The efficiency of the b-tagging to events after event selection (Chapter 7) except b-tagging requirement is evaluated as a function of b-quark p_T using jets with $R = 0.2$, 0.3 and 0.4. The jet flavours are known by truth matching

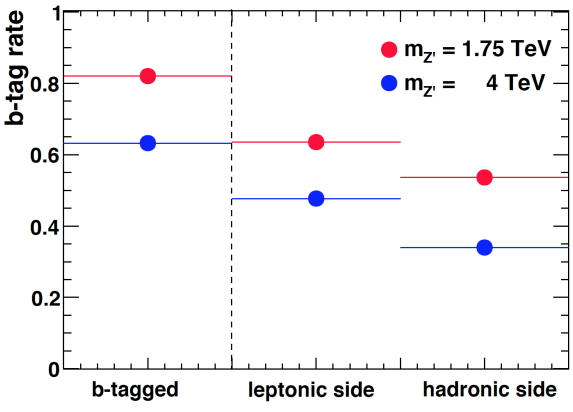

Figure 8.3: The b-tagging rate at combined, leptonic and hadronic side using $Z' \to t\bar{t}$ sample. The b-tagging working point is 70 %.

in the simulation. Figure 8.7(b) shows the comparison of b-tagging efficiency to b-quarks from the hadrnoically-decaying top with different size of R in the Z' signal of mass $= 4$ TeV. Better performance is found with smaller R, and the best result with the track-jet. In comparison with the b-tagging performance to isolated b-quarks from the leptonically-decaying top shown in Figure 8.7(a), comparable performance in the dense environment can be achieved in the case of the track-jet with $R = 0.2$, as shown in Figure 8.7(b). As shown in Figure 8.8, the b-tagging performance is relatively improved by $30 \sim 40$ %, by using a new method, track-jet with $R = 0.2$.

8.2.2 Calibration of the b-tagging efficiency

The potential difference between data and simulation in the b-tagging efficiency is taken into account by scale factor, which has been estimated by the independent sample requiring isolated b-jet in the event. The scale factor is then tested in the main analysis sample dominated by the $t\bar{t}$ events. Possible contribution of the $t\bar{t}$ resonance signal can be ignored because the scale factor is the ratio of efficiency in data and Monte Carlo that is also derived from the ratio of tagged and pretagged events.

The data and simulated samples after the event selection (Chapter 7) except b-tagging requirement are used. To enhance the purity of the b-jets in selected events, a tag and probe method is performed; when seeing the leptonic (hadronic) side, the existence of at least one b-tagged $R = 0.2$ track-jet in the hadronic (leptonic) side is required as a tag. Then, the b-enriched sample is obtained on the other side (probe). The b-tagging efficiency is then calculated as a function of p_T of the closest jet to the lepton (leptonic top) or large-R jet (hadronic top), where a new b-jet component is subtracted by using the Monte Carlo predictions (denoted as 'non-$t\bar{t}$' in equa-

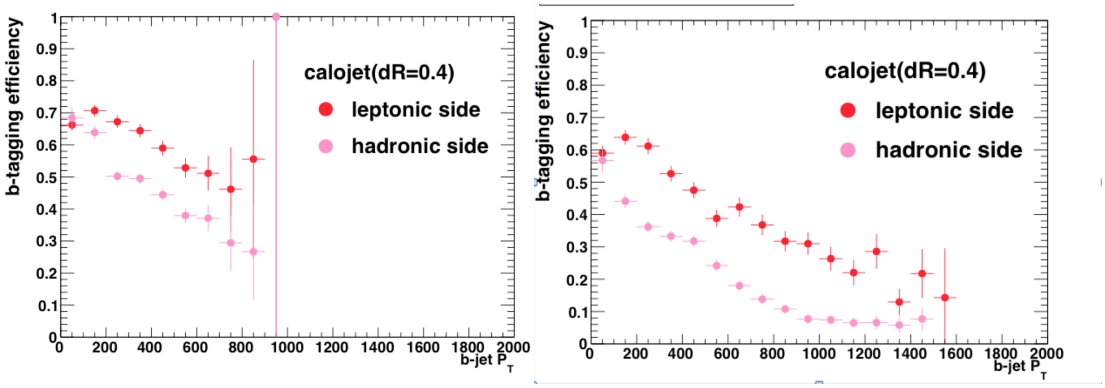

(a) (b)

Figure 8.4: b-tagging efficiency with $R = 0.4$ calo-jet as a function of p_T for Z' mass (a) 1.75 TeV and (b) 4 TeV.

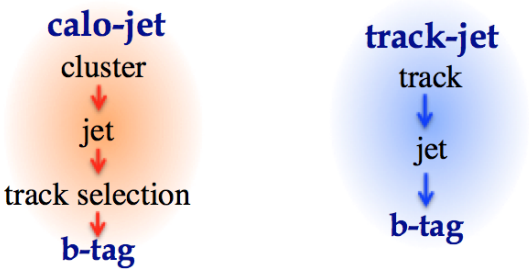

Figure 8.5: The concept of the b-tagging between calo-jet and track-jet.

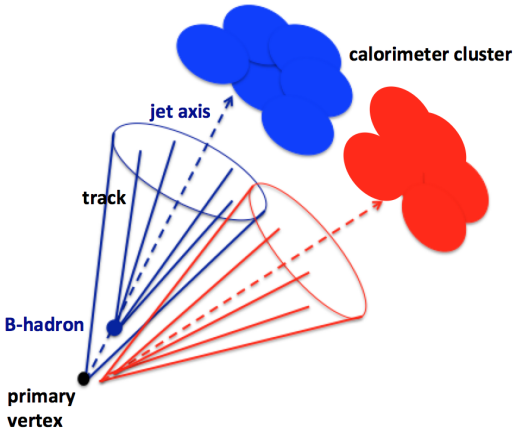

Figure 8.6: The concept of the difference b-tagging between calo-jet and track-jet

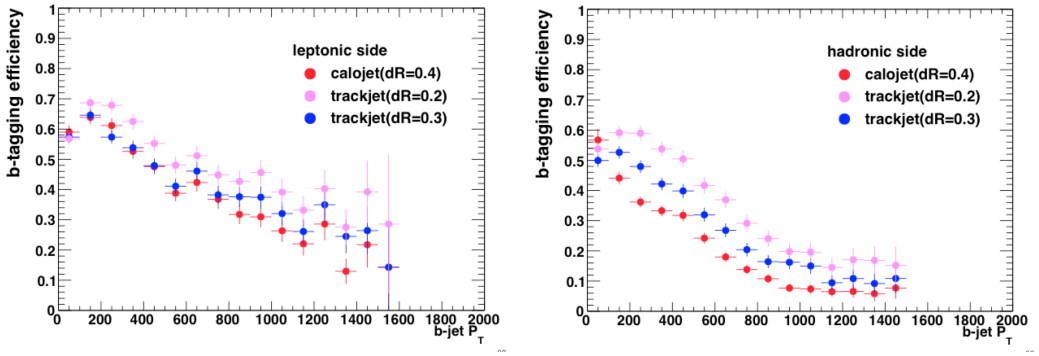

(a) (b)

Figure 8.7: b-tagging performance (a) for isolated b-jets as a function of p_T in the $t\bar{t}$ leptonic side and for (b) dense environment, hadronic side from Z' of mass 4 TeV.

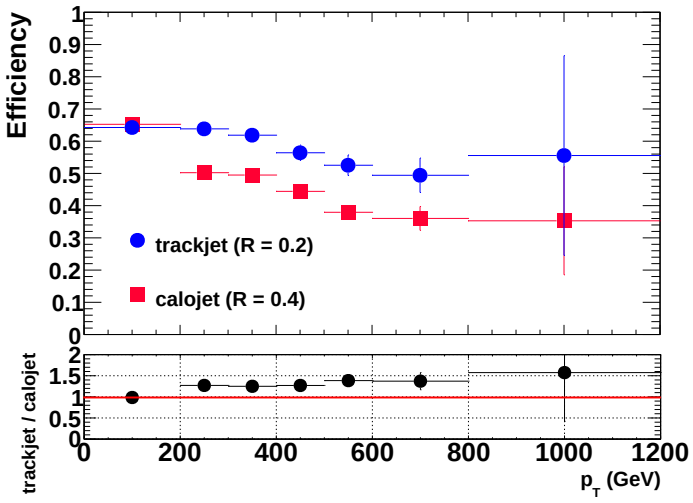

Figure 8.8: The b-tagging efficiency comparison between track-jet with $R = 0.2$ (new method) and calo-jet with $R = 0.4$ (old method in Run1) in the hadronic side.

tion 8.1).

$$b\text{-tagging efficiency (event fraction)} = \frac{\text{b-tagged} - \text{b-tagged non } t\bar{t}}{\text{pre-tagged} - \text{non-}t\bar{t}}. \tag{8.1}$$

Figure 8.9 and Figure 8.10 show the b-tagging efficiency and ratio of the data/MC when applying the b-tagging scale factor. In conclusion, the b-tagging scale factor estimated by the isolated b-jet is applicable to the b-jet in the dense environment.

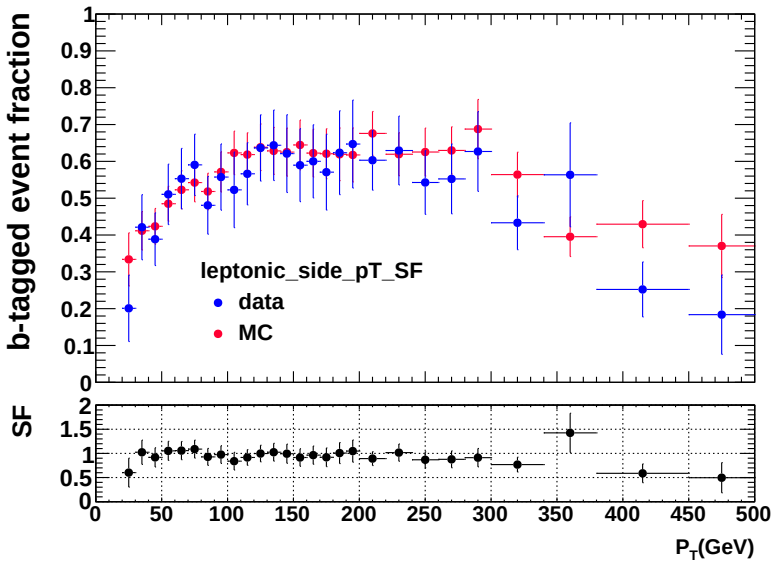

Figure 8.9: *b*-tagging efficiency and data/MC when applying *b*-tagging scale factor at the leptonic side.

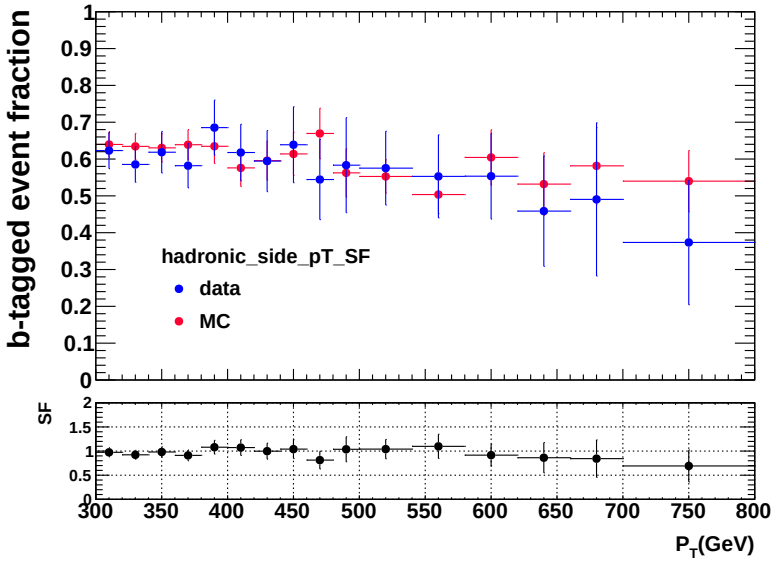

Figure 8.10: *b*-tagging efficiency and data/MC when applying *b*-tagging scale factor at the hadronic side.

Chapter 9

Data driven estimation of backgrounds

Since the simulation does not perfectly reproduce data, W+jets and QCD multi-jet background components are estimated using data. This method is established in Run1 analysis [26, 152] and optimized for Run2 implemented in [153–155]. In fact, the QCD multi-jet background is very small component especially in this boosted regime, $\sim 0.03\%$, as shown in Chapter 11.

9.1 W+jets background

W+jets background normalization is estimated by a data driven method since its production rate and flavour fractions are not well described in simulation. This method exploits the large asymmetry in the production rate of W^+ and W^- in proton-proton collisions since there are more valence u quarks than d quarks. The charge asymmetry of W is estimated by Monte Carlo simulations more reliably than the production rate. The number of W+jets events in the data can be obtained by:

$$\begin{aligned} N_{\mathrm{Data,W}} = N_{\mathrm{Data,W^+}} + N_{\mathrm{Data,W^-}} &= \left(\frac{N_{\mathrm{MC,W^+}} + N_{\mathrm{MC,W^-}}}{N_{\mathrm{MC,W^+}} - N_{\mathrm{MC,W^-}}}\right)(D^{+}_{\mathrm{asym}} - D^{-}_{\mathrm{asym}}) \\ &= \left(\frac{r_{\mathrm{MC}}+1}{r_{\mathrm{MC}}-1}\right)(D^{+}_{\mathrm{asym}} - D^{-}_{\mathrm{asym}}). \end{aligned} \tag{9.1}$$

Here, $r_{MC} = N_{MC,W^+}/N_{MC,W^-}$ is the ratio of number of W+jets events with a positive charged lepton to that with a negative charged lepton, and is calculated using SHERPA simulation [156, 157]. $D^{+(-)}_{\mathrm{asym}}$ is the number of observed events with a positive (negative) charged lepton, corrected for contributions from charge asymmetric processes other than W+jets, e.g. single top, W or Z, by subtracting the estimated amount by simulation. In the difference $(D^{+}_{\mathrm{asym}} - D^{-}_{\mathrm{asym}})$, charge symmetric contributions such as $t\bar{t}$ are cancelled and only the number for W+jets events is retained. The scale factor is obtained as the ratio of $N_{\mathrm{Data,W}}$ and $N_{\mathrm{MC,W}}$.

In order to reduce the statistical uncertainty in the scale factor estimation, the normalization region, where the W+jets events are enhanced, is defined by the event selection criteria but without

requiring the b-tag and requiring that the event fails the top tagging. The scale factors obtained are used for correcting the Monte Carlo estimation of W+jets background in the signal region. The value of the scale factor is 0.82 ± 0.18 for the electron channel and 0.73 ± 0.12 for the muon channel.

9.2 QCD backgrounds

The simulation of the background events involving non-prompt leptons and jets misidentified as leptons, mainly originating from QCD multi-jet production, suffers from large systematic and statistical uncertainties. The QCD multi-jet contribution is estimated using data by the Matrix Method [158, 159]. It exploits the fact that loose leptons contain more fakes from QCD multi-jet than tight leptons. The number of loose leptons N_L can be divided into the numbers of prompt leptons and fake leptons.

$$N_L = N_{prompt} + N_{QCD}. \tag{9.2}$$

The number of tight leptons N_T can be given by:

$$N_T = \varepsilon \times N_{prompt} + f \times N_{QCD}, \tag{9.3}$$

where ε (f) is the probability of prompt (non-prompt) leptons passing the loose criteria and also satisfies the tight criteria. By solving the equations 9.2 and 9.3, $f \times N_{QCD}$ is obtained as:

$$f \times N_{QCD} = \frac{(\varepsilon - 1)\, f}{\varepsilon - f} N_T + \frac{\varepsilon\, f}{\varepsilon - f} N_A, \tag{9.4}$$

where N_A is the number of events with anti-tight lepton selection ($N_A = N_L - N_T$).

The value of ε is calculated using MC samples of $t\bar{t}$ events. The value of f is obtained using data. A QCD enriched sample containing loose leptons is selected with the requirements of no isolation, $E_T^{\text{miss}} < 20$ GeV and $E_T^{\text{miss}} + m_{T,w} < 60$ GeV. For the electron channel, $d_0 < 5$ mm is required while $d_0 < 3$ mm for the muon channel. By applying the tight selection, N_T is calculated. The f is obtained as N_T / N_L after subtracting the small N_{prompt} contribution using MC simulation.

The QCD background in the $t\bar{t}$ event selection is calculated using equation 9.4 with N_T and N_A in the signal region. A systematic uncertainty of 50 % is assigned, including that arising from MC subtraction.

Chapter 10

Systematic Uncertainties

To evaluate the results of this study, the following systematic uncertainties that can change the normalization and shape of $m_{t\bar{t}}$ distribution are considered.

Experimental uncertainties

The total uncertainty in the luminosity in 2015 dataset is 2.1 %, which depends on the calibration of the luminosity scale, and this is applied as a constant shift of the normalizations of the simulated events. It is estimated by the method in reference [66] for Run2 2015 data.

10.1 Uncertainties on the reconstructed objects

For the physics objects described in Chapter 6-7, the relevant quantities for the objects are shifted to by the amount of associated systematic uncertainty to evaluate the effects on the normalization and shape of the reconstructed $m_{t\bar{t}}$ distribution.

Leptons

For the electron or muon in the events, the trigger, reconstruction and identification efficiencies as well as the resolution and scale of the momentum are accounted for the systematic uncertainties.

Small-R jets

The jet energy scale uncertainties and jet energy resolution uncertainty for $R = 0.4$ jets which are discussed in section 6.2 are considered. The jet energy resolution (JER) uncertainty is estimated by smearing the nominal JER by the observed differences in JER between MC simulation and data measured using in-situ technique extrapolated to Run2 at $\sqrt{s} = 13$ TeV from Run1 at $\sqrt{s} = 8$ TeV. The jet energy scale is also derived from$\sqrt{s} = 8$ TeV and extrapolated to$\sqrt{s} = 13$ TeV [107]. The estimated uncertainty is symmetrized and used as an input to the fit.

Large-R jets

The uncertainty such as jet mass and τ_{32} coming from the top-tagging described in section 6.4 is also considered. They are derived from $\sqrt{s} = 8$ TeV [160] and uncertainties are extrapolated to $\sqrt{s} = 13$ TeV.

b-tagging of the track-jets

Taking account on the correlation and over-profiling, the uncertainties are broken down into eigenvector: 6, 4 and 12 eigen vectors for each b-, c-, light- flavor quarks respectively, and 2 eigenvectors specifically for the extrapolation of the scale factor in high p_T are considered. In the high p_T region, flavours are correlated. c- and light- flavour had very small impact on the result.

10.2 Uncertainties on the background estimations

Uncertainties for $t\bar{t}$ background

The $t\bar{t}$ cross section is calculated from NNLO+NNLL theory [161]. It is $\sigma_{t\bar{t}} = 832^{+46}_{-52}$ pb for a top quark mass of 172.5 GeV. The $t\bar{t}$ generator uncertainty, accounting for the difference between generator implementations for the hard processes, is evaluated by comparing the acceptance and shape between POWHEG+HERWIG and MCNLO+HERWIG [162–167]. The uncertainty of the electroweak correction of the loop factor (Sudakov corrections [168]) is estimated to be 10 % of their deviation from unity [154].

The cross section is shifted by Parton distribution function (PDF) variation uncertainty. According to the recommendation from PDF4LHC [169], the PDF and α_s uncertainties are calculated [95, 96, 96, 101, 170].

For the ISR/FSR uncertainty estimation, the set of POWHEG + PYTHIA6 are used as shape comparison between nominal set and other modified sets which modified shower radiation, factorization and renormalization scale ($\times 2$ and $\times 0.5$) and NLO radiation for QCD [171–173].

Uncertainties for single top background

The cross-section uncertainty is regarded as ± 5.3 % [174], corresponding the theoretical uncertainty on NNLO in QCD [175–177].

10.3 Impact of the systematics

The estimated impact of the uncertainties in the electron and muon channels are shown in Table 10.1. The effect of the systematic uncertainties on the mass spectra and differences between electron and muon channels are shown in Appendix 12 and Appendix 12, respectively.

Table 10.1: Systematic impact on the background yields in each channel, in percentage values.

Systematics	**Electron channel**	**Muon channel**
large-R jet	16	16
small-R jet	1.0	0.8
b-tagging eff	1.4	1.6
b-tagging c mistag	0.6	0.6
b-tagging light mistag	1.3	0.9
lepton	1.5	1.5
luminosity	2.0	2.0
E_T^{miss}	0.1	0.1
QCD	0.0	0.0
single top cross section	0.3	0.2
$t\bar{t}$ electroweak correction	0.0	0.0
$t\bar{t}$ generator	5.4	1.7
$t\bar{t}$ ISR/FSR	1.8	4.1
$t\bar{t}$ PDF	1.5	1.7
$t\bar{t}$ parton shower	5.8	11.4
$t\bar{t}$ cross section	5.4	5.4
W+jets	0.0	0.0
Total	18.8	21.1

Chapter 11

Results and Discussion

The number of data events observed after the event selection is summarized in Table 11.1 (electron channel) and Table 11.2 (muon channel) together with the expected background yields from the Standard Model processes considered. Figure 11.1 shows the distribution of reconstructed

Table 11.1: Event yields for the electron boosted channel. Uncertainties on background estimation are also shown.

Type	Yield
$t\bar{t}$	3214 ± 626
W+jets	197 ± 47
single top	173 ± 34
Z+jets	28 ± 11
multi-jet	1.0 ± 0.5
diboson	46 ± 11
Total	3658 ± 689
Data	3531

Table 11.2: Event yields for the muon boosted channel. Uncertainties on background estimation are also shown.

Type	Yield
$t\bar{t}$	3136 ± 697
W+jets	199 ± 43
single top	166 ± 33
Z+jets	27 ± 11
multi-jet	0.9 ± 0.5
diboson	37 ± 8
Total	3566 ± 752
Data	3222

invariant mass of $t\bar{t}$ system ($m_{t\bar{t}}$). The data are in good agreement with the background predictions within the statistical and systematic uncertainties, and no significant data excess in a way as expected from the production of a $t\bar{t}$ resonance is observed. In the following sections, limits are set on the cross-section of $t\bar{t}$ resonance production.

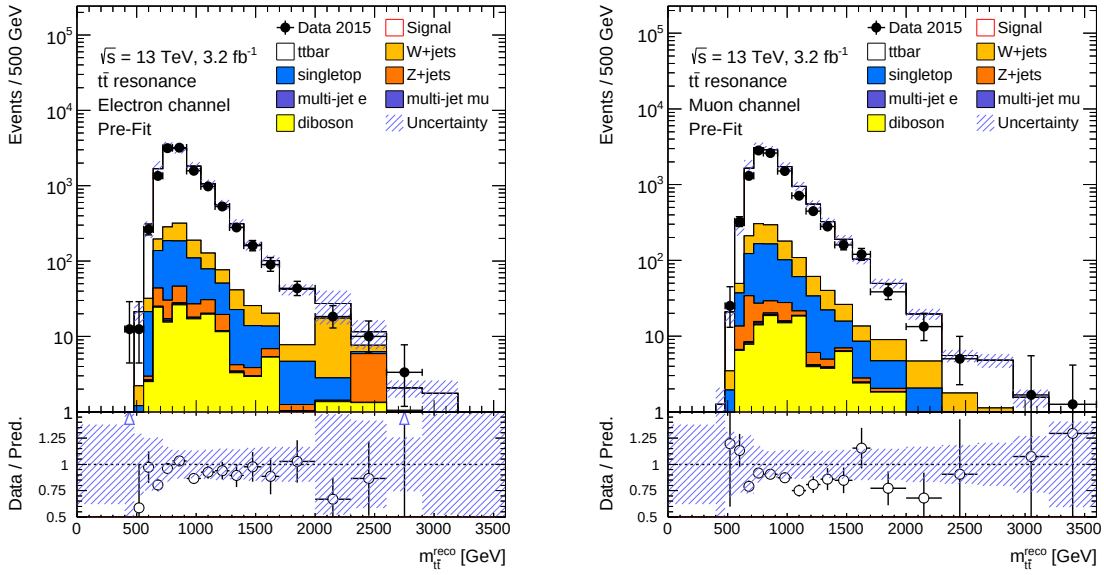

Figure 11.1: The invariant mass of $t\bar{t}$ distribution, electron channel (left) and muon channel (right).

11.1 Limit setting

Limits on the production cross-section of signal are computed by a frequentist approach using the CLs method at the 95 % confidence level (CL) [178–180]. This method is based on the comparison of two hypotheses: background only and background+signal.

11.1.1 Profile likelihood

The likelihood function for a specific signal assumption is defined using Poisson probability for the observed number of events and Gaussian probability describing the constrains on the systematic uncertainties associated with the signal and background yields:

$$L(\mu,\Theta) = \prod_{i=0}^{\text{channels,bins}} \text{Poisson}(n_i|\nu_i)\text{Gauss}(\Theta), \tag{11.1}$$

where ν_i is the expected number of events in bin i of the $m_{t\bar{t}}$ histogram, expressed as

$$\nu_i = \mu \cdot s_i \cdot C_s(\Theta) + b_i \cdot C_b(\Theta) \tag{11.2}$$

The parameter μ is the relative signal strength with respect to the assumed $t\bar{t}$ resonance cross-section. Expected signal and background yields are s_i and b_i, respectively. $C(\Theta)$ represents the shift of expected yield due to systematic effects parameterized as a function of nuisance parameters Θ. The signal yield s_i is defined by:

$$s_i = a_i \sigma_{sig} \mathrm{Br}(t\bar{t}) \cdot L, \tag{11.3}$$

where the a_i is the signal acceptance for bin i, σ_{sig} is the production cross-section for the resonance, $\mathrm{Br}(t\bar{t})$ is the branching fraction to $t\bar{t}$ and L is the integrated luminosity of the data sample [154, 181, 182]. The Poisson probability for observing n_i events in bin i is given by:

$$\mathrm{Poisson}(n_i|\nu_i) = \frac{\nu^{n_i} e^{-\nu_i}}{n_i!}. \tag{11.4}$$

Variation of nuisance parameters, generically represented by Θ, is constrained by the Gaussian probability,

$$\mathrm{Gauss}\,(\Theta|0,\sigma) = \frac{1}{\sqrt{2\pi}\sigma} \exp\left(-\frac{\Theta^2}{2\sigma^2}\right). \tag{11.5}$$

here σ is the 1-*sigma* variation of parameter Θ.

The profile likelihood ratio $\Lambda(\mu)$ is defined by:

$$\Lambda(\mu) = \begin{cases} \dfrac{L(\mu, \hat{\hat{\Theta}}(\mu))}{L(0, \hat{\Theta})} & (\hat{\mu} < 0), \\ \dfrac{L(\mu, \hat{\hat{\Theta}}(\mu))}{L(\hat{\mu}, \hat{\Theta})} & (\hat{\mu} \geq 0). \end{cases} \tag{11.6}$$

where $\hat{\hat{\Theta}}(\mu)$ is the value of Θ that maximize L for a given value of μ. In the denominator, $\hat{\mu}$ and $\hat{\Theta}$ are the values that maximizes the Likelihood, i.e. the best fit values of μ and Θ. In the case of negative $\hat{\mu}$, it is forced to 0 which is the best value under the condition of zero or positive signal strength for the $t\bar{t}$ resonance production [180].

11.1.2 Test static

The test static $\tilde{q}_\mu$ is defined by equation 11.7,

$$\tilde{q}_\mu = \begin{cases} -2\ln\Lambda(\mu) & (\hat{\mu} \leq \mu) \\ 0 & (\hat{\mu} > \mu) \end{cases} = \begin{cases} -2\ln \dfrac{L(\mu, \hat{\hat{\Theta}}(\mu))}{L(0, \hat{\Theta})} & (\hat{\mu} \leq 0), \\ -2\ln \dfrac{L(\mu, \hat{\hat{\Theta}}(\mu))}{L(\hat{\mu}, \hat{\Theta})} & (0 \leq \hat{\mu} \leq \mu), \\ 0 & (\hat{\mu} > \mu). \end{cases} \tag{11.7}$$

This represents the increase of $-2\ln L(\mu)$ with respect to the minimum value $-2\ln L(\hat{\mu})$ under the constraint of $0 \leq \hat{\mu} \leq \mu$. The upper bound on $\hat{\mu}$ is imposed to ensure a one-sided confidence interval, i.e. an upward fluctuation of the data giving a large value of $\hat{\mu}$ is not used as an evidence against a smaller value of μ being tested, which can lead to a two-sided confidence interval (an accidental discovery).

11.1.3 Limit on μ

For a given value of μ, using the pdf's of $\tilde{q_\mu}$, $f(q|\mu,\Theta)$, for two hypothesis, background only ($\mu = 0$) and background+signal, p-values are calculated:

$$p_\mu = \int_{\tilde{q}_{\mu,\mathrm{obs}}}^{\infty} f\left(\tilde{q}_\mu|\mu,\hat{\Theta}_{\mu,\mathrm{obs}}\right) d\tilde{q}_\mu \quad (\mathrm{signal}+\mathrm{background}) \tag{11.8}$$

$$1-p_b = \int_{\tilde{q}_{\mu,\mathrm{obs}}}^{\infty} f\left(\tilde{q}_\mu|0,\hat{\Theta}_{0,\mathrm{obs}}\right) d\tilde{q}_\mu \quad (\mathrm{background\ \ only}). \tag{11.9}$$

The value CL_s is defined by the ratio these p-values:

$$CL_s = \frac{p_\mu}{1-p_b}. \tag{11.10}$$

For the experimental data, the value of CL_s is calculated as a function of μ and the value of μ which gives $CL_s = 0.05$ is defined as the limit of μ at the 95 % confidence level. It is used as a robust procedure to avoid an accidental exclusion of background only hypothesis. TRexFitter [183], RooStats [184] and RooFit [185] were used to perform this limit setting procedure. The limit on cross-section times branching ratio is defined by $\mu\sigma_{sig}\mathrm{Br}(t\bar{t})$.

11.1.4 Limits on Z' signal

The expected and observed limits at the 95 % CL on the cross-section times branching ratio of the Z'_{TC2} signal are shown in Figure 11.2 as a function of $m_{Z'}$. Signal points used in this study are, $m_{Z'} = 400$ GeV, 500 GeV, 750 GeV, 1 TeV, 1.25 TeV, 1.5 TeV, 1.75 TeV, 2 TeV, 2.25 TeV, 2.5 TeV, 2.75 TeV, 3 TeV, 4 TeV and 5 TeV as shown in Table 5.2 in Chapter 5. The dashed line shows expected limits when no signal is in data. The green and yellow bands show the $\pm1\sigma$ (68 %) and $\pm2\sigma$ (95 %) ranges, respectively. The red dots are the observed limits. Values of cross-section times branching ratio greater than ~ 0.1 pb are excluded for the production of Z' scenario. The red lines show the cross-section times branching ratio for Z', corrected for k-factor 1.3 presenting the QCD correlation factor LO to NLO. Two values of resonance width are considered, $\Gamma/m_{Z'} = 1.2$ % and 3.0 %. From a comparison with the cross-section limit, mass range of Z' in 0.7 - 2.4 TeV and 0.5 - 3.0 TeV are excluded at the 95 % CL for the assumed resonance width of 1.2 % and 3.0 %, respectively. The $m_{t\bar{t}}$ distributions after profiling of the nuisance parameters are shown in Figure 11.3. The fitting results of nuisance parameter impact on fitting is shown in Appendix 12.

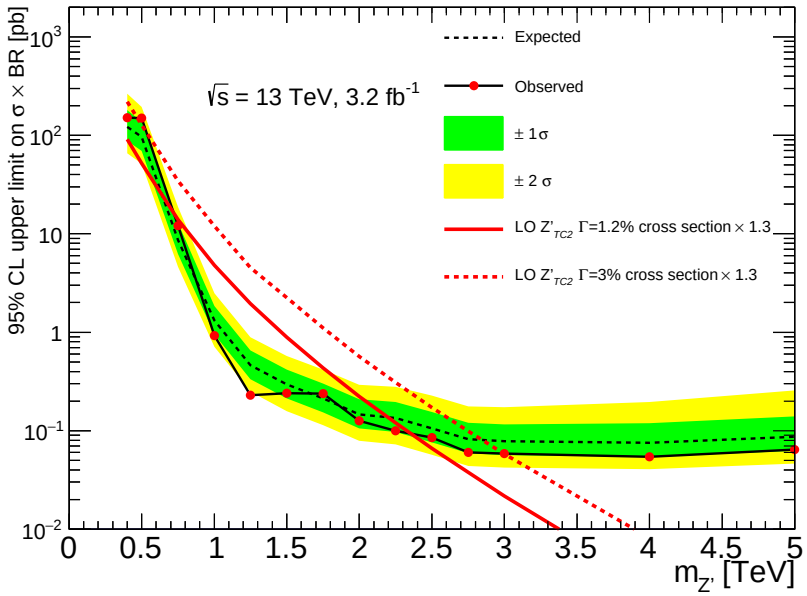

Figure 11.2: The 95 % CL limits on the cross-section times branching ratio of the Z'_{TC2} signal using observed data.

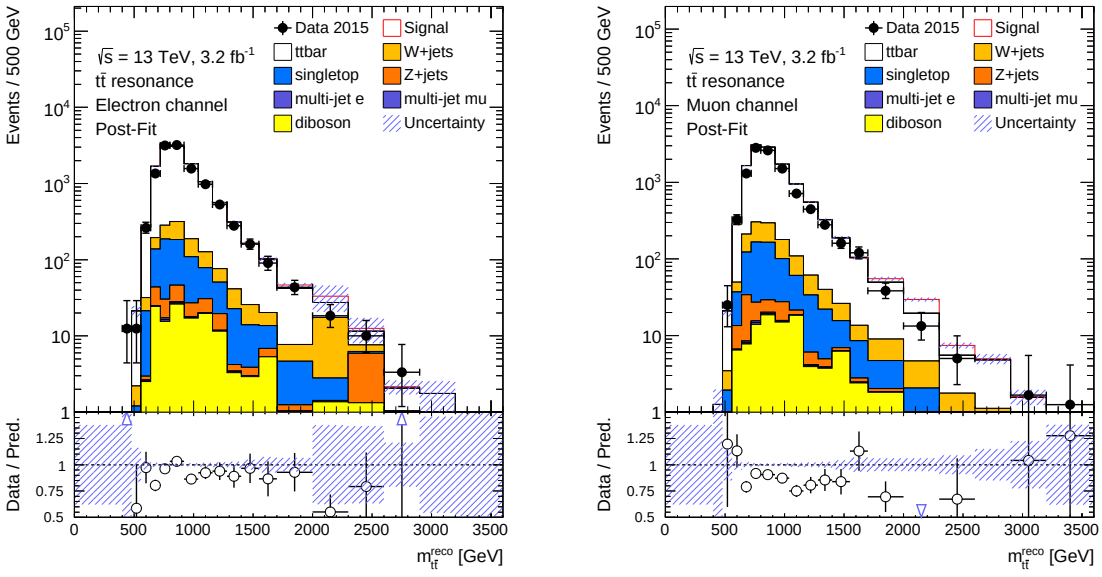

Figure 11.3: $m_{t\bar{t}}$ distributions after fitting with the profiling of the nuisance parameters for the electron (left) and muon (right) channels.

11.1.5 Limits on KK graviton signal

The 95 % CL limits on the cross-section times branching ratio for KK graviton are obtained as shown in Figure 11.4. Signal points used in this study are; $m_{KK} = 500$ GeV, 750 GeV, 1 TeV, 1.5 TeV, 2 TeV and 3 TeV, 4 TeV as shown in Table 5.3. The values are similar to those for Z' limits, but the slight difference reflects the acceptance difference arising from different angular distributions (spin 1 and spin 2). Theoretical cross-section times branching ratio is shown as the red curve. The cross-section times branching fraction larger than 2 times the model value is excluded for $m_{KK} = 1.0$ TeV and 3 times for $m_{KK} = 0.75$ TeV.

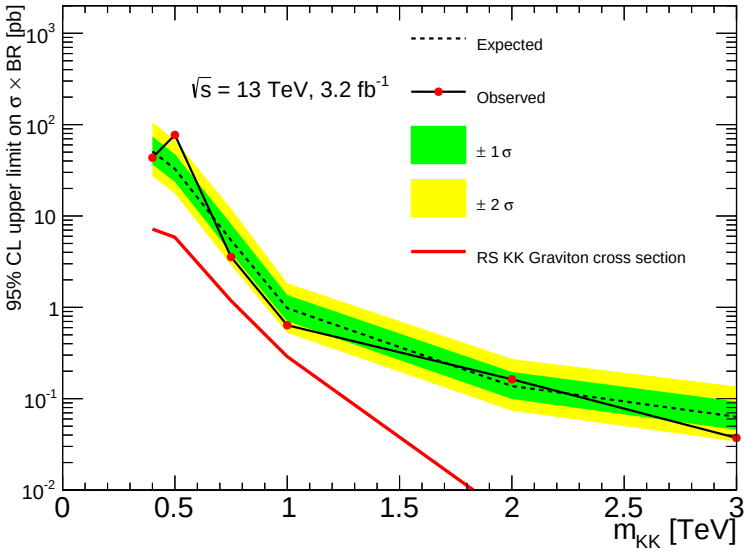

Figure 11.4: The 95 % CL limit on the cross-section times branching ratio of the KK graviton signal.

11.1.6 Comparison with the latest results from another experiment

In this year 2016, the ATLAS and CMS made public the results using the 2015 data almost at the same time [154, 186], this section describes how it was in the CMS search. Using the integrated luminosity 2.6 fb^{-1}, the CMS set limits at 95 % CL on the production of new particle with semi-leptonic channel. Top-color Z' excluded 0.6 TeV $< m_{Z'}(\Gamma/m) = 1\ \% < 2.3$ TeV (Figure 11.5), 0.5 TeV $< m_{Z'}(\Gamma/m) = 10\ \% < 3.4$ TeV and 0.5 TeV $< m_{Z'}(\Gamma/m) = 30\ \% < 4.0$ TeV.

Slightly better result of Figure 11.2 was obtained than that of CMS's, though they are similar taking account of systematics. The detector of ATLAS and CMS are built in different principle then the procedure of object reconstruction is also different with each other. The systematics estimation in ATLAS analysis is more conservative than that of CMS's (e.g. the multi-jet background

is neglected in CMS analysis). No excess was found in both analyses.

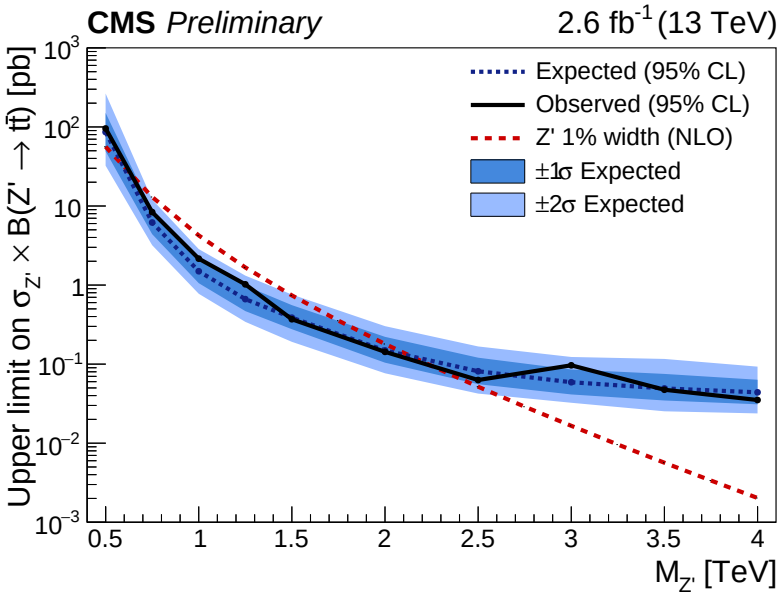

Figure 11.5: The 95 % CL limit on the cross-section times branching ratio of the Z' with $\Gamma/m =$ 1 % signal [186].

Chapter 12

Summary and conclusion

In spite of the completeness of the Standard Model predictions by the Higgs boson discovery, some phenomena can not be explained by current model and beyond the Standard Model physics is considered. For example, the large discrepancy between GUT or Plank scale and the electroweak scale called the hierarchy problem, and several models that solve the problem are expected. These models such as top-color model and extradimension model predict new particles that decaying into $t\bar{t}$. Usually, the search is performed by searching excess on the invariant mass of the $t\bar{t}$ spectrum, and high mass search is needed.

This study was performed for searching new heavy particles that decay into $t\bar{t}$ with the center-of-mass energy $\sqrt{s} = 13$ TeV in the LHC-ATLAS experiment. The dataset corresponding to an integrated luminosity of 3.2 fb^{-1} was used. Using the boosted technique, the search required the lepton+jets channel where W form a top decays leptonically and the other hadrninally. The hadronically decaying top can be regarded as large-R jet. The events must pass the single lepton trigger, have exactly one lepton, large-R jet with top-tagged, small-R jet, missing energy (E_T^{miss}) and at least one b-tagged with track-jet of $R = 0.2$. The large-R jet uses trimming algorithm to suppress pile-up effects and subjets are reclustered with k_t algorithm. The top tagging uses both invariant mass of the jet and N-subjettiness ratio τ_{32} to reject multi-jet background. The previous search used $R = 0.4$ calo-jet for b-tagging, but there were problems with low efficiency in the hadronic side. Using the smaller radius jet made from $R = 0.2$ track-jet, higher b-tagging efficiency (about 30 % improved) was obtained in spite of such dense environment. In addition, applying the new cut variables related to the center-of-mass angle, the dominant background, the Standard Model $t\bar{t}$ were reduced to half whereas the signals remained (about 10 % improved).

No evidence for new physics has been observed in the $t\bar{t}$ invariant mass spectra. Upper limits on the cross-section times branching ratio have been set for new particles. From a comparison with the model cross-section, mass of Z' was excluded in the range $m_{Z'} < 2.4$ TeV for $\Gamma/m = 1.2$ % and $m_{Z'} < 3$ TeV for $\Gamma/m = 3$ %. For KK graviton, cross-section times branching fraction 2 times the model value or larger was excluded for $m_{KK} = 1.0$ TeV and 3 times for $m_{KK} = 0.75$ TeV. By the end of Run2, the total integrated luminosity will be 100 fb^{-1}, the search sensitivity will reach the KK graviton.

Acknowledgements

I would like to express gratitude to many people that have supported and helped my Ph.D studies. I was happy to have chance to study this work in CERN with great scientists.

First of all, I would like to thank my supervisor Prof. Tatsuo Kawamoto who always gave advises and encouragements throughout my time as a student of the University of Tokyo. I learned a great amount about physics through discussion with him. I would like to express my gratitude to Prof. Koji Terashi who supervised this analysis. From him, I got many useful advices and accurate instructions for the analysis strategy and this thesis. Big thanks for Dr. Takuya Nobe who also supervised this analysis and corrected this thesis very carefully. I always surprised he producing new idea in a smart way.

I would like to thank Dr. Danilo Enoque Ferreira De Lima who is a great leader in the ATLAS ttbar resonance team and always helped and gave useful advice for me. I also wanted to thank other ATLAS ttbar resonance team members, especially Dr. Silvestre Marino Romano, Prof. Samuel Calvet for providing useful information.

I would like to thank to high-p_T calibration on di-jet event team; Prof. Yuji Enari, Prof. Michael Kagan, Ms. Anna Shchebakoba, Ms. Chiara Ricci, Prof. Sara Strandberg, Prof. Aurelio Juste Rozas, Prof. Tim Scanlon and other flavour-tagging calibration team members. Though this calibration work is not directly for this Ph.D thesis, I had many useful discussions and experiences.

I would like to thank all the people in ICEPP and other related institutes, in particular Prof. Shoji Asai, Prof. Junichi Tanaka, Prof. Tomio Kobayashi, Prof. Sachio Komamiya, Prof. Hiroshi Sakamoto, Prof. Naoko Kanaya, Prof. Shinpei Yamamoto, Prof. Koji Nakamura, Prof. Tatsuaya Masubuchi, Dr. Takashi Yamanaka, Dr. Tomoyuki Saito, Dr. Keita Hanawa, Dr. Takayuki Yamazaki, and Prof. Toshio Namba gave me lectures and good suggestions. Prof. Tetsuro Mashiomo, Prof. Yoshizumi Inoue and Mr. Nagata Matsui provided comfortable computing environments in Tokyo. ICEPP secretary, Mrs. Masako Shiota, Ms. Shizue Tezuka, Mrs. Yoko Takemoto, Mrs. Kayo Yamaura always supported for arrangement for trips to CERN and conferences and other many office work. Staffs in physics office, 'kyomu', in the university supported for university life.

I would like to special thanks to Dr. Keisuke Yoshiara who always give good suggestions since 7 years ago, and his and his wife Seiko's warm support always encourage me. Also special thanks to Mr. Masahiro Morinaga who always helped me from Master's course. I am very

grateful to colleagues and other institute members in CERN and Tokyo, Dr. Yuto Minami, Mr. Shion Chen, Mr. Tomohiro Yamazaki, Mr. Masahiro Yamatani, Mr. Chikuma Kato, Mr. Tatsuya Mori, Ms. Chihiro Kozakai, Mr. Shunsuke Adachi, Dr. Yohei Yamaguchi, Dr. Yutaro Iyama, Mr. Kotaro Kimura, Dr. Toshiaki Inada, Mr. Yudai Seino, Mr. Kenta Uno, Mr. Ryunosuke Iguchi, Mr. Koki Maekawa, Mr. Kenji Shu, Mr. Xian Fan, and other younger and senior members for their kindness and warm support. I also thanks to the ttbar resonance Japanese team, Dr. Junpei Maeda, Dr. Masato Aoki, and Mr. Shota Suzuki.

Finally, I deeply appreciate to my parents and my sister and my grand parents, my husband Yuki and my friends for their biggest support.

Appendix A
Systematic uncertainties plots

The effect of the systematic uncertainties on the mass spectra of total background is shown in Figures A.2–A.31. They show the systematic shifts with the nominal spectrum with “up” and “down” variations.

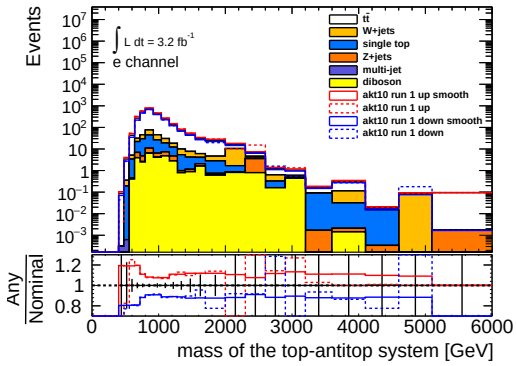

(a) Boosted JES, run 1 extrapolation, e+jets channel.

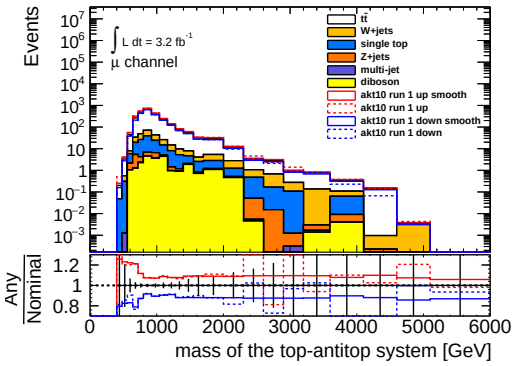

(b) Boosted JES, run 1 extrapolation, μ+jets channel.

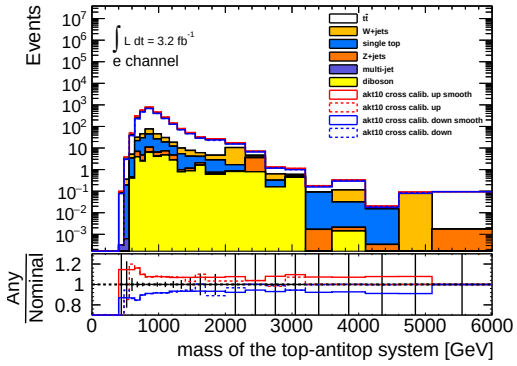

(c) Boosted JES, cross-calibration, e+jets channel.

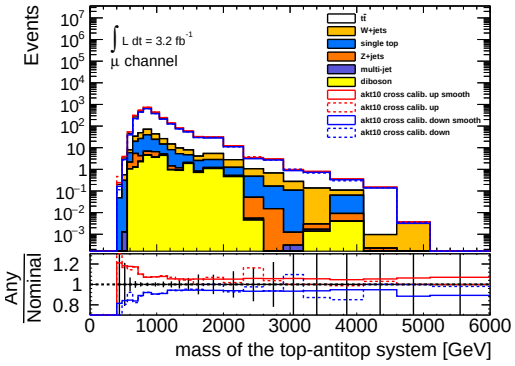

(d) Boosted JES, cross-calibration, μ+jets channel.

Figure A.2: Effect of various systematics before and after smoothing for electron (left) and muon (right) channels.

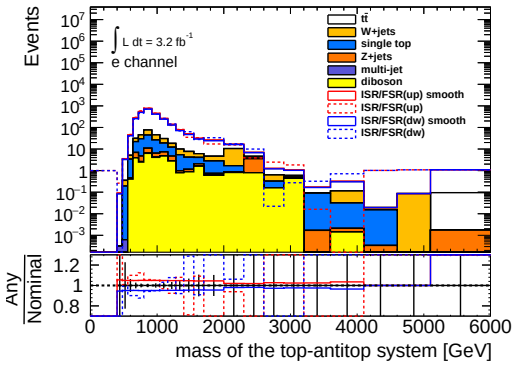

(a) ISR/FSR, e+jets channel.

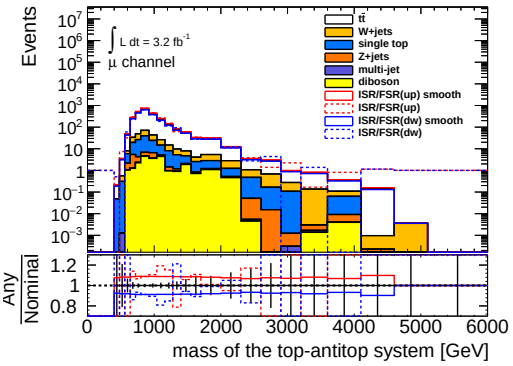

(b) ISR/FSR, μ+jets channel.

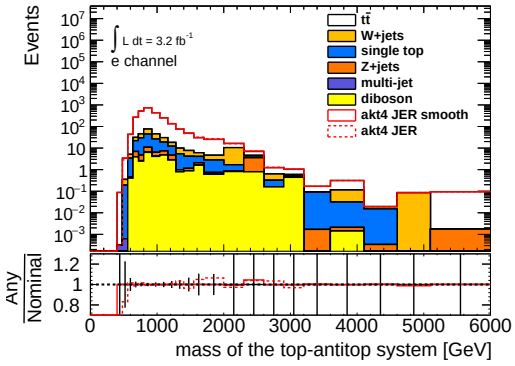

(c) JER , e+jets channel.

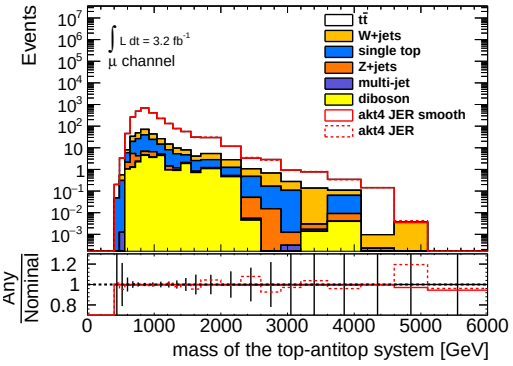

(d) JER , μ+jets channel.

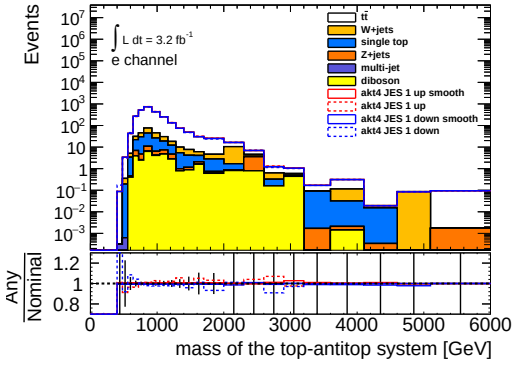

(e) JES component 1, e+jets channel.

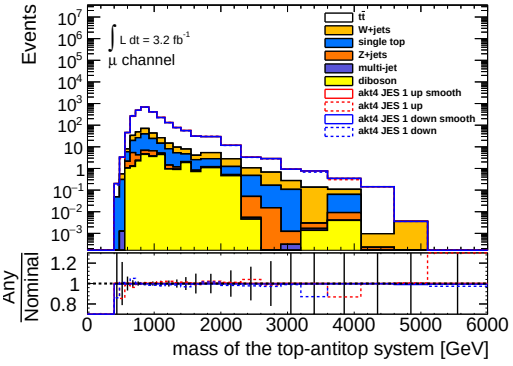

(f) JES component 1, μ+jets channel.

Figure A.3: Effect of various systematics before and after smoothing for electron (left) and muon (right) channels.

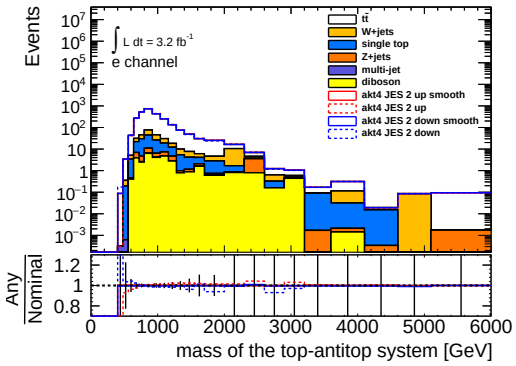

(a) JES component 2, e+jets channel.

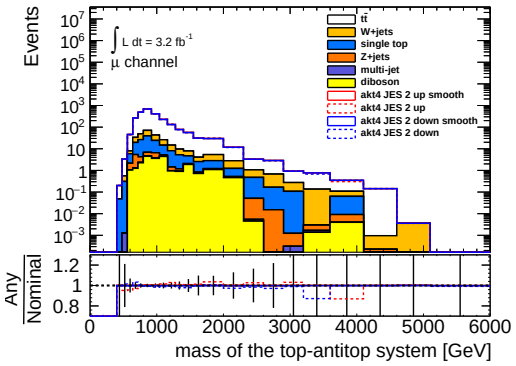

(b) JES component 2, μ+jets channel.

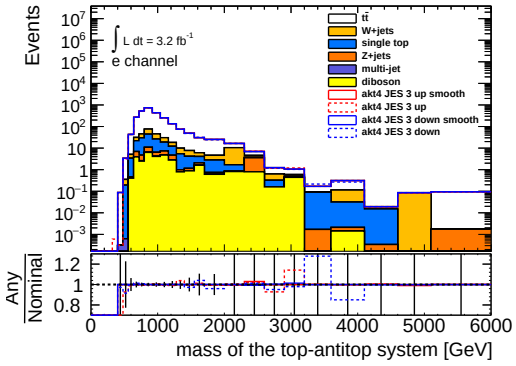

(c) JES component 3, e+jets channel.

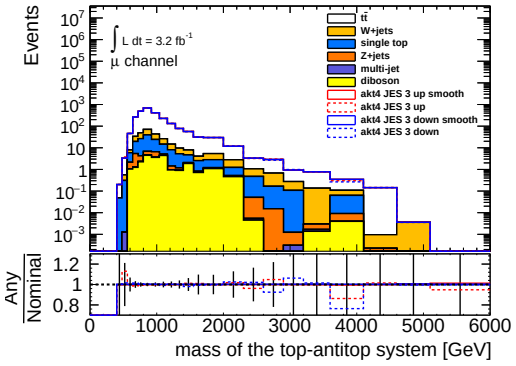

(d) JES component 3, μ+jets channel.

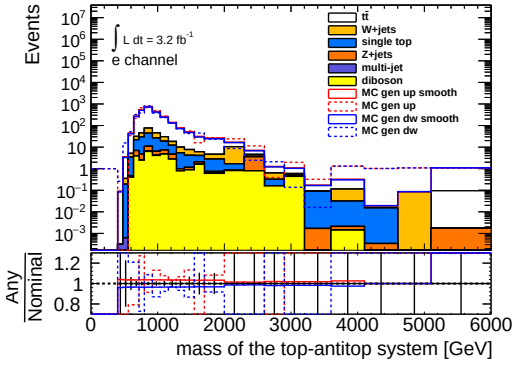

(e) Monte Carlo generator, e+jets channel.

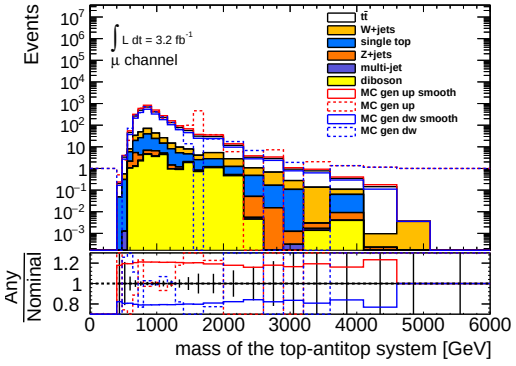

(f) Monte Carlo generator, μ+jets channel.

Figure A.4: Effect of various systematics before and after smoothing for electron (left) and muon (right) channels.

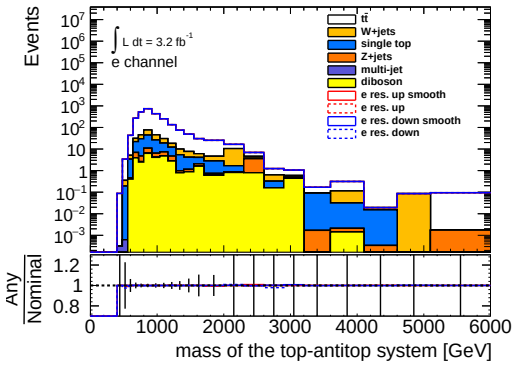

(a) Electron resolution, e+jets channel.

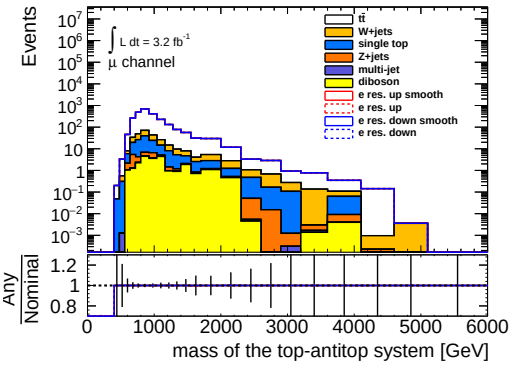

(b) Electron resolution, μ+jets channel.

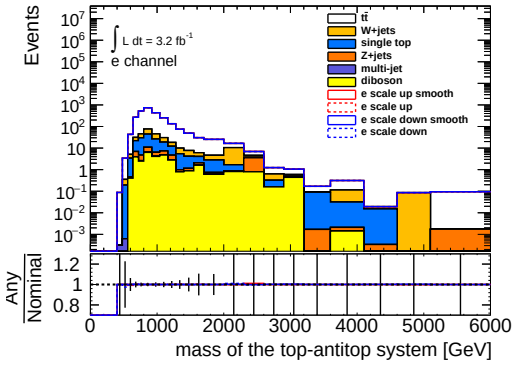

(c) Electron energy scale, e+jets channel.

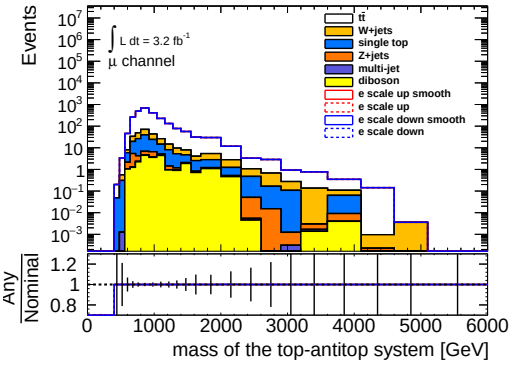

(d) Electron energy scale, μ+jets channel.

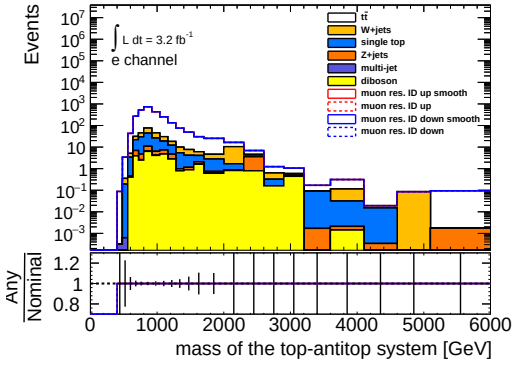

(e) Muon resolution (inner detector), e+jets channel.

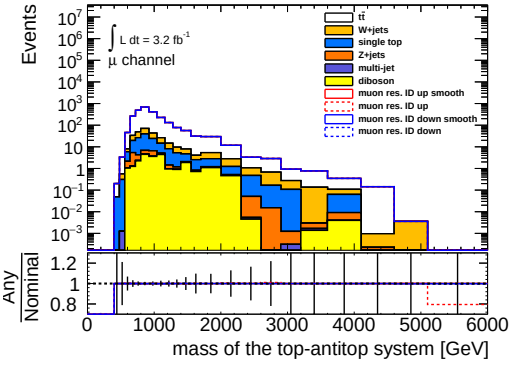

(f) Muon resolution (inner detector), μ+jets channel.

Figure A.5: Effect of various systematics before and after smoothing for electron (left) and muon (right) channels.

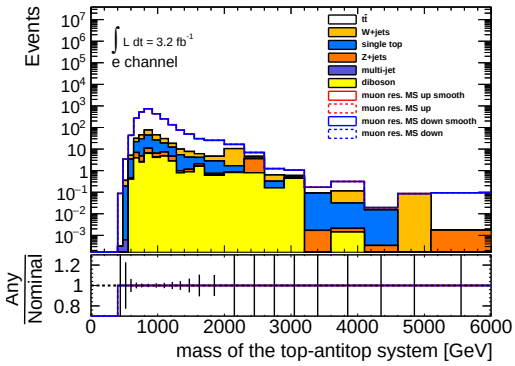

(a) Muon resolution (muon spectrometer), e+jets channel.

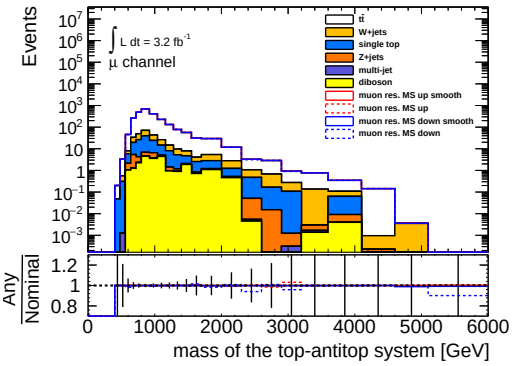

(b) Muon resolution (muon spectrometer), μ+jets channel.

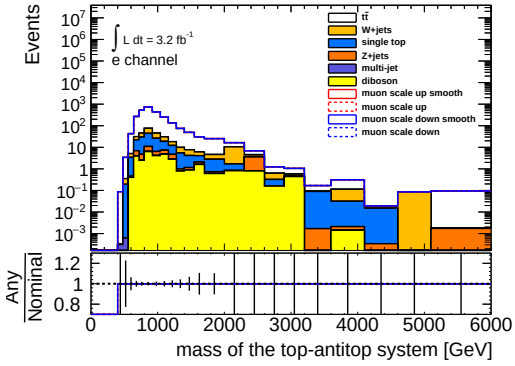

(c) Muon momentum scale, e+jets channel.

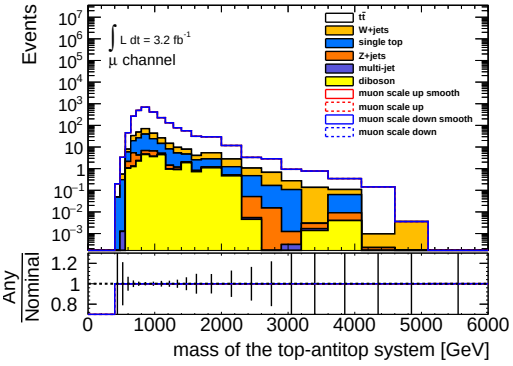

(d) Muon momentum scale, μ+jets channel.

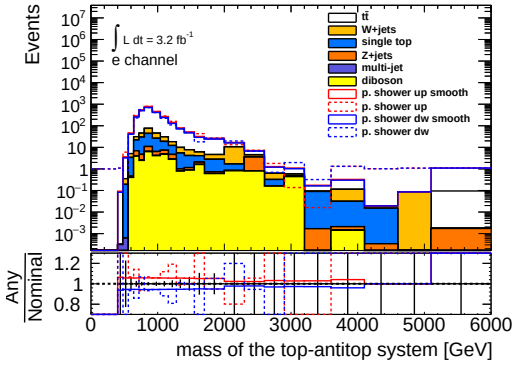

(e) Parton shower, e+jets channel.

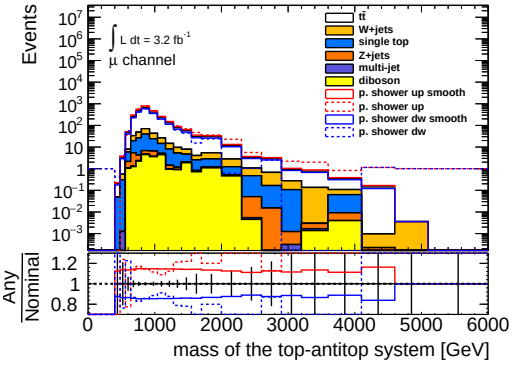

(f) Parton shower, μ+jets channel.

Figure A.6: Effect of various systematics before and after smoothing for electron (left) and muon (right) channels.

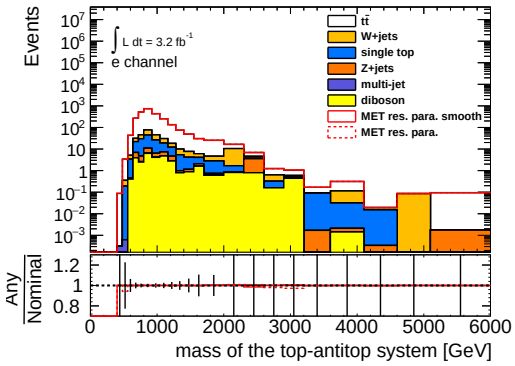

(a) E_T^{miss} 1, e+jets channel.

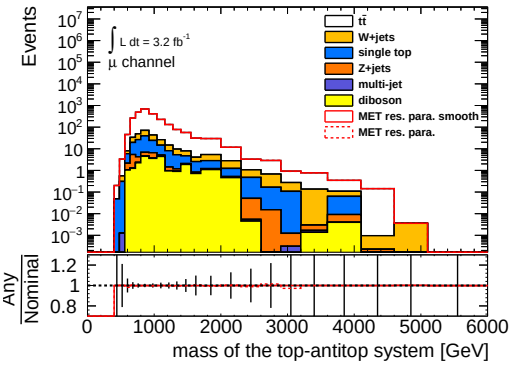

(b) E_T^{miss} 1, μ+jets channel.

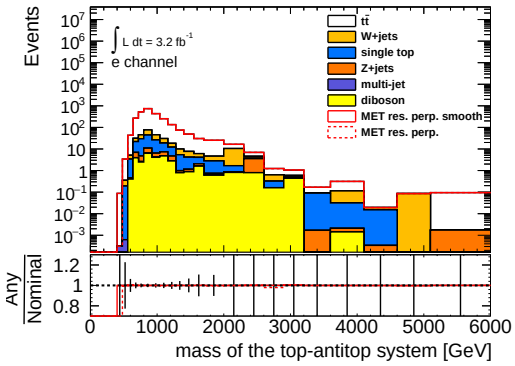

(c) E_T^{miss} 2, e+jets channel.

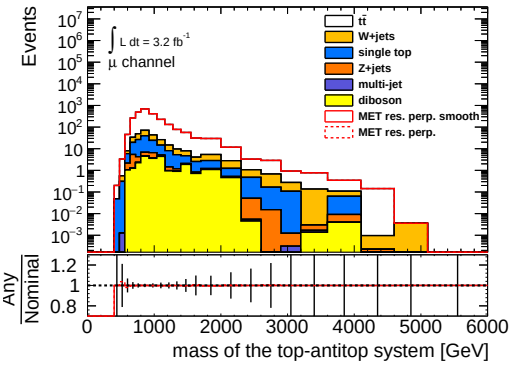

(d) E_T^{miss} 2, μ+jets channel.

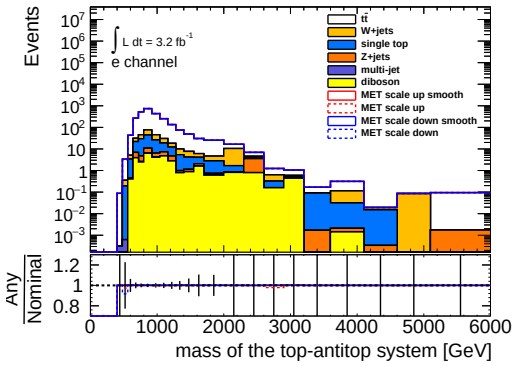

(e) E_T^{miss} 3, e+jets channel.

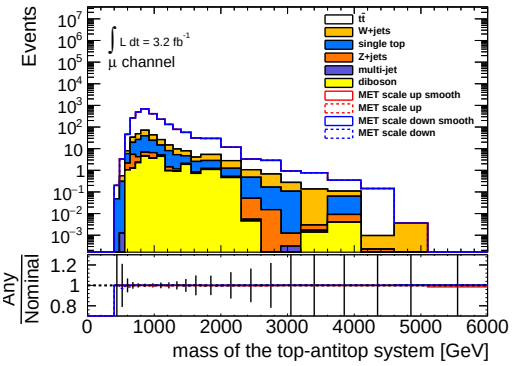

(f) E_T^{miss} 3, μ+jets channel.

Figure A.7: Effect of various systematics before and after smoothing for electron (left) and muon (right) channels.

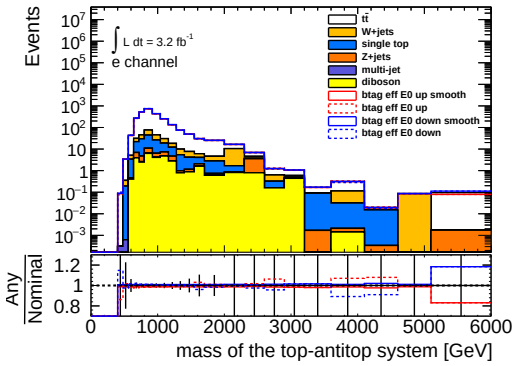

(a) b-tagging of b, component 0, e+jets channel.

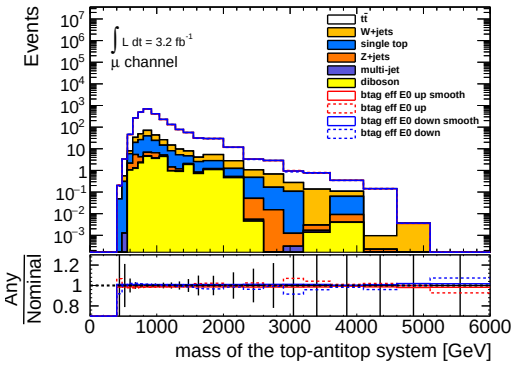

(b) b-tagging of b, component 0, μ+jets channel.

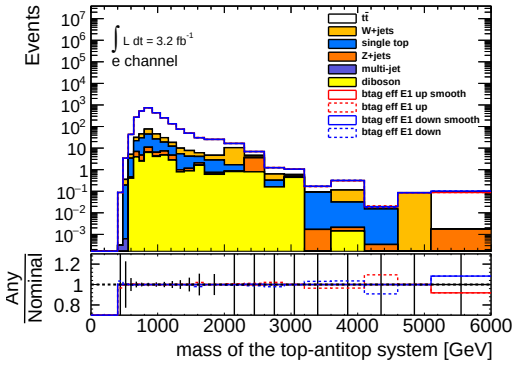

(c) b-tagging of b, component 1, e+jets channel.

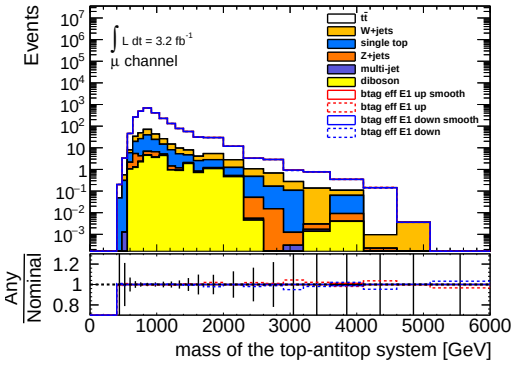

(d) b-tagging of b, component 1, μ+jets channel.

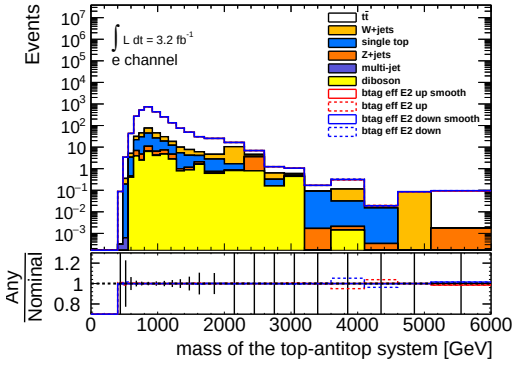

(e) b-tagging of b, component 2, e+jets channel.

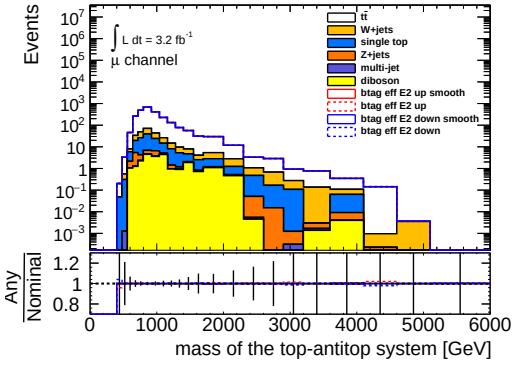

(f) b-tagging of b, component 2, μ+jets channel.

Figure A.8: Effect of various systematics before and after smoothing for electron (left) and muon (right) channels.

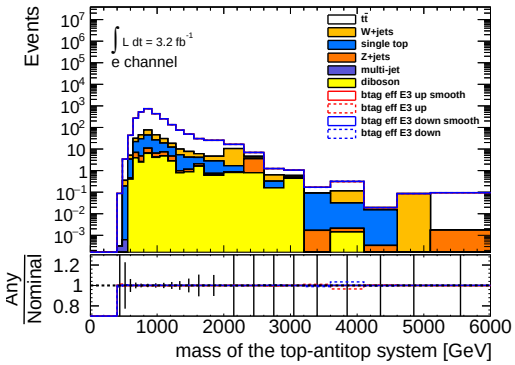

(a) b-tagging of b, component 3, e+jets channel.

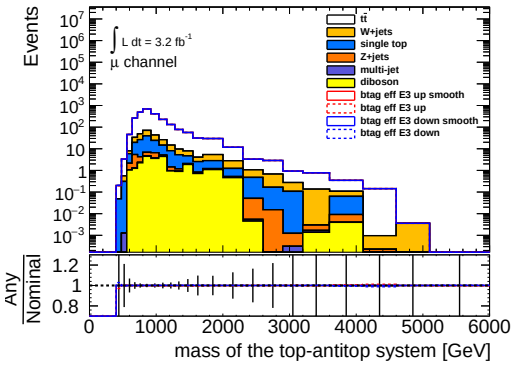

(b) b-tagging of b, component 3, μ+jets channel.

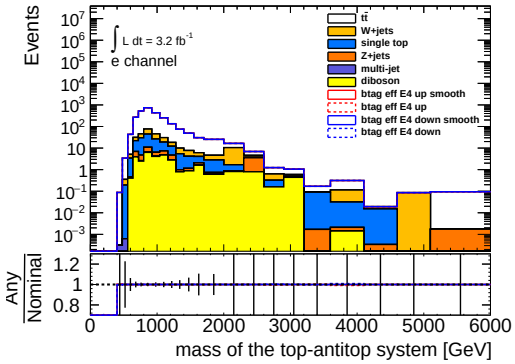

(c) b-tagging of b, component 4, e+jets channel.

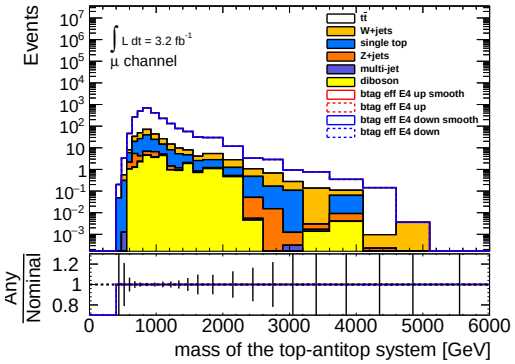

(d) b-tagging of b, component 4, μ+jets channel.

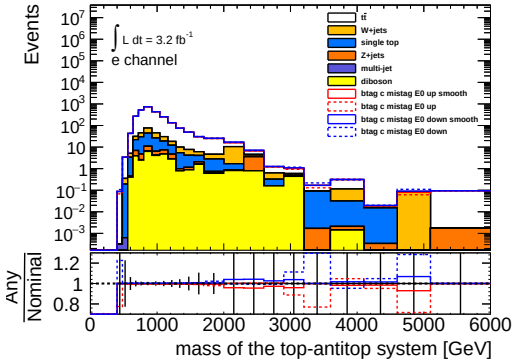

(e) b-tagging of c, component 0, e+jets channel.

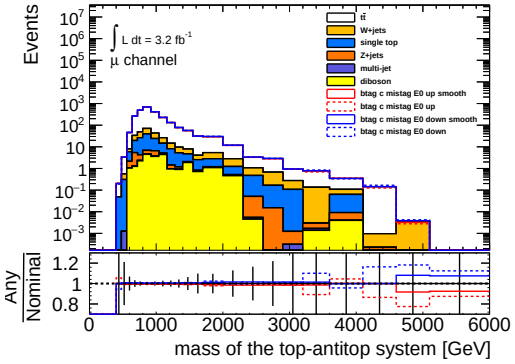

(f) b-tagging of c, component 0, μ+jets channel.

Figure A.9: Effect of various systematics before and after smoothing for electron (left) and muon (right) channels.

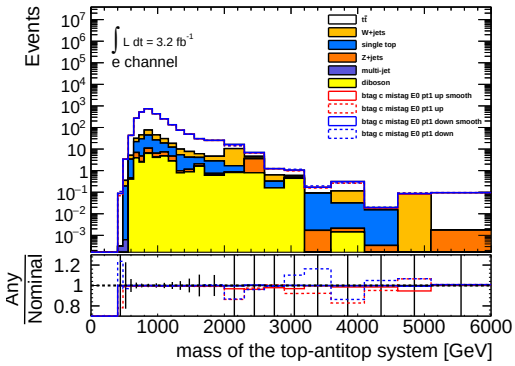

(a) b-tagging of c, component 0, low p_T , e+jets channel.

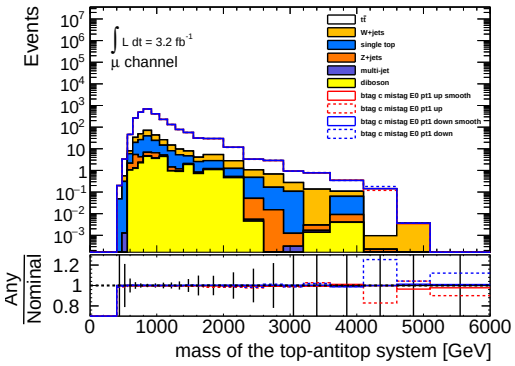

(b) b-tagging of c, component 0, low p_T , μ+jets channel.

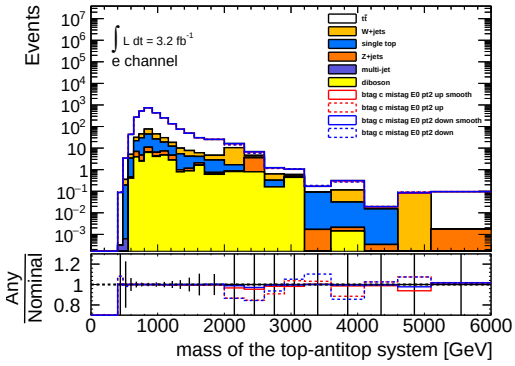

(c) b-tagging of c, component 0, medium p_T , e+jets channel.

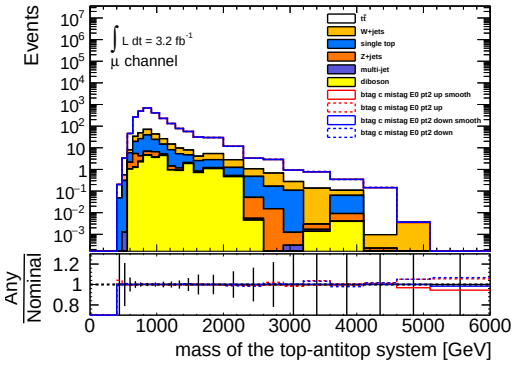

(d) b-tagging of c, component 0, medium p_T , μ+jets channel.

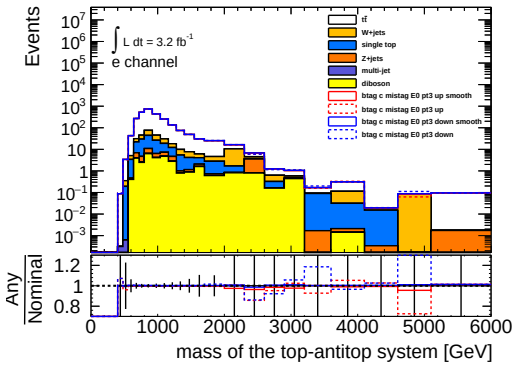

(e) b-tagging of c, component 0, high p_T , e+jets channel.

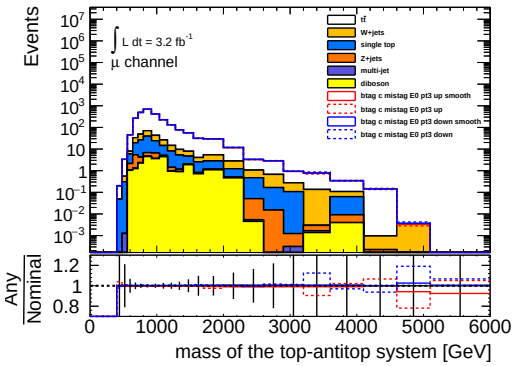

(f) b-tagging of c, component 0, high p_T , μ+jets channel.

Figure A.10: Effect of various systematics before and after smoothing for electron (left) and muon (right) channels.

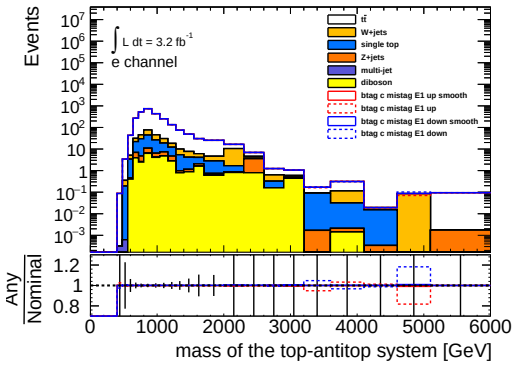

(a) b-tagging of c, component 1, e+jets channel.

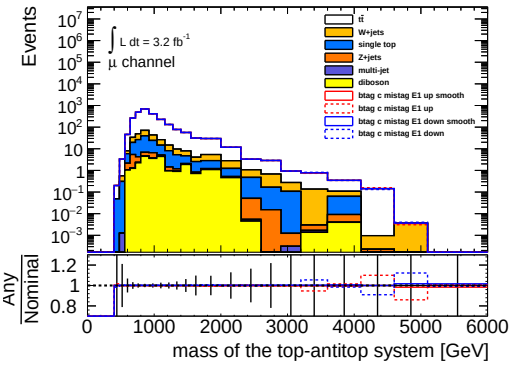

(b) b-tagging of c, component 1, μ+jets channel.

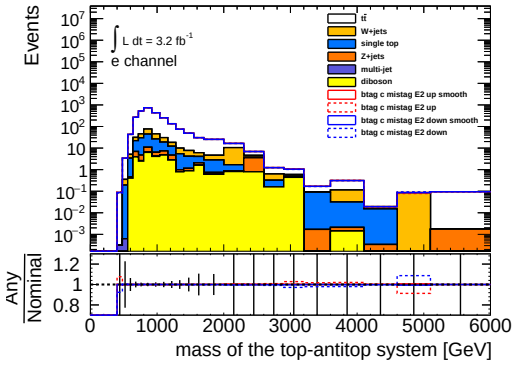

(c) b-tagging of c, component 2, e+jets channel.

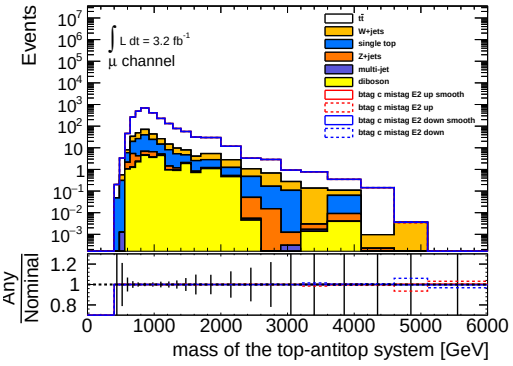

(d) b-tagging of c, component 2, μ+jets channel.

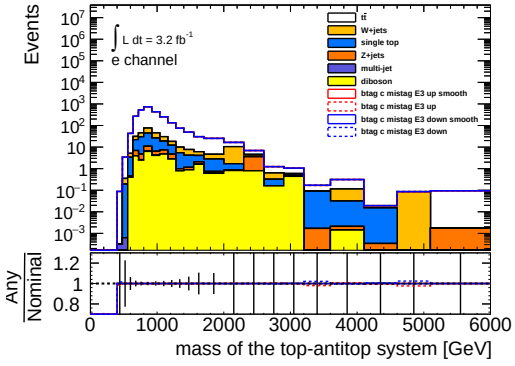

(e) b-tagging of c, component 3, e+jets channel.

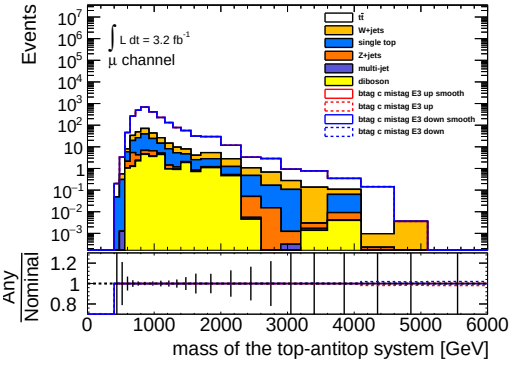

(f) b-tagging of c, component 3, μ+jets channel.

Figure A.11: Effect of various systematics before and after smoothing for electron (left) and muon (right) channels.

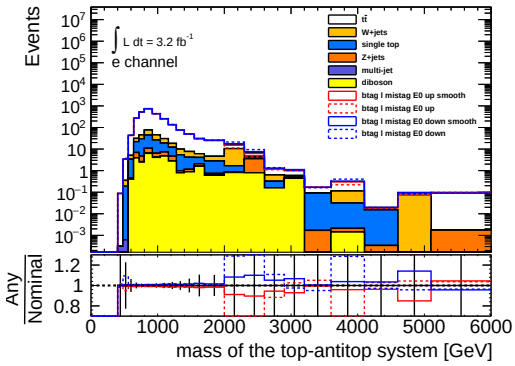

(a) b-tagging of light, component 0, e+jets channel.

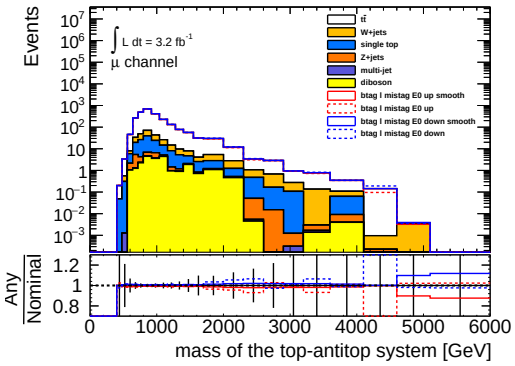

(b) b-tagging of light, component 0, μ+jets channel.

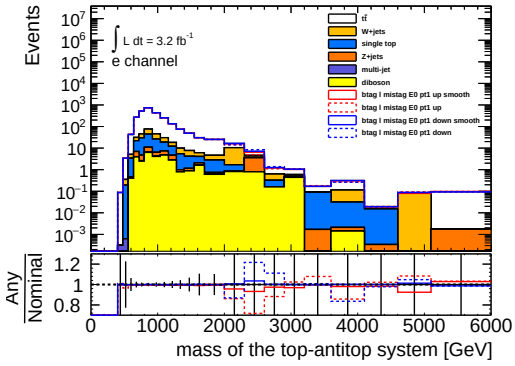

(c) b-tagging of light, component 0, low p_T , e+jets channel.

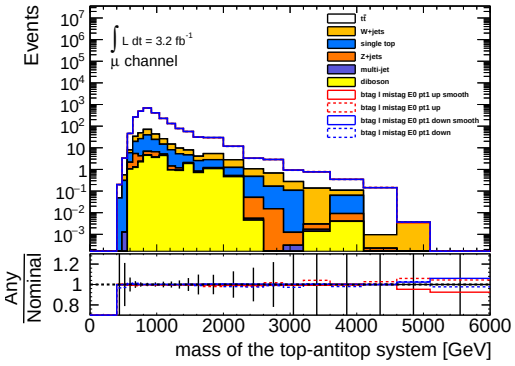

(d) b-tagging of light, component 0, low p_T , μ+jets channel.

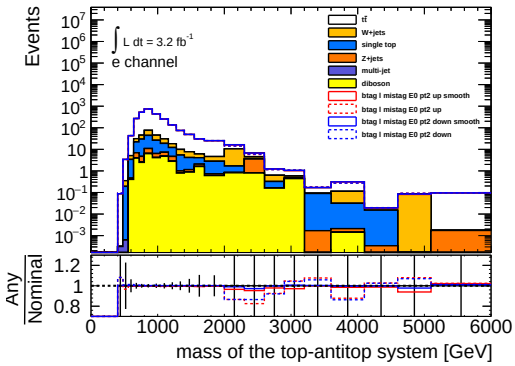

(e) b-tagging of light, component 0, medium p_T , e+jets channel.

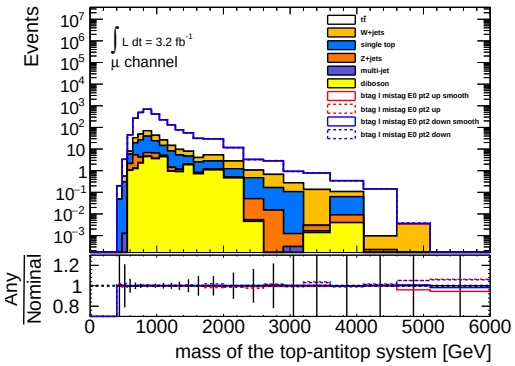

(f) b-tagging of light, component 0, medium p_T , μ+jets channel.

Figure A.12: Effect of various systematics before and after smoothing for electron (left) and muon (right) channels.

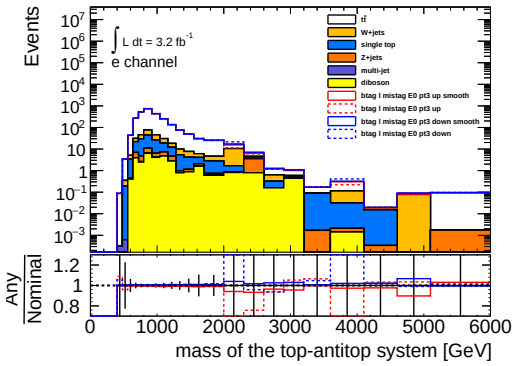

(a) b-tagging of light, component 0, high p_T , e+jets channel.

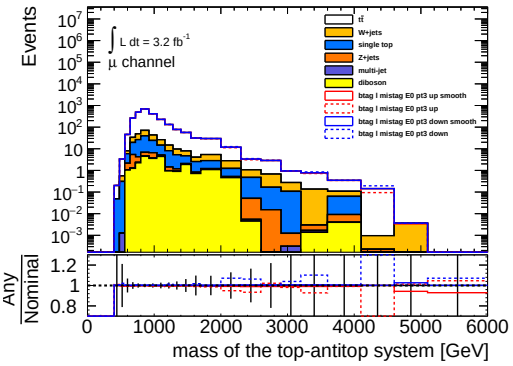

(b) b-tagging of light, component 0, high p_T , μ+jets channel.

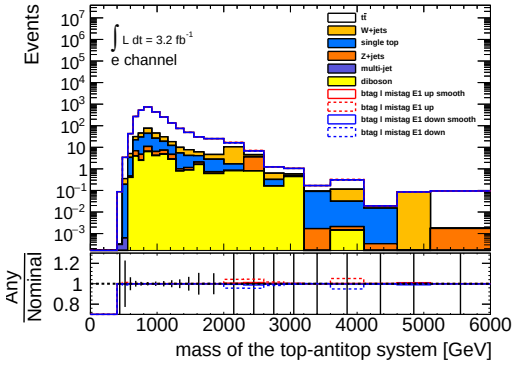

(c) b-tagging of light, component 1, e+jets channel.

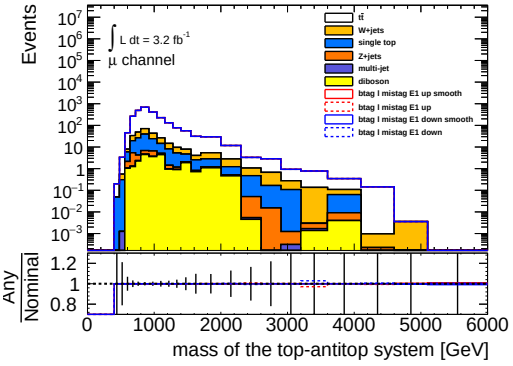

(d) b-tagging of light, component 1, μ+jets channel.

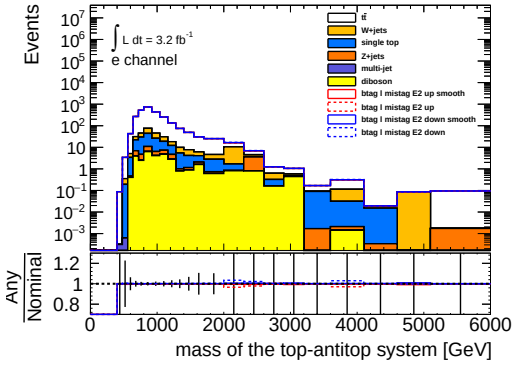

(e) b-tagging of light, component 2, e+jets channel.

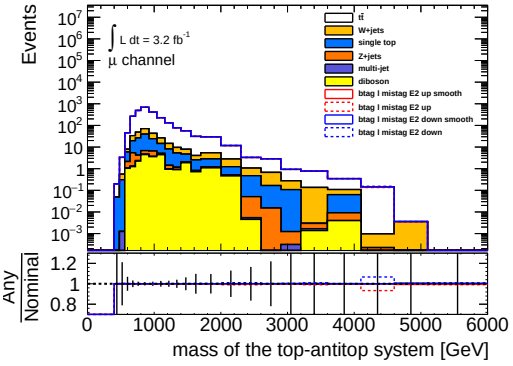

(f) b-tagging of light, component 2, μ+jets channel.

Figure A.13: Effect of various systematics before and after smoothing for electron (left) and muon (right) channels.

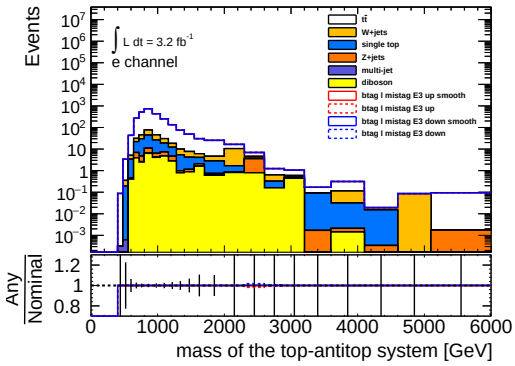

(a) b-tagging of light, component 3, e+jets channel.

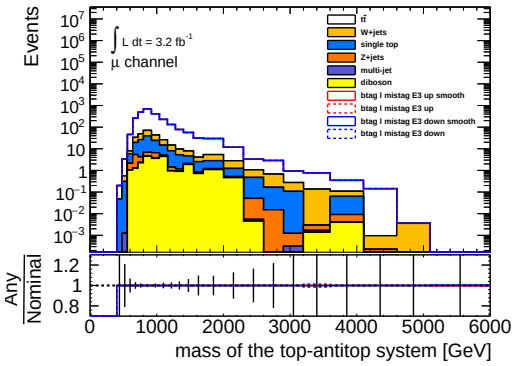

(b) b-tagging of light, component 3, μ+jets channel.

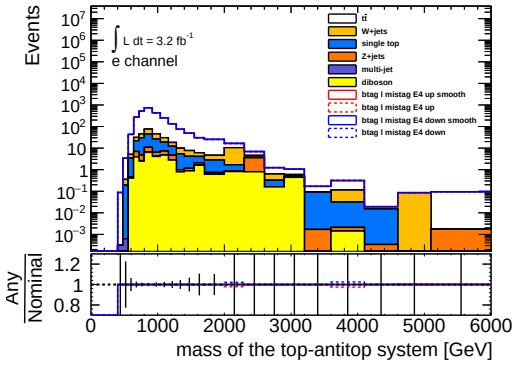

(c) b-tagging of light, component 4, e+jets channel.

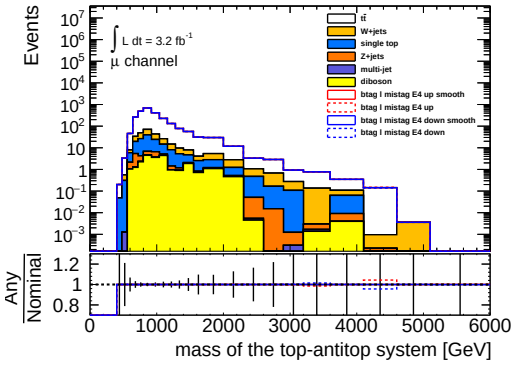

(d) b-tagging of light, component 4, μ+jets channel.

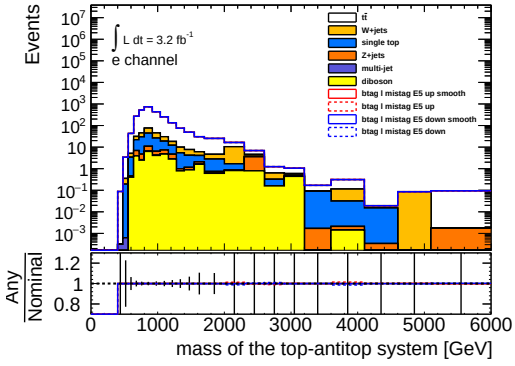

(e) b-tagging of light, component 5, e+jets channel.

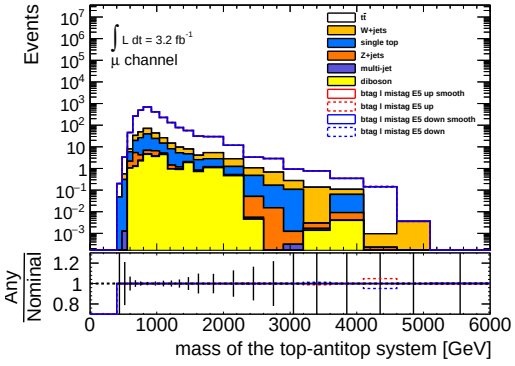

(f) b-tagging of light, component 5, μ+jets channel.

Figure A.14: Effect of various systematics before and after smoothing for electron (left) and muon (right) channels.

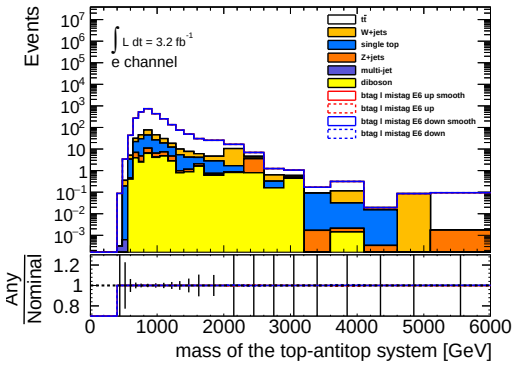

(a) b-tagging of light, component 6, e+jets channel.

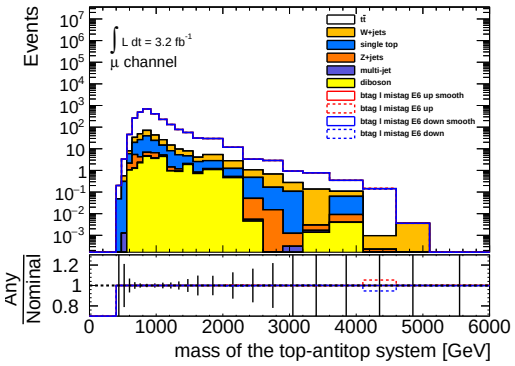

(b) b-tagging of light, component 6, μ+jets channel.

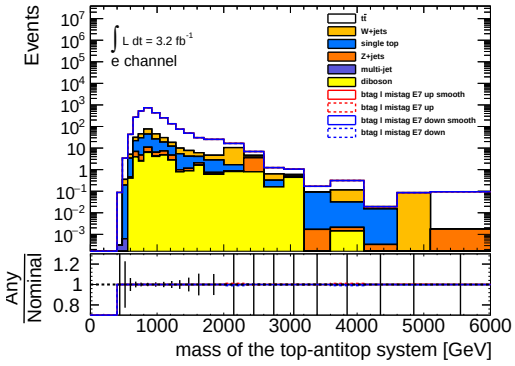

(c) b-tagging of light, component 7, e+jets channel.

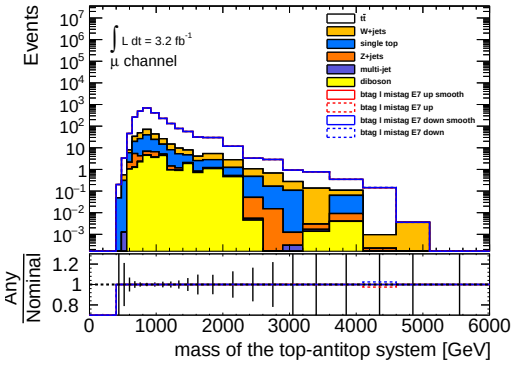

(d) b-tagging of light, component 7, μ+jets channel.

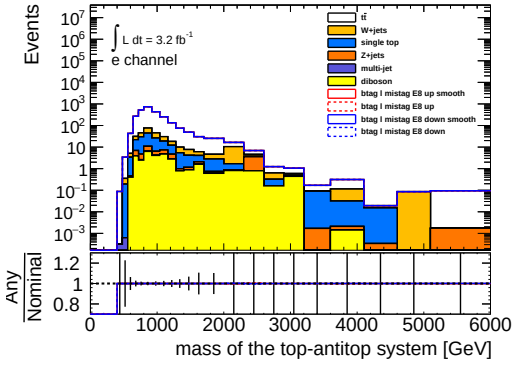

(e) b-tagging of light, component 8, e+jets channel.

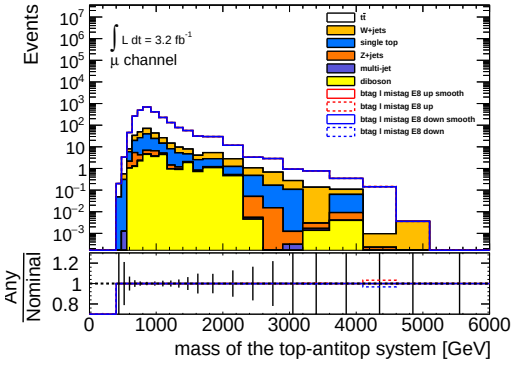

(f) b-tagging of light, component 8, μ+jets channel.

Figure A.15: Effect of various systematics before and after smoothing for electron (left) and muon (right) channels.

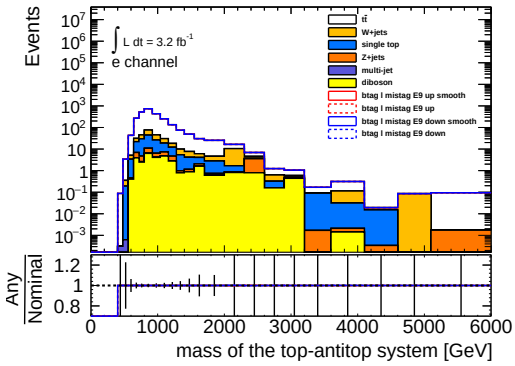

(a) b-tagging of light, component 9, e+jets channel.

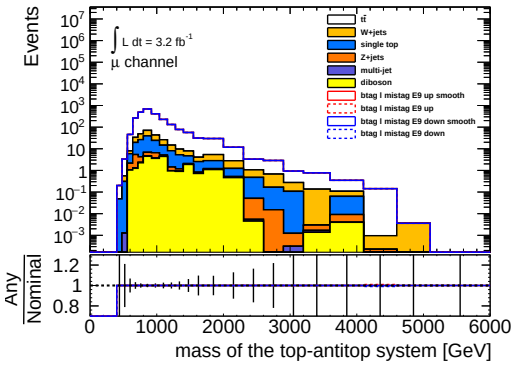

(b) b-tagging of light, component 9, μ+jets channel.

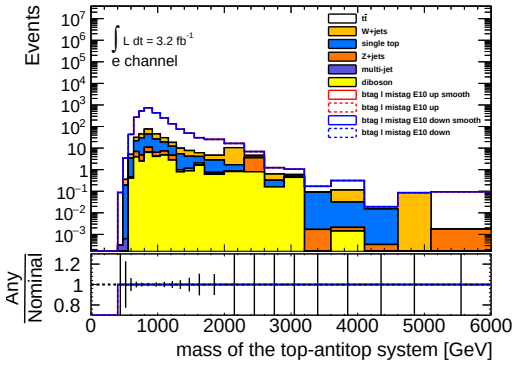

(c) b-tagging of light, component 10, e+jets channel.

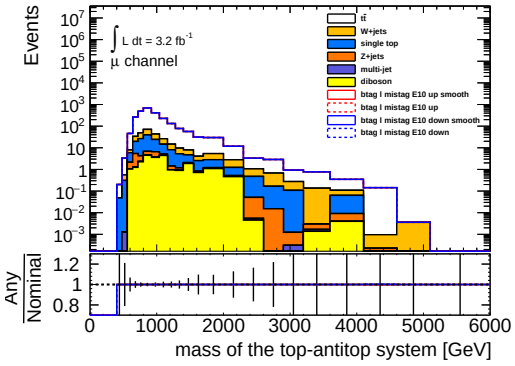

(d) b-tagging of light, component 10, μ+jets channel.

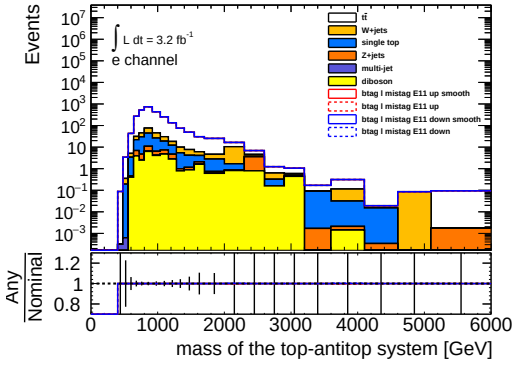

(e) b-tagging of light, component 11, e+jets channel.

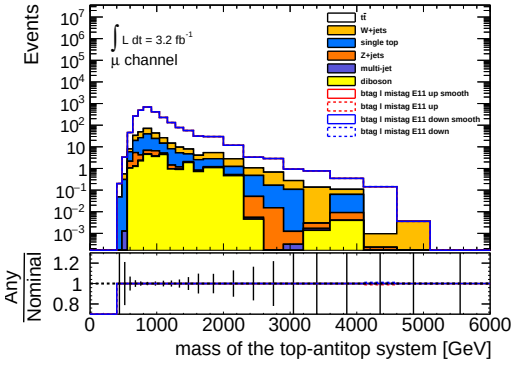

(f) b-tagging of light, component 11, μ+jets channel.

Figure A.16: Effect of various systematics before and after smoothing for electron (left) and muon (right) channels.

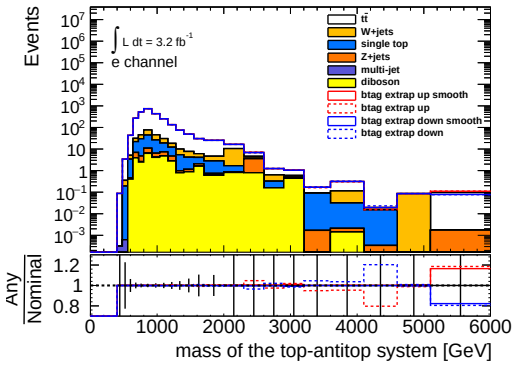

(a) b-tagging of light/b at high p_T , e+jets channel.

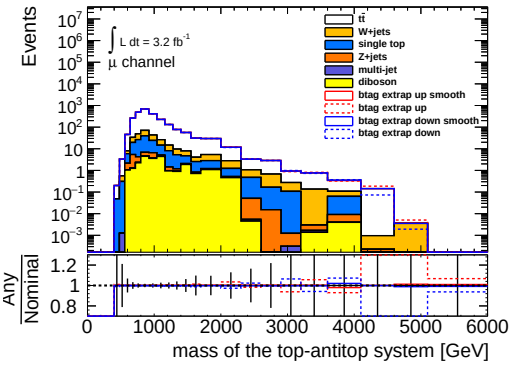

(b) b-tagging of light/b at high p_T , μ+jets channel.

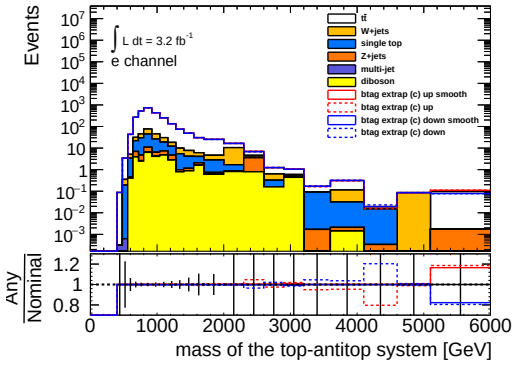

(c) b-tagging of c at high p_T , e+jets channel.

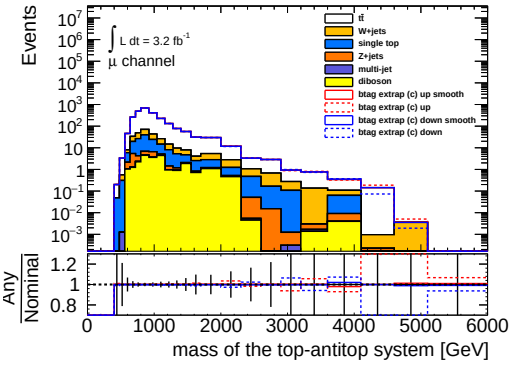

(d) b-tagging of c at high p_T , μ+jets channel.

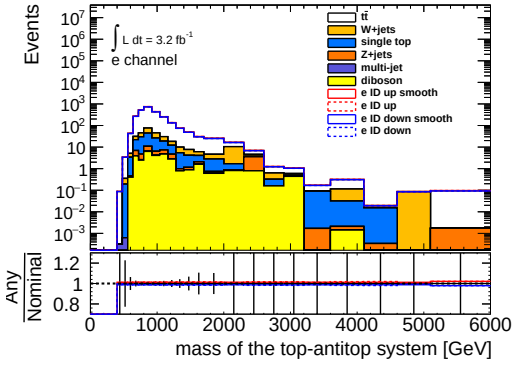

(e) Electron inner detector SF, e+jets channel.

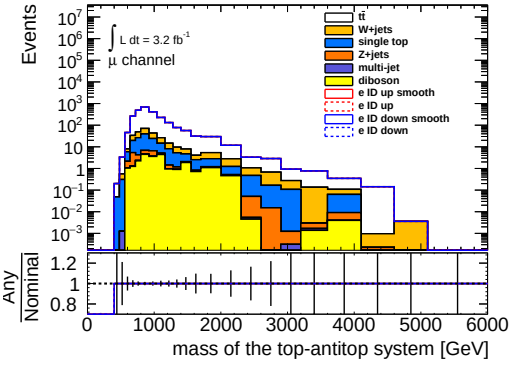

(f) Electron inner detector SF, μ+jets channel.

Figure A.17: Effect of various systematics before and after smoothing for electron (left) and muon (right) channels.

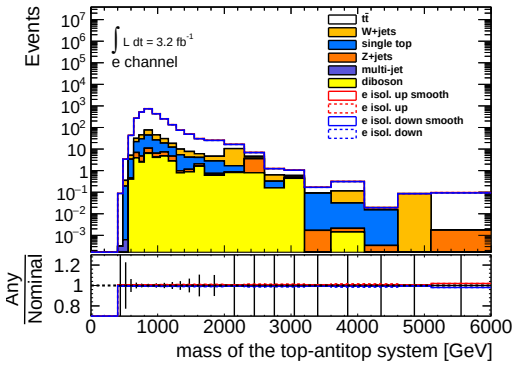

(a) Electron isolation SF, e+jets channel.

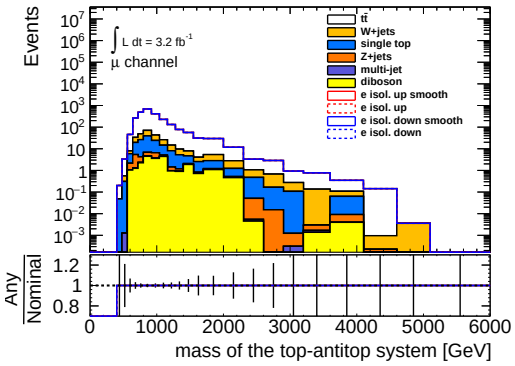

(b) Electron isolation SF, μ+jets channel.

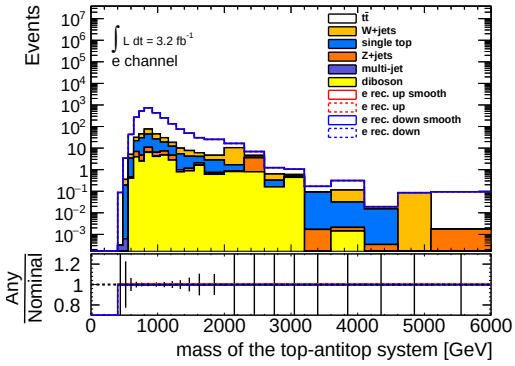

(c) Electron reconstruction SF, e+jets channel.

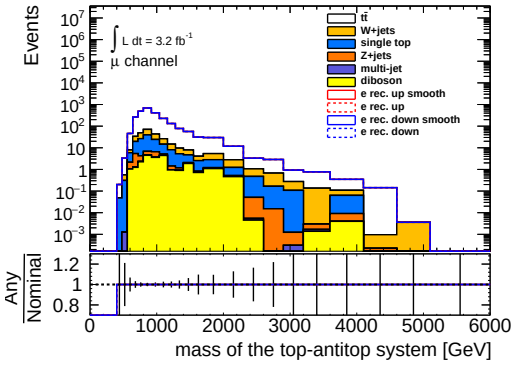

(d) Electron reconstruction SF, μ+jets channel.

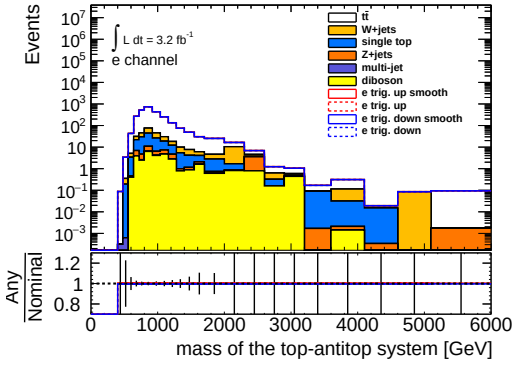

(e) Electron trigger SF, e+jets channel.

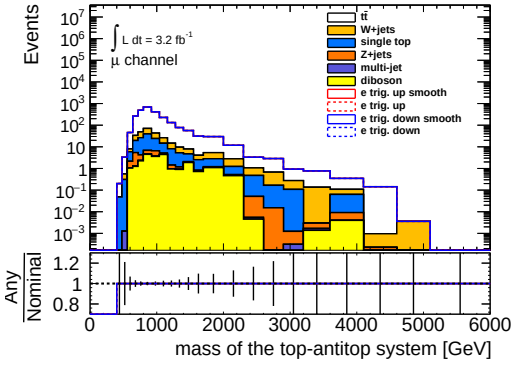

(f) Electron trigger SF, μ+jets channel.

Figure A.18: Effect of various systematics before and after smoothing for electron (left) and muon (right) channels.

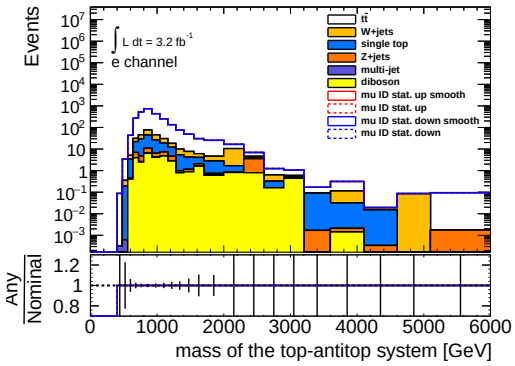

(a) Muon inner detector SF (stat), e+jets channel.

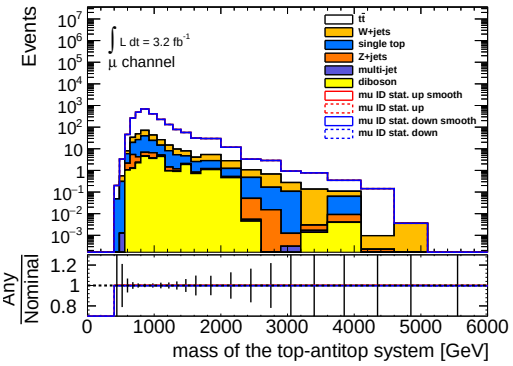

(b) Muon inner detector SF (stat), μ+jets channel.

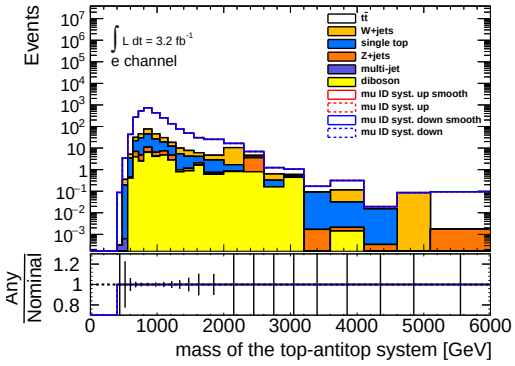

(c) Muon inner detector SF (syst), e+jets channel.

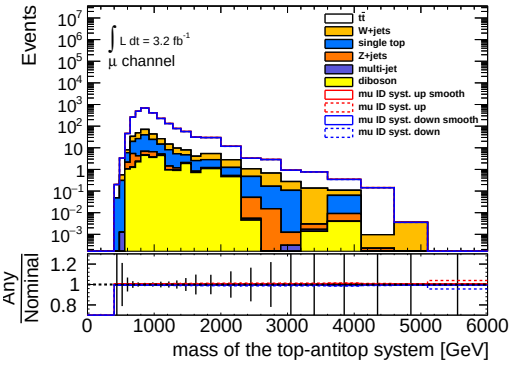

(d) Muon inner detector SF (syst), μ+jets channel.

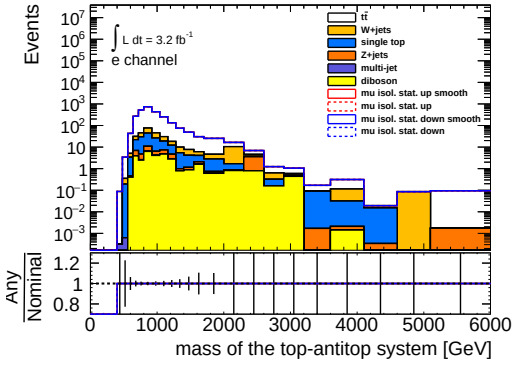

(e) Muon isolation SF (stat), e+jets channel.

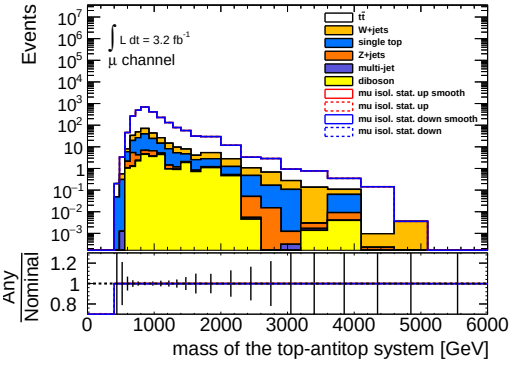

(f) Muon isolation SF (stat), μ+jets channel.

Figure A.19: Effect of various systematics before and after smoothing for electron (left) and muon (right) channels.

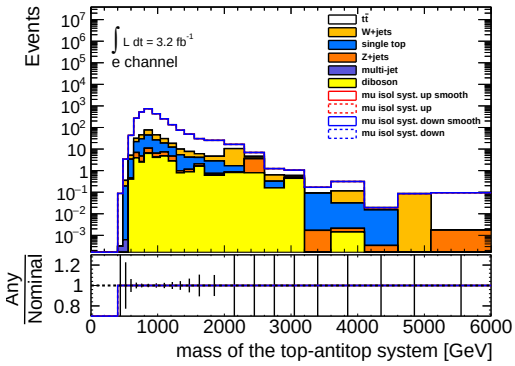

(a) Muon isolation SF(syst), e+jets channel.

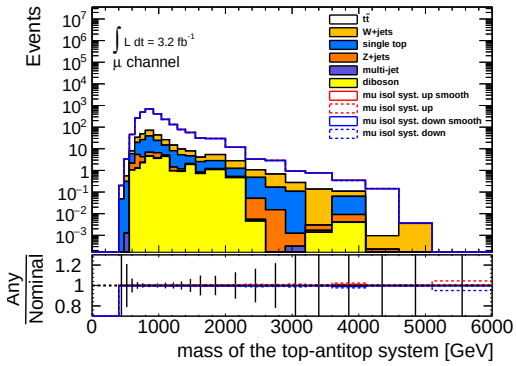

(b) Muon isolation SF(syst), μ+jets channel.

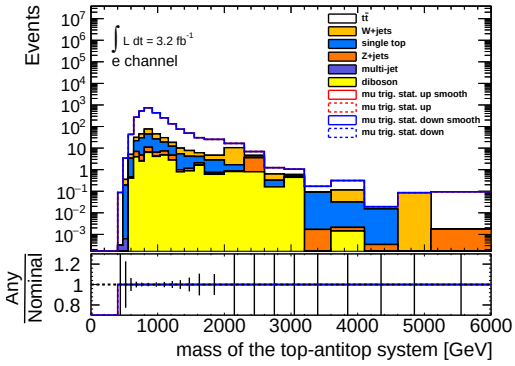

(c) Muon trigger SF (stat), e+jets channel.

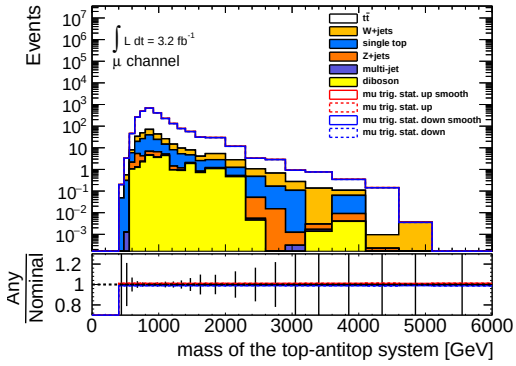

(d) Muon trigger SF (stat), μ+jets channel.

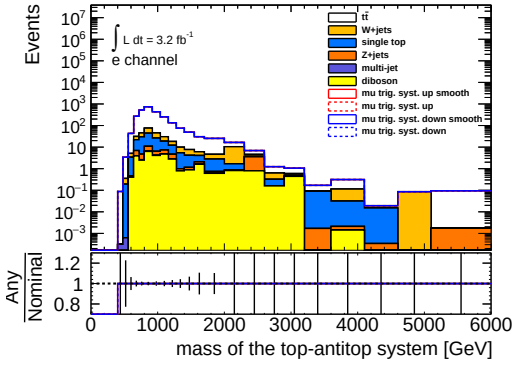

(e) Muon trigger SF (syst), e+jets channel.

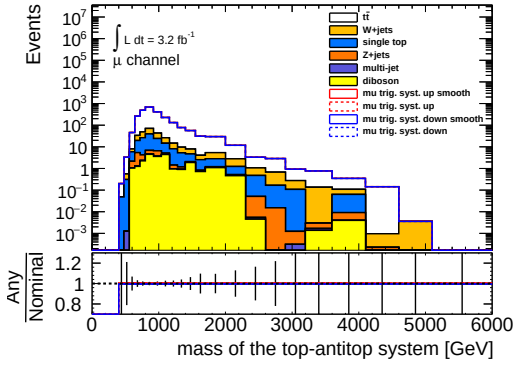

(f) Muon trigger SF (syst), μ+jets channel.

Figure A.20: Effect of various systematics before and after smoothing for electron (left) and muon (right) channels.

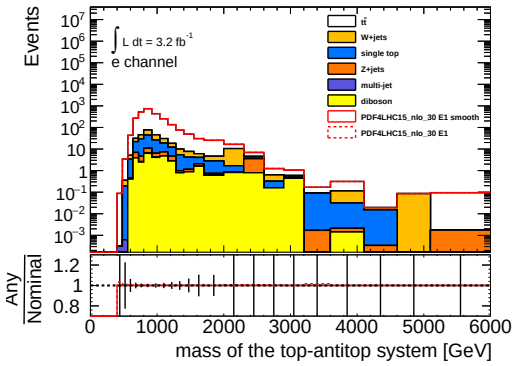

(a) PDF eigenvector 1, e+jets channel.

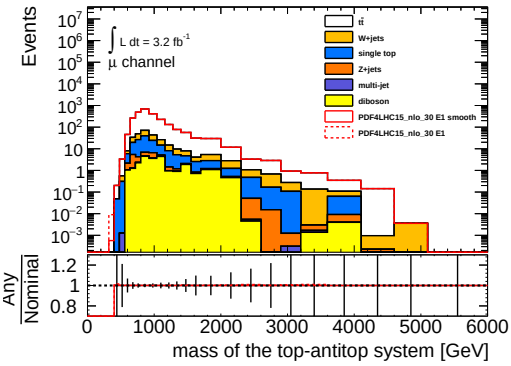

(b) PDF eigenvector 1, μ+jets channel.

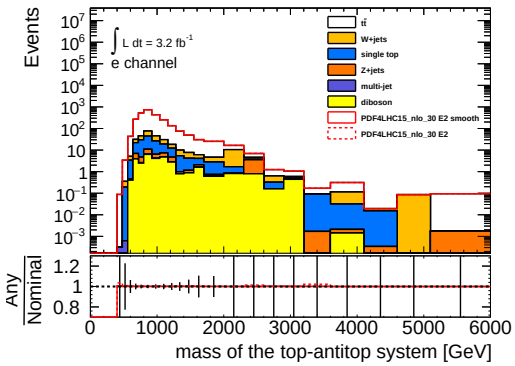

(c) PDF eigenvector 2, e+jets channel.

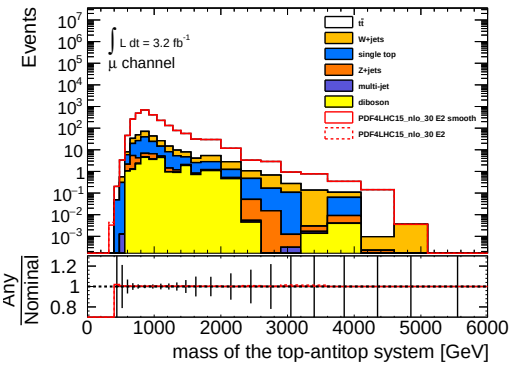

(d) PDF eigenvector 2, μ+jets channel.

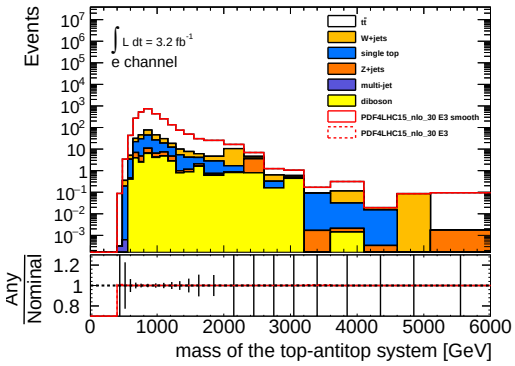

(e) PDF eigenvector 3, e+jets channel.

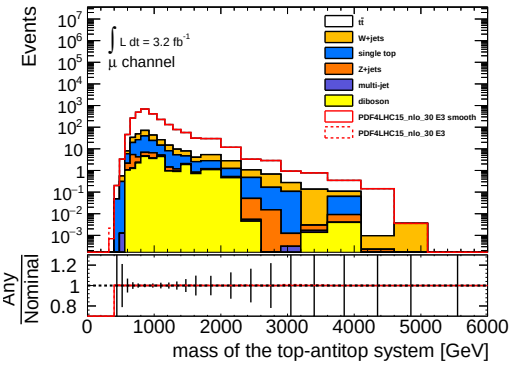

(f) PDF eigenvector 3, μ+jets channel.

Figure A.21: Effect of various systematics before and after smoothing for electron (left) and muon (right) channels.

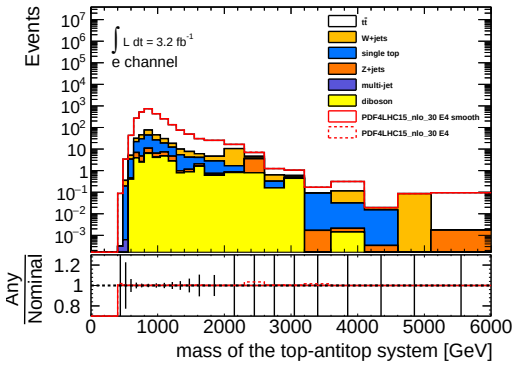

(a) PDF eigenvector 4, e+jets channel.

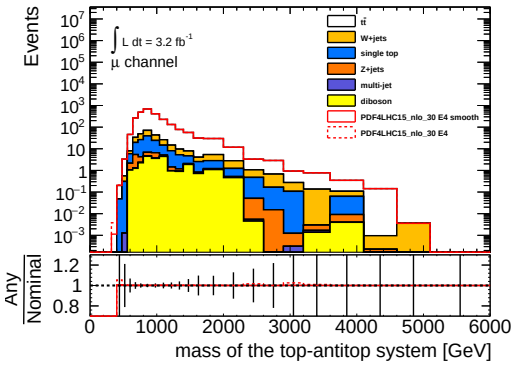

(b) PDF eigenvector 4, μ+jets channel.

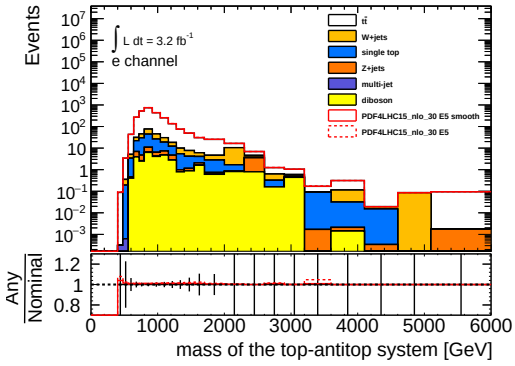

(c) PDF eigenvector 5, e+jets channel.

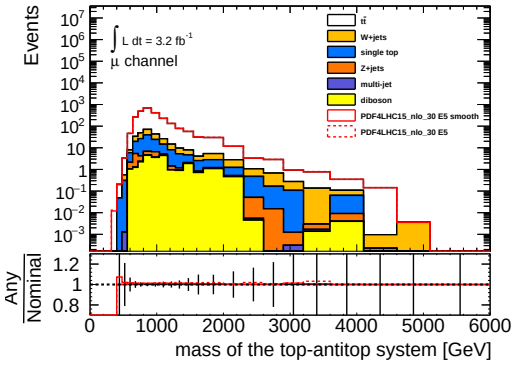

(d) PDF eigenvector 5, μ+jets channel.

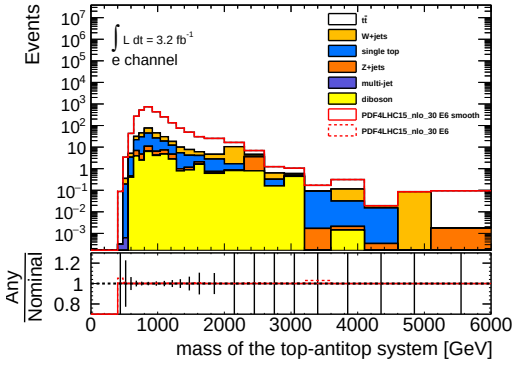

(e) PDF eigenvector 6, e+jets channel.

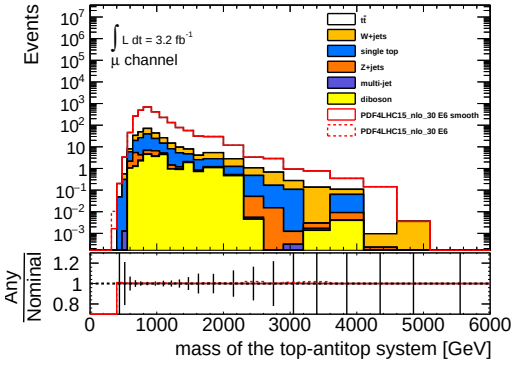

(f) PDF eigenvector 6, μ+jets channel.

Figure A.22: Effect of various systematics before and after smoothing for electron (left) and muon (right) channels.

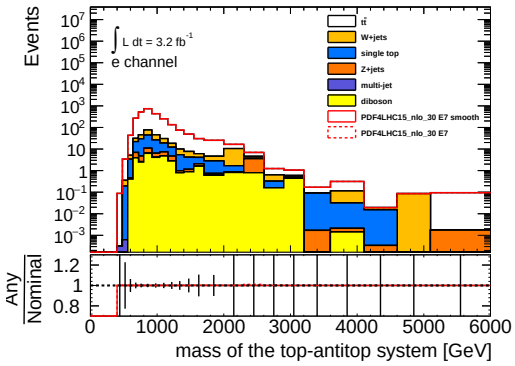

(a) PDF eigenvector 7, e+jets channel.

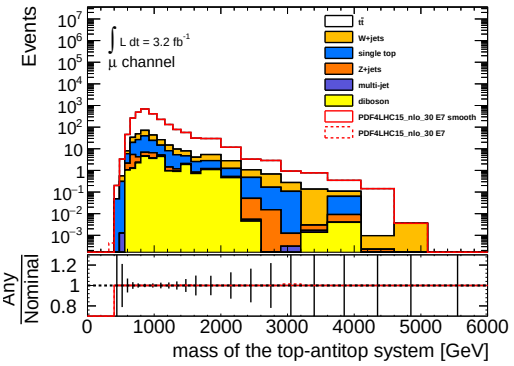

(b) PDF eigenvector 7, μ+jets channel.

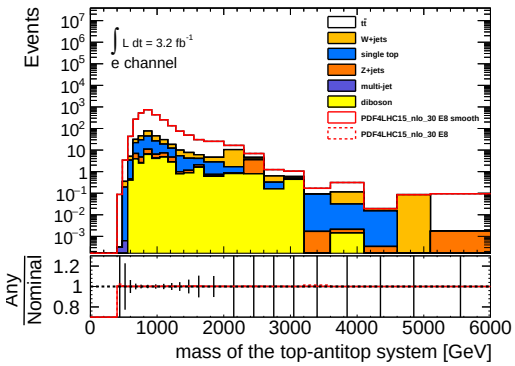

(c) PDF eigenvector 8, e+jets channel.

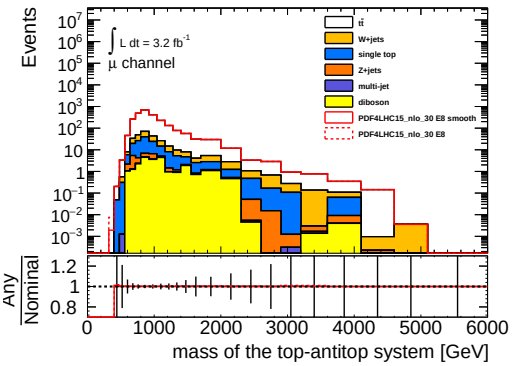

(d) PDF eigenvector 8, μ+jets channel.

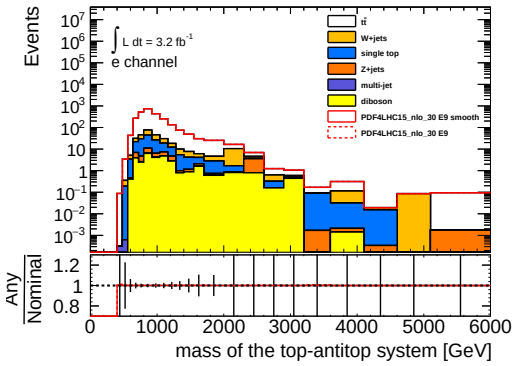

(e) PDF eigenvector 9, e+jets channel.

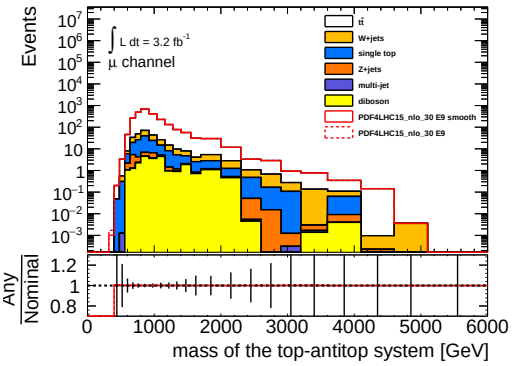

(f) PDF eigenvector 9, μ+jets channel.

Figure A.23: Effect of various systematics before and after smoothing for electron (left) and muon (right) channels.

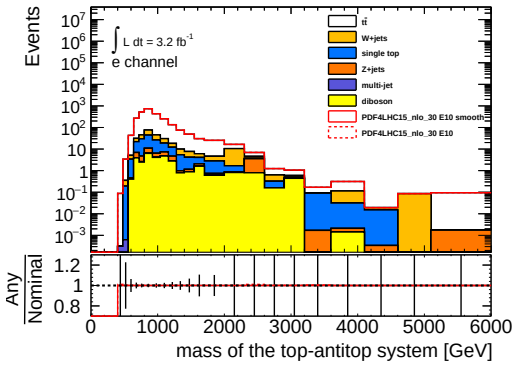

(a) PDF eigenvector 10, e+jets channel.

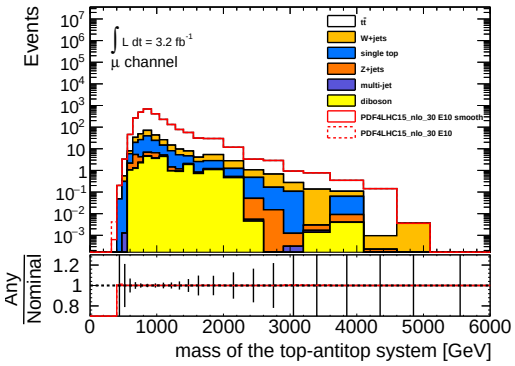

(b) PDF eigenvector 10, μ+jets channel.

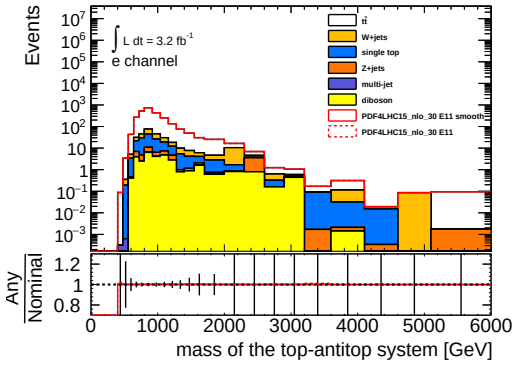

(c) PDF eigenvector 11, e+jets channel.

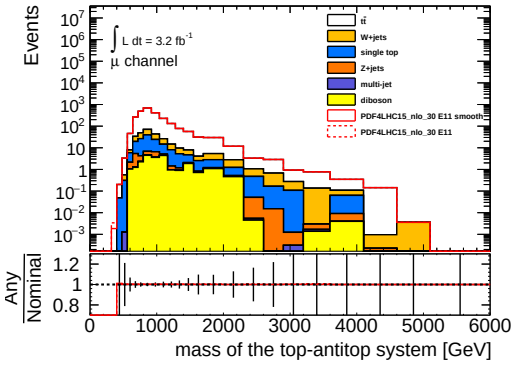

(d) PDF eigenvector 11, μ+jets channel.

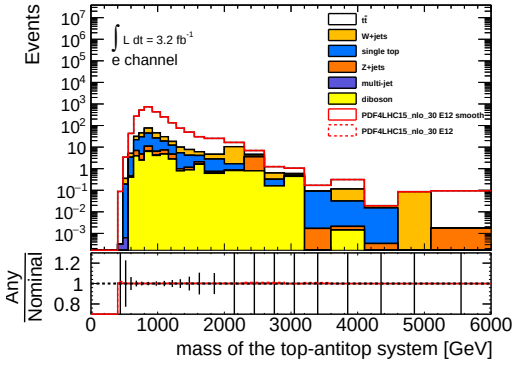

(e) PDF eigenvector 12, e+jets channel.

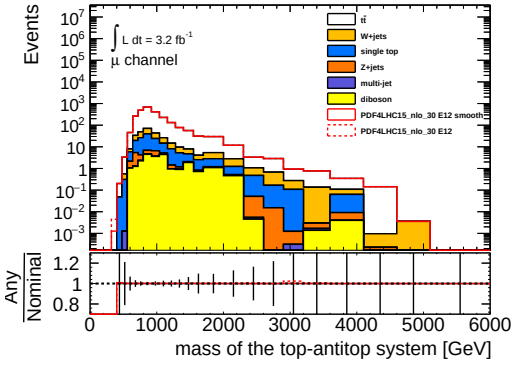

(f) PDF eigenvector 12, μ+jets channel.

Figure A.24: Effect of various systematics before and after smoothing for electron (left) and muon (right) channels.

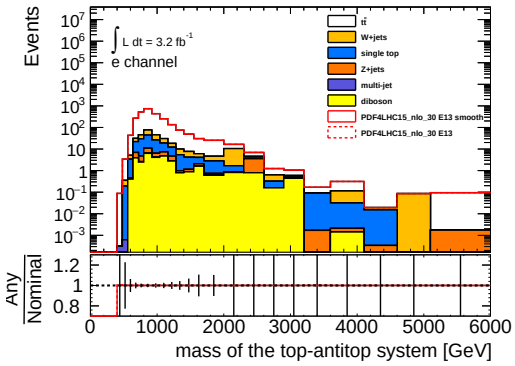

(a) PDF eigenvector 13, e+jets channel.

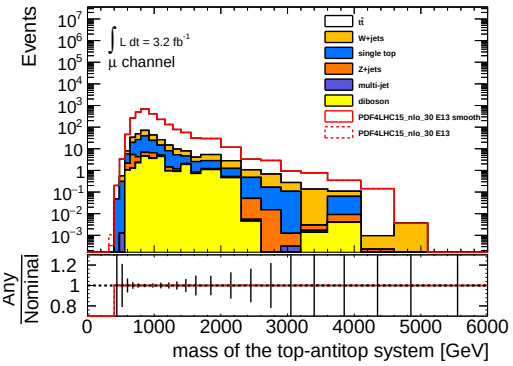

(b) PDF eigenvector 13, μ+jets channel.

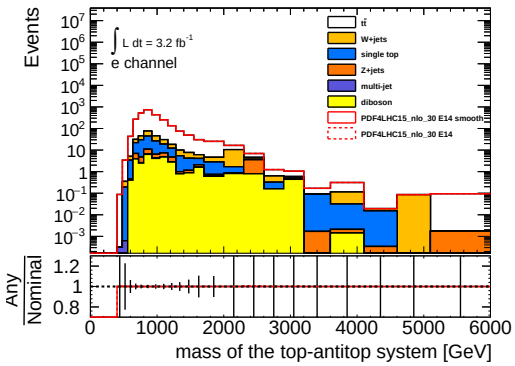

(c) PDF eigenvector 14, e+jets channel.

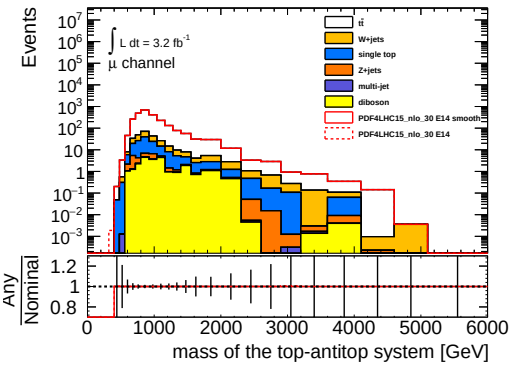

(d) PDF eigenvector 14, μ+jets channel.

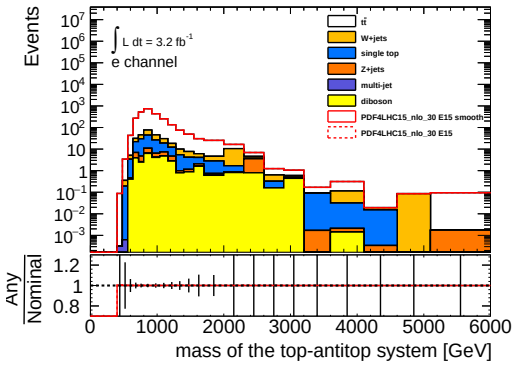

(e) PDF eigenvector 15, e+jets channel.

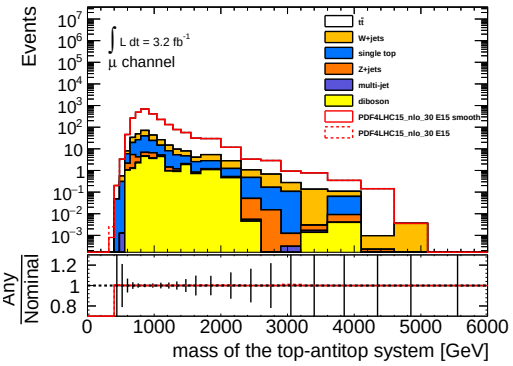

(f) PDF eigenvector 15, μ+jets channel.

Figure A.25: Effect of various systematics before and after smoothing for electron (left) and muon (right) channels.

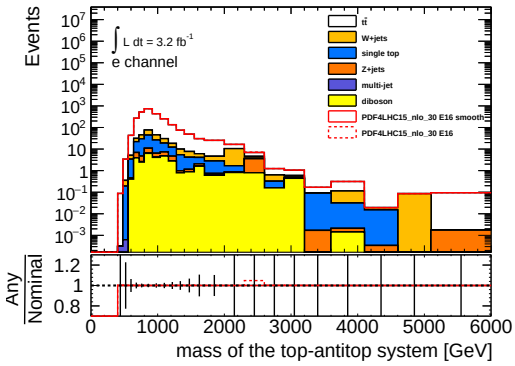

(a) PDF eigenvector 16, e+jets channel.

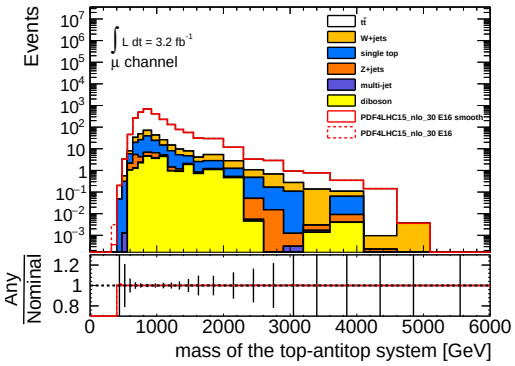

(b) PDF eigenvector 16, μ+jets channel.

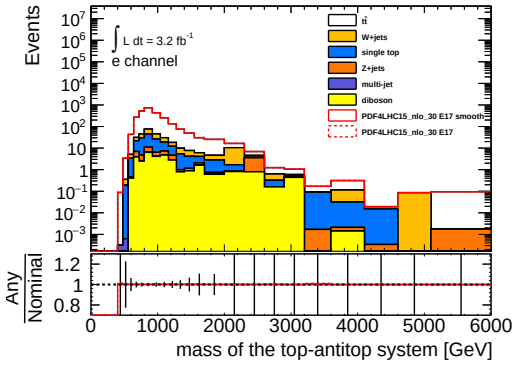

(c) PDF eigenvector 17, e+jets channel.

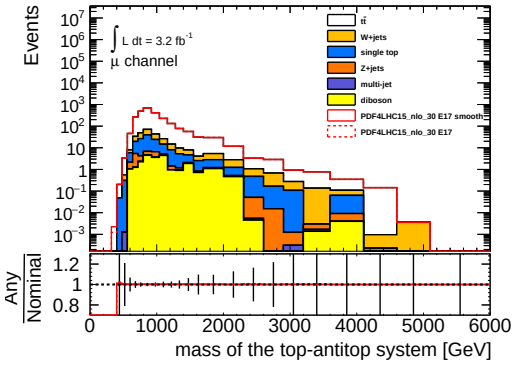

(d) PDF eigenvector 17, μ+jets channel.

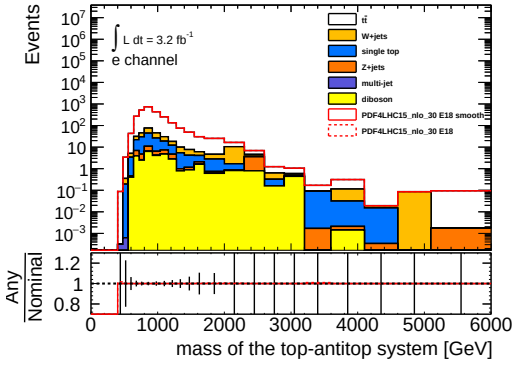

(e) PDF eigenvector 18, e+jets channel.

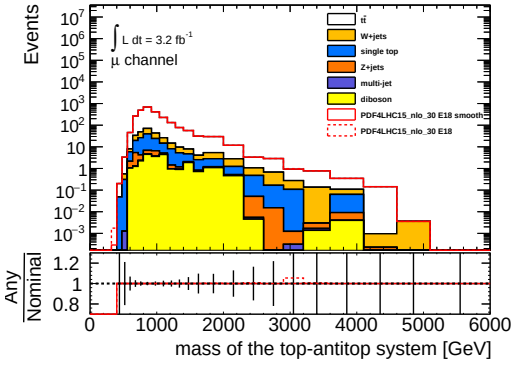

(f) PDF eigenvector 18, μ+jets channel.

Figure A.26: Effect of various systematics before and after smoothing for electron (left) and muon (right) channels.

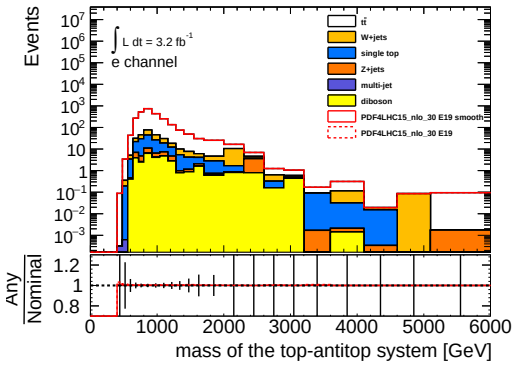

(a) PDF eigenvector 19, e+jets channel.

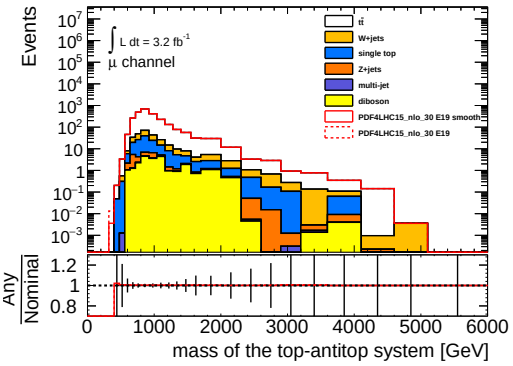

(b) PDF eigenvector 19, μ+jets channel.

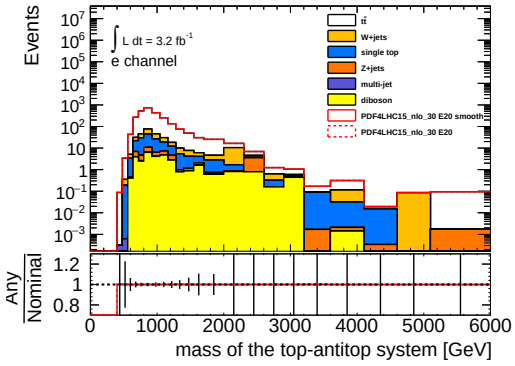

(c) PDF eigenvector 20, e+jets channel.

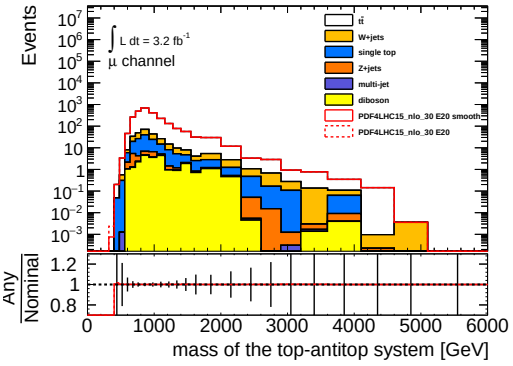

(d) PDF eigenvector 20, μ+jets channel.

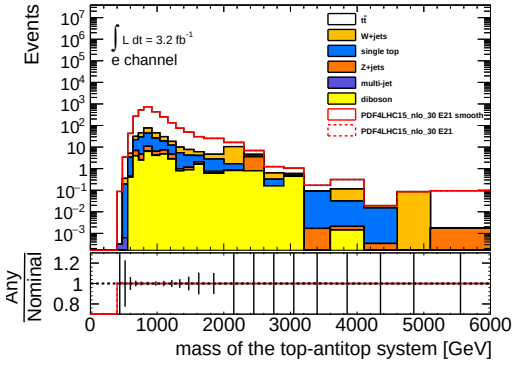

(e) PDF eigenvector 21, e+jets channel.

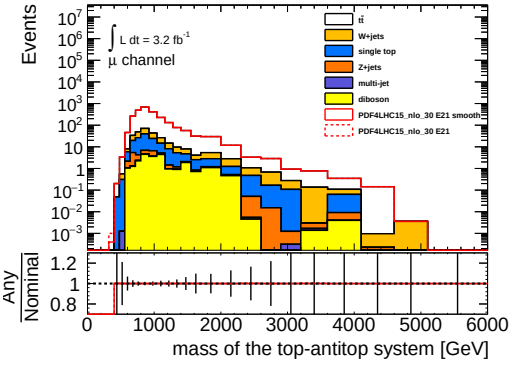

(f) PDF eigenvector 21, μ+jets channel.

Figure A.27: Effect of various systematics before and after smoothing for electron (left) and muon (right) channels.

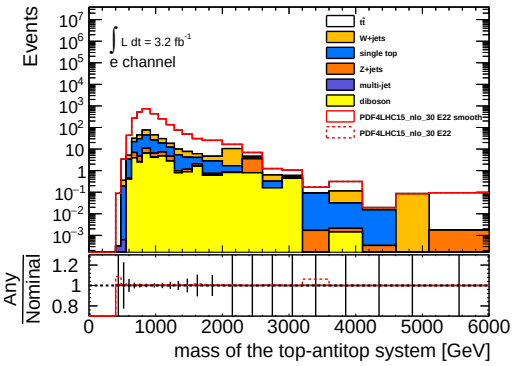

(a) PDF eigenvector 22, e+jets channel.

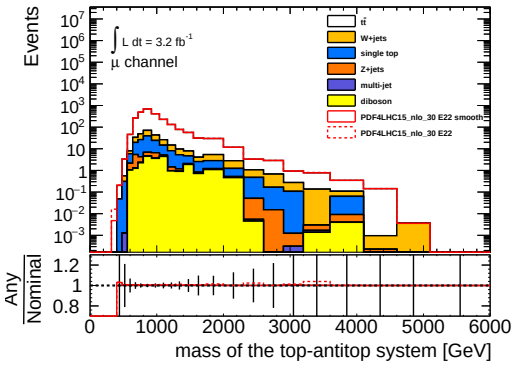

(b) PDF eigenvector 22, μ+jets channel.

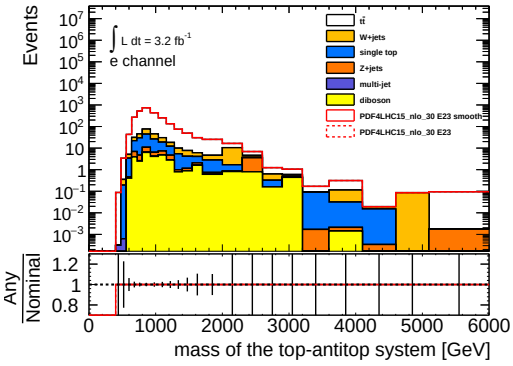

(c) PDF eigenvector 23, e+jets channel.

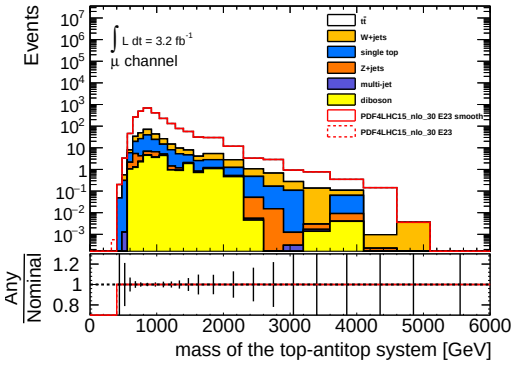

(d) PDF eigenvector 23, μ+jets channel.

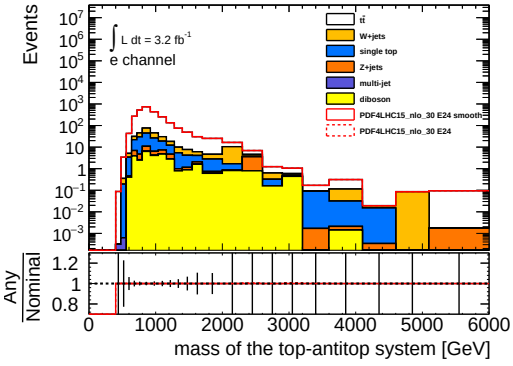

(e) PDF eigenvector 24, e+jets channel.

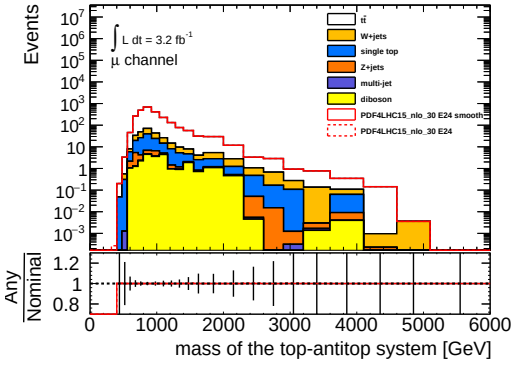

(f) PDF eigenvector 24, μ+jets channel.

Figure A.28: Effect of various systematics before and after smoothing for electron (left) and muon (right) channels.

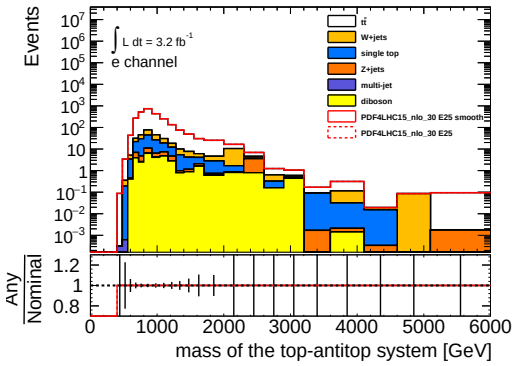

(a) PDF eigenvector 25, e+jets channel.

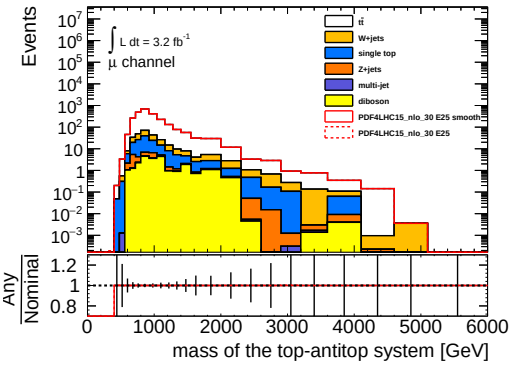

(b) PDF eigenvector 25, μ+jets channel.

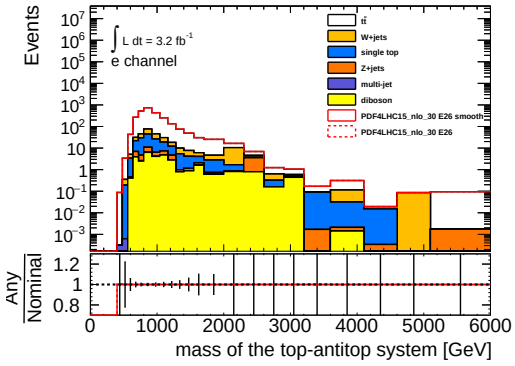

(c) PDF eigenvector 26, e+jets channel.

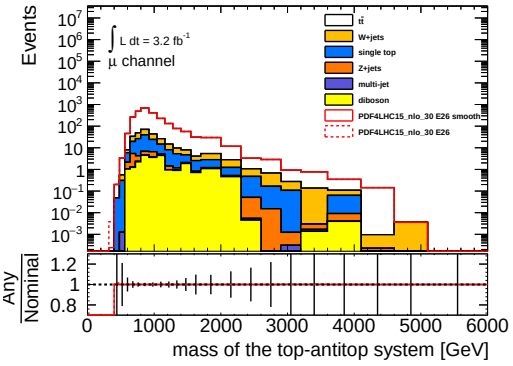

(d) PDF eigenvector 26, μ+jets channel.

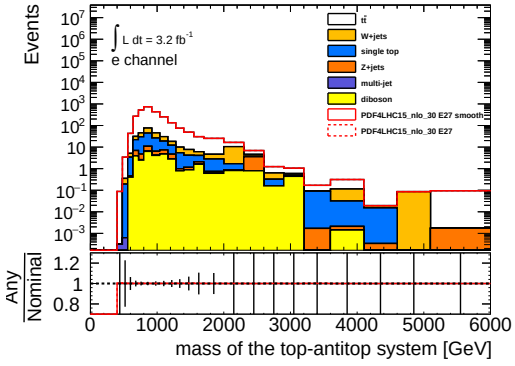

(e) PDF eigenvector 27, e+jets channel.

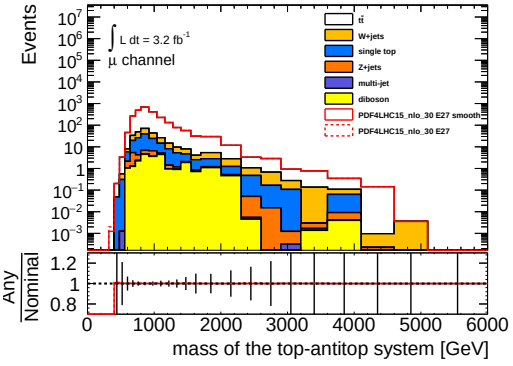

(f) PDF eigenvector 27, μ+jets channel.

Figure A.29: Effect of various systematics before and after smoothing for electron (left) and muon (right) channels.

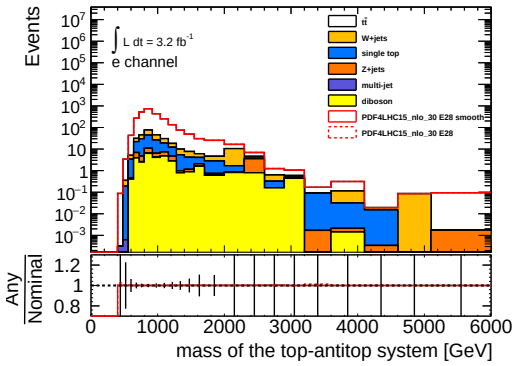

(a) PDF eigenvector 28, e+jets channel.

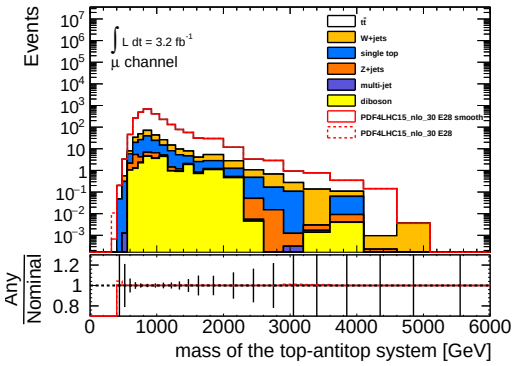

(b) PDF eigenvector 28, μ+jets channel.

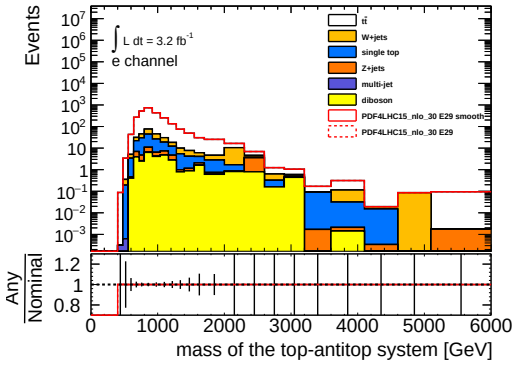

(c) PDF eigenvector 29, e+jets channel.

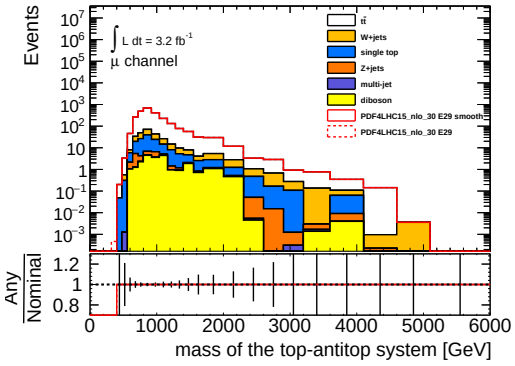

(d) PDF eigenvector 29, μ+jets channel.

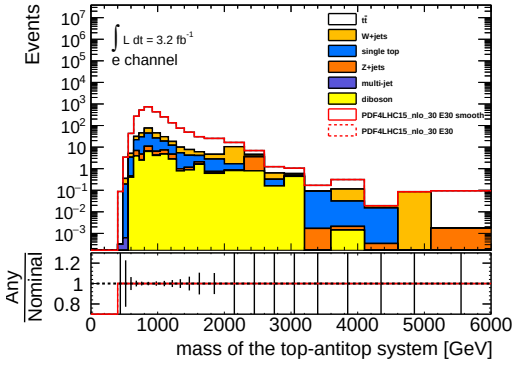

(e) PDF eigenvector 30, e+jets channel.

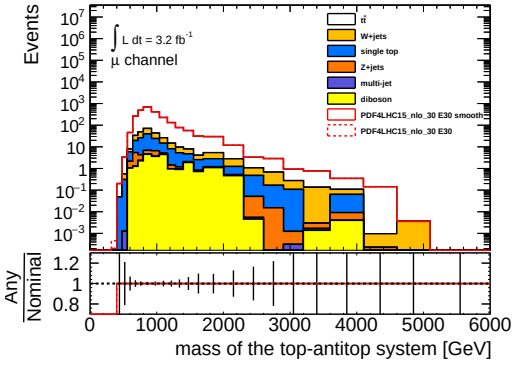

(f) PDF eigenvector 30, μ+jets channel.

Figure A.30: Effect of various systematics before and after smoothing for electron (left) and muon (right) channels.

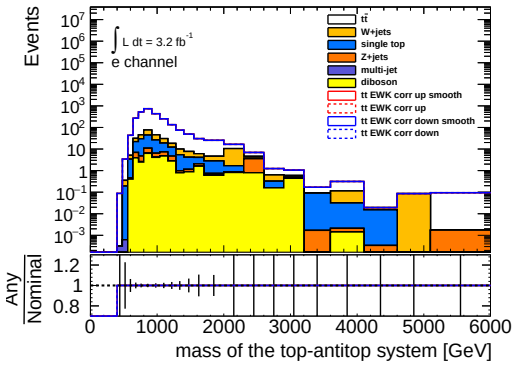

(a) Electroweak Correction for $t\bar{t}$, e+jets channel.

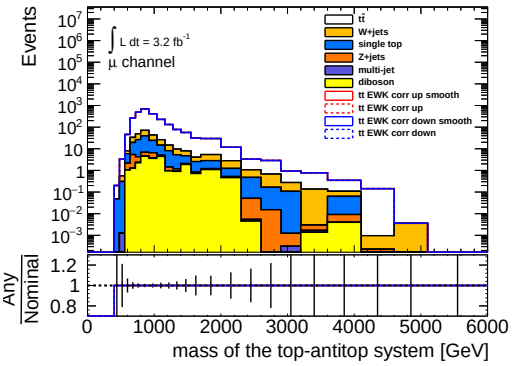

(b) Electroweak Correction for $t\bar{t}$, μ+jets channel.

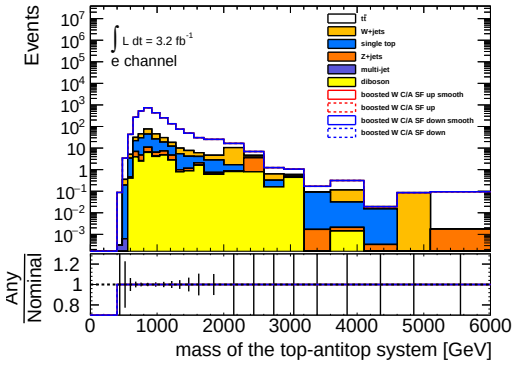

(c) W+jets normalization, e+jets channel.

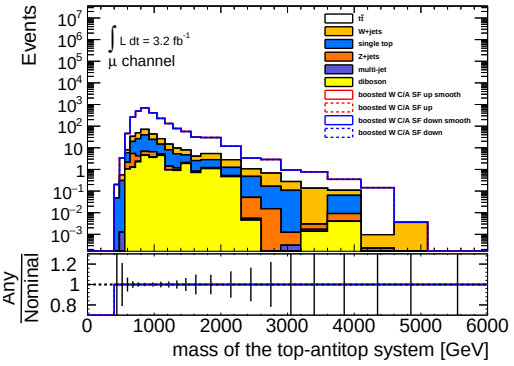

(d) W+jets normalization, μ+jets channel.

Figure A.31: Effect of various systematics before and after smoothing for electron (left) and muon (right) channels.

Appendix B
Comparison between channels e/μ

Difference between electron and muon channels with systematic uncertainties are shown here.

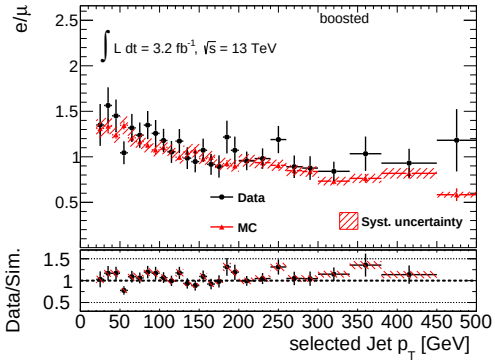

Figure B.2: Selected jet p_T

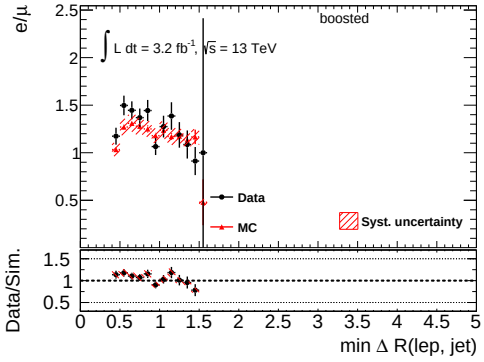

Figure B.3: min $\Delta R(jet, lepton)$

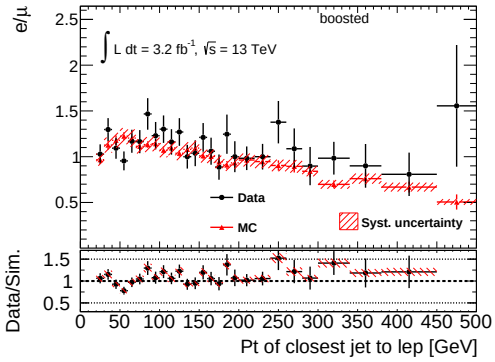

Figure B.4: close to lepton jet p_T

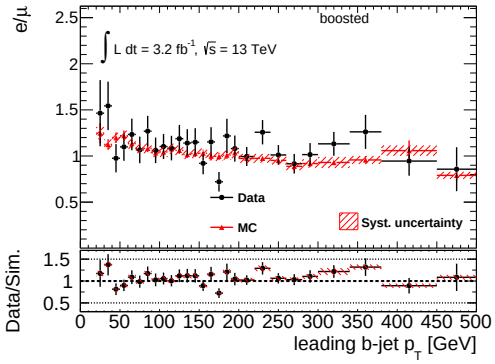

Figure B.5: leading b-jet p_T

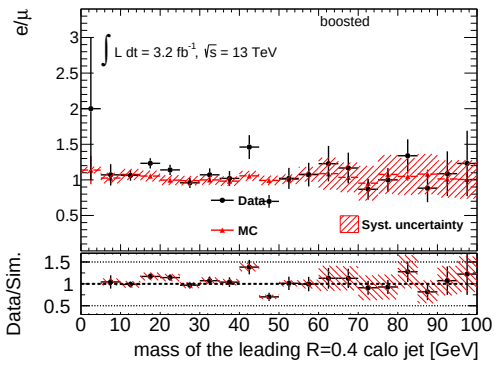

Figure B.6: mass of the leading $R = 0.4$ calo-jet

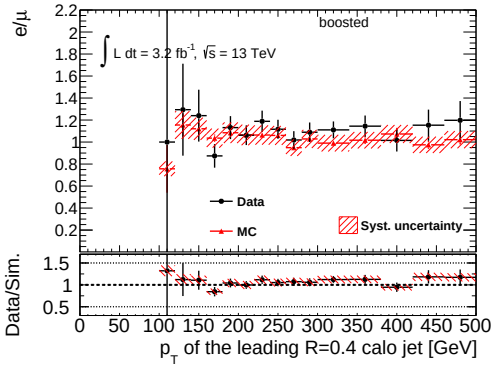

Figure B.7: p_T of the leading $R = 0.4$ calo-jet

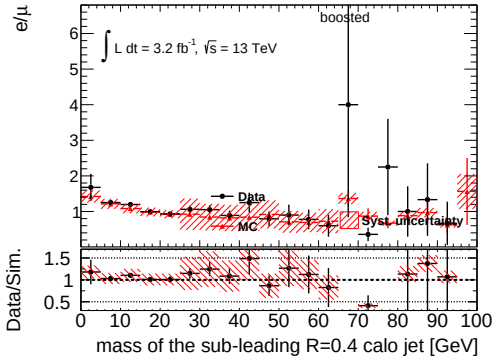

Figure B.8: mass of the sub-leading $R = 0.4$ calo-jet

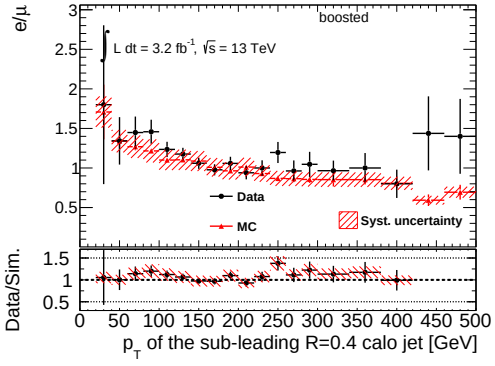

Figure B.9: p_T of the sub-leading $R = 0.4$ calo-jet.

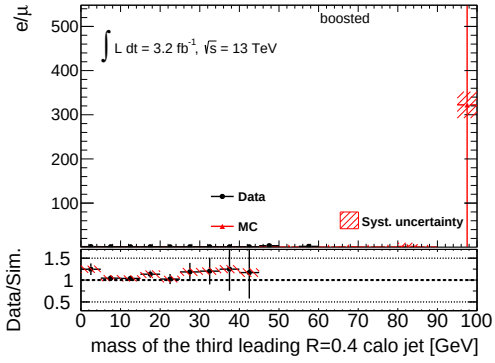

Figure B.10: mass of the third leading $R = 0.4$ calo-jet

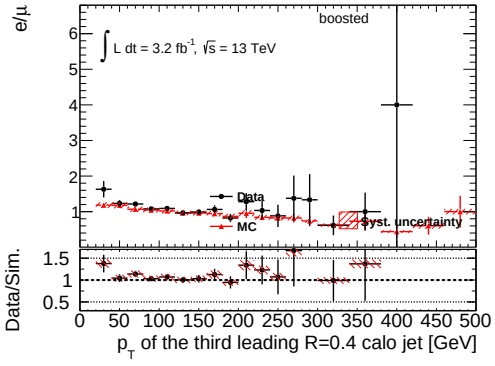

Figure B.11: p_T of the third leading $R = 0.4$ calo-jet.

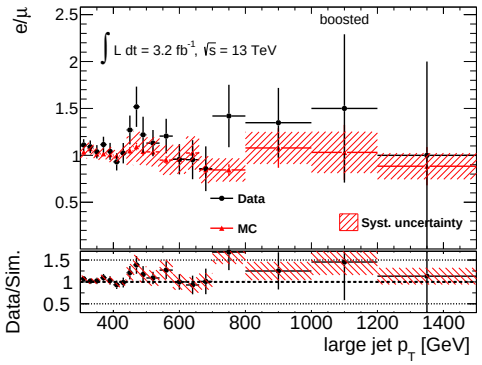

Figure B.12: Large-R jet p_T

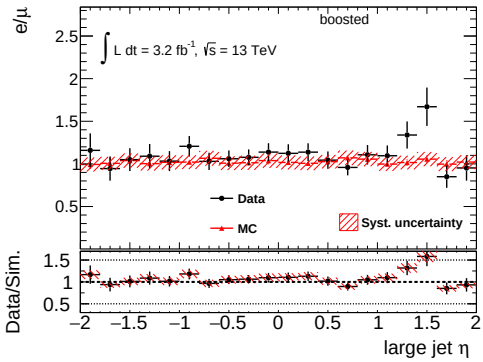

Figure B.13: Large-R jet η

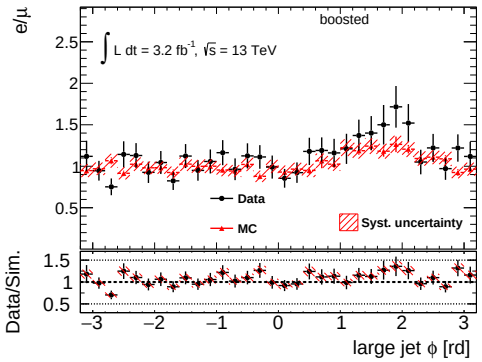

Figure B.14: Large-R jet ϕ

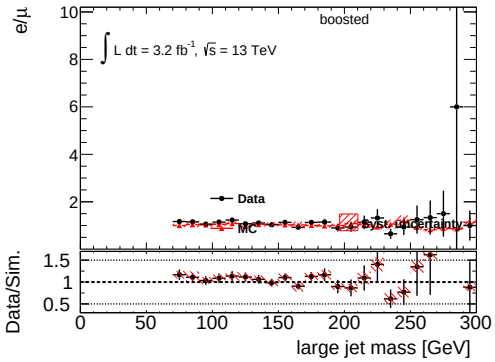

Figure B.15: Large-R jet mass

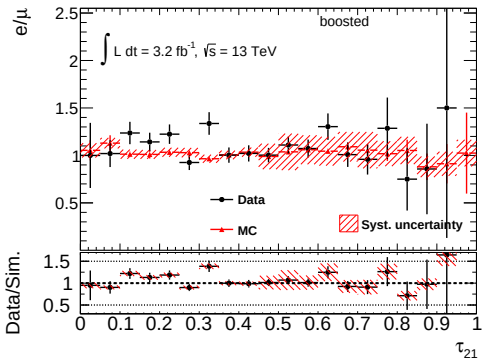

Figure B.16: Large-R jet τ_{21}

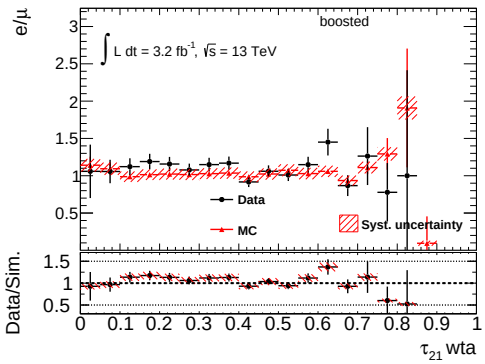

Figure B.17: Large-R jet τ_{21}^{wta}

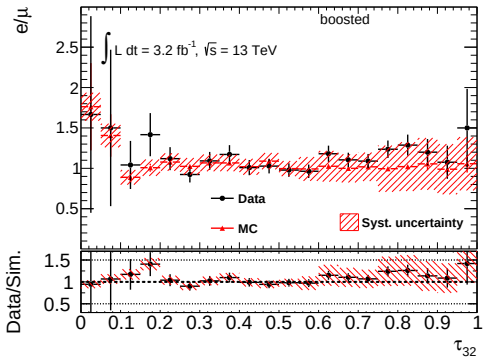

Figure B.18: Large-R jet τ_{32}

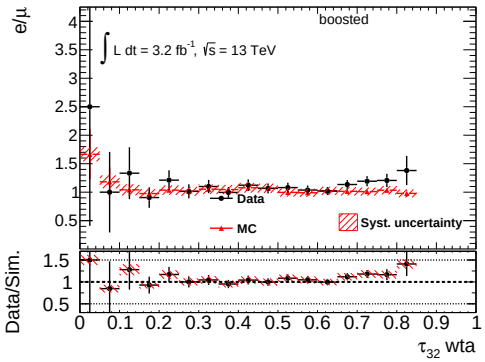

Figure B.19: Large-R jet τ_{32}^{wta}

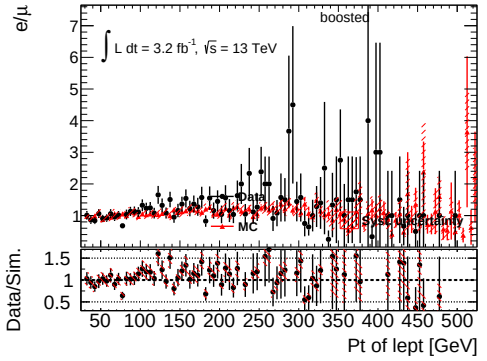

Figure B.20: Lepton p_T

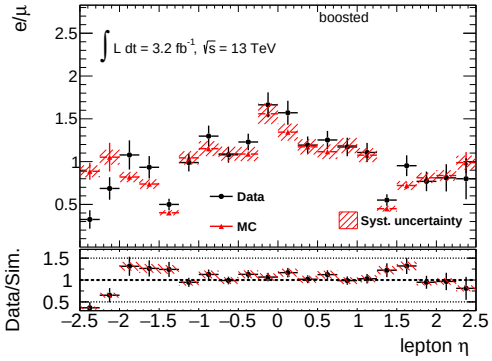

Figure B.21: Lepton η

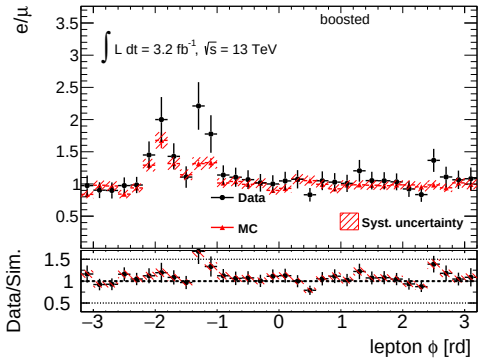

Figure B.22: Lepton ϕ

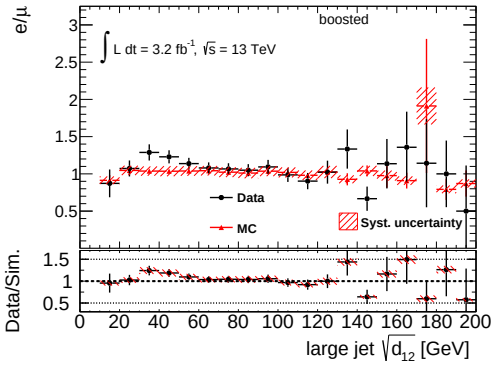

Figure B.23: Large-R jet$\sqrt{d_{12}}$

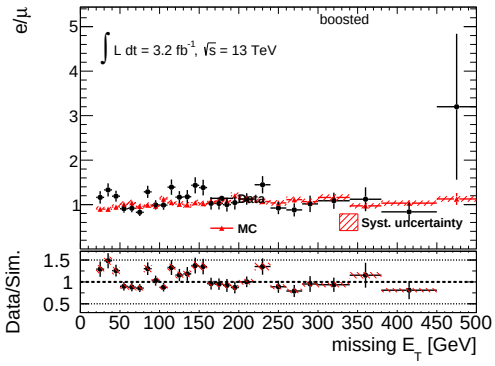

Figure B.24: E_T^{miss}

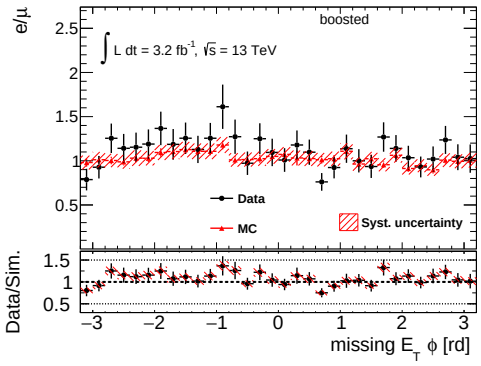

Figure B.25: ϕ of E_T^{miss}

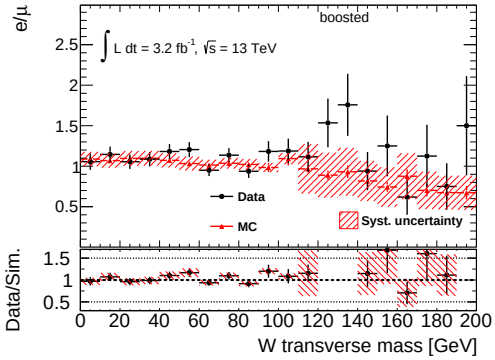

Figure B.26: W transverse mass

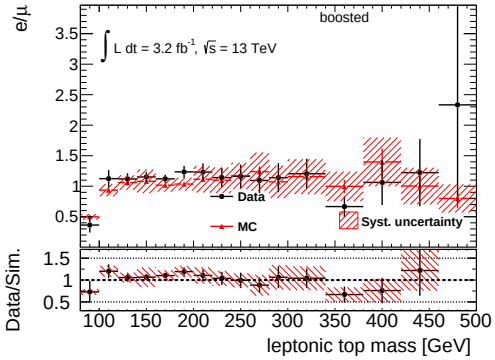

Figure B.27: leptonic top mass

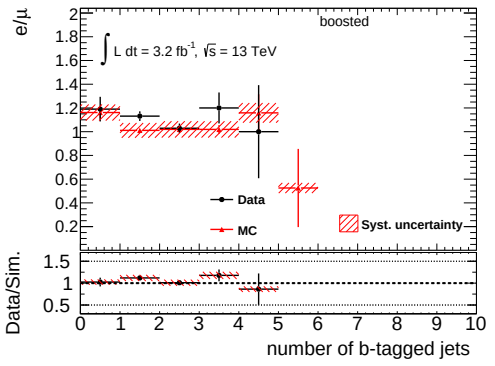

Figure B.28: number of b-tagged jets

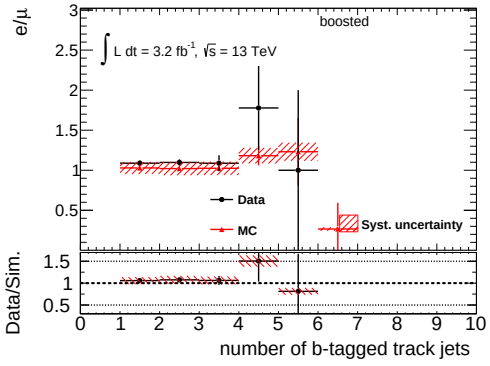

Figure B.29: number of b-tagged track-jets

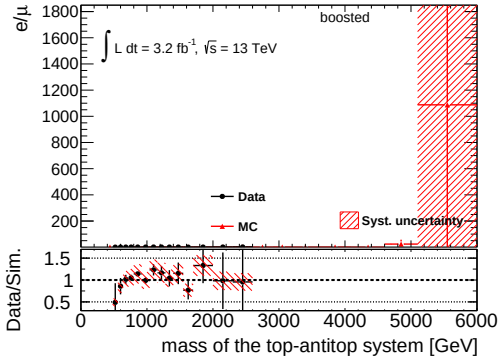

Figure B.30: invariant $t\bar{t}$ mass system

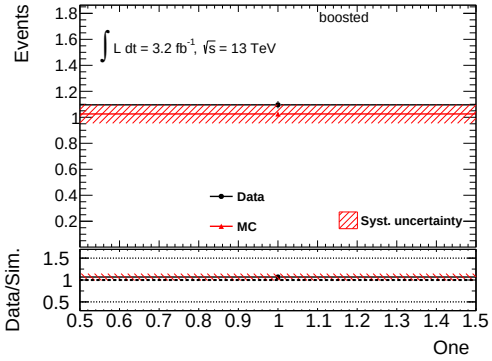

Figure B.31: yields

Appendix C
Nuisance parameter impact on fitting

Figure C.2 shows the nuisance parameter used in this fit and their dependence is shown in Figure C.3.

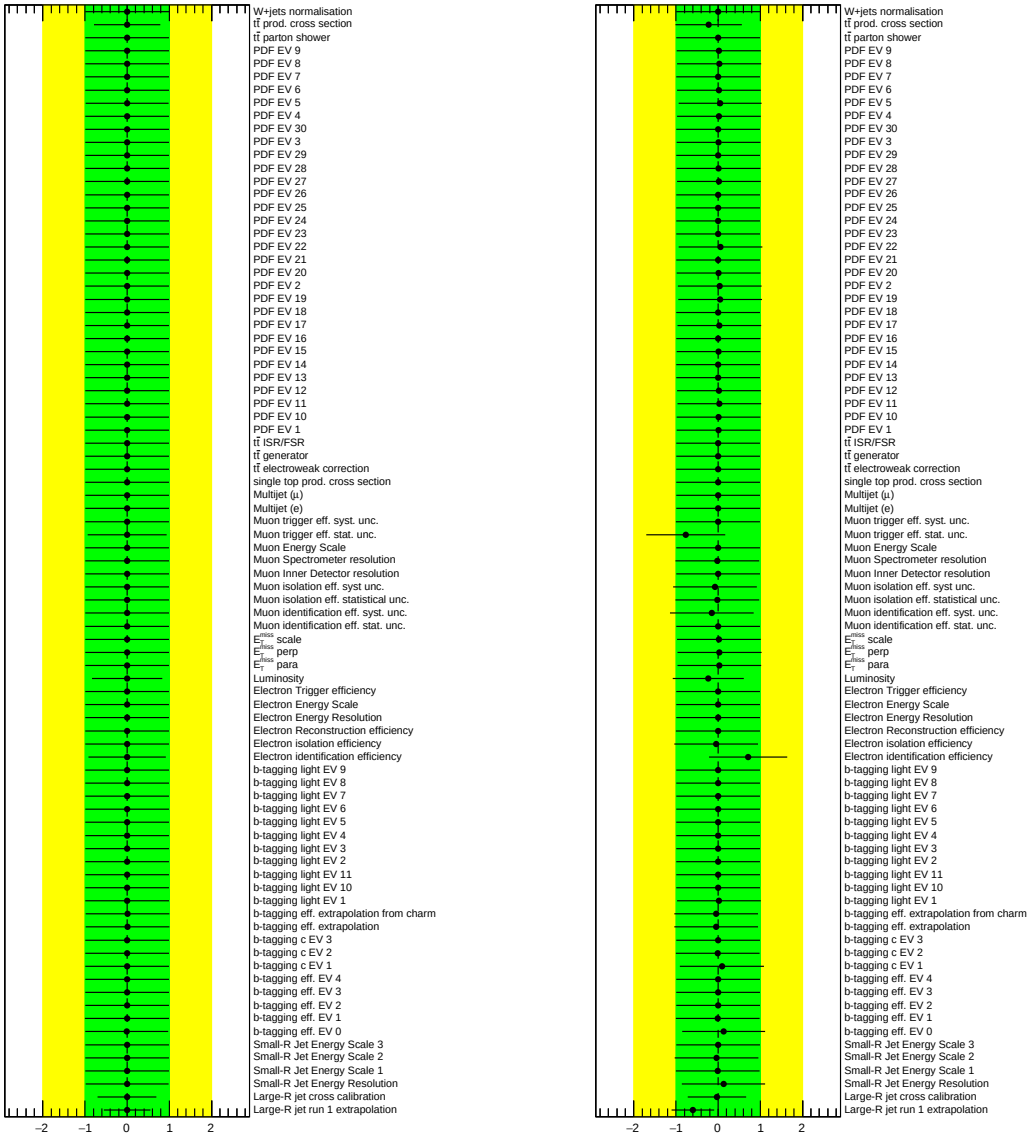

Figure C.2: The pull of the nuisance parameters for a fit performed under the hypothesis background+Z'(2.25 TeV), for the Asimov pseudo-data (left) and data (right).

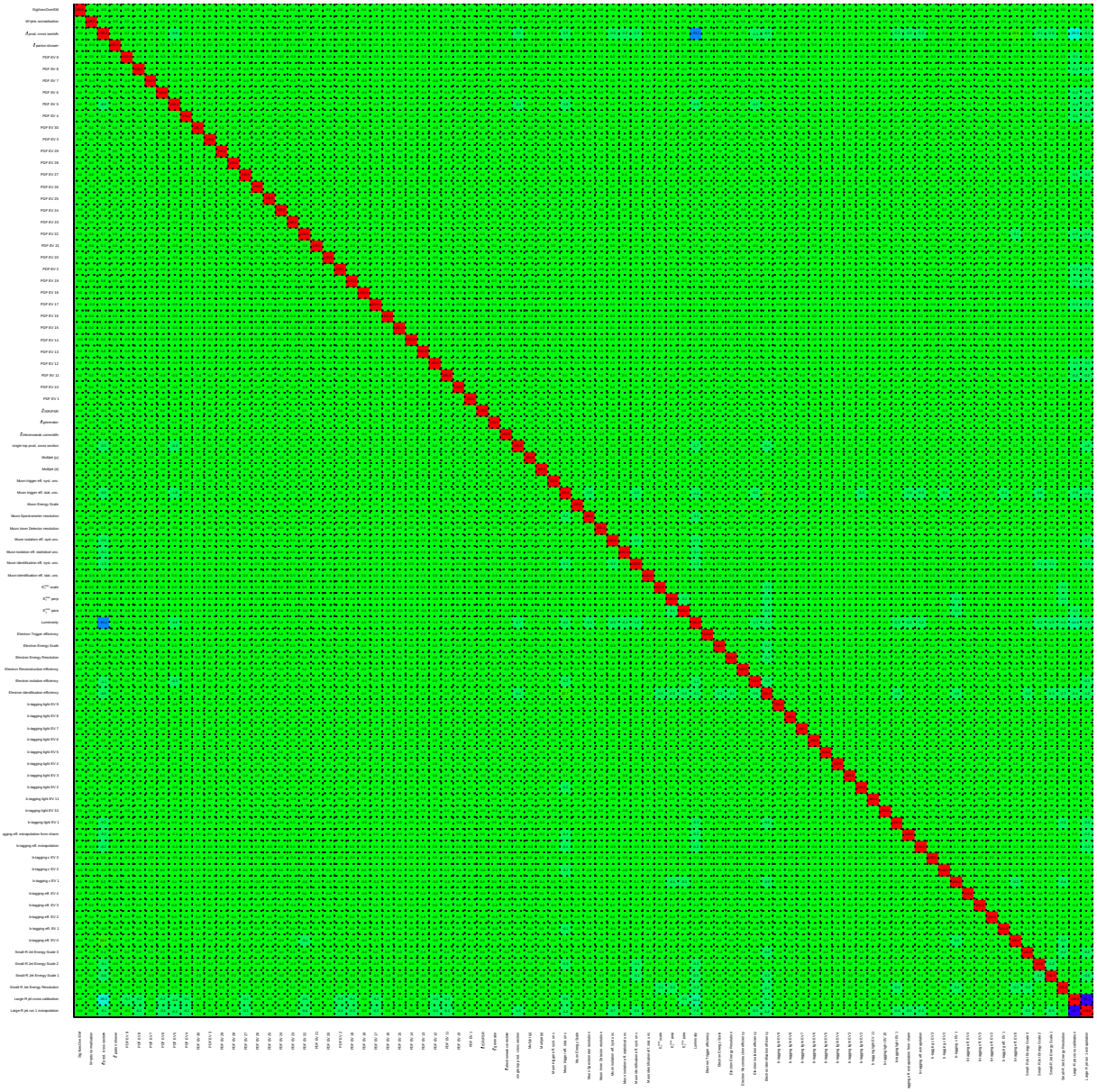

Figure C.3: The nuisance parameter correlation matrix used in this fit.

Appendix D
Resolved regime

The events were separated orthogonal into boosted and resolved regime. The resolved regime contains 4 separated small-R jets selected by the χ^2 method to matching top quarks.

12.1 Comparison of data to signal and backgrounds in the resolved regime

Figure D.2, D.3 and D.4 shows the distributions for leptons. Figure D.5–D.10 show the p_T

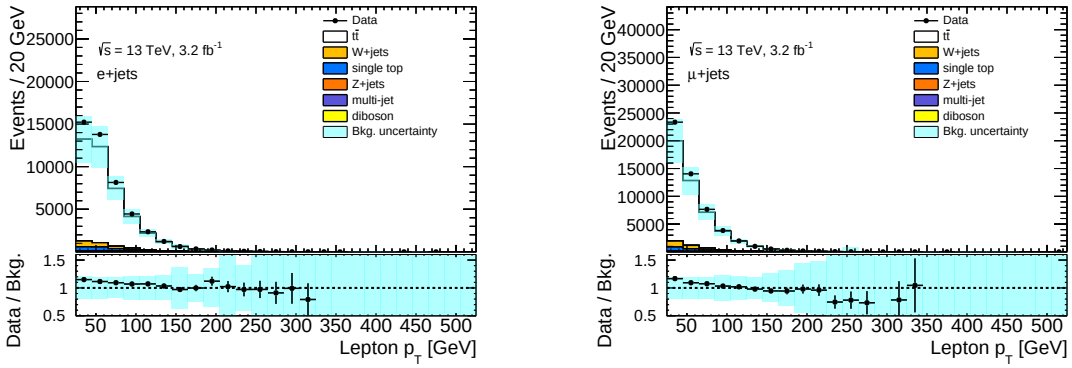

Figure D.2: Lepton p_T distributions, electron (left) and muon (right).

and mass distributions of the leading, the sub-leading and the third-leading small-R jets. Figure D.11 show the p_T distributions of the leading b-tagged small-R jets. Figure D.12 show the minimum distance of ΔR between the small-R jet and the lepton. Figure D.13 D.14 shows E_T^{miss} distribution. The number of b-tagged track-jet is shown in Figure D.15.

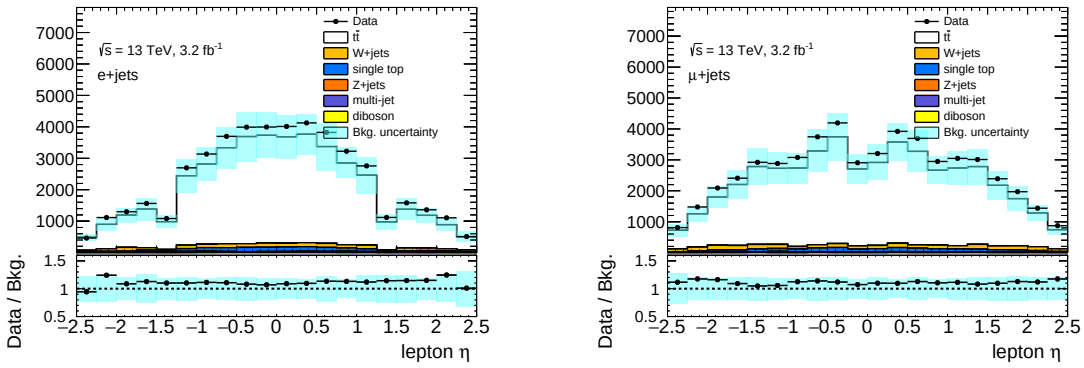

Figure D.3: Lepton η distributions, electron (left) and muon (right).

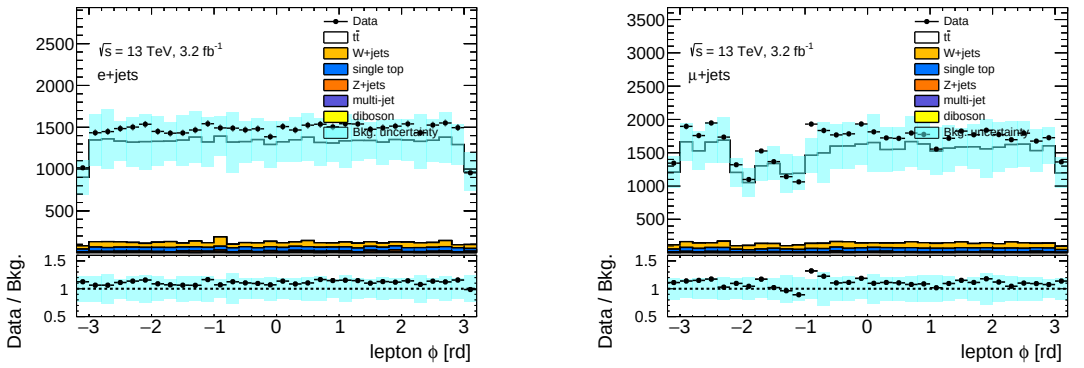

Figure D.4: Lepton ϕ distributions, electron (left) and muon (right).

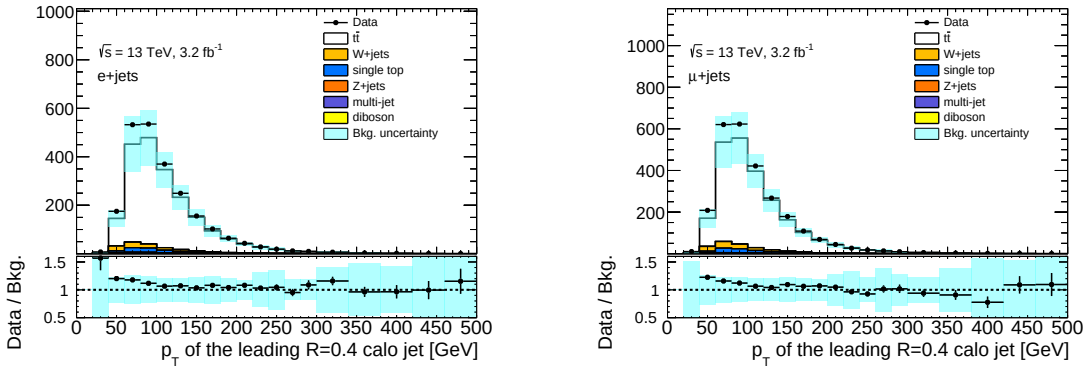

Figure D.5: Leading small-R jet p_T distributions, electron channel (left) and muon channel (right).

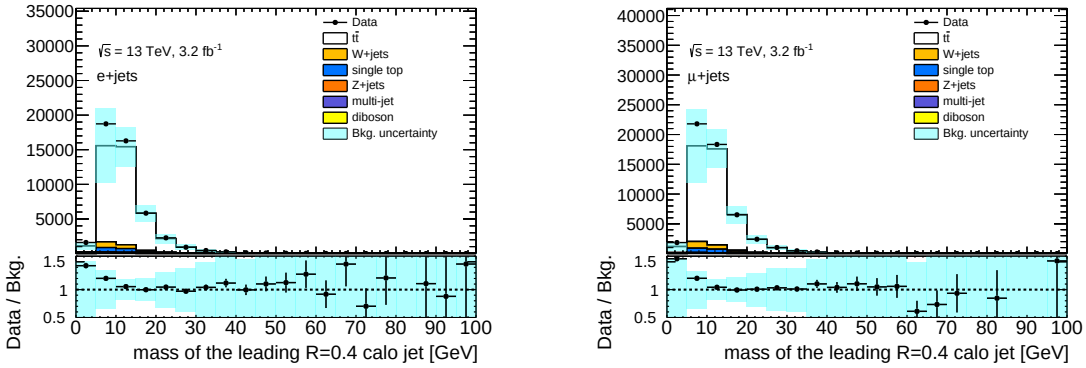

Figure D.6: Leading small-R jet mass distributions, electron channel (left) and muon channel (right).

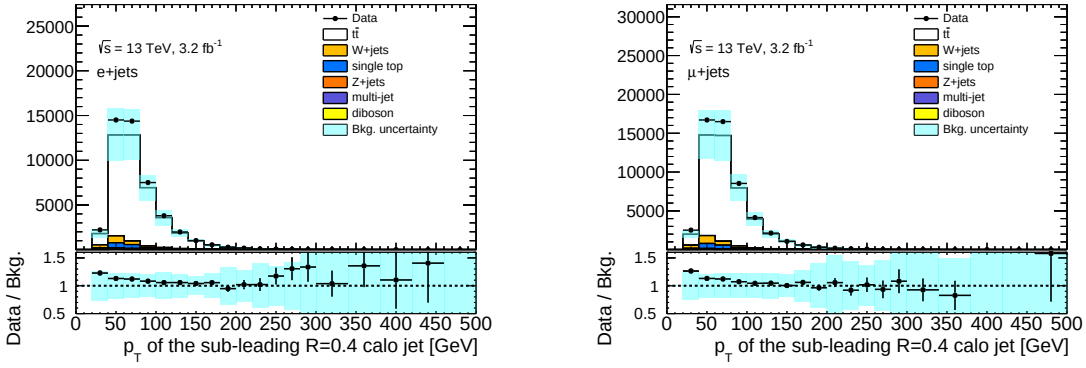

Figure D.7: Sub-leading small-R jet p_T distributions, electron channel (left) and muon channel (right).

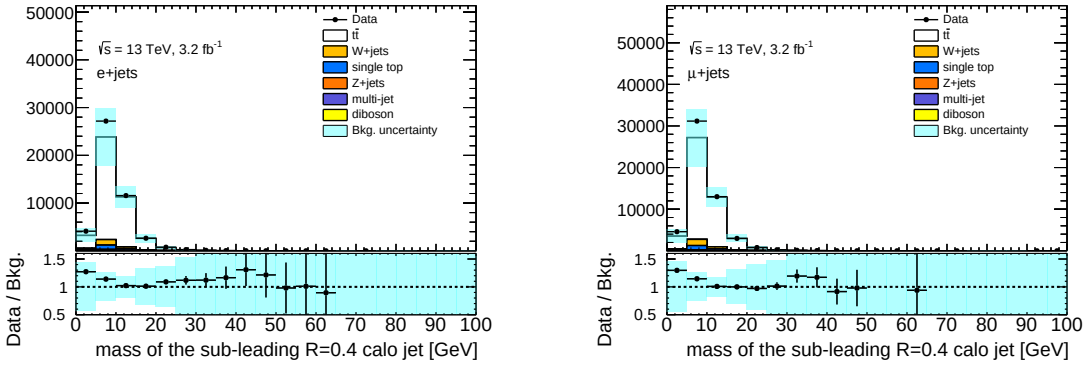

Figure D.8: Sub-leading small-R jet mass distributions, electron channel (left) and muon channel (right).

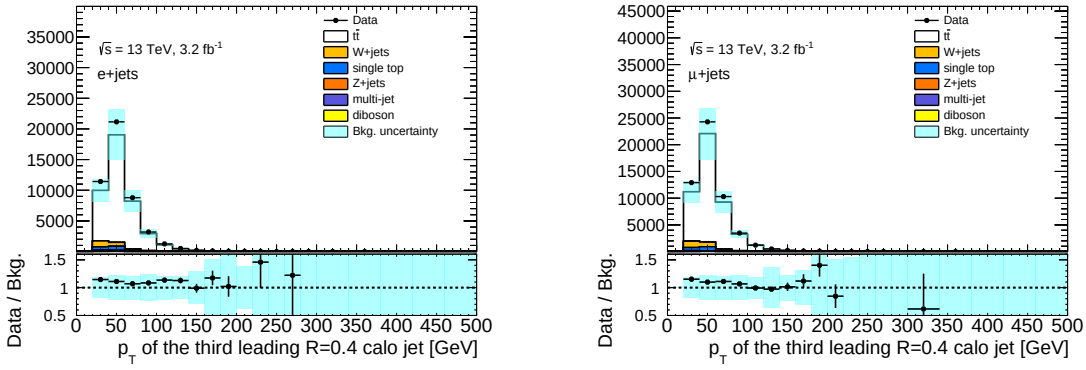

Figure D.9: Third leading small-R jet p_T distributions, electron channel (left) and muon channel (right).

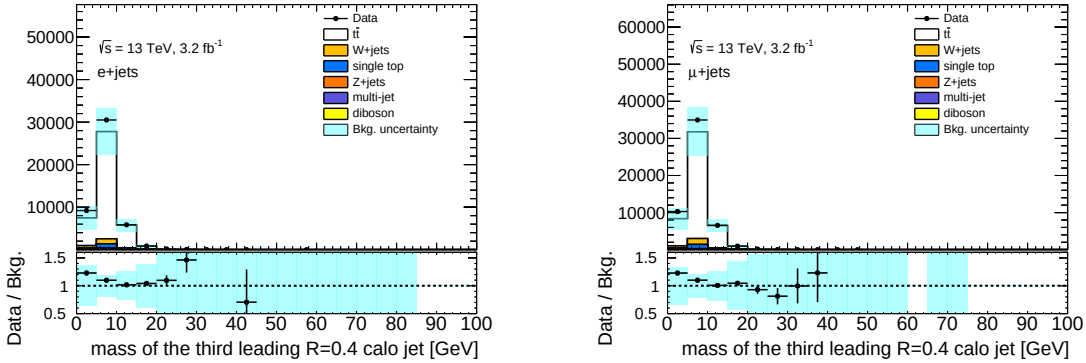

Figure D.10: Third leading small-R jet mass distributions, electron channel (left) and muon channel (right).

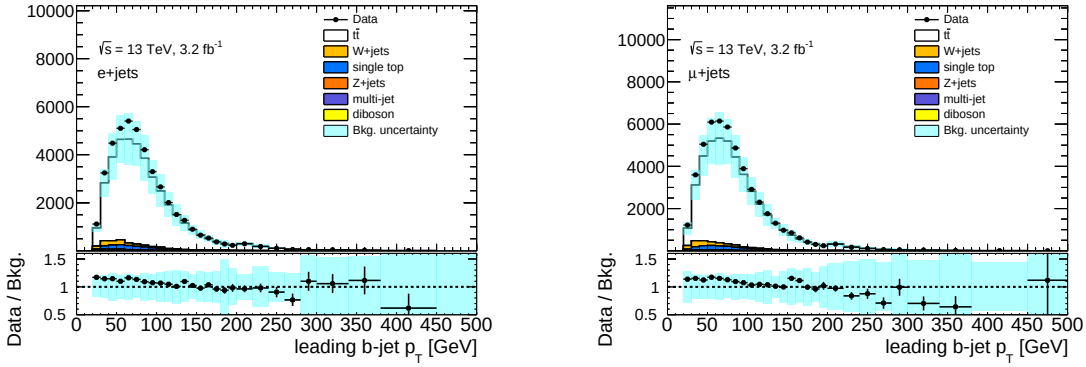

Figure D.11: Leading small-R b-jet p_T distributions, electron channel (left) and muon channel (right).

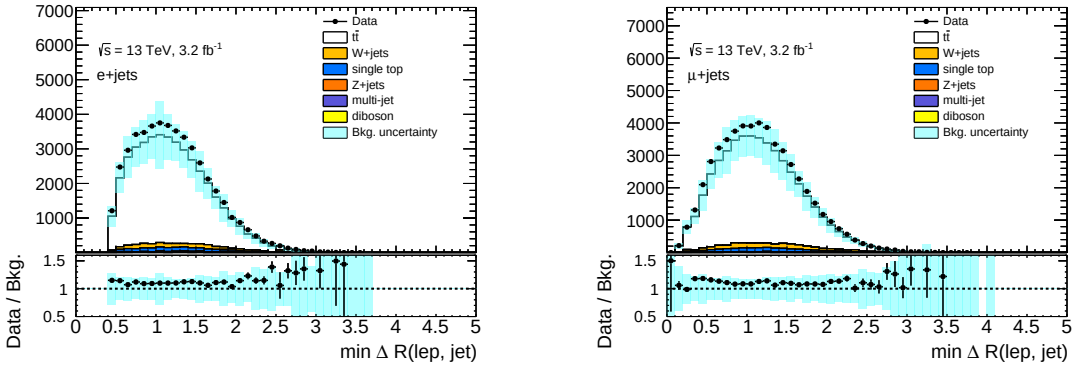

Figure D.12: The distance distribution of ΔR of between the small-R jet which is close to the lepton and lepton, electron (left) and muon (right).

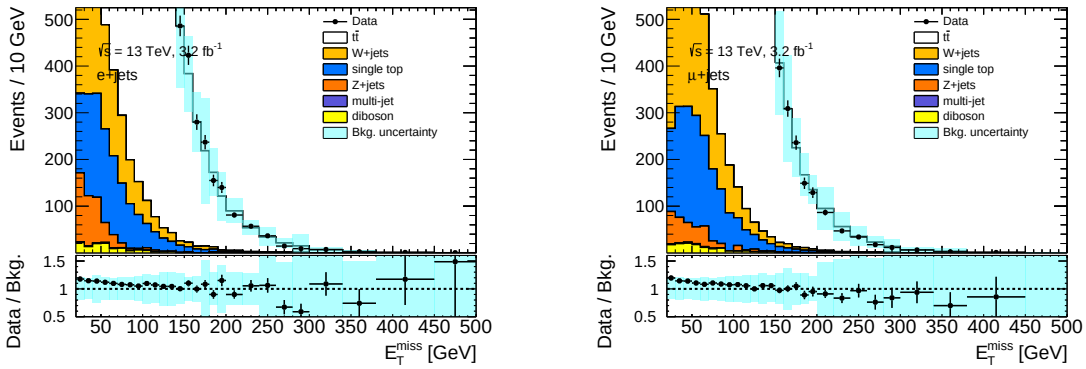

Figure D.13: E_T^{miss} distributions, electron channel (left) and muon channel (right).

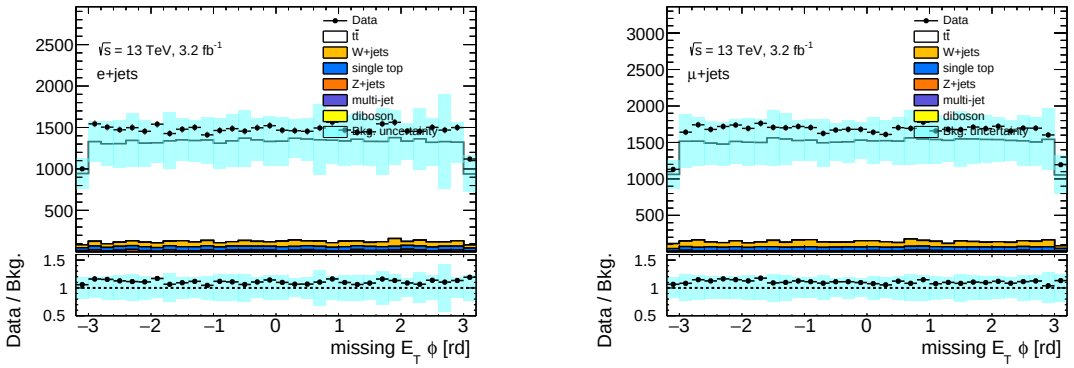

Figure D.14: ϕ of E_T^{miss} distributions, electron channel (left) and muon channel (right).

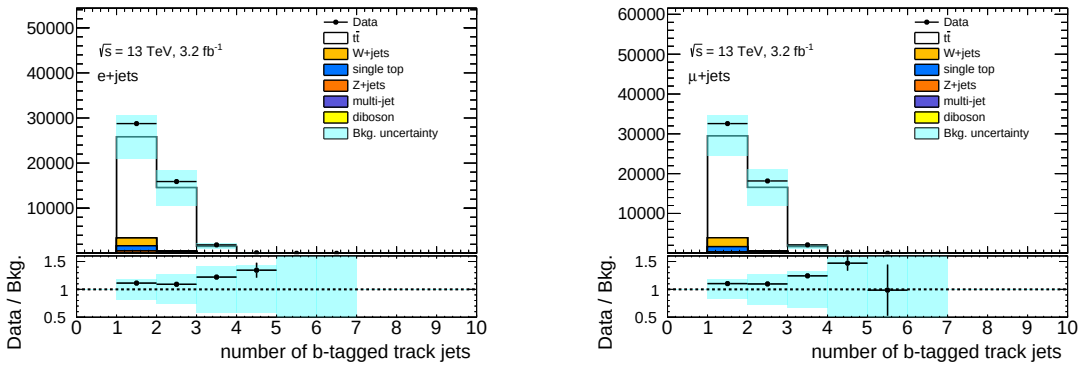

Figure D.15: Number of b-tagged track-jets, electron channel (left) and muon channel (right).

12.1.1 Event reconstruction

For selecting the jets from top quark decays, a χ^2 defined in equation D.2 that constrains the expected top quark and W boson masses was used [187].

$$\chi^2 = \left(\frac{m_{jj} - m_{\mathrm{W}}}{\sigma_{\mathrm{W}}}\right)^2 + \left(\frac{m_{jjb} - m_{jj} - m_{th} - m_{\mathrm{W}}}{\sigma_{th-\mathrm{W}}}\right)^2 + \left(\frac{m_{j\ell\nu} - m_{t\ell}}{\sigma_{t\ell}}\right)^2 + \left(\frac{(p_{T\ ,jjb} - p_{T\ ,j\ell\nu}) - (p_{T\ ,th} - p_{T\ ,t\ell})}{\sigma_{diff p_T}}\right)^2 \tag{D.2}$$

where $m_{\mathrm{W}} = 83.3$ GeV, $m_{th,\mathrm{W}} = 91.1$ GeV, $m_{t\ell} = 168.2$ GeV, $\sigma_{\mathrm{W}} = 10.8$ GeV, $\sigma_{th-\mathrm{W}} = 14.2$ GeV, $\sigma_{t\ell} = 20.6$ GeV, $p_{T\ ,th} - p_{T\ ,t\ell} = -8.7$ GeV and $\sigma_{diff p_T} = 55.5$ GeV. The first term constrains the hadronically decaying W boson, the second term means the hadronically decaying top quark, the third term corresponds the semileptonically decaying top quark, and the last term constrains the top quark transverse momentum. Figure D.16 show the χ^2 distribution. Figures D.17–D.18

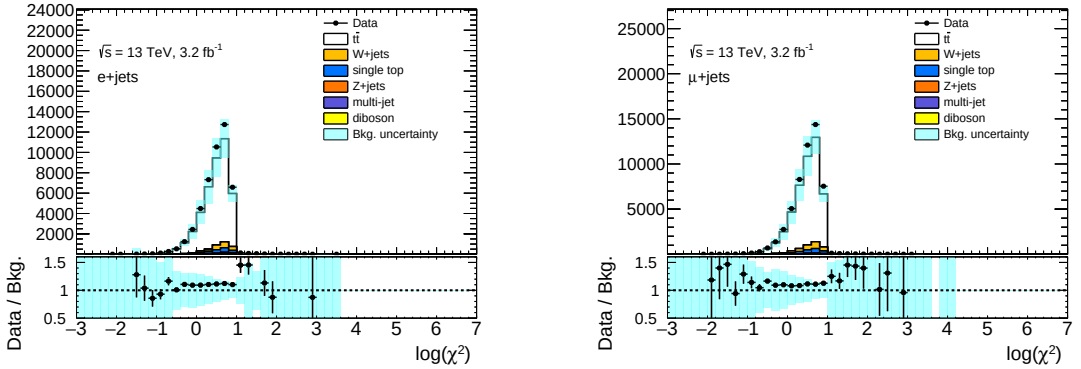

Figure D.16: The χ^2 distribution, electron channel (left) and muon channel (right).

show the reconstructed top mass of the leptonic side and hadronic side respectively. Figure D.19 show the reconstructed invariant mass of top-antitop system $m_{t\bar{t}}$.

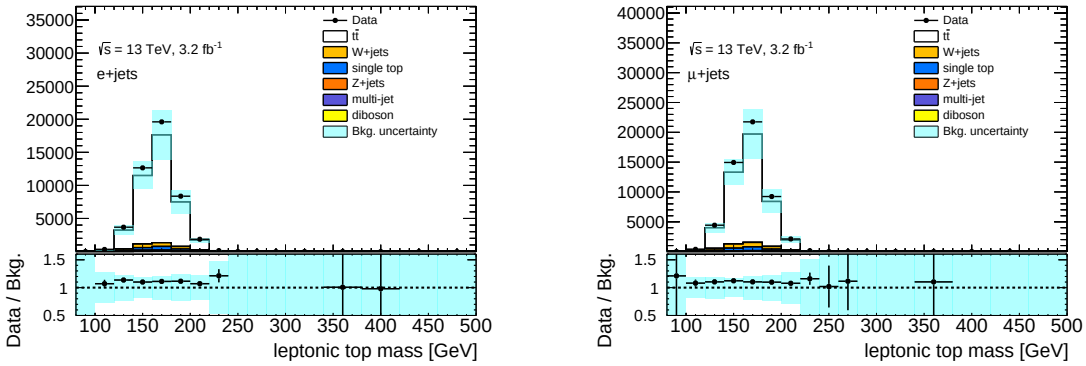

Figure D.17: The reconstructed top mass distribution at the leptonic side, electron channel (left) and muon channel (right).

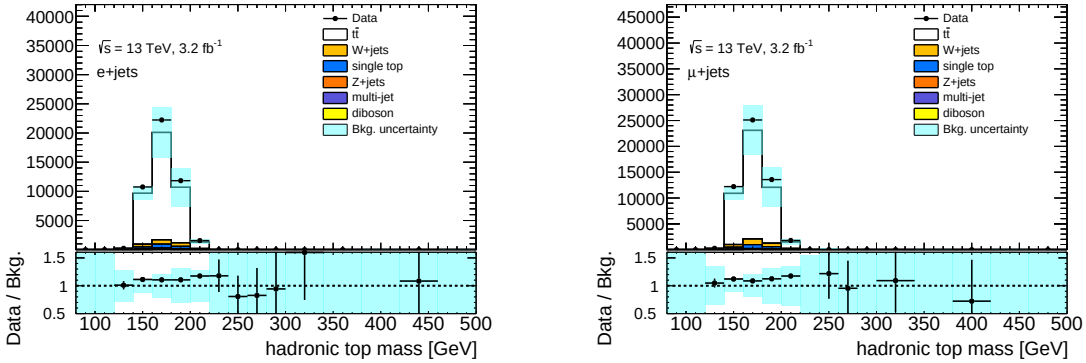

Figure D.18: The reconstructed top mass distribution at the hadronic side, electron channel (left) and muon channel (right).

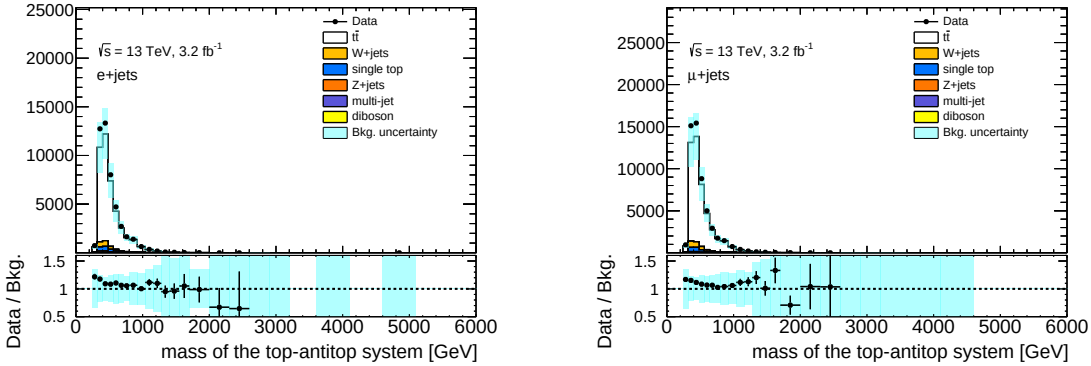

Figure D.19: The invariant mass of $t\bar{t}$ distribution, electron channel (left) and muon channel (right).

Bibliography

[1] Particle Data Group. http://pdg.lbl.gov/.

[2] The ATLAS Collaboration. Observation of a new particle in the search for the Standard Model Higgs boson with the ATLAS detector at the LHC. *Phys. Lett.*, B716:1–29, 2012. arXiv:hep-ex/1207.7214[hep-ex].

[3] The CMS Collaboration. Observation of a new boson at a mass of 125 GeV with the CMS experiment at the LHC. *Phys. Lett.*, B716:30–61, 2012. arXiv:hep-ex/1207.7235[hep-ex].

[4] LHC homepage. http://lhc.web.cern.ch/lhc/.

[5] CERN Bullten. `https://cds.cern.ch/journal/CERNBulletin/2012/35/News%20Articles/1473657`.

[6] CERN ; The Large Electron-Positron Collider. `http://home.cern/about/accelerators/large-electron-positron-collider`.

[7] Fermilab ; The Tevatron. http://www.fnal.gov/pub/tevatron/.

[8] Howard Georgi and S. L. Glashow. Unity of All Elementary-Particle Forces. *Phys. Rev. Lett.*, 32:438, 1974. `http://journals.aps.org/prl/abstract/10.1103/PhysRevLett.32.438`.

[9] H. Georg. The State of the Art - Gauge Theories. (Talk). *AIP Conf. Proc.*, 23:575–582, 1975. `http://scitation.aip.org/content/aip/proceeding/aipcp/10.1063/1.2947450`.

[10] J. C. Pati and A. Salam. Lepton Number as the Fourth Color. *Phys. Rev. D*, 10:275–289, 1974. `http://journals.aps.org/prd/pdf/10.1103/PhysRevD.10.275`.

[11] Jonathan L. Feng. Naturalness and the Status of Supersymmetry. arXiv:1302.6587 [hep-ph].

[12] Lisa Randall and Raman Sundrum. Large Mass Hierarchy from a Small Extra Dimension. *Phys. Rev. Lett.*, 83:3370–3373, 1999. `http://journals.aps.org/prl/pdf/10.1103/PhysRevLett.83.3370`, arXiv:hep-ph/9905221 [hep-ph].

[13] Lisa Randall and Raman Sundrum. An Alternative to compactification. *Phys. Rev. Lett.*, 83:4690–4693, 1999. http://journals.aps.org/prl/pdf/10.1103/PhysRevLett.83.4690, arXiv:hep-th/9906064 [hep-th].

[14] H. Davoudiasl, J. Hewett and T. Rizzo. Experimental probes of localized gravity: On and off the wall. *Phys. Rev.D*, 63:075004, 2001. http://journals.aps.org/prd/abstract/10.1103/PhysRevD.63.075004, arXiv:hep-ph/0006041 [hep-ph].

[15] Kaustubh Agashe, Hooman Davoudiasl, Gilad Perez, and Amarjit Soni. Warped gravitons at the CERN LHC and beyond. *Phys. Rev.D*, 76:036006, 2007. http://journals.aps.org/prd/pdf/10.1103/PhysRevD.76.036006, arXiv:hep-ph/0701186 [hep-ph].

[16] C. T. Hill. Topcolor assisted technicolor. *Phys. Lett. B*, 345:483–489, 1995. arXiv:hep-ph/9411426[hep-ph].

[17] J. R. Andersen *et al.* Discovering Technicolor. *Eur. Phys. J. Plus*, 126:81, 2011.

[18] W. Beenakker, M. Kramer, T. Plehn, M. Spira, and P. M. Zerwas. Stop production at hadron colliders. *Nucl. Phys.*, B515:3–14, 1998. arXiv:hep-ph/9710451[hep-ph].

[19] W. Beenakker, S. Brensing, M. Kramer, A. Kulesza, E. Laenen, and I. Niessen. Supersymmetric top and bottom squark production at hadron colliders. *JHEP*, 1008:098, 2010. arXiv:1006.4771.

[20] G.C. Branco, *et al.* Theory and phenomenology of two-Higgs-doublet models. *Phys. Rept.*, 516:1–102, 2012. arXiv:1106.0034.

[21] Lillie, Ben and Randall, Lisa and Wang, Lian-Tao. The Bulk RS KK-gluon at the LHC. *JHEP*, 09:074, 2007.

[22] CDF Collaboration, T. Aaltonen *et al.* A search for resonant production $t\bar{t}$ pairs in 4.8 fb^{-1} of integrated luminosity of $p\bar{p}$ collisions at$\sqrt{s} = 1.96$ TeV. *Phys. Rev.*, D84:072004, 2011. arXiv:hep-ex/1107.5063[hep-ex].

[23] CDF Collaboration, T. Aaltonen *et al.* Search for resonant production of $t\bar{t}$ decaying to jets in $p\bar{p}$ collisions at $\sqrt{s} = 1.96$ TeV. *Phys. Rev.*, D84:072003, 2011. arXiv:hep-ex/1108.4755[hep-ex].

[24] DØ Collaboration. Search for $t\bar{t}$ resonances in the lepton plus jets final states in $p\bar{p}$ collisions at$\sqrt{s} = 1.96$ TeV. *Phys. Lett.*, B668:98–104, 2008. arXiv:hep-ex/0804.3664[hep-ex].

[25] The CMS Collaboration. Search for resonant t t-bar production in proton-proton collisions at $\sqrt{s)} = 8$ TeV. *Phys. Rev. D*, 93:012001, 2016. http://journals.aps.org/prd/abstract/10.1103/PhysRevD.93.012001, arXiv:1506.03062.

[26] Georges Aad et al. A search for $t\bar{t}$ resonances using lepton-plus-jets events in proton-proton collisions at $\sqrt{s} = 8$ TeV with the ATLAS detector. *JHEP*, 08:148, 2015.

[27] ATLAS Collaboration. Search for $t\bar{t}$ resonances in the lepton plus jets final state with ATLAS using 4.7 fb^{-1} of pp collisions at $\sqrt{s} = 7$ TeV. *Phys. Rev. D*, 88(1):012004, 2013.

[28] R. M. Harris and S. Jain. Cross Sections for Leptophobic Topcolor Z' Decaying to Top-Antitop. *Eur. Phys. J.*, C72:2072, 2012.

[29] Aine Kobayashi, Anna Shcherbakova, Chiara Rizzi, Aurelio Juste Rozas, Sara Kristina Strandberg, and Yuji Enari. Measurement of the b-Tagging Efficiency of the MV1 algorithm for High pT in pp Collisions at $\sqrt{s} = 8$ TeV using multi-jet events. Technical Report ATL-COM-PHYS-2015-630, CERN, Geneva, Jul 2015. `https://cds.cern.ch/record/2032163`.

[30] PDG. The TOP QUARK. http://pdg.lbl.gov/2015/reviews/rpp2015-rev-top-quark.pdf.

[31] Makoto Kobayashi and Toshihide Maskawa. CP-Violation in the Renormalizable Theory of Weak Interaction. *Prog. Theor. Phys.*, 49:652, 1973.

[32] Discoveries at Fermilab The Top Quark. `http://www.fnal.gov/pub/inquiring/physics{/\penalty\exhyphenpenalty}/discoveries/top_quark.html`.

[33] The CDF experiment. http://www-cdf.fnal.gov.

[34] The CDF Collaboration. Observation of Top Quark Production in $\bar{p}$p Collisions with the CDF Detector at Fermilabi. *FEMILAB-PUB-95*, 022-E, 1995. CDF/PUB/TOP/PUBLIC/3040.

[35] The DØ experiment. http://www-d0.fnal.gov.

[36] The ATLAS Collaboration. Search for WZ resonances in the fully leptonic channel using pp collisions at $\sqrt{s} = 8$ TeV with the ATLAS detector. *arXiv:1406.4456[hep-ex]*, 2014. `http://www.sciencedirect.com/science/article/pii/S0370269314006066`.

[37] R. Foadi. 125 GeV Higgs from a not so light Technicolor Scalar, 2012. *arXiv:1211.1083[hep-ph]*.

[38] R. M. Harris, C. T. Hill and S. J. Parke. Cross-section for topcolor Z-prime(t) decaying to t anti-t: Version 2.6 (1999). *arXiv:hep-ph/9411426[hep-ph]*.

[39] R. M. Harris, C. T. Hill and S. J. Parke. Cross Section for Topcolor Z' decaying to top-antitop. *arXiv:hep-ph/9911288[hep-ph]*.

[40] Koji Terashi. Exotics theories and analysis, ICEPP CERN summer school lecture slides, 2013.

[41] `https://twiki.cern.ch/twiki/bin/viewauth/AtlasProtected/KKGravitonToTTbar`.

[42] The ATLAS Collaboration. b-tagging in dense environments. Technical report, ATL-PHYS-PUB-2014-014, CERN, Geneva, August 2014.

[43] ATLAS experiment - Top Public Results page. https://twiki.cern.ch/twiki/bin/view/AtlasPublic/TopPublicResults.

[44] The ATLAS Collaboration. ATLAS Experiment at the CERN Large Hadron Collider, 2008. *JINST*, 3:S08003, 2008.

[45] CERN homepage. http://home.cern.

[46] Lyndon Evans and Philip Bryant. *JINST*, 3:S08001, 2008. LHC machine, 2008.

[47] ATALS homepage. http://atlas.cern.

[48] CMS homepage. http://cms.web.cern.ch.

[49] ATLAS Data Summary 2015 pp at 13 TeV. https://atlas.web.cern.ch/Atlas/GROUPS/DATAPREPARATION/DataSummary/2015/daysum.py.

[50] L.Ponce on behalf of the LHC team, LHC Machine Status report, Dec. 2015. https://indico.cern.ch/event/460278/contributions/1130099/attachments/1197697/1741410/LHCStatusDec2015.pdf.

[51] ATLAS EXPERIMENT - Public Results homepage. https://twiki.cern.ch/twiki/bin/view/AtlasPublic/WebHome.

[52] Letter of Intent for the Phase-I Upgrade of the ATLAS Experiment. Technical Report CERN-LHCC-2011-012. LHCC-I-020, CERN, Geneva, Nov 2011. http://cds.cern.ch/record/1402470.

[53] Ted Liu and T. Kawamoto. Proceedings of the 2nd International Conference on Technology and Instrumentation in Particle Physics (TIPP 2011) ATLAS: Status, Limitations and Upgrade Plans. *Physics Procedia*, 37:170 – 180, 2012. http://www.sciencedirect.com/science/article/pii/S187538921201680X.

[54] M. Capeans et al. ATLAS Insertable B-Layer Technical Design Report. *CERN-LHCC-2010-013*, 2010. https://cds.cern.ch/record/1291633.

[55] A. Yamamoto *et al.* The ATLAS central solenoid. *Nucl. Instrum. Meth.*, A 584:53, 2008.

[56] The ATLAS Collaboration. Studies of the ATLAS Inner Detector material using $\sqrt{s} =$ 13 TeV pp collision data. 2015.

[57] The ATLAS Collaboration. Track Reconstruction Performance of the ATLAS Inner Detector at $\sqrt{s} = 13$ TeV. Technical Report ATL-PHYS-PUB-2015-018, ATL-PHYS-PUB-2015-018, CERN, Geneva, July 2015.

[58] https://twiki.cern.ch/twiki/bin/view/AtlasProtected/InDetTrackingDC14.

[59] ATLAS Inner detector: technical design report. 1. Technical report, CERN, 1997, CERN-LHCC-97-016. https://cds.cern.ch/record/331063.

[60] ATLAS Inner detector: technical design report. 2. Technical report, CERN, 1997, CERN-LHCC-97-017. https://cds.cern.ch/record/331064.

[61] A. Abdesselam et al. The barrel modules of the ATLAS semiconductor tracker. *Nucl. Instrum. Meth.*, A568:642–671, 2006.

[62] A. Abdesselam et al. The ATLAS semiconductor tracker end-cap module. *Nucl. Instrum. Meth.*, A575:353–389, 2007.

[63] E. Abat et al. The ATLAS Transition Radiation Tracker (TRT) proportional drift tube: Design and performance. *JINST*, 3:P02013, 2008.

[64] M. Aharrouche *et al.*, ATLAS Electromagnetic Barrel Calorimeter Collaboration. Energy Linearity and Resolution of the ATLAS Electromagnetic Barrel Calorimeter in an Electron Test-Beam. *Nucl. Instrum. Meth.*, A569:601–623, 2006. arXiv:phyisics/0608012v1[physics.ins-det].

[65] Sandro Palestini. The Muon Spectrometer of the ATLAS Experiment. Technical report, 2003. (Proc. Suppl.).

[66] The ATLAS Collaboration. Improved luminosity determination in pp collisions at $\sqrt{s} =$ 7 TeV using the ATLAS detector at the LHC. *Eur. Phys. J*, C 73:2518, 2013. http://link.springer.com/article/10.1140/epjc/s10052-013-2518-3.

[67] H. Burkhardt M. Lamont S. M. White, R. Alemany-Fernandez. First Luminosity scans in the LHC. Technical report, CERN, Geneva. http://accelconf.web.cern.ch/AccelConf/IPAC10/papers/mopec014.pdf.

[68] S. Van Der Meer. Technical report. ISR-PO/68-31, KEK68-64.

[69] https://twiki.cern.ch/twiki/bin/view/Atlas/TdaqOrgStructure.

[70] The LHC experiments Comittee ; LHCC. Technical Design Report for the Phase-I Upgrade of ATLAS TDAQ System. Technical report, CERN, CERN-LHCC-2013-018 ; ATLAS-TDR-023, Geneva, September 2013.

[71] The ATLAS Collaboration. 2015 start-up trigger menu and initial performance assessment of the ATLAS trigger using Run-2 data. Technical report, CERN, ATL-DAQ-PUB-2016-001, Geneva, March 2016.

[72] Jumpei Maeda on behalf of the ATLAS-Japan. Status report of the ATLAS experiment. Technical report, Tohoku Gakuin University, March 2016. JPS 71th Annual Meeting.

[73] the Worldwide LHC Computing Grid homepage. http://wlcg.web.cern.ch/.

[74] Luminosity summary plots for Run2. https://twiki.cern.ch/twiki/bin/view/AtlasPublic/LuminosityPublicResultsRun2.

[75] ATLAS Twiki Pileup Reweighting, Extended Pileup Reweighting. https://twiki.cern.ch/twiki/bin/viewauth/AtlasProtected/PileupReweighting, https://twiki.cern.ch/twiki/bin/view/AtlasProtected/ExtendedPileupReweighting.

[76] The ATLAS Collaboration. Pile-up subtraction and suppression for jets in ATLAS. 2013. https://cds.cern.ch/record/1570994.

[77] The ATLAS Collaboration. The ATLAS Simulation Infrastructure. *Eur.Phys.J*, C70:823, 2010. arXiv:physics.ins-det/1005.4568[physics.ins-det].

[78] ATLAS simulation wikipage. https://twiki.cern.ch/twiki/bin/view/AtlasComputing/AtlasSimulation.

[79] A. Agostinelli et al. *Nucl. Instrum. Meth. A*, 506:250, 2003.

[80] J.M. Campbell, J.W. Huston, W.J. Stirling. Hard Interactions of Quarks and Gluons: a Primer for LHC Physics. *Rept. Prog. Phys.*, 70:89, 2007. arXiv:hep-ph/0611148, https://arxiv.org/abs/hep-ph/0611148.

[81] Field, Rick D. The Underlying event in hard scattering processes. *eConf*, C010630:P501, 2001. https://arxiv.org/abs/hep-ph/0201192.

[82] G. Aad et al. The ATLAS Simulation Infrastructure. *Eur. Phys. J.*, C70:823–874, 2010.

[83] Torbjorn Sjostrand, Stephen Mrenna, Peter Skands. PYTHIA 6.4 Physics and Manual. *JHEP*, 05:026, 2006. Comput. Phys. Comm. 178 (2008) 852, arXiv:hep-ph/0603175[hep-ph].

[84] PYTHIA 8 online manual. http://home.thep.lu.se/~torbjorn/pythia81html/Welcome.html,.

[85] Sjostrand, Torbjorn and Mrenna, Stephen and Skands, Peter Z. A Brief Introduction to PYTHIA 8.1. *Comput. Phys. Commun.*, 178:852–867, 2008.

[86] G.Corcella, I.G.Knowles, G.Marchesini, S.Moretti, K.Odagiri, P.Richardson, M.H.Seymour, B.R.Webber. HERWIG 6.5: an event generator for Hadron Emission Reactions With Interfering Gluons (including supersymmetric processes). *JHEP*, 01:010, 2001. arXiv:hep-ph/0011363[hep-ph].

[87] Paolo Nason. A New Method for Combining NLO QCD with Shower Monte Carlo Algorithms. *JHEP*, 11:040, 2004. arXiv:hep-ph/0409146[hep-ph].

[88] Paolo Nason, Bryan Webber. Next-to-Leading-Order Event Generators. arXiv:hep-ph/1202.1251v1[hep-ph].

[89] Sherpa homepage. https://sherpa.hepforge.org/trac/wiki.

[90] Frank Krauss, Andreas Schaelicke, Steffen Schumann, Gerhard Soff. Simulating W/Z+jets production at the CERN LHC. *Phys. Rev.*, D72:054017, 2005. arXiv:hep-ph/0503280, https://arxiv.org/abs/hep-ph/0503280.

[91] J. Alwall, R. Frederix, S. Frixione, V. Hirschi, F. Maltoni, O. Mattelaer, H.-S. Shao, T. Stelzer, P. Torrielli, M. Zaro. The automated computation of tree-level and next-to-leading order differential cross sections, and their matching to parton shower simulations. *JHEP*, 07:079, 2014. arXiv:1405.0301 [hep-ph].

[92] S. Frixione, B.R. Webber. Matching NLO QCD computations and parton shower simulations. *JHEP*, 06:029, 2002. arXiv:hep-ph/0204244[hep-ph].

[93] D. J. Lange. The EvtGen particle decay simulation package. *Nucl. Instrum. Meth.*, A462:152–155, 2001.

[94] Peter Skands. Tuning Monte Carlo Generators: The Perugia Tunes. *Phys. Rev.*, D82:074018, 2010.

[95] Hung-Liang Lai et al. New parton distributions for collider physics. *Phys. Rev. D*, 82:074024, 2010.

[96] Jun Gao et al. CT10 next-to-next-to-leading order global analysis of QCD. *Phys. Rev. D*, 89:033009, 2014.

[97] M. Aliev, H. Lacker, U. Langenfeld, S. Moch, P. Uwer, et al. HATHOR: HAdronic Top and Heavy quarks crOss section calculatoR. *Comput.Phys.Commun.*, 182:1034–1046, 2011.

[98] Johann H. Kuhn, A. Scharf, and P. Uwer. Electroweak corrections to top-quark pair production in quark-antiquark annihilation. *Eur.Phys.J.*, C45:139–150, 2006.

[99] Johann H. Kuhn, A. Scharf, and P. Uwer. Electroweak effects in top-quark pair production at hadron colliders. *Eur.Phys.J.*, C51:37–53, 2007.

[100] J. H. Kuhn, A. Scharf, and P. Uwer. Weak Interactions in Top-Quark Pair Production at Hadron Colliders: An Update. *Phys. Rev.*, D91(1):014020, 2015.

[101] Richard D. Ball et al. Parton distributions with LHC data. *Nucl. Phys. B*, 867:244–289, 2013.

[102] ATLAS Experiment Public Results, ATLAS Stand-Alone Event Displays. `https://twiki.cern.ch/twiki/bin/view/AtlasPublic/EventDisplayStandAlone`.

[103] W. Lanpl, S. Lasplace, D. Lelas, P. Loch, H. Ma, S. Menke, S. Rajagopolan, D. Rousseau, S. Snyder, G. Unal. Calorimeter Clustering Algorithms : Description and Performance. 2008. `https://cds.cern.ch/record/1099735`.

[104] Maetteo Cacciari, Gavin P. Salam and Gregory Soyez. The anti-k_t jet clustering algorithm. *JHEP*, 0804:063, 2008. arXiv:hep-ph/0802.1189[hep-ph].

[105] Aad, G. and others, The ATLAS Collaboration. Expected Performance of the ATLAS Experiment - Detector, Trigger and Physics. 2009.

[106] `https://twiki.cern.ch/twiki/bin/view/AtlasProtected/HowToCleanJets2015`.

[107] The ATLAS Collaboration. Jet Calibration and Systematic Uncertainties for Jets Reconstructed in the ATLAS Inner Detector at$\sqrt{s} = 13$ TeV. Technical Report ATL-PHYS-PUB-2015-015, ATL-PHYS-PUB-2015-015, CERN, Geneva, July 2015.

[108] The ATLAS Collaboration. Jet energy measurement with the atlas detector in proton-proton collisions at $\sqrt{s} = 7$ TeV. *Eur. Phys. J.*, C73:2304, 2011. arXiv:hep-ex/1112.6426[hep-ex].

[109] Aad, Georges and others, ATLAS Collaboration. Jet energy measurement and its systematic uncertainty in proton-proton collisions at $\sqrt{s} = 7$ TeV with the ATLAS detector. *Eur. Phys. J.*, C75:17, 2015.

[110] The ATLAS Collaboration. Data-driven determination of the energy scale and resolution of jets reconstructed in the ATLAS calorimeters using dijet and multijet events at$\sqrt{s} = 8$ TeV. Technical Report ATLAS-CONF-2015-017, ATLAS-CONF-2015-017, CERN, Geneva, April 2015.

[111] Monte Carlo Calibration and Combination of In-situ Measurements of Jet Energy Scale, Jet Energy Resolution and Jet Mass in ATLAS. Technical Report ATLAS-CONF-2015-037, CERN, Geneva, Aug 2015. `https://cds.cern.ch/record/2044941`.

[112] Public plots: Jet energy uncertainties using full 13 TeV 2015 dataset. `http://atlas.web.cern.ch/Atlas/GROUPS/PHYSICS/PLOTS/JETM-2016-002/`.

[113] The ATLAS Collaboration. Tagging and suppression of pileup jets with the ATLAS detector. 2016. `https://cds.cern.ch/record/1700870`.

[114] A. Hoecker, P. Speckmayer, J. Stelzer, J. Therhaag, E. von Toerne, and H. Voss. Tmva: Toolkit for multivariate data analysis. *PoS*, ACAT:040, 2007. arXiv:physics/0703039[physics.data-an].

[115] Georges Aad et al. Performance of jet substructure techniques for large-*R* jets in proton-proton collisions at $\sqrt{s}$ = 7 TeV using the ATLAS detector. *JHEP*, 09:076, 2013.

[116] David Krohn, Jesse Thaler, Lian-Tao Wang. Jet Trimming. Technical report, 2010. arXiv:0912.1342 [hep-ph].

[117] The ATLAS collaboration. Performance of jet substructure techniques for large-R jets in proton-proton collisions at $\sqrt{s} = 7$ TeV using the ATLAS detector. *Journal of High Energy Physics*, 2013(9):1–83, 2013. `http://dx.doi.org/10.1007/JHEP09(2013)076`.

[118] S. Catani *et al.* New clustering algorithm for multi-jet cross-sections in e^+e^- annihilation. *Phys.Lett*, B269:432, 1991.

[119] S. Catani *et al.* Longitudinally invariant K_t clustering algorithms for hadron hadron collisions. *Nucl.Phys.*, B406:187, 1993.

[120] ATLAS Collaboration. Topological cell clustering in the ATLAS calorimeters and its performance in LHC Run 1. *submitted to Eur. Phys. J C*, 2016.

[121] The ATLAS Collaboration. Boosted hadronic top identification at ATLAS for early 13 TeV data. Technical Report ATL-PHYS-PUB-2015-053, ATL-PHYS-PUB-2015-053, CERN, Geneva, December 2015.

[122] Boosted hadronic top identification at ATLAS for early 13 TeV data. Technical Report ATL-PHYS-PUB-2015-053, CERN, Geneva, Dec 2015. `https://cds.cern.ch/record/2116351`.

[123] J. Thaler and K. Van Tilburg. Identifying Boosted Objects with N-subjettiness. *JHEP*, 1103:015, 2011. arXiv:hep-ph/1011.2268[hep-ph].

[124] J. Thaler and K. Van Tilburg. Maximizing Boosted Top Identification by Minimizing N-subjettiness. *JHEP*, 1202:093, 2012. arXiv:hep-ph/1108.2701[hep-ph].

[125] A. J. Larkoski, D. Neill and J. Thaler. Jet Shapes with the Broadening Axis. *JHEP*, 1404:017, 2014. arXiv:hep-ph/1401.2158[hep-ph].

[126] The ATLAS Collaboration. Performance of jet substructure techniques for large-R jets in proton-proton collisions at$\sqrt{s} = 7$ TeV using the ATLAS detector. Technical report, 2013.

[127] M. Cacciari and G. P. Salam. Pileup subtraction using jet areas. Technical report, 2008. arXiv:0707.1378 [hep-ph].

[128] The ATLAS collaboration. Electron efficiency measurements with the ATLAS detector using the 2015 LHC proton proton collision data. 2016.

[129] The ATLAS Collaboration. Electron performance measurements with the ATLAS detector using the 2010 LHC proton-proton collision data. *Eur. Phys. J.*, C72:1909, 2012.

[130] Thijs G. Cornelissen, M. Elsing, I. Gavrilenko, J. F. Laporte, W. Liebig, M. Limper, K. Nikolopoulos, A. Poppleton, and A. Salzburger. The global chi**2 track fitter in ATLAS. *J. Phys. Conf. Ser.*, 119:032013, 2008.

[131] ATLAS Collaboration. Expected photon performance in the ATLAS experiment. Technical report, ATL-PHYS-PUB-2011-007, CERN, Geneva, April 2011. `https://cds.cern.ch/record/1345329`.

[132] `https://twiki.cern.ch/twiki/bin/view/AtlasProtected/EGammaIdentificationRun2`.

[133] Georges Aad et al. Muon reconstruction performance of the ATLAS detector in proton proton collision data at $\sqrt{s}$ =13 TeV. *Eur. Phys. J.*, C76(5):292, 2016.

[134] J. Illingworth and J. Kittler. A survey of the Hough transform. *Computer Vision, Graphics, and Image Processing*, 44:87–116, 1988. issn: 0734-189X, http://www.sciencedirect.com/science/article/pii/S0734189X88800331.

[135] ATLAS Collaboration. Measurement of the muon reconstruction performance of the atlas detector using 2011 and 2012 lhc proton proton collision data. *Eur. Phys. J.*, C74:3130, 2014.

[136] ATLAS Collaboration. Muon reconstruction performance of the ATLAS detector in proton proton collision data at $\sqrt{s} = 13$ TeV. Technical report, CERN, Geneva, Mar 2016.

[137] The ATLAS Collaboration. Performance of Missing Transverse Momentum Reconstruction in Proton-Proton Collisions at $\sqrt{s} = 7$ TeV with ATLAS. *Eur. Phys. J.*, C72:1844, 2012. arXiv:hep-ex/1108.5602[hep-ex].

[138] CERN LHC ; ATLAS ; Particle Physics Experiment. Using Event Weights to account for differences in Instantaneous Luminosity and Trigger Prescale in Monte Carlo and Data. Technical report, ATL-COM-SOFT-2015-119, CERN, May 2015.

[139] ATLAS Public plots : Missing transverse energy (E_T^{miss}) performance and systematic uncertainties using the full 2015 dataset. http://atlas.web.cern.ch/Atlas/GROUPS/PHYSICS/PLOTS/JETM-2016-003.

[140] Public Egamma Trigger Plots for Collision Data. https://twiki.cern.ch/twiki/bin/view/AtlasPublic/EgammaTriggerPublicResults.

[141] Public Muon Trigger Plots for Collision Data. https://twiki.cern.ch/twiki/bin/view/AtlasPublic/MuonTriggerPublicResults.

[142] https://twiki.cern.ch/twiki/bin/view/AtlasProtected/IsolationSelectionTool.

[143] ATLAS Collaboration. Muon reconstruction performance in early $\sqrt{s} = 13$ TeV data. Technical report, ATL-PHYS-PUB-2015-037, CERN, Geneva, Aug 2015. https://cds.cern.ch/record/2047831.

[144] https://twiki.cern.ch/twiki/bin/view/AtlasProtected/BTaggingBenchmarks.

[145] Kevin Kröninger, Andreas B. Meyer, Peter Uwer. Top-Quark Physics at the LHC. 2015. arXiv:1506.02800 [hep-ex].

[146] B.C. Allanach, K. Odagiri, M.A. Parker, B.R. Webber. Searching for Narrow Graviton Resonances with the ATLAS Detector at the Large Hadron Collider. *JHEP*, 9:019, 2000. arXiv:hep-ph/0006114.

[147] The ATLAS Collaboration. Expected performance of the ATLAS b-tagging algorithms in Run-2. Technical report, ATL-PHYS-PUB-2015-022, CERN, Geneva, July 2015.

[148] The ATLAS Collaboration. Impact parameter-based b-tagging algorithms in the 7 TeV collision data with the ATLAS detector: the TrackCounting. Technical report, ATLAS-CONF-2010-041, CERN, Geneva, July 2010. https://cds.cern.ch/record/1277681.

[149] The ATLAS Collaboration. Performance of the ATLAS Secondary Vertex b-tagging Algorithm in 7 TeV Collision Data. Technical Report ATLAS-CONF-2010-042, ATLAS-CONF-2010-042, CERN, Geneva, July 2010. https://cds.cern.ch/record/1277682.

[150] The ATLAS Collaboration. Commissioning of the ATLAS high-performance b-tagging algorithm in the 7 TeV collision data. Technical report, ATLAS-CONF-2011-102, CERN, Geneva, July 2011. https://cds.cern.ch/record/1369219.

[151] The ATLAS Collaboration. Flavor Tagging with Track Jets in Boosted Topologies with the ATLAS Detector. Technical report, ATL-PHYS-PUB-2014-013, CERN, 2014. https://cds.cern.ch/record/1750681.

[152] Danilo Enoque Ferreira de Lima. Top-antitop cross section measurement as a function of the jet multiplicity in the final state and beyond the Standard Model top-antitop resonances search at the ATLAS detector at CERN. 2014. Ph.D. Thesis, School of Phyisics and Astonomy College of Science and Engineering.

[153] ATLAS Twiki TtbarResonances2015. https://twiki.cern.ch/twiki/bin/viewauth/AtlasProtected/TtbarResonances2015.

[154] The ATLAS Collaboration. Search for heavy particles decaying to pairs of highly-boosted top quarks using lepton-plus-jets events in proton-proton collisions at $\sqrt{s} = 13$ TeV with the ATLAS detector. 2016. https://cds.cern.ch/record/2141001.

[155] The ATLAS Collaboration. A search for top-antitop resonances using proton-proton collisions at $\sqrt{s} = 13$ TeV. Technical report, ATL-COM-PHYS-2015-294, CERN, 2015. https://cds.cern.ch/record/2010613.

[156] ATLAS Collaboration. Measurement of the charge asymmetry in top quark pair production in pp collisions at $\sqrt{s} = 7$ TeV using the ATLAS detector. *Eur. Phys. J. C*, 72:2039, 2012.

[157] ATLAS Collaboration. Measurements of top quark pair relative differential cross-sections with ATLAS in pp collisions at $\sqrt{s} = 7$ TeV. *Eur. Phys. J. C*, 73:2261, 2013.

[158] ATLAS Collaboration. Measurement of the top quark pair production cross-section with ATLAS in the single lepton channel. *Phys. Lett. B*, 711:244–263, 2012.

[159] ATLAS Collaboration. Estimation of non-prompt and fake lepton backgrounds in final states with top quarks produced in proton–proton collisions at $\sqrt{s} = 8$ TeV with the ATLAS Detector, 2014. ATLAS-CONF-2014-058, http://cdsweb.cern.ch/record/1951336.

[160] ATLAS Collaboration. Identification of high transverse momentum top quarks in pp collisions at $\sqrt{s} = 8$ TeV. *JHEP*, 06:093, 2016. arXiv:1603.03127 [hep-ex], https://arxiv.org/abs/1603.03127.

[161] `https://twiki.cern.ch/twiki/bin/view/LHCPhysics/TtbarNNLO`.

[162] Matteo Cacciari, Michal Czakon, Michelangelo Mangano, Alexander Mitov, and Paolo Nason. Top-pair production at hadron colliders with next-to-next-to-leading logarithmic soft-gluon resummation. *Phys. Lett. B*, 710:612–622, 2012.

[163] Michal Czakon and Alexander Mitov. Top++: A Program for the Calculation of the Top-Pair Cross-Section at Hadron Colliders. *Comput. Phys. Commun.*, 185:2930, 2014.

[164] Martin Beneke, Michal Czakon, Pietro Falgari, Alexander Mitov, and Christian Schwinn. Threshold expansion of the gg(qq-bar)$\rightarrow$ QQ-bar + X cross section at O(alpha(s)**4). *Phys. Lett. B*, 690:483–490, 2010.

[165] M. Beneke, P. Falgari, S. Klein, and C. Schwinn. Hadronic top-quark pair production with NNLL threshold resummation. *Nucl. Phys. B*, 855:695–741, 2012.

[166] U. Langenfeld, S. Moch, and P. Uwer. New results for t anti-t production at hadron colliders. In *Proceedings, 17th International Workshop on Deep-Inelastic Scattering and Related Subjects (DIS 2009)*, 2009. `https://inspirehep.net/record/825772/files/arXiv:0907.2527.pdf`.

[167] Peter Baernreuther, Michal Czakon, and Alexander Mitov. Percent Level Precision Physics at the Tevatron: First Genuine NNLO QCD Corrections to $q\bar{q} \rightarrow t\bar{t} + X$. *Phys. Rev. Lett.*, 109:132001, 2012.

[168] Aneesh V. Manohar and Michael Trott. Electroweak Sudakov corrections and the top quark forward-backward asymmetry. *Physics Letters B*, 711:313–316, 2012. `http://www.sciencedirect.com/science/article/pii/S0370269312004054`.

[169] Botje, Michiel and Butterworth, Jon and Cooper-Sarkar, Amanda and de Roeck, Albert and Feltesse, Joel and others. The PDF4LHC Working Group Interim Recommendations. 2011.

[170] A.D. Martin, W.J. Stirling, R.S. Thorne, and G. Watt. Parton distributions for the LHC. *Eur. Phys. J. C*, 63:189–285, 2009.

[171] Jon Butterworth et al. PDF4LHC recommendations for LHC Run II. *J. Phys. G*, 43:023001, 2016.

[172] ATLAS Collaboration. Measurement of $t\bar{t}$ production with a veto on additional central jet activity in pp collisions at $\sqrt{s} = 7$ TeV using the ATLAS detector. *Eur. Phys.J*, C72:2043, 2012. arXiv:1203.5015 [hep-ex].

[173] ATLAS Collaboration. Comparison of Monte Carlo generator predictions to ATLAS measurements of top pair production at 7 TeV, 2015. ATL-PHYS-PUB-2015-002.

[174] Top systematics 2015. https://twiki.cern.ch/twiki/bin/view/AtlasProtected/TopSystematics2015.

[175] Nikolaos Kidonakis. Two-loop soft anomalous dimensions for single top quark associated production with a W^- or H^-. *Phys. Rev. D*, 82:054018, 2010.

[176] Nikolaos Kidonakis. NNLL resummation for s-channel single top quark production. *Phys. Rev. D*, 81:054028, 2010.

[177] Nikolaos Kidonakis. Next-to-next-to-leading-order collinear and soft gluon corrections for t-channel single top quark production. *Phys. Rev. D*, 83:091503, 2011.

[178] A. L. Read. Presentation of search reqults: The CL(s) technique. *J.Phys.*, G28:2693, (2002).

[179] Procedure for the LHC Higgs boson search combination in summer 2011. Technical Report ATL-PHYS-PUB-2011-011, CERN, Geneva, Aug 2011. https://cds.cern.ch/record/1375842.

[180] Tatsuo Kawamoto. *Statistics in Particle Physics, Lecture slides in The University of Tokyo*. http://home.cern.ch/kawamoto/lecture12.html.

[181] HistFactoryLikelihood. https://twiki.cern.ch/twiki/pub/RooStats/WebHome/HistFactoryLikelihood.pdf.

[182] Eilam Gross Ofer Vitells Glen Cowan, Kyle Cranmer. Asymptotic formulae for likelihood-based tests of new physics. *Eur.Phys.J.*, C71:1554, (2011). arXiv:physics.data-an/1007.1727[physics.data-an].

[183] TRexFitter. https://twiki.cern.ch/twiki/bin/view/AtlasProtected/TtHFitter.

[184] RooStats. https://twiki.cern.ch/twiki/bin/view/RooStats/WebHome.

[185] RooFit. http://roofit.sourceforge.net.

[186] The CMS Collaboration. Search for $t\bar{t}$ resonances in boosted semileptonic final states in pp collisions at$\sqrt{s} = 13$ TeV. Mar. 2016. https://cds.cern.ch/record/2138345.

[187] The ATLAS Collaboration. 2013. A search for $t\bar{t}$ resonances in the lepton plus jets final state using $15 fb^{-1}$ of pp collisions at$\sqrt{s} = 8$ TeV.